Spatter and powder evolution in laser powder bed fusion of Nickel-based superalloys

Alexander Gasper

Thesis submitted to the University of Nottingham for the degree of

Doctor of Philosophy

Submitted April 2019

Abstract

Laser powder bed fusion (PBF-LB) technology has matured sufficiently to allow direct manufacture for a range of applications. However, there are still variabilities in processing and difficulties in qualifying parts due to defects inherent to the process. These hinder the wider adoption of the technology and its application in more demanding components, for industries such as aerospace and powder generation, where failure cannot be tolerated. The generation of spatter during processing is an aspect of the process which is considered detrimental, is inherent to the melting process, but has received minimal attention to date. The work in this thesis aims to increase understanding of the spatter particles generated, their influence on the powder in the system, and their effect on parts.

The Nickel-based superalloy Inconel 718, commonly used in turbine applications, is used as an exemplar material to investigate spatter, however, the findings have wider implications. Analysis of the spatter particles showed that they differ from the virgin material in size, shape, and the presence of Al and Ti oxides. These identifiers were used to classify the particles according to their generation mechanism (cold-entrainment, hot-entrainment, and melt ejection) proposed in previous studies. The oxides on the spatter particles were shown to form at the melt pool surface and remain at the surface of the melt ejection. The oxidation and spatter generation was shown to be an issue across four different PBF-LB systems and two powder sources, illustrating that this is a general issue. The spatter particles were identified to be detrimental to the process, particularly in the case of large particles, up to 500 µm, and oxidised particles. Another Nickel-based superalloy, Hastelloy X, was investigated for comparison and showed that although similar spatter was observed, a different oxide regime resulted in spatter with predominantly Si and Cr oxides. A secondary Hastelloy X alloy showed that this oxide formation could be controlled with a reduction in the Si content in the powder, which transitioned the oxidation to be driven by Ti and Al, as in the Inconel 718.

Further analysis of the particle characteristics quantified the difference between the virgin and spatter powders. This showed that on average 50% of the spatter particles were non-spherical, compared to 16% in the virgin gas atomised material. Spatter contained between 2.5-18% of oxidised particles for Inconel 718 across the different PBF-LB systems, and 30% in Hastelloy X. The spatter characteristics were assessed for their size which showed that 44-52% of the non-spherical, 29-99% of the oxidised particles, and 41-78% of all spatter could be removed using common sieve sizes of 45, 53, and 63 µm. The proportion of oxidised spatter

particles was established to be linked to the oxygen pickup of the material and the processing environment in each PBF-LB system. Re-processing of the spatter powder showed that it continued to deteriorate through repeated use for each characteristic. These results illustrated the contribution of incorporated spatter particles in the recycling of powder.

A new method was proposed to investigate the powder bed and estimate the spatter distribution. The results found spatter and oxidised particles in all sections of the powder bed, including >200 µm particles found closest to the gas inlet where the gas flow is greatest, which is in agreement with other studies that found increased spatter content in the powder bed near the gas outlet. The maximum content of spatter in the powder bed was 2.41%, with an average of 1.63% for a build utilisation of 9.1%. The method showed small variations in the particle size distribution and packing density across the bed and larger variations between builds, indicating powder handling produces greater variability in the powder bed content than the recoating mechanism. It was established that these variations could contribute to increased porosity in components.

The effect of spatter particles on the fatigue crack growth (FCG) of PBF-LB material was assessed for 0% spatter (virgin material), 50% spatter, and 100% spatter feedstock powder. Microscopy indicated that the spatter particles had no major effect on the microstructure of the specimen produced but lead to higher oxygen content in the samples, as found with the spatter powder. The fatigue testing showed that the PBF-LB samples performed worse than wrought Inconel 718 material and increased spatter content corresponded to an increase in FCG rate and decrease in cycles to failure. The effect of spatter on the FCG performance was attributed to the increased incidence of defects in material processed with high proportions of spatter. It was shown that large spatter particles and oxides caused lack-of-fusion defects and fatigue cracks propagated between these and the oxide and nitride inclusions, which remained in the parts during processing. Spatter particles were also shown to be capable of creating critical defects which initiate cracks and onset of failure in components.

This work provides an understanding of oxide and spatter formation in PBF-LB and its role throughout the process. As a result of this research, it has been established that the generation of spatter is a gas atomisation process in PBF-LB which creates a secondary powder source different from the virgin material. Therefore, current PBF-LB processing is always some combination of spatter and feedstock powder. These particles can produce critical defects, decreasing the mechanical performance of parts, and contributing to variation in the process. Therefore, it is crucial that their effect is understood.

Acknowledgements

There is no doubt that like most PhDs, my journey to the final destination has been a series of ups and downs. Having never previously seen myself as the kind of person to do a PhD, I have thoroughly enjoyed being a scientist and working on a topic that excites me and I am passionate about. There are of course many people who have helped me to achieve what I have over the years of this PhD, and to finally produce this somewhat weighty tome. Firstly though, as conceited as it might seem, I would like to thank myself. I have had a lot to learn throughout this time, a lot of things I have found difficult, and times that I struggled. For my own sake, and as a hope that all PhD students who have found it difficult at times (I think that is most) will, I would like to pat myself on the back and say well done Alex. Well done for getting through it and producing something that you are proud of, and I hope all PhD students do so. Now for those who helped along the way.

I would like to thank my supervisors Adam 'Sir Megs/The Scouse Rocket' Clare and Ian 'Sm'Ashcroft for their support through my PhD. I would particularly like to thank Adam, who has guided me from the first day and has helped me both with work and outside of work. I would say I lucked out in teaming up with a supervisor who was also a footy and cricket fan and was never adverse to a Friday session with the Nomads and a few ales. I am particularly appreciative of our supervision meetings with the dulcet tones of Blowers and Aggers on TMS in the background. To Ian, I would like to thank you and apologise for the laborious efforts to review and improve my writing. Although in the context it might not have been, I will take the comment that my writing often reads 'more like a James Joyce novel than a scientific paper' as a compliment and hope that if my scientific/engineer career doesn't go well that I have a backup. I would also like to thank Dr. Chris Hyde for his support with designing and undertaking my fatigue experiments.

I would like to thank Oerlikon Metco and Oerlikon AM for their support and sponsorship of my PhD. With that I would like to thank Florian Maurer for believing in me and bringing me into Oerlikon. Thank you to Konstantin von Niessen and Jeet Sharma for their support early through the PhD and for my time in Westbury. I am appreciative for all those at the facility at Westbury for taking me in and helping me, particularly to Walter and Lu for their generous

and memorable hospitality. For the latter part of my PhD I would like to give special thanks to Blanka Szost, Xiqian (April) Wang, and Dan Johns for their amazing support and supervision, and also to the rest of the team in Munich.

Much of the work in this thesis could not have been done without the support of a range of technicians. I am indebted to Mark Hardy, who without his hard work, the metal AM section of our lab would not be able to function. Thanks for all your help and for making the time in the lab much more enjoyable. Many thanks to Jason Greaves for his extensive time and effort in helping me to design and complete the fatigue testing. I would also like to thank a range of other technicians who have helped me across many other areas: Alex Jackson-Crisp, Justo Ferreira, Joe White, Mark East, Tom Buss, Martin Roe, Chris Parmenter, and Nigel Neate.

During my PhD, I had the honour of receiving a JSPS Short-Term Fellowship for which I spent three months undertaking research at the Joining and Welding Research Institute at Osaka University. I am indebted to Prof. Masahiro Tsukamoto-sensei and Dr. Yuji Sato-san for supporting me and being the most incredible and hospitable hosts. You really made my time in Japan incredible and I look forward to returning.

There are many friends and colleagues I would like to thank who have helped me through the difficult points and have made the years of my PhD much more enjoyable. My biggest thanks is to Duncan Hickman, who won't appreciate how much help he has provided me in getting this PhD done, with all of our little chats, discussing through thoughts, ideas, and problems, without which I wouldn't have had half my best ideas/solutions. Big thanks to my Hong Kong and ice cream brother, Hatim Cader, for his help and friendship, particularly with writing up the thesis and providing me with invaluable feedback. A big thanks to Zhengkai 'Big Z' Xu, Luke Toddhunter, Paddy Bointon, Sal La Cavera, Adam Thompson, and Carlo Campanelli for being great friends and making the hours/weeks/years in the office fly by. Thank you as well to the rest of my friends, particularly the News Team ones, who have always been there for me.

To Mum, Dad, Rob, and Will, thank you very much for all your support throughout the whole journey to where I am today. You are all amazing and I love you all. And to my partner Hannah, thank you with everything I have. I hope one day you will finally understand how much you help me and how important you are to me.

List of Publications

Publication included in thesis

A.N.D. Gasper, B. Szost, X. Wang, D. Johns, S. Sharma, A.T. Clare, I.A. Ashcroft, Spatter and oxide formation in laser powder bed fusion of Inconel 718, Addit. Manuf. (2018). doi:10.1016/J.ADDMA.2018.09.032.

A. N. D. Gasper, D. Hickman, A. T. Clare, I. Ashcroft, S. Sharma, X. Wang, B. Szost, D. Johns , Oxide and spatter powder formation during laser powder bed fusion of Hastelloy X, Pow. Tech (2019). doi:10.1016/j.powtec.2019.06.004

Publication not included in thesis

A.N.D. Gasper, S. Catchpole-Smith, A.T. Clare, In-situ synthesis of titanium aluminides by direct metal deposition, J. Mater. Process. Technol. 239 (2017). doi:10.1016/j.jmatprotec.2016.08.031.

Table of Contents

Table of Figures

Table of Tables

Table of Equations

Nomenclature

AM – Additive manufacturing

CT – Compact tension

DED – Direct energy deposition

FCG – Fatigue crack growth

FCGR – Fatigue crack growth rate

PBD – Powder bed density

PBF-LB – Laser powder bed fusion, or powder bed fusion – laser beam

PBF-EB – Powder bed fusion – electron beam

PSD – Particle size distribution

XCT - X-ray computer tomography

Chapter 1 Introduction

1.1 Additive manufacturing and laser powder bed fusion

Many industries are beginning to take advantage of the possibilities that additive manufacturing (AM) can provide, including the complex structures that can be created, in exploring new materials, and in producing bespoke and small batch manufacture. The geometric design freedoms allow benefits such as the consolidation of multiple components, design optimisation, increased functionality, and increased resource utilisation. The technology has progressed from being used for rapid prototyping and tooling and is beginning to move towards industrialisation and mass production. For the manufacture of metal components, laser powder bed fusion (PBF-LB) is the leading process and has begun to be used for serial production for some components. However, the production of structural components using the technology still has many challenges for industry and academia. The wider adoption of the technology is hampered by inconsistencies and variability in the process and parts produced. These issues inhibit the adoption of the technology for highly demanding applications, such as in aerospace and power generation, where they could potentially provide great advantages over current components but where failure cannot be tolerated.

One issue which can cause variations in builds and resulting properties due to random defects is spatter, a process by-product from the laser-material interaction. Spatter is a phenomenon generally associated with welding where molten material is ejected from the weld zone and can be seen by the eye as sparks. Spatter can be seen in PBF-LB as streaks shown in Figure 1.1. PBF-LB is essentially a powder micro-welding process, which adds a level of complexity over the welding of a solid body [1]. Spatter in PBF-LB involves material ejection from the melt pool, as in welding, but also has the effect of redistributing powder in the area surrounding the melt pool, due to entrainment from vapour pressure produced by the vaporisation of some of the melt pool [2]. Whereas with welding, the material ejected is not an issue as long as the integrity of the weld is satisfactory, in PBF-LB the ejected and redistributed material can cause issues from landing on and effecting other areas of the powder bed, or removing material so there is not sufficient to process, hence creating voids. The generation of this spatter raises

questions such as; what is the new material produced by this process, what are the effects on the powder in the system, and what resultant affects are there on part properties. These are key questions for the development of components for high performance applications, such as in the aerospace industry. The development of a random defect due to spatter incorporation makes it difficult for the technology to compete for manufacturing components such as turbine blades which are currently manufactured as defect-free single crystals, even if AM can incorporate more complex functionality.

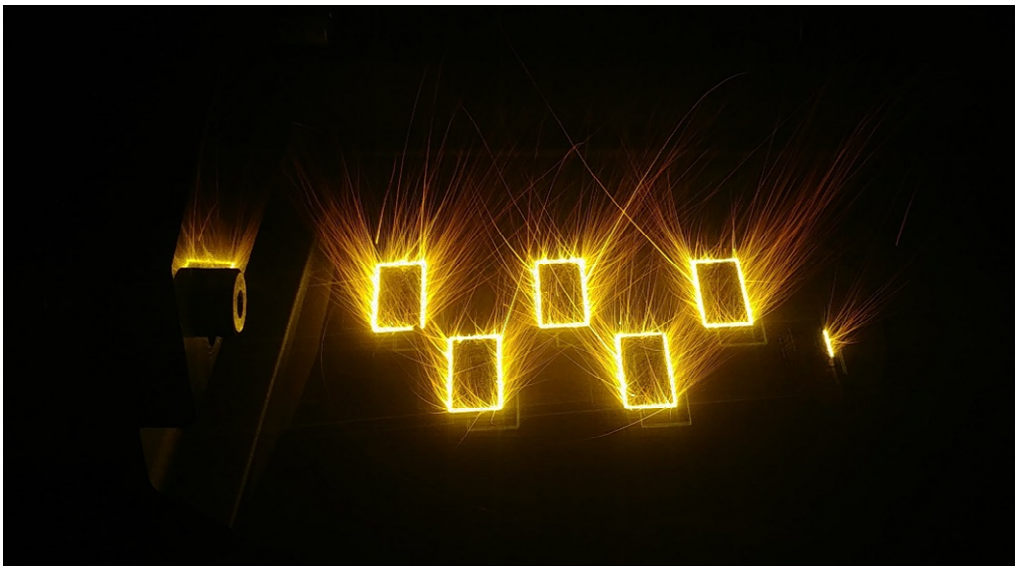

Figure 1.1 Long exposure image of spatter generation of Inconel 718 on the Trumpf LMF TruPrint1000 machine during the border scan of a set of specimen produced for Chapter 8

Spatter is also a problem for build utilisation, this being the proportion of the available powder bed build volume which is consolidated to produce the parts. For PBF-LB to be economic it generally requires high utilisation of the build volume. A higher utilisation of the build area leads to the generation of more spatter and, hence, the potential for more defects. As far as is known, spatter is inherent to the laser welding process and although it can be reduced through changing laser parameters or characteristics these may not be desirable parameters for other build quality metrics. A key element of this work is establishing that the material ejection from the melt pool is a powder atomisation/manufacturing process and creates a secondary powder system within the PBF-LB process. This has implications for the powder used in the process, which is another cause of variability in PBF-LB, particularly as, for the process to be economic, powder must be recycled from one build to the next. The issues regarding spatter are not currently well understood and the work in this thesis aims to

increase understanding and consideration for the implications that spatter can have on the process. This is important as PBF-LB systems are currently being driven to use higher powered lasers, multiple lasers, and larger build volumes which will all exacerbate issues due to spatter.

Another source of defects in PBF-LB, which is linked to spatter generation is the formation of oxides during processing. The PBF-LB process occurs in a chamber flooded with inert gas to reduce oxidation. Even so, oxide formation is an aspect which has been identified in some PBF-LB research to occur and have an impact on the part quality and performance of components [3–5]. Machine manufacturers have generally just stated that their machines operate in an inert environment to minimise oxidation without any further comment on levels of oxidation which may occur. Some manufacturers have made attempts to address and qualify oxidation pickup in their systems, such as Renishaw plc [6,7], however the formation of oxides has not been addressed. The primary issue with oxidation in PBF-LB is related to the intrinsically additive nature of the process, with parts being manufactured by a procession of many micro welds. In a conventional casting process oxides will have a chance to form as slag and be at the surface of the material. This is not possible in PBF-LB due to the high cooling rates, flow currents in the melt pool, and the additive nature of the process, which builds parts layer-by-layer which will tend to trap any oxides within the bulk material. These will play a role in the static and dynamic performance of the part, hence, it is important to understand and qualify them in the process.

1.2 Thesis aim, objective, and methodologies

Aim of the research:

This work aims to provide a new understanding of spatter and oxidation in PBF-LB, particularly for Nickel-based superalloys, and the implications it can have on the process. The work intends to provide an insight into the changes in the virgin material through PBF-LB processing and, specifically, the generation of spatter and the effect of this on the powder feedstock. A further aim is to understand the proportion of spatter in the powder bed and the effect these particles may have on the fatigue properties of parts produced. Ultimately the work aims to provide greater understanding to an aspect of PBF-LB process that has the potential to introduce

defects and variability into the components and through this help to improve the process for greater adoption of the technology.

In order to achieve these aims, the work addresses the following objectives:

- Establish the difference between spatter and virgin feedstock material and understand the link between spatter particle characterisation and the generation mechanisms. This will be achieved through analysis of spatter powder generated which is separate from the powder bed
- Understand oxide formation in the processing of Nickel-based superalloys, in both parts and in spatter, as inclusion of oxides in parts can inhibit processing and decrease mechanical performance. Parts and spatter are to be investigated for oxides and an experiment designed to investigate formation at the melt pool. The oxide formation in different alloys and compositions is to be investigated to understand material specific considerations for oxide formation
- Investigate the difference in spatter generated by different PBF-LB systems and quantify the characteristics of the particles using particle imaging and compositional analysis. This allows measurement of the evolution of the powder through processing and the influence of the PBF-LB architecture
- Investigate a methodology to assess and understand the distribution of spatter and other powder characteristics across the powder bed and how this contributes to part quality. The method intends to take samples of the powder bed across the build plate and assess the powder contents for metrics of particle size, packing, and spatter content to understand possible location dependence of variation in the process
- Establish the effect of spatter on the fatigue crack growth performance of PBF-LB parts using different levels of spatter powder as a feedstock. The fatigue results can then give an indication of the effect of the level of spatter processed in the powder bed on the properties of the parts produced

Based on the research objectives outlined above, a research methodology is illustrated in Figure 1.2 with relation to the PBF-LB process chain. Section 1.3 provides greater detail of each chapter.

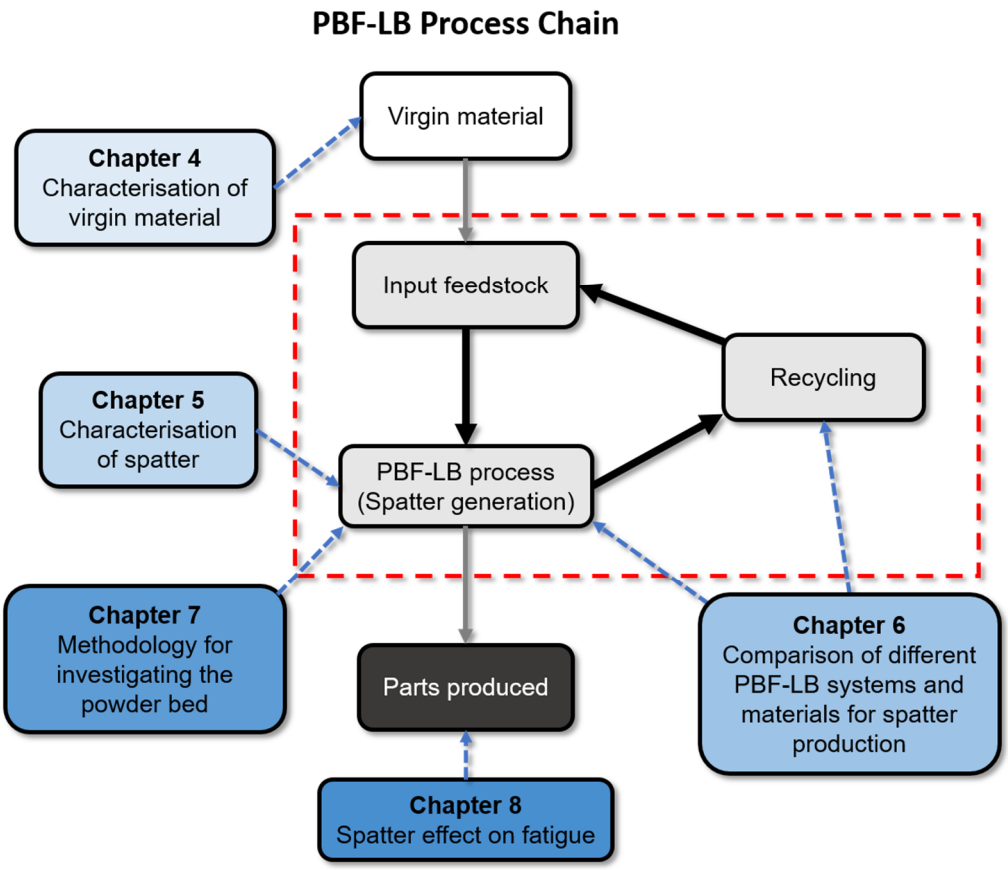

Figure 1.2 Research methodology and relation to the PBF-LB process chain

The spatter particles generated, and their effect on the PBF-LB process, has not been widely explored to date. The work in this thesis contributes knowledge to the field regarding the particles which are formed from the spatter process, their potential implications through the PBF-LB process, and potential for influencing mechanical properties of parts produced. The work investigates Nickel-based superalloys which have not been explored in the literature with regards to the generation of spatter, but, many of the findings are general for the process. In achieving the aims listed, new methodologies are developed with regards to the investigation of the powder bed properties and in investigating a small quantity of material through FCGR testing of CT specimen. Chapter 2 reviews the work published to date within the field and highlights the knowledge gaps which this thesis explores.

1.3 Thesis structure

A description of the contents of each of the following chapters of the thesis is presented below:

Chapter two presents a summary of research work conducted in the field to date and highlights areas where this study fills gaps in the current knowledge of the scientific community. The literature review first discusses the PBF-LB process generally and then the laser-material interaction in more detail and research into spatter. The next section summarises the manufacture of metal powders for metal AM and explores the characteristics of metallic powders with regards to their role in the PBF-LB process. Finally, a summary of the Nickel-based superalloys investigated and fatigue crack growth testing of PBF-LB components is given.

The third chapter describes the materials and methods used in conducting the research for this thesis. It describes the manufacturing machines used, experimental design of the studies, and the characterisation and testing equipment used in all studies, making it possible for other researchers to repeat the experiments reported here. Chapters 6-8 have chapter specific methods sections for any new methods introduced that are specific to these chapters.

Chapter four characterises the virgin materials used in the study for metallurgical and process characteristics. The powders are characterised for their size, shape, morphology, and to ensure there is no presence of contaminants which may affect results for further investigations. The characterisation establishes the parameters of the virgin material in order to establish a basis to understand the effect of processing on the powder.

Chapter five characterises spatter powder that is generated during processing. The spatter is characterised for its evolution from the original material. Unique oxidation effects are investigated and the results give a greater understanding of the laser-material interaction during processing. The spatter generated is mostly out-of-specification from the virgin material which raises quality concerns for the process. Evidence of the effects of spatter particles on parts is shown. Spatter is assessed for a second Nickel-based superalloys in order to understand the effects of different micro-alloying elements. Further, processing of an alloy

with reduced Si content is investigated to further understand the effects micro-alloying elements on oxide formation and the requirement for greater control on alloy chemistry in PBF-LB materials.

Chapter six analyses spatter and oxidation between different machines in order to aid understanding of the variation that can be present within the same technology. The spatter powder is analysed more thoroughly to provide quantitative assessment of the particles shape, size, and oxidation in order to understand the implications on recycling of powder in PBF-LB.

Chapter seven investigates a methodology for assessing the powder in the powder bed to understand the variations that are inherent within this. The research assesses the density of the powder packing of the bed and also the powder content of the bed. Variations indicate this may be difficult to control and could have impact on the quality of parts. The study confirms that spatter, seen as detrimental, preferentially effects certain sections of the build bed.

In chapter eight the effect of the inclusion of spatter powder, and particularly the retention of oxides, on the fatigue performance is assessed. Compact tension samples are created for three different levels of incorporated spatter powder. These specimen are used to assess the fatigue crack growth of the different spatter powder levels and suggest a method to predict an allowable level of spatter in a build or powder batch.

Chapter nine summarises the findings and the key understandings of the work before highlighting the significance for the field and concluding remarks.

Chapter ten proposes key areas of future research and direction for the field based upon the work. This is presented for short and long-term considerations.

Chapter 2 Literature review

This chapter serves to introduce PBF-LB and the elements which form the basis for the subsequent investigations and discussions. The first section of the chapter focusses on the mechanisms in the process and the laser-material interaction. This is the basis for understanding the generation of spatter, and hence understand its role in the process and subsequent part properties. The powders which are used in the process are then discussed with regards to the manufacturing techniques used and how the powder characteristics can affect the final results of the manufactured parts. A key section of this is the recyclability of the powders in processing as an important aspect of this thesis is an examination of the link between spatter and recycling in the process. The later sections of the chapter introduce the materials and research that has been conducted for Inconel 718 and Hastelloy X and fatigue crack propagation testing for AM materials. The end of the chapter highlights gaps in the current knowledge and understanding that this work aims to fill.

2.1 Laser powder bed fusion

The PBF-LB process uses a high energy laser beam, with a spot size of ~50-200 μm, to selectively heat and melt a thin layer of metal powder that is spread across a build plate. A slice, or cross section, of the desired components is selectively melted on the powder layer. After processing of the layer by the laser, the powder bed lowers to allow a new layer of powder to be spread (layers ~20-100 μm thick). This system of spreading (commonly known as recoating) and melting is repeated layer-by-layer until the 3D components are complete. The build plate is then removed from the build chamber, excess powder is collected in the overflow, and the part separated from the build plate [8]. A general schematic of the process can be seen in Figure 2.1.

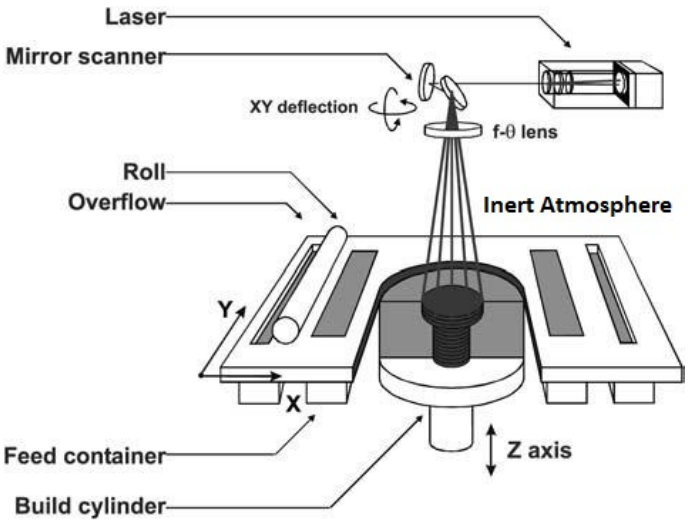

Figure 2.1 Schematic of typical PBF-LB machine setup [9]

Each PBF-LB system and each manufacturer has unique elements but all are comprised of a few common systems. The principal components of the PBF-LB system are a powder delivery system and an energy delivery system. The powder delivery system controls the supply of powder, a coater to spread a powder layer over the build area, and an overflow for the collection of excess powder. The powder is often stored and supplied from a feed container adjacent to the build plate, as in Figure 2.1, or in a hopper and dispensed in front of the recoater. The energy delivery system typically comprises a laser, optics, and a scanner system that allows the delivery of focussed energy to any spot on the build plate. To date systems have been predominantly single laser-based systems, with laser powers of 50-400 W. More recently, many OEMs have started producing larger machines with multiple lasers (typically up to 4) and with higher power outputs (up to 1 kW lasers are becoming commonplace).

The whole system is situated in a build chamber in an inert gas environment, typically Argon or Nitrogen. There is a gas flow across the powder bed and the optical lens which is designed to prevent the powder's exposure to oxygen and clear spatter and metal fumes that may be produced from the lasers interaction with the powder bed [10]. The build plate is often heated to reduce the thermal gradient between the melt pool and the build plate, which causes residual stress in components. Typically systems have the capability to heat the build plate up to 250 °C, however, efforts have been made to increase the build plate up to 500 °C or more [11,12]. This would allow greater thermal control over builds, an advantage which PBF-EB has over PBF-LB due to its ability to run a pre-heat scan over the powder layer before melting [13].

A short-coming of PBF-LB at present is the requirement for post-processing. Heat-treatments are commonly used to remove residual stresses and to produce desired final microstructures [14]. Parts generally need to be manufactured with support structures which require, generally manual, removal before finishing. Due to the rough surface finish on parts produced by PBF-LB some form of machining or finishing is generally used to bring components to tolerance for applications [15].

2.1.1 Mechanisms of laser-material interaction in PBF-LB

Despite the principle of the PBF-LB process being relatively simple, the underlying physics and interactions are highly complex and occur over a wide range of times and scales during the processing. Whilst the layer thicknesses and laser speeds are in the magnitude of µm and ms^{-1}, respectively, the parts can be in the order of cm^3 and build times can be hours or days. Additionally, there are many factors within the process that can affect the final part quality, Yadroitsava *et al.* described around 130 possible parameters [16]. The fundamental mechanism of the PBF-LB process is the energy delivered by the laser beam melting sections of metal powder which then rapidly solidify. This is the building block which full 3D parts are produced from. The manipulation of the processing parameters (laser powder, hatch spacing, layer thickness, scanning strategy, etc.) changes the energy delivery, primarily effecting the rate of melting and solidification. This also effects the re-melting of material from subsequent passes of the laser, be it adjacently, overlapping, or from the next layer [17].

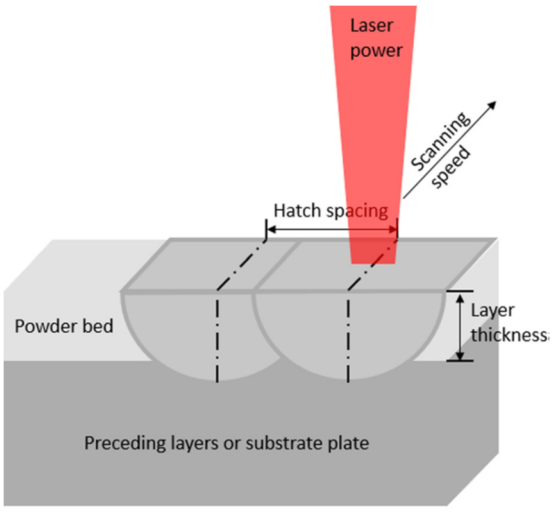

Figure 2.2 PBF-LB Process parameters: laser power, scanning speed, hatch spacing, and layer thickness From Yap et al. [18]

Although there are many parameters that influence the energy delivered in the laser-material interaction, this is primarily dependent on the laser power, scanning speed, hatch spacing, spot size, and layer thickness. These process parameters are commonly adjusted to optimise the process and are depicted in Figure 2.2. These parameters, together with the laser irradiation absorptance, contribute to the volumetric energy density, which dictates the heating and melting process. An understanding of how these factors affect the material and the melt pool are crucial to understanding how the material will process. In the heating and development of the melt pool, the heat capacity and latent heat, which are dependent on the material and proportional to the mass under influence, must be taken into account. The energy density is a measure of energy input to the powder bed and is commonly used to map the success of processing. This is often defined either as a linear energy density ($J.mm^{-1}$)(Equation 2-1), energy flux ($J.mm^{-2}$)(Equation 2-2), or a volumetric energy density ($J.mm^{-3}$)(Equation 2-3). Li *et al.* showed that generally, insufficient energy density, usually a combination of too low laser power (*P*), high scanning speed (*v*), and/or large layer thickness (*t*) results in the balling phenomenon, due to lack of wetting of the melt pool with the previous layer and lack-of-fusion defects [19]. At the other end of the spectrum, Yadroitsava *et al.* demonstrated that excessive energy density, due to too high laser power, low scan speed, and/or thin layer thickness may result in the keyhole effect commonly seen in welding with higher levels of spatter and vaporisation of material [16]. The area of the laser beam incident on the powder bed (A), dictated by the beam diameter, is the other parameter used to calculate the energy densities. The hatch spacing does not factor into the calculable energy density but can play a major effect on the thermal profile/history of the material and poor hatch spacing commonly leads to porosity in built parts as adjacent melt lines do not fuse together completely [20].

$$E_{linear} = \frac{P}{v} \quad 2\text{-}1$$

$$E_{flux} = \frac{P}{vA} \quad 2\text{-}2$$

$$E_{voiumetric} = \frac{P}{vAt} \quad 2\text{-}3$$

PBF-LB systems started as a development of the selective laser sintering printers, using CO_2 lasers (λ=10.6 μm) before moving to Nd: YAG and more recently to Yb: YAG fibre lasers (λ=1.064 μm) due to the higher absorptance of metallic powders to radiation with wavelengths around the infrared region. The absorption for a number of common materials for CO_2 and Nd:YAG lasers can be seen in Table 2.1. Due to the importance of the laser system to the PBF-LB process, the technology is expected to be closely linked to the development of laser technology and advancements made in the field may have knock on effects in future PBF-LB systems. For instance, recent developments in blue [21,22] and green [23] lasers have been utilised to process materials with low absorptance at infrared (1.064 μm) wavelengths, such as copper.

Table 2.1 Absorptivity (%) of various materials in a loose powder state at the operating wavelengths of Nd:YAG and CO_2 lasers (adapted from: [22,24,25]*)*

Material	Nd:YAG laser (1.06 μm)	CO2 laser (10.6 μm)
Metals (%)		
Fe	64	45
Sn	66	23
Ti	77	59
Pb	79	-
Co-alloy (1% C; 28% Cr; 4% W)	58	25
Cu-alloy (10% Al)	63	32
Ni-alloy I (13% Cr; 3% B; 4% Si; 0.6% C)	64	42
Ni-alloy II (15% Cr; 3.1% Si; 4%; 0.8% C)	72	51
Ceramics (%)		
Al_2O_3	3	96
SiO_2	4	96
CuO	11	76
SiC	78	66
Cr_3C_2	81	70
TiC	82	46
WC	82	48

Laser light impinging on a material surface can be absorbed, reflected, transmitted, or re-radiated. In PBF-LB processing, the radiation that is absorbed and reflected play important roles. A material's laser absorptivity is defined as the fraction of the energy absorbed by the material over the energy flux incident upon the material. This has a great effect on the energy efficiency of the PBF-LB process.

The absorptivity of a particular material can be affected by the type of laser that is used and materials respond differently to irradiation of different wavelengths. The absorptivity can also be affected by the angle of the laser incident upon the material and can change based upon the temperature of the material. For many metals and alloys in solid phase, the absorptivity in the infrared range can be approximated by an increasing relationship with temperature [26]. By far the majority of research work into laser processing and laser-material interaction has been for interaction with solid bulk material. The powder beds in PBF-LB present a much more complex and less understood interaction [1]. During the PBF-LB process the laser is irradiated into a thin layer of powder which is fully, or partially, supported by solid bulk material, in the form of the substrate or previously melted layers, and partially by unmelted powder sections. The absorptivity of a volume of powder material can be drastically different to that of the corresponding bulk material. For bulk materials a rougher surface correlates to a higher absorptivity as it causes the irradiation to be reflected and absorbed several times, increasing the overall absorptivity. A powder bed takes this concept further as the irradiation reflects between particles many times and can cause a drastic increase in the energy absorbed. More recent studies have shown that the absorptivity of the material by the laser is more complicated than just the powder or solid material absorptivities and that the molten metal also plays a major role in the laser material interaction [27–29]. Trapp *et al.* [27] showed that the absorptivity of the powder material was higher than the molten material, and that melting of powder and solid material are comparable once the material is molten. Relevant molten absorption figures could not be found for comparison in Table 2.1.

Tolochko *et al.* [24] found in their experiment into the absorptivity of laser energy by powders for AM, that the presence of residual oxygen in the chamber was significantly detrimental to the absorptivity of the powders and in case completely hampered melting. This can be seen by the low absorptivity of oxides such as Al_2O_3, SiO_2, and CuO in Table 2.1 and indicates the detrimental effect oxidation in PBF-LB could have on the melting and processing of materials.

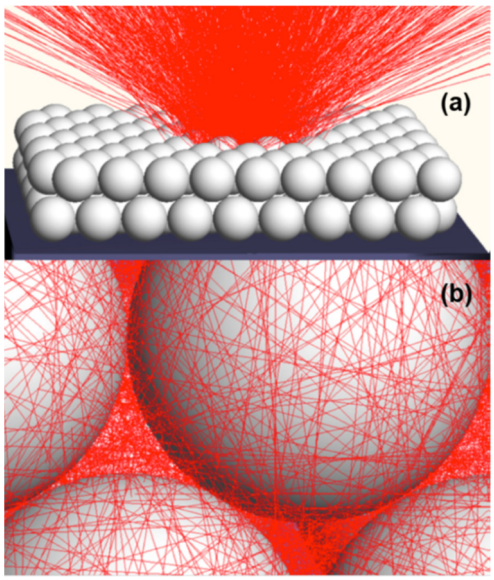

Figure 2.3 a) Typical rays during illumination of the ideal array. b) Detail of ray trajectories in (a), showing multiple scattering from spheres. Taken from King et al. [10]

Within the powder bed, absorption depends on the powder material, the distribution of the particle sizes, the spatial distribution of the particles, and the laser beam size and profile. Simulations by King *et al.* [10], of two layers of representative spheres stacked in a hexagonal structure were analysed using ray tracing methods to simulate the incident laser, as depicted in Figure 2.3. It was demonstrated that little more than 1% of the power from the laser penetrates beneath the two layers for both reflective materials such as Al and more absorbent materials like stainless steel. The majority is absorbed by the top layer of spheres. However, this is for a very simplified model with perfectly arranged mono-modal spheres and does not account for the dynamic nature of the powder bed during melting and interaction with the laser, which will be discussed further in Section 2.1.2.

Boley *et al.* [30] simulated and showed that the absorptance varies depending on the area of powder that the laser is incident upon and the particle sizes it interacts with. They performed this study for three different characteristic particle size distributions, mono-modal, Gaussian, and bi-modal, the latter two shown in Figure 2.4. They concluded that the role of multiple scattering means that the absorption value is strongly affected by the particle size distribution and their geometrical arrangement. The bi-modal distribution produced the highest absorptivity, due to the greater multiple scattering from the smaller particles, and the most reflective materials where most sensitive to this, increasing by a factor of nearly two. For more moderately absorbing materials such as stainless steel the change in absorption from the

lowest to the highest, the Gaussian to the bi-modal distribution, was 7% increased absorptivity. An important aspect of the change in absorptivity is the ratio of the beam spot size to the size of the particles, with the smaller particles in the bi-modal distribution contributing to less reflection back out of the melt pool. The studies by Boley *et al.* [30] and King *et al.* [10] both suggested that variations in particle distribution in the powder bed, and the corresponding changes in absorptivity, could play a role in the inconsistencies in melting witnessed in experimental studies of single tracks and full parts [31].

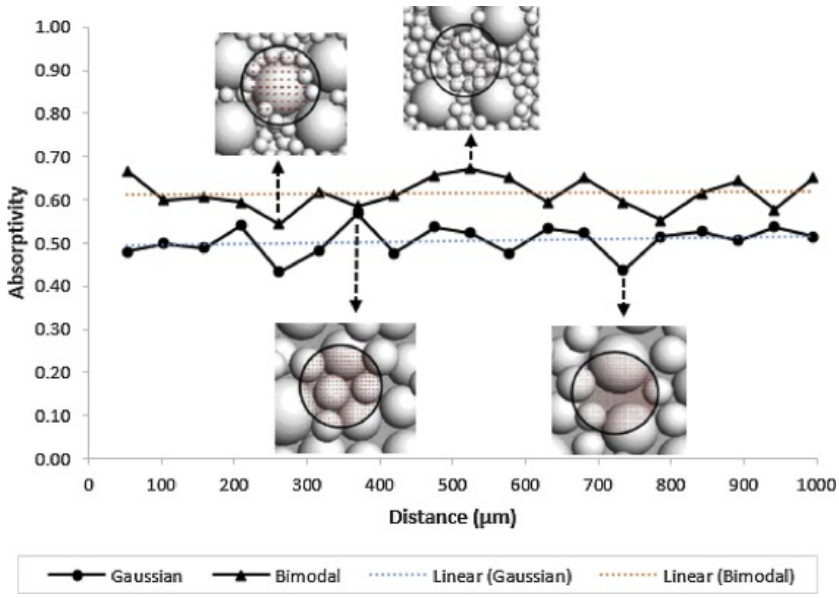

Figure 2.4 Absoprtivity α as calculated along the beam path for a) Gaussian particle distribution and b) bi-modal particle distribution. The material is stainless steel. The schematics show the powder incident beam size ($1/e^2$) at locations with high and low absorption related to beam – particle size ratio. From King et al. [10]

2.1.2 Spatter

2.1.2.1 Formation principles

During melting, bright streaks resembling welding sparks are visibly seen to emit from the melt pool, as shown in Figure 1.1. Commonly referred to as spatter, these particles are widely dispersed in the chamber and can fall onto areas of the powder bed still to be processed. Spatter formation has been studied previously in laser welding and drilling, providing a good basis for understanding some of the formation mechanisms [32–34]. It is generally accepted that spatter is caused by the phenomenon known as recoil pressure [35]. When the

temperature of the melt pool surface approaches and exceeds the vaporization temperature, a high-pressure metallic vapour away from the melt is produced [36]. This causes a high recoil pressure as a downward force on the melt pool, causing rapid motion within it and leading to expulsion of liquid metal from the melt pool. The development of the melt ejection can be seen in Figure 2.5 in the welding process. Many studies have discussed the influence of the laser processing parameters on this phenomenon, of which laser power and laser traverse speed have been shown to exert the greatest influence [37,38].

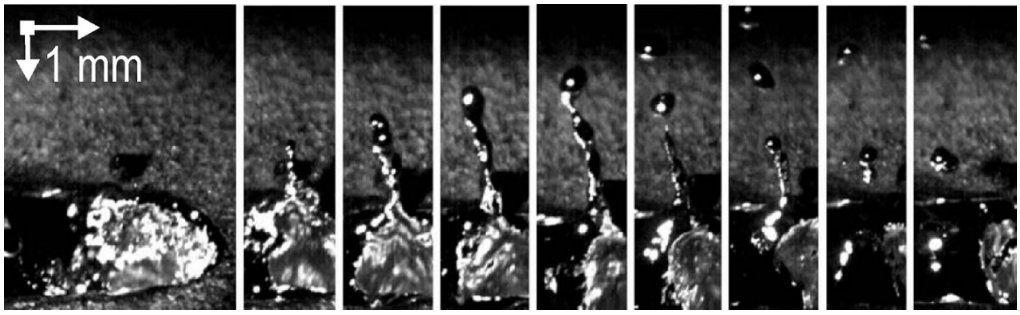

Figure 2.5 A high speed imaging sequence (500 µs steps) of droplets being ejected from a laser weld pool. The acceleration of a proportion of the melt in the vertical direction creates a column of melt which later disintegrates into droplets. From Kaplan & Powell [32]

The laser's interaction with a powder bed in PBF-LB, as opposed to a solid body in welding, adds to the complexity of the melt pool dynamics. Khairallah *et al*. [1] modelled the powder using a three-dimensional powder-scale model analysing the dynamic melt flow during laser interaction. This simulation confirmed the importance of recoil pressure and also Marangoni convection [17] in the melt pool in producing spatter ejection. Matthews *et al*. [39] built upon this by demonstrating the production of a vapour jet stream in the wake of the laser beam (flowing in the opposite direction to the laser) and the entrainment of powder near the melt pool creating a denuded zone either side of it as shown in Figure 2.6. These denuded zones have less powder in them, which has subsequent effects for the adjacent tracks yet to be scanned. Ly *et al*. [2] demonstrated that what is commonly referred to as spatter in PBF-LB is distinct from spatter in welding and is generated through a number of different mechanisms. Spatter can be divided into two categories, it is either ejected directly from the melt pool due to recoil-pressure (as in welding), or the spatter is produced by particles being entrained by the vapour jet in the wake of the laser beam. Both mechanisms produce new particles redistributed from the melt pool. The entrained spatter can be further categorised. Powder that travels through the laser and is heated to a similar degree to the melt ejection spatter is

classified as entrained hot ejection spatter. Powder that passes behind the laser and is not visibly heated is referred to as entrained cold ejection spatter. These phenomena are summarised in Figure 2.7 and can be seen in Figure 2.8 and also in videos produced by Bidare *et al.* [40] and in situ X-ray imaging by Leung *et al.* [41].

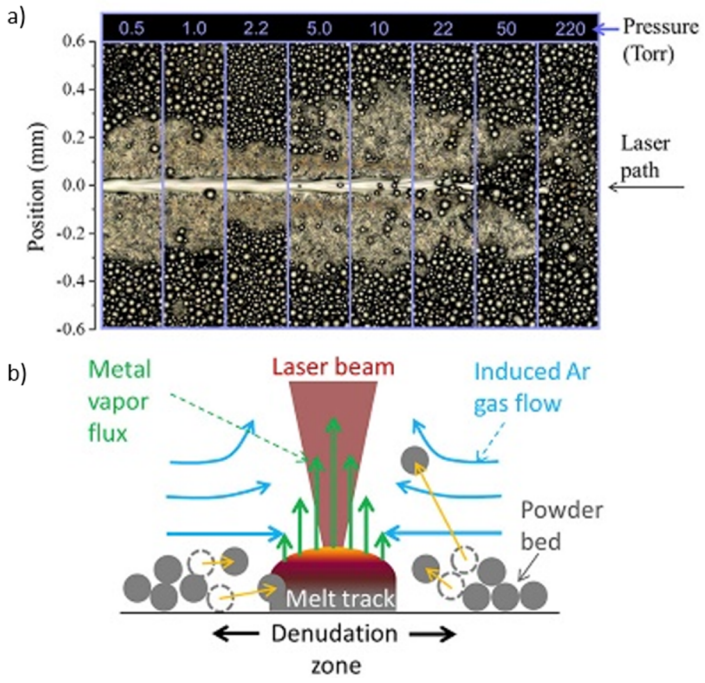

Figure 2.6 a) Montage of 1.2 × 0.25 mm optical micrographs of the solidified melt track within a powder layer following scanning laser exposure as a function of ambient Ar pressure (shown above image slices in Torr). Three distinct regions can be identified near the laser path center, namely track accumulation zone, the denuded zone, and the background powder zone. b) Schematic depicting the action of evaporated metal flux on the flow pattern of the surrounding Ar gas and displacement of particles in the powder bed. Particles are either drawn into the melt pool, adding to melt pool material consolidation, or are ejected upward (and rearward). Particle collisions from glancing irradiation can also act to expel powder outward. From Matthews et al. [39]

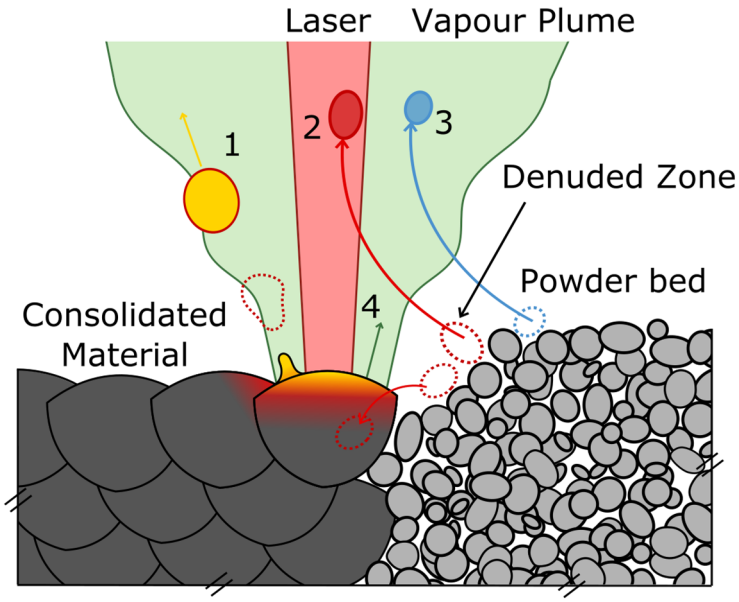

Figure 2.7 Schematic of laser material interaction, laser scanning direction out of page: the schematic depicts the generation of (1) melt ejection spatter, (2) hot entrained spatter, (3) cold entrained spatter, and (4) metal vapour ejection and vapour plume

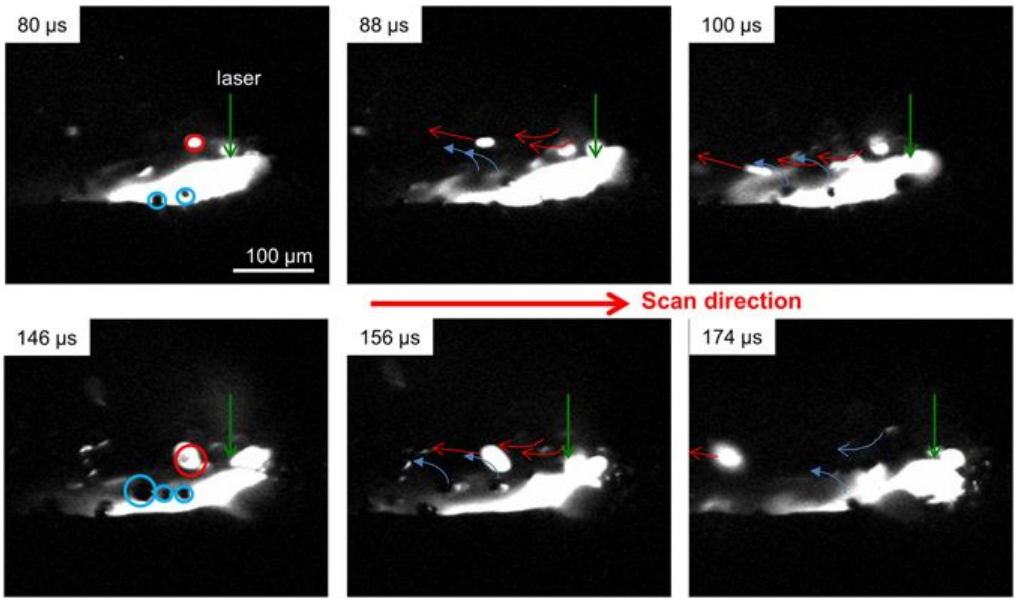

Figure 2.8 High resolution imaging of the melt pool formation of SS316L at 500 kfps. The series of images show the time progression from 80 µs to 174 µs. As the laser is scanned from left to right, particles are observed being swept up and backward with the arrow denoting the movement. The first image at 80 µs shows the location of the laser spot (green arrow) at the front of the melt pool. Hot particles are white in the image (circled in red) and cold particles are black (circled in blue). At 88 µs, the cold particles are lifted up and swept in a motion depicted by the blue arrows. Similarly hot particles that exit the laser beam is swept in a motion depicted by the red arrows. At 146 µs, new cold and hot particles are being entrained and the process repeats. Taken from Ly et al. [2]

Simulations by Khairallah *et al*. [1] showed a melt protrusion ahead of a depression where the laser melts, which is pushed along as the laser traverses. When the vapour flux away from the melt pool exceeds the surface tension then the liquid protrusion is expelled as spatter. This can be ejected with force and dispersed throughout the chamber, or can spill out in the powder near the melt pool. Khairallah *et al*. [1] and Matthews *et al*. [39], concluded that the vapour flux, with an exponential relation to temperature and 'over-shoot' beyond the boiling point of the material, has the greatest effect on the expulsion of spatter as the vapour flux generates the recoil pressure to overcome the melt surface tension. The peak temperature rise at the surface can be approximated by [2]:

$$\Delta T \propto \frac{P}{\sqrt{v}} \qquad 2\text{-}4$$

Therefore, a higher vapour recoil pressure is expected with a higher *P* or lower *v*. Gunenthiram *et al.* [42] analysed the quantity of spatter produced in SS316L and 4047 aluminium-silicon powder related to the *P* and *v* as a volumetric energy density. Their results showed an increase with the volumetric density as shown in Figure 2.9a, related to an anticipated reduction in *v* and/or increase in *P*, increased the quantity of spatter produced. The trend was particularly apparent for SS316L, shown by the empty circles in Figure 2.9a, however, the trend was not as clear for the processing of aluminium 4047. Ly *et al*. [2] compared two sets of processing parameters experimentally and through simulations to assess the generation of spatter. They found that the melt pool geometry affected the direction of ejection of spatter. They processed SS316L using *P* = 150 W and *v* = 0.5 $m.s^{-1}$, and *P* = 200 W and *v* = 1.5 $m.s^{-1}$. They showed that the slower scan speed created a deeper melt pool (keyhole welding), which has a higher proportion of liquid melt > 2000 K, and that spatter droplets are ejected vertically from the melt pool. The faster scan speed showed a shallower and wider depression from the recoil pressure. Both melt pools had the high temperature region at the front of the melt pool, with the keyhole welding having a higher proportion at the bottom of the melt pool and the higher scan speed having a thinner high temperature region. For the higher scan speed, the spatter ejected normal to the high temperature depression at the front of the melt pool, this leads to the majority of ejection at an approximately 30˚ angle in the opposite direction to the laser scan path. These findings for an increase in angle of spatter ejection with increased scan speed support findings in welding literature [43].

As well as the influence of processing parameters, the generation of spatter has been shown to be considerably different between materials. Figure 2.9a&b shows from Gunenthiram *et al's* [42] study that there was a significantly lower quantity of spatter produced by aluminium 4047 compared to SS316L. This can be seen visibly during processing and was found to be up to 7 times less spatter generated. It is indicated that a number of material factors contribute to this significant difference. Despite the aluminium alloy having a much lower melting and boiling temperature, it has a much lower absorption coefficient and enthalpy of vaporisation. The aluminium alloys also have a higher thermal diffusivity, therefore, much more of the heat generated is diffused into the bulk solid around the melt pool. These factors limit the vaporisation flux of the alloy and reduce the spatter generation. It is clear that a range of material properties, relevant to the melt and heating of the alloy, influence the spatter which is generated from PBF-LB processing of a material and each material needs to be understood.

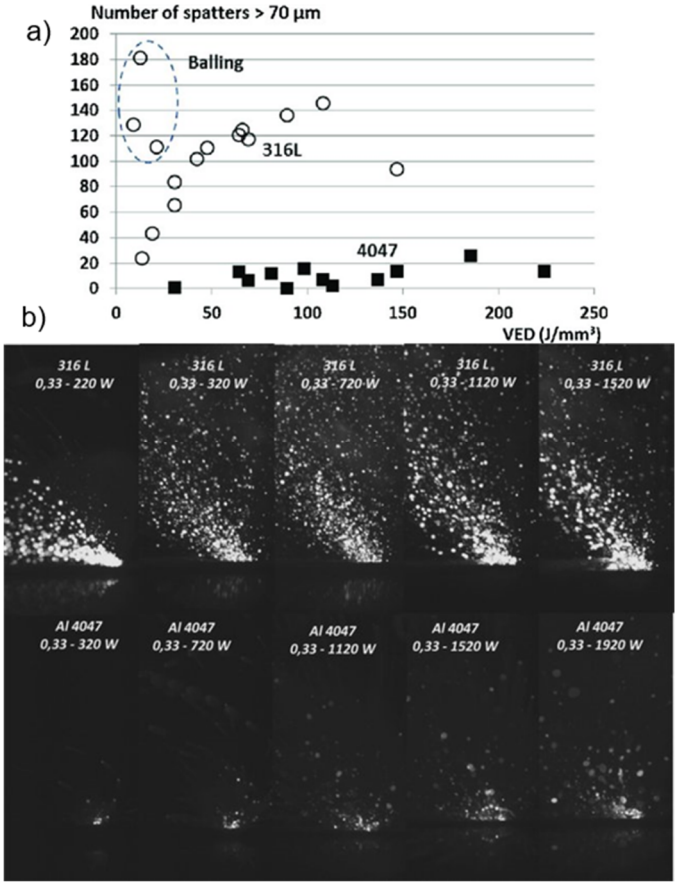

Figure 2.9 a) Superimposition of 1000 recorded images of spatters (V s = 0.33 m/s) for 316L steel (upper) and 4047 aluminium-silicon (lower). From 220 W (left) to 1520 W (right) on 316L and from 320 W (left) to 2320 W on A4047. b)

2.1.2.2 Spatter during processing

Spatter is generally considered detrimental to the PBF-LB process, but little is understood about the nature of the particles produced and their effect when incorporated into parts. Simonelli *et al.* [5] produced the first study characterising spatter produced from PBF-LB, demonstrating the presence of surface oxides on spatter particles, and discussing the potential issues this could cause. Their study investigated three material systems: Stainless Steel 316L, Al-10Si-Mg, and Ti-6Al-4V. They showed that spatter produced spherical particles which were larger than the starting material, as seen in Figure 2.10 top, and that these particles had a different microstructure to the virgin powder, which is likely due to their higher thermal mass and corresponding slower cooling rate. In Figure 2.10 middle and bottom they demonstrated the presence of oxide formations in a very low proportion of spatter particles, with oxide thicknesses of up to 5 μm.

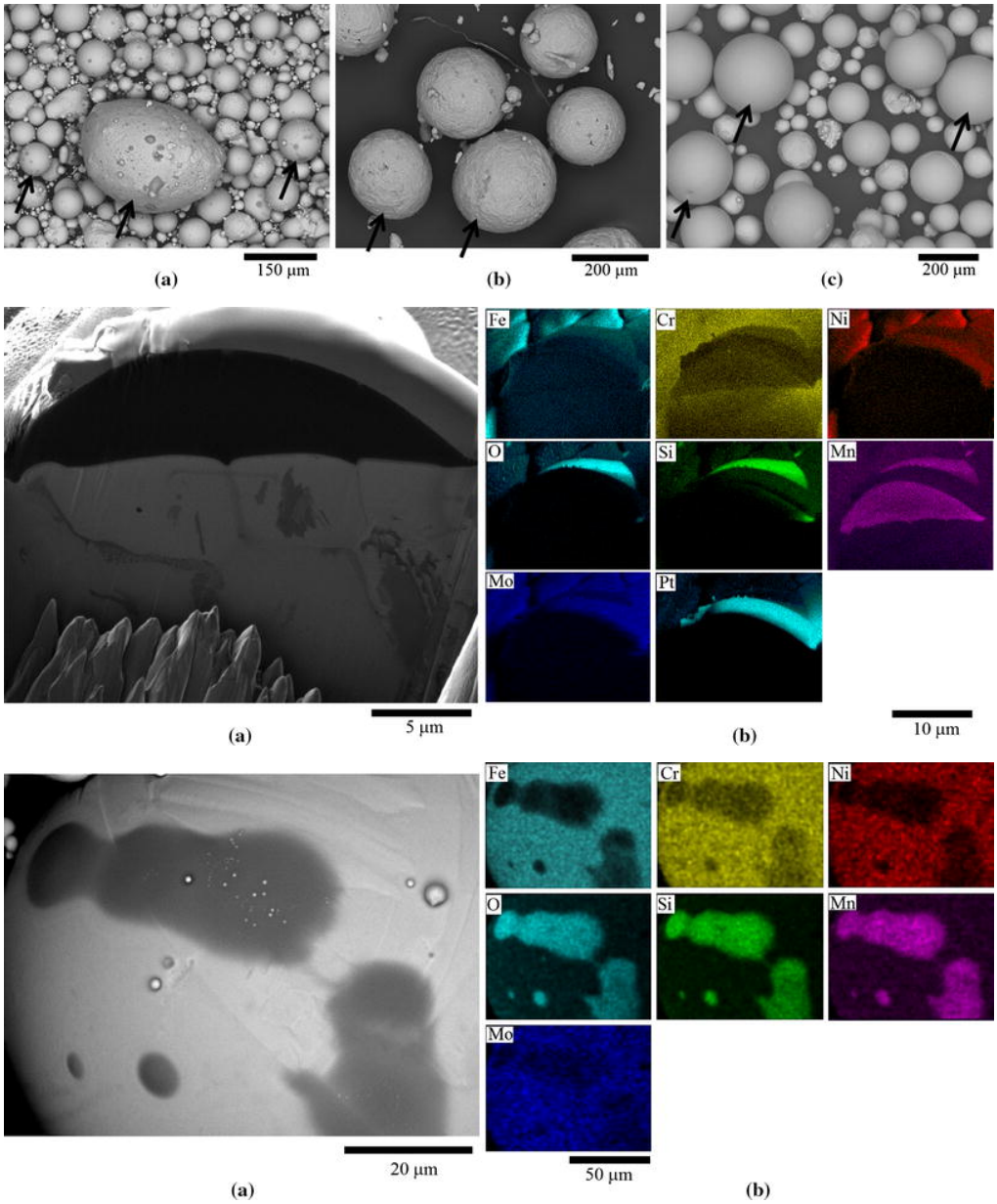

Figure 2.10 (Top) Backscatter images showing (a) the 316L stainless steel, (b) the Al-10Si-Mg, and (c) the Ti-6Al-4V starting powders (feedstock material) and the laser spatter that has originated during SLM; the black arrows indicate examples of laser spatter particles. (Middle) (a) FIB image showing the cross section of an arbitrary oxide found on the surface of the 316L stainless steel laser spatter; (b) Energy Dispersive X-ray Spectroscopy (EDS) maps indicating the distribution of the alloying elements in the oxide. (Bottom) (a) Backscatter image showing the oxide patches on the surface of the 316L stainless steel laser spatter; (b) EDS maps indicating the distribution of the alloying elements in the surface oxides. From Simonelli et al. [5]

Since then, studies investigating spatter have been produced by Liu *et al*. [44], also for SS316L, and Wang *et al*. [45], for CoCr. Liu *et al.* defined spatter as material collected from powder that had been used five times and then sieved with a 200-mesh, which corresponds to a mesh opening of 74 µm. Their powder was listed with a starting particle size distribution of d_{10} =

22.5 µm, d_{50} = 39.02 µm and d_{80} = 56.04 µm and an average particle size 42.83 µm. They showed that their SS316L spatter particles were of much greater size, with particles up to 400 µm in size, although they had already sieved above 74 µm. They showed that this 400 µm particle had an increased oxygen peak on EDS spectra compared with a virgin powder particle. They produced tensile specimens with the five times used and un-sieved powder which exhibited reduced tensile performance than specimen produced with virgin material, this was attributed to pores and defects caused by the spatter particles and irregular powder.

Wang *et al.* [45] analysed spatter particles through a similar method, reusing the same powder 6 times and then sieving through 200 mesh again and collecting the residue, with the original powder listed as having an average particle size of 32 µm. They first proposed that spatter particles can be characterised by their different morphologies as shown in Figure 2.11. Type I particles were identified as recoil pressure droplet ejection due to their spherical nature. As Type I ejection is perpendicular to the powder bed particles travels higher and further and solidify as a sphere before impacting the powder bed. They characterised Type II particles by the adhesion of many smaller particles to the surface. This was attributed to these particles travelling sideways out of the melt pool and impacting with smaller particles in the powder bed which attach to the surface. The issue with this theory is that the particles adhered to the surface are much smaller than the virgin powder, the largest adhered particle shown is ~18 µm, which is feasible in their PBF-LB powder, but the rest of the much smaller particles are unlikely to be. These much smaller particles are also highly unlikely to be at the surface of the powder bed as they would generally fall through gaps in the powder bed and settle towards the bottom during spreading of the powder layer. Additionally, from their high speed images the particles they denote as Type II are much smaller in mass than Type I, which the particles presented do not appear to be. Type III is proposed to be spatter ejected from the front of the melt pool directly towards the bed. It is proposed that this spatter does not have time to fully form as a sphere before impacting the powder bed and solidifies in an irregular shape with adhered particles. As well as the similar reasons for Type II particles, more recent work by Bidare *et al.* [40] showed that spatter particles can detonate mid-air, which more likely causes these irregular spatter particles. Wang *et al.* demonstrated that spatter particles lead to increased oxygen and carbon content in the powder, with almost a doubling in the content of both in the spatter particles compared to the virgin material, even when processing in an oxygen level reported to be <0.02%. However, the analysis was only conducted via EDS, which

is less sensitive for light elements. The authors proposed that to improve the issues with oxygen pickup and oxide formation the build chamber could be evacuated prior to filling with high-purity argon.

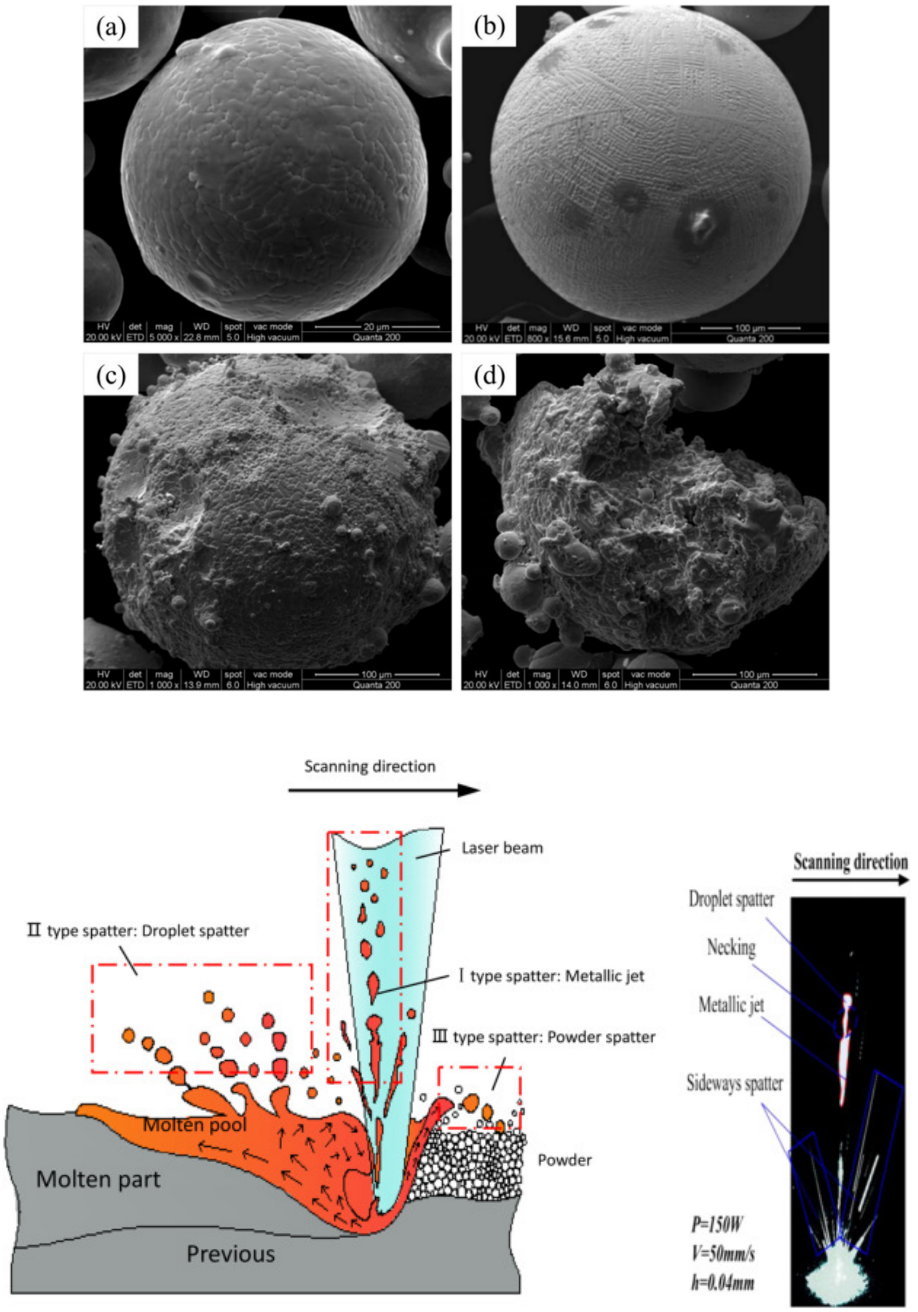

Figure 2.11 (Above) SEM images of initial powders and splashing particles (a) morphology of initial powder particles; (b) morphology of spherical splashing (type-I splashing); (c) morphology of coarse spherical morphology (type-II splashing); (d) morphology of irregular splashing (type-III splashing). (Below) Formation mechanisms of spatter a) three different types of spatters and b) typical spatter behavior during PBF-LB. From Wang et al. [45]

A study by Lutter-Günther *et al.* [46] investigated and characterised the spatter produced by the PBF-LB processing of Al-10Si-Mg. They characterised the spatter into three categories based on their morphology as shown in Figure 2.12. These are blown powder (or redistributed virgin material), spherical spatter, which is large and spherical with some small dark spots on the surface which were identified as Al_2O_3 and MgO, and thirdly, large spatter agglomerates. They found that the spatter had an Oxygen content of 2116 ± 93 ppm, an increase to that of the virgin material, of 869 ± 37 ppm, and they also found that the spatter above and below their 75 µm sieve size had the same Oxygen content. This would indicate that the redistributed 'virgin' powder had a similar Oxygen increase to the melt ejected spatter powder. The authors used a unique method, utilising a sheet mask over the powder bed with an open slot which is the geometry of the part (shown in Figure 2.12), to collect and calculate the quantity of spatter produced during processing. Their extrapolation from their collection of 40 layers of processing was that for the mass of solidified part manufactured, the equivalent of 16.7% of this mass was also produced as spatter. This will be unique to the machine, processing parameters, and material but is the first attempt reported to be able to quantify this metric. They also measured the quantity of the spatter which remained within their 75 µm sieve specification which was between 50-56.7% across the builds they analysed.

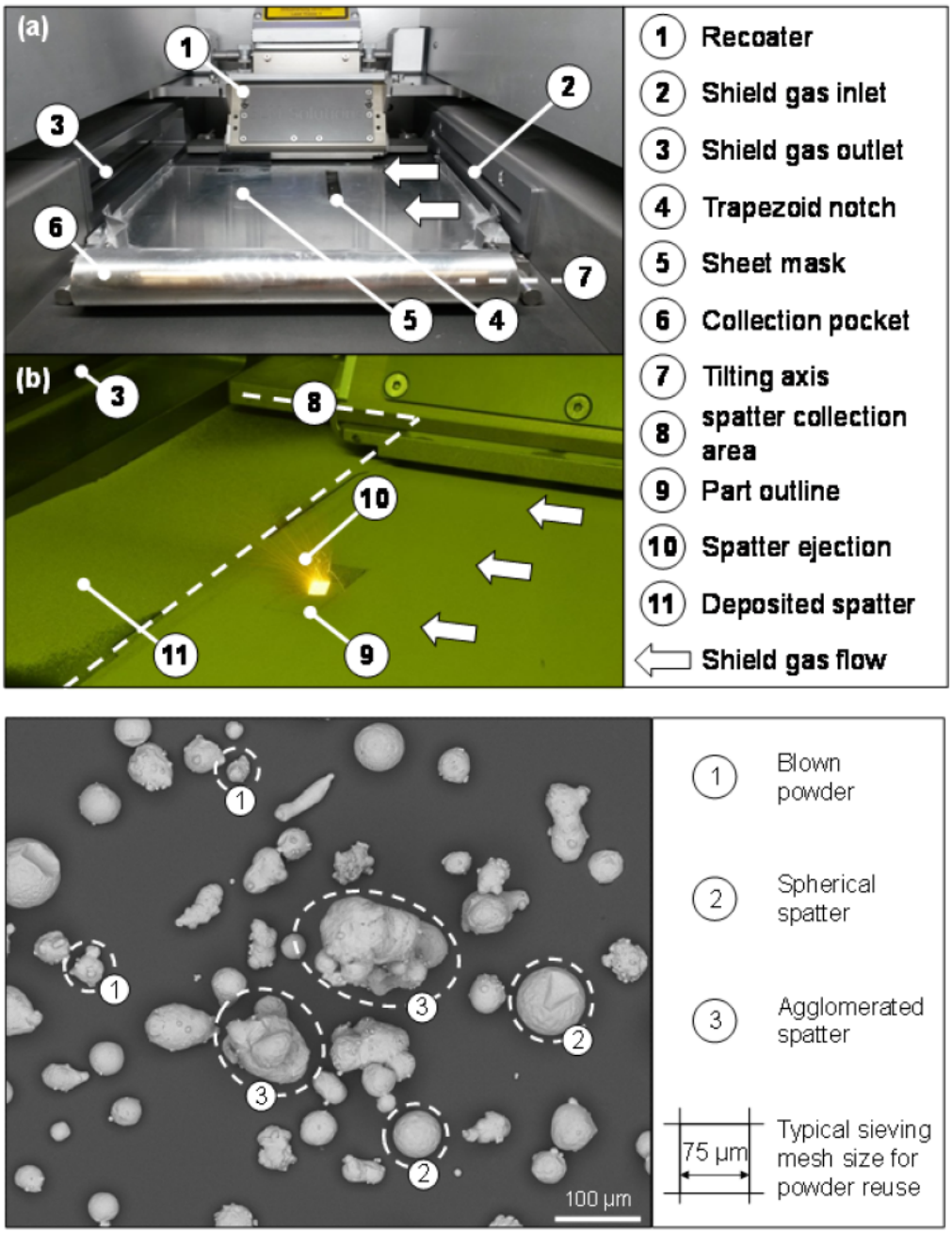

Figure 2.12 (Above) Image of systems used to collect spatter powder and (below) SEM image of collected spatter particles from PBF-LB processing of Al-10Si-Mg powder. From Lutter-Günther et al. [46]

The spatter particles generated during processing are redistributed throughout the chamber. Some are found outside of the powder bed and may be directed by a gas flow, however, some of the spatter lands back into the powder bed. Ladewig *et al.* [47] discussed how the gas flow influences the removal of the process by-products such as spatter and the redistribution of the spatter across the bed. They showed how spatter redeposited onto the consolidated parts

and onto areas of the powder bed can lead to defects in the parts. Figure 2.13c shows spatter particles redistributed and connected to the top surface of a consolidated part, and the circled red section in (b) shows lack-of-fusion defects detected by ultrasonic testing. These lack-of-fusion defects are attributed to redeposition of spatter as they were able to remove them through optimisation of the gas flow across the bed as shown in (a).

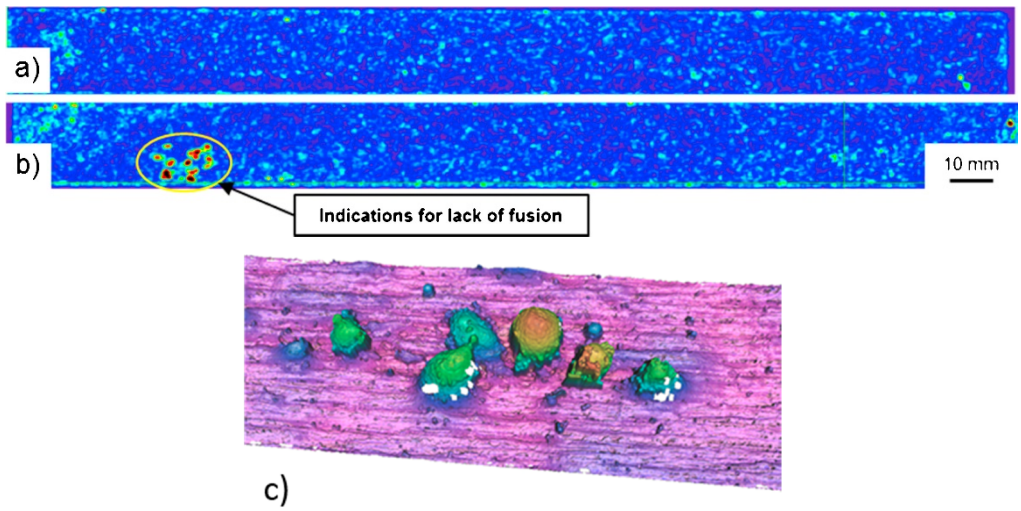

Figure 2.13 Ultrasonic investigation of the specimen. (a) Built with flow rate at 4.0 V and (b) Built with flow rate at 2.0 V, and (c) confocal microscopy reconstruction of spherical particles produced by redeposition of process by-products. Original image has no scale bar. From Ladewig et al. [47]

Anwar & Pham [48–50] further investigated the effects of gas flow and redistribution of spatter across the powder bed. They first used an analysis of variance (ANOVA) experiment to determine which factor (gas flow speed and scanning direction) contributed most to the quantity of powder collected by the side of the build chamber near the gas outlet, where the gas flow directs most of the process by-products. They showed that both gas flow and scanning direction had an effect, with a higher gas flow and scanning against the gas flow leading to the highest amount of spatter collected by the outlet. The direction of the scanning effect will be related to how spatter ejection direction is influenced by the process parameters used, as shown by Bidare *et al.* [40], and as they established in their subsequent studies. For the parameters used by Anwar & Pham, spatter was generally ejected in the opposite direction to the laser scanning, so when it was scanning against the gas flow the spatter was being ejected in the direction of the gas flow. Their subsequent study developed on the ANOVA investigation to assess the tensile performance of the parts produced and part location. The study assessed the effect of whether the parts are built on the half of the build

chamber by the gas outlet or the half by the gas inlet. These sets of specimen were done as separate builds, and again the study collected and analysed the quantity of spatter that built up by the gas outlet. The parts positioned closest to the gas inlet had the highest UTS, however, the effect of part placement was minimal on the UTS of the specimen. This is anticipated as the gas flow is stronger by the inlet so removes more spatter but overall the samples have a similar performance as this has a minor effect compared to the other factors assessed. It is likely there would have been larger effects with parts built on both sides in the same build, to establish the effect of particles redistributed from the parts near the inlet onto the parts near the outlet. Their investigation also showed some correlation between the mass of powder collected next to the powder bed, and therefore the amount of spatter removed, and the UTS of the specimen as shown in Figure 2.14.

a)

2^3 design experiment.

Factor	Low (−)	High (+)
A: Scan direction	−*x*	+*x*
B: Part location	Left	Right
C: Gas velocity	30%	60%

b)

Plus and Minus table for 2^3 design experiment.

	Factor						
Run	*A*	*B*	*C*	*AB*	*BC*	*AC*	*ABC*
1	−	−	−	+	+	+	−
a	+	−	−	−	+	−	+
b	−	+	−	−	−	+	+
ab	+	+	−	+	−	−	−
c	−	−	+	+	−	−	+
ac	+	−	+	−	−	+	−
bc	−	+	+	−	+	−	−
abc	+	+	+	+	+	+	+

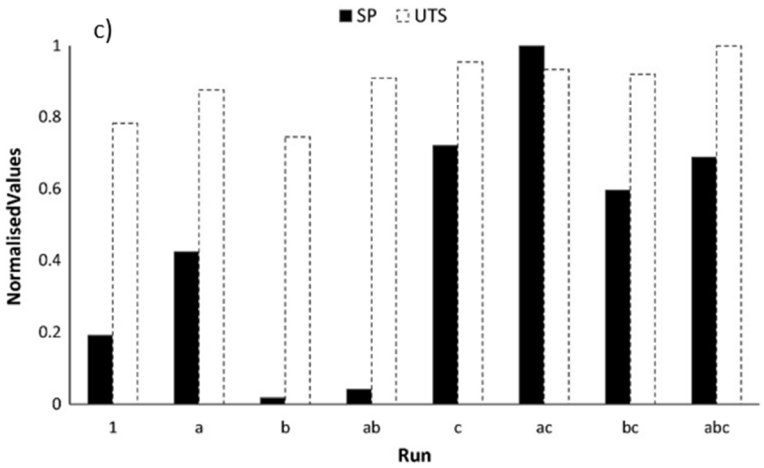

Figure 2.14 a) ANOVA factors investigated, b) design of experiments, and c) normalised plots for spattered powder and UTS. From Anwar & Pham [49]

Anwar & Pham then proposed an image analysis technique for assessing the distribution of spatter across the powder bed [50]. The schematic of their experiment is shown in Figure 2.15. They used optical images and image analysis to assess how much spatter was on the powder bed and then correlated this to the powder in the bed by collecting and measuring it directly. They demonstrated a possible method to assess the problem in situ. They were able to show

a trend of decreasing spatter redistribution from column D through to A in the image pixel analysis and their mass measurements, as well as a size distribution of spatter particles along the columns showing that the smaller spatter particles are blown further and the larger particles are more likely to stay close to the part in the powder bed. Whilst they were able to show a positive correlation between the collected spatter mass and spatter pixels, this was only with an R = 0.46. This first attempt to analyse this problem had a few short comings the authors proposed needed to be addressed in future studies. They encountered the compromise of image resolution and area of measurement, with 1px correlating to ~63 µm, which is the sieve size they measured spatter above, which makes the error based on noise and thresholding of the image high. The thresholding technique is also sensitive as it relies on colour difference between the spatter particles and the virgin material, which has been reported to be true for some spatter but not all. In the study, only three processed layers were analysed. This is a very small quantity of powder to analyse via collection and sieving, leading to errors which could be addressed with a larger sample size. The authors also gave little detail about how they collected powder samples from the bed for the specific region, there is great chance for error in this technique and the handling of these small quantity of powders. Their method, however, does provide a good basis to build upon for analysing spatter distribution in the bed.

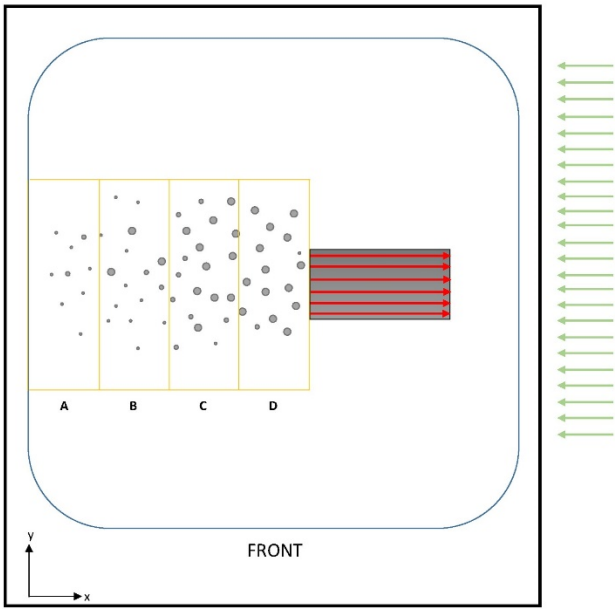

Figure 2.15 Layout of scanning region of 40 × 80 mm, with spatter on powder bed distributed on equal columns of 40 × 120 mm each. Red arrows resemble unidirectional laser scan vectors while green arrows represent inert gas flow. The scanning order was set from the top going downwards (−y direction). From Anwar & Pham [50]

As discussed, the generated spatter, distributed back into the powder, effects what material is actually being consolidated and effects the powder bed and final part. Ladewig *et al.* [47] demonstrated how spatter particles can lead to lack-of-fusion defects, due to their large size or increasing the thickness of the powder bed layer, as well as the redeposited spatter bonding to the top surface of the component. These large particles fused to the surface, shown in Figure 2.13c, can be removed by the recoater, leaving holes in the part surface and relocating the large particle elsewhere in the bed. Or if they don't break off they are capable of damaging the recoater [51]. Nguyen *et al.* [52] studied the effect of spatter on parts built downstream in the gas flow where spatter is blown to. Figure 2.16 shows their evidence of large spatter particles causing porosity and lack-of-fusion defects beneath them due to the laser being unable to fully melt the large particles. Large spatter can also cause issues in the powder bed, such as 'corn rowing', where large particles are dragged by the recoater and leave streaks in the powder bed, as depicted and discussed in Section 2.2.2 [53–55]. It is known that these spatter particles cause these defects and Liu *et al.* [44,56] and Anwar & Pham [50] showed this can be linked to decreased mechanical performance. Also, as Lutter-Günther *et al.* [46] demonstrated, spatter contributes to the pickup of Oxygen in the powder, contributing to degradation in the quality of material inherent in the recycling of the powder, which will be discussed later. Tang and Pistorius [3] showed how pick up of Oxygen can drive porosity and spatter particles can include oxides which remain in parts [5]. There is still much to be understood in terms of the connection between spatter and the effect it has on the performance of PBF-LB parts, with regards to the types of defects formed, how they connect to the part properties, and the likelihood and severity of the effects.

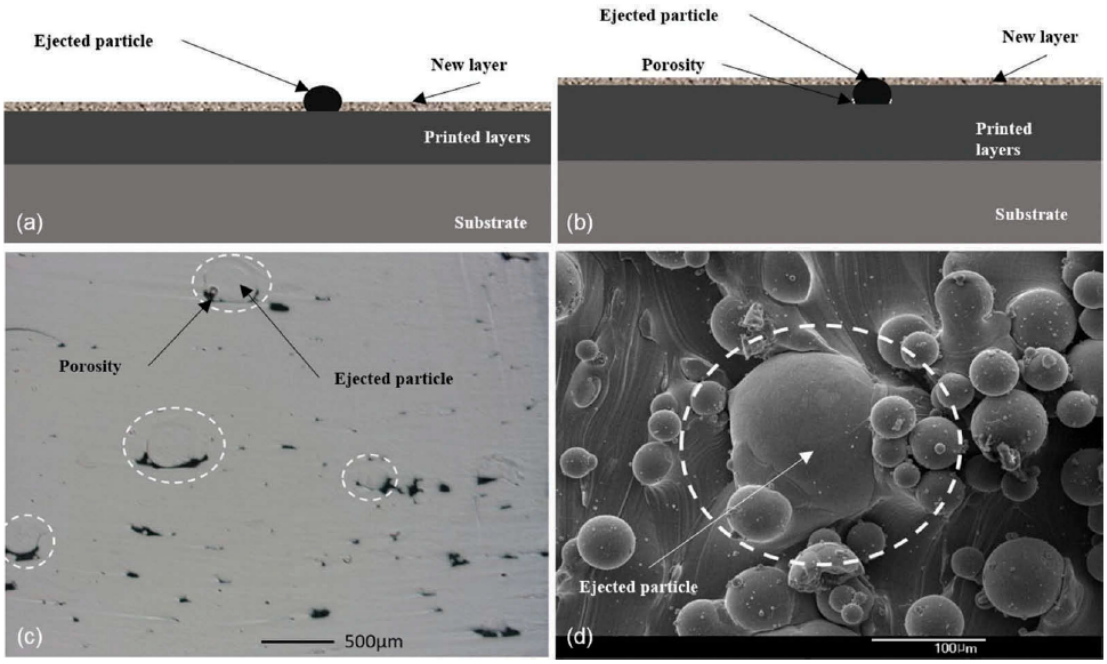

Figure 2.16 Formation of porosity: (a) ejected particle, (b) porosity formation after printing, (c) OM of porosity of a printed part and (d) SEM of inclusion of an ejected particle (dashed white circle). From Nguyen et al. [52]

Most investigations into spatter in PBF-LB used conventional single laser machines. Many manufacturers have now released multi-laser systems which will only serve to exacerbate issues with spatter as each individual laser creates its own spatter. Andani *et al.* [57] investigated the effects of spatter in the multi-laser processing of Al-10Si-Mg. Their study used high speed cameras to show the amount of spatter produced during simultaneous two-laser melting, as shown in Figure 2.17. They demonstrated a similar particle size distribution to single laser spatter but over a doubling in quantity. This is an area which will require much greater investigation, but there is still much work to be done in understanding spatter particles and their effect on components before adding the extra complexity of multi-lasers. However, the industry is accelerating more rapidly than the research into these topics.

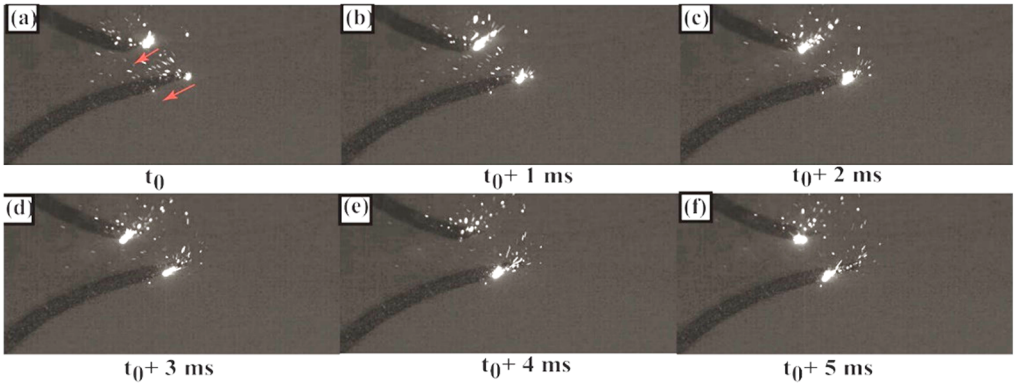

Figure 2.17 High-speed camera images during PBF-LB process while two laser beams are working closely. The time interval between each image is 1 millisecond. The red arrows in (a) show the laser track paths. From Andani et al. [57]

The generation of spatter is inherent to the metal welding process, however, it is indicative of the lack of appreciation of the issues that can be caused by spatter that minimal research has been conducted to date on strategies to mitigate or avoid the phenomena. Mumtaz & Hopkinson [58] identified from conventional welding techniques that utilising and controlling a pulsed laser can help to reduce the overshoot of laser power delivery which leads to the vaporisation and ejection of spatter from the melt pool. They found a few pulse shapes which were able to reduce the vapour plume height produced, which reduced the generation of spatter. This is promising, however, their studies were only performed on thin walls and more investigation is required to understand how this would apply to full parts. Sato *et al.* [59–61] carried out studies into PBF-LB manufacturing without the generation of spatter. Using a bespoke vacuum PBF-LB system they successfully processed titanium alloys without generating spatter. The issue is that they achieved this by greatly reducing the scanning speed of the laser to control the heating and melting. Their spatter-free processing was achieved at scanning speeds <50 $mm.s^{-1}$, which considering conventional machines process up to 5000 $mm.s^{-1}$, and that slow build rates are an aspect holding back AM, is not a practical solution for industrial manufacturing purposes.

For an aspect of the PBF-LB process that is inherent to the process and is considered detrimental, there is a surprisingly small amount of research in this area. There are significant gaps in current knowledge, particularly as spatter in different materials and PBF-LB systems will differ.

2.2 Powders in PBF-LB

By far the majority of PBF-LB research has been directed towards optimising the processing of different alloys [62], characterising and engineering microstructures [63], and relating these to part performance [64]. However, there has been less consideration of the powder material feedstock and the powder bed once processed by the laser. Mindt *et al*. [53] described this as the 'overseen first-order process input'. It has been shown that powder characteristics influence the powder bed, due to the effect on flow [65], packing behaviour [66], and laser-material interaction [30] and, hence, the final part produced [67]. Knowledge of the powder bed is important to aid understanding of the laser-material interaction required to create the solid metallic material.

2.2.1 Manufacture and metallurgy

Metal powder manufacture is not new, or unique to AM. Data from 2013 estimated a worldwide metal powder industry at a value of approximately US$6.9 billion, with a capability of producing 1.12 million metric tonnes per year [68]. As part of that valuation, the AM metal powder market valued at US$33.6 million or 0.0047%. This puts into perspective that despite the amount of hype around metal AM, with regards to the conventional powder manufacturers, the metal AM market is nowhere near as significant as the powder metallurgy and metal injection moulding (MIM) industries they mainly supply. The powder for metal AM can be made through the same conventional powder techniques and it is important to explore these to understand the formation of the powders used. The most conventional techniques with applicability to AM are water atomisation, gas atomisation, and plasma atomisation, an example of the powders produced is shown in Figure 2.18. Each technique has characteristic advantages and disadvantages and produces different particle size distributions (PSD), morphology, composition, and contaminants.

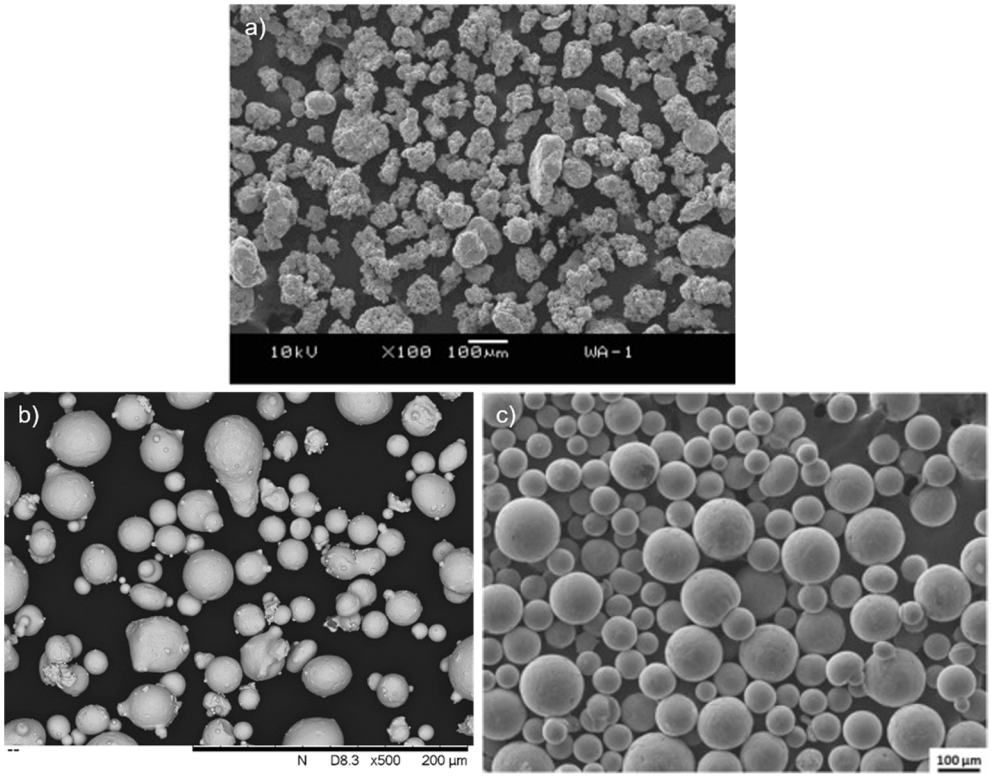

Figure 2.18 Examples of powder produced from different atomisation techniques: a) water atomisation (Copper) [69]*; b) gas atomisation (Inconel 718); and c) plasma rotating electrode process (Titanium aluminide)* [70]

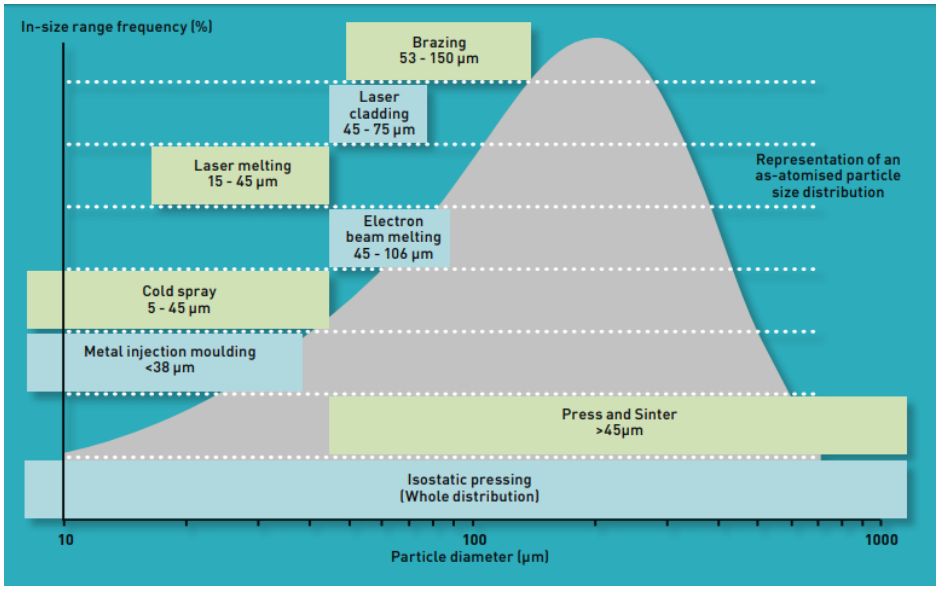

Figure 2.19 Applications for different PSDs [71]

Gas atomised powder is the most commonly used powder in metal AM. It provides the most reasonable compromise between PSD, morphology, and minimisation of Oxygen content and other undesirable elements and contaminants [72]. The sieve cut for PBF-LB is generally larger

than MIM powders and smaller than other processes such as PBF-EB and DED making it an ideal extra market, as shown in Figure 2.19. The general process for atomisation is that the feedstock is first melted in a furnace and the molten metal is then transferred to a tundish, which is a crucible that controls the flow of the melt into the atomiser. The melt flows the tundish into the atomiser nozzle where it then encounters gas jets, these atomise the melt and disperse it into the chamber, as depicted in Figure 2.20. The chamber is designed so that the fine liquid alloy spray has a chance to rapidly solidify before hitting the chamber wall and being collected at the bottom of the chamber [73]. Argon or Nitrogen gas is commonly used as the atomising media to reduce the pickup of Oxygen and to increase the solidification rate of the atomised metal. Air can be used as the atomising media but this generally produces more irregular powder and more risk of oxidation and contamination.

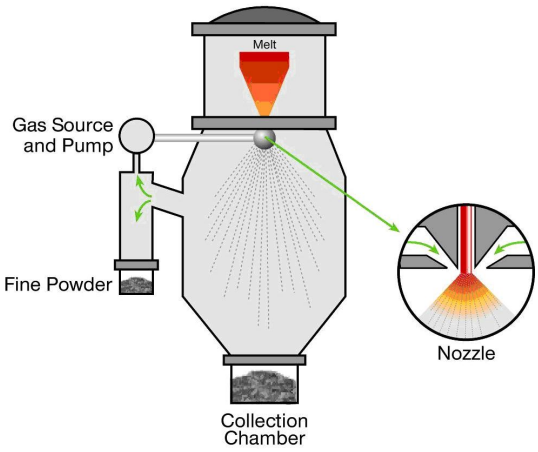

Figure 2.20 Schematic of the gas atomisation process [68]

For high end applications and highly reactive alloys advanced gas atomisation techniques are used. This can be crucial for non-static components in extreme conditions such as those in combustion stages of turbine engines as contaminant material can be picked up from crucibles and atomising nozzles which remain in the powder and subsequent part [68]. This is particularly relevant for any alloys used in these critical applications, or that contain high proportions of highly reactive materials such as Al and Ti. To address this, vacuum induction melting is used at the furnace stage to further reduce the chance of Oxygen and Nitrogen pickup and control interstitial elements; this process is known as vacuum induction gas atomisation (VIGA) [74]. VIGA still generally involves the transfer of melt to the tundish and flow through the nozzle, which still presents the opportunity for contamination. The next

option is electrode induction gas atomisation (EIGA). EIGA involves using a rod of the alloy which is fed into an electrode induction coil which melts and flows into a gas stream, as shown in Figure 2.21 [75].

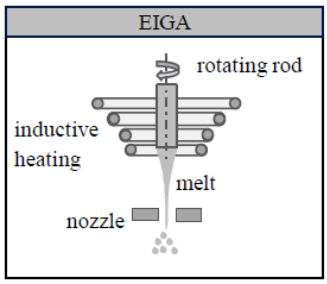

Figure 2.21 EIGA process schematic [76]

One drawback of gas atomised powders is that they have irregularities, such as elongations, agglomerations, satellites, splat caps, and hollow particles [73]. These can be reduced with fine tuning of the process but this is difficult to achieve and cannot be completely removed. Plasma atomisation is capable of producing more highly spherical powders [77,78]. In plasma atomisation the alloy feedstock is in wire form and feeds into a set of plasma torches and gas jets which simultaneously melt and atomise it. A more advanced version of this process is the plasma rotating electrode process (PREP) which is seen as the highest grade for spherical metal powders [79], and can be seen in Figure 2.18c.

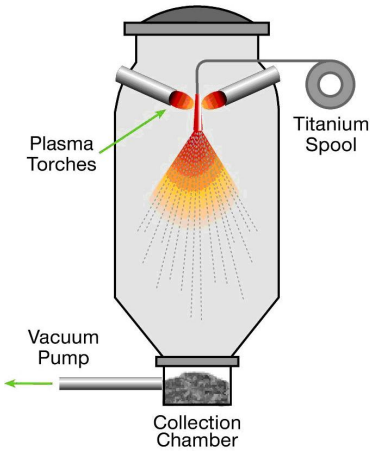

Figure 2.22 Schematic of the plasma atomisation process [68]

Water atomisation is similar to gas atomisation but uses water as the atomising media. It is the most cost effective of the atomisation techniques, however, it produces the least spherical and most irregular particles due to the high cooling rate of the melt in the water meaning the particle solidifies before forming a sphere [72]. The process also requires additional steps to

dry the powder and the use of water greatly increases the oxidation of the powder. Water atomised powder is not commonly used in PBF-LB however it can be used successfully with optimisation of the processing parameters and the cost saving are vast if the application allows for the increased Oxygen content. An important area of research for PBF-LB is not just the highest quality powders for the high performance applications but also what can be achieved using cheaper and simpler materials, for the process, and for the supply chain. A summary of the characteristics of each process is presented in Table 2.2.

Table 2.2 Summary of powder characteristics by manufacturing process. Reproduced from Dawes et al. [68]

Manufacturing Process	Particle size (μm)	Advantages	Disadvantages	Common uses
Water atomisation	0-500	-High throughput -Range of particle sizes -Only requires feedstock in ingot form	-Post processing required to remove water -Irregular particle morphology -Satellites present -Wide PSD -Low yield of powder between 20–150 μm	Non-reactive
Gas atomisation (inc EIGA, VIGA)	0-500	-Wide range of alloys available -Suitable for reactive alloys -Only requires feedstock in ingot form -High throughput -Range of particle sizes -Use of EIGA allows for reactive powders to be processed -Spherical particles	-Satellites present -Wide PSD -Low yield of powder between 20–150 μm	Ni, Co, Fe, Ti (EIGA), Al
Plasma atomisation	0-200	-Extremely spherical particles	-Requires feedstock to either be in wire form or powder form -High cost	Ti (Ti64 most common)
Plasma Rotating Electrode Process	0-100	-High purity powders -Highly spherical powder	-Low productivity -High cost	Ti Exotics
Centrifugal atomisation	0-600	-Wide range of particle sizes with very narrow PSD	-Difficult to make extremely fine powder unless very high speed can be achieved	Solder pastes, Ti and steel shot

2.2.2 The role of powders in PBF-LB

Powders play a key role in the PBF-LB process and are critical to the quality of the parts produced. The powders generally go through the procedure shown in Figure 2.23 during PBF-LB process. For the majority of research, virgin powder will be used as it provides the best results and has the most consistent and known properties. However, one of the advantages of AM is that material is produced on demand and only where it is needed, so in the case of PBF-LB only the powder required for the part is consolidated and the remaining powder is 'unused'. This powder can be recycled for future use, which is crucial for PBF-LB to be economically viable as a manufacturing process [80]. If this powder is not reused then the material efficiency of PBF-LB is analogous to traditional subtractive manufacturing techniques, such as CNC milling, where the feedstock material is orders of magnitude cheaper.

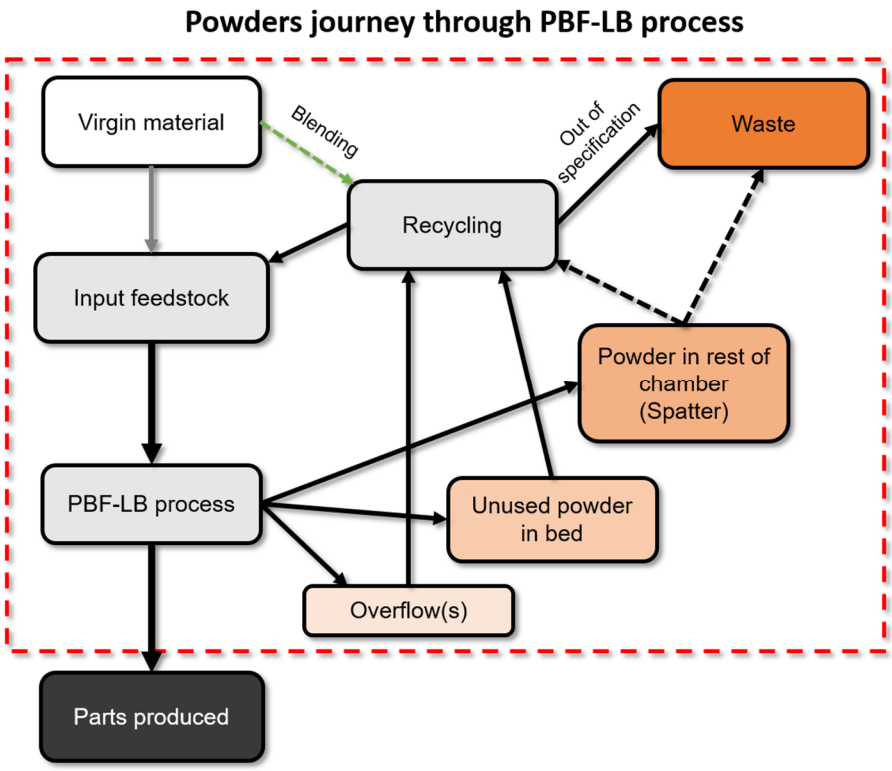

Figure 2.23 Schematic of the journey of powder within the PBF-LB process

The properties of the powder used has a significant influence on the process and the parts produced. Figure 2.24 shows an Ishikawa diagram for the properties which influence the performance of the metal powder in PBF-LB. The complexity of this diagram means that most

end users only consider a small subset of the influencing parameters. However, in order to produce predictable and consistent components and properties it is necessary to have a consistent and known powder bed, which is closely correlated to the process and machine parameters used [68]. The relationship between the powder properties, processing in the machine, and the final properties of parts is highly complex and not yet fully understood. Research in this field is growing and helping to understand these problems, however, changes in powder can be subtle, and be influenced by many factors, which has lead to studies drawing different conclusions to seemingly the same questions.

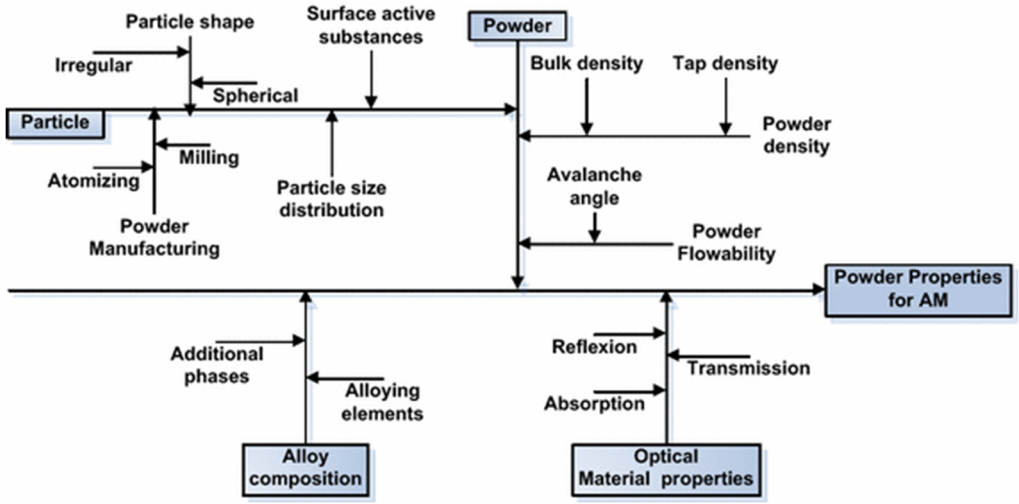

Figure 2.24 Ishikawa diagram with influencing parameters for metal powders. From Spierings et al. [65]

Powder size and distribution play a major role in PBF-LB processing, where good flowability is required to allow good delivery and spreadability of the powder as it is input to the processing zone. A fine balance must be struck between particles large enough to provide good flowability whilst also delivering satisfactory resolution and tolerances [81]. Smaller particles have the tendency to agglomerate easily as attraction from Van der Waals forces cause cohesive forces between particles [82], this leads to poor flowability and, hence, poor powder deposition [83]. Powder sizes for PBF-LB usually range from 20 to 100 µm, with the most common specifications being +15-45 and +20-63 µm. With regards to sieve fractions, '+' indicates what is retained by the sieve and '-' what passes through a sieve. So +15-45 µm denotes powder that passes through a sieve with 45 µm mesh opening but does not pass, and is retained by, a 15 µm mesh opening. A range of relatively coarse and fine particles within this range is also desired to increase packing density; finer particles are able to fill gaps between much larger space efficient particles, and PBF-LB powders usually have a Gaussian

size distribution [84]. Some work has been done into different size distributions, particularly bi-modal distributions, as these can have higher packing densities as depicted in Figure 2.25. It was shown that higher densities are achievable using these powders however many other factors make them less practical for AM [85–87]. The drawbacks of the bi-modal system however are that often a size difference of 7:1 or 10:1 are needed for the smaller powders which puts them in a hazardous size range. Producing bi-modal powders, and particularly the fine powders, is expensive and difficult. Also, producing the designed bi-modal distribution in the powder layer throughout the handling, hopper/storage, and recoating mechanism is problematic.

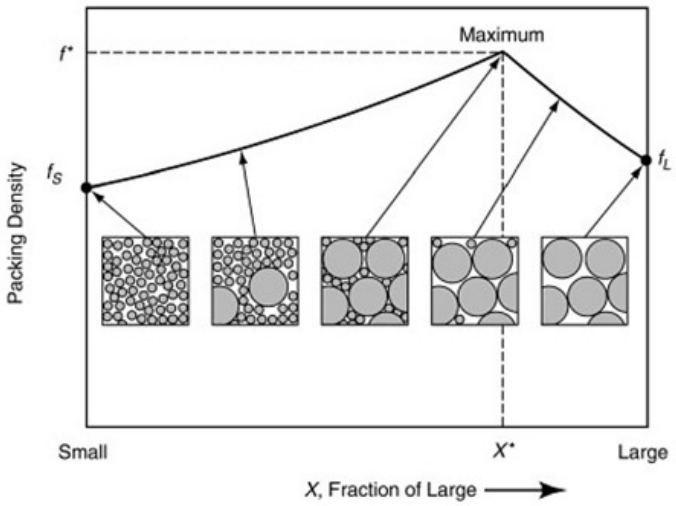

Figure 2.25 Particle size composition vs packing density [88]

The PSD is commonly measured either via sieving, laser diffraction, or image analysis techniques. Sieve analysis provides a simple approach, according to ASTM B214 [89], where the powder is passed through a set of sieves of decreasing mesh sizes and the quantity retained in each sieve size produces the bins of a histogram, creating a PSD. The advantage of using the sieve method is that it gives accurate quantities for each mesh size, is simple to operate, and can analyse both very small and large amounts of powder accurately. The disadvantage of sieving is that the bin size between meshes is quite large so the resolution of the PSD produced is low, it is time intensive, and the length of time over which the sieving is carried out can effect results. This is due to the fact that as long as two dimensions of the particle are beneath that sieve size the particle can eventually align to pass through the mesh even if another dimension is much larger, for example elongated or needle-like particles. An

alternative method is using laser diffraction techniques which allow individual measurement of a large number of particles in a short time and repeatable measurements using appropriate sampling and dispersion techniques according to ASTM B822 [90]. During the measurement the particles, flowing in either air or liquid, pass through a laser beam, which diffracts as it interacts with the particles. The diffraction patterns are reconstructed using an algorithm (most commonly Mie theory or Fraunhofer approximation [91]) to reconstruct an approximated circular equivalent value for each particle. This is ideal for spherical particles but becomes less accurate with elongated and more irregular particles. The collection of these individual reconstructions are then fit to an assumed distribution to create a PSD. Laser diffraction is incredibly powerful and commonly used but often without consideration of the limitations of the technique and the particle sizes being taken as true values [92]. The media used for the laser diffraction can affect the results too, water may break up agglomerates better which may seem to give a more true result of the powder, but if the powder will be operating in a gas, as in PBF-LB, then using air may be more appropriate. Sieve analysis and laser diffraction are difficult to compare as sieve analysis works with sharp cut offs for sizes whereas laser diffraction results are fitted to a distribution, producing tails at either end of the distribution that represents particles outside of the range of a sieve cut. Also, elongated particles which may pass through a mesh will be approximated by the diffraction pattern to be of a circular equivalent larger than the mesh size, as depicted in Figure 2.26.

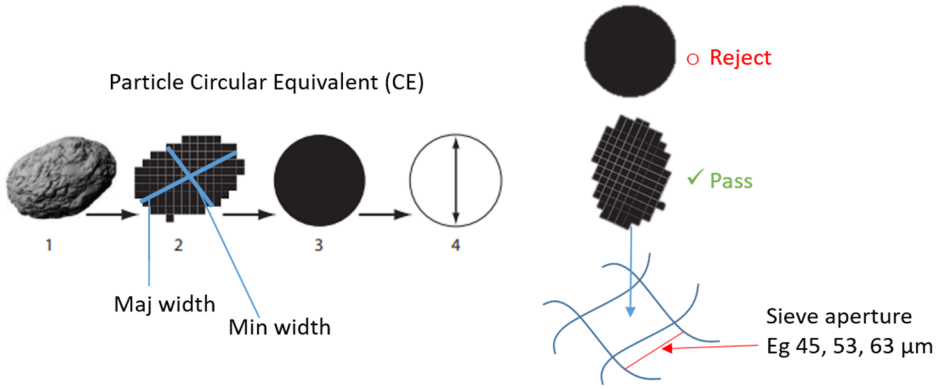

Figure 2.26 (Left) Circular Equivalent (CE) of particle. (Right) Depiction of how a particle can align to pass through a mesh size and the difficulty of comparing laser diffraction results with sieve data – the minimum width of the particle will pass through the mesh opening when the particles maximum width does not pass and also the particles CE does not pass. Adapted from [93]

Image analysis is also used to assess PSDs, either from SEM or optical images. Image analysis will take the raw image, threshold it, identify individual particles, then analyse the pixels to

provide data on the particle. Image analysis provides an advantage over laser diffraction by providing direct raw data from the particle and not an approximation, although there is some influence from the focus and thresholding used. The drawbacks of the process are that it can be time consuming for image collection and data processing, however, instruments such as the Morphologi G3 (Malvern, UK) and Camsizer X2 (Retsch, Germany) are commonly used to automate this process and analyse and process large numbers of particles. Laser diffraction and image analysis can also be used to provide particle distributions on volume as well as diameter. A major advantage of the image analysis process is that much more information can be extracted from the data with regards to shape as well as size. For size distribution measurements, the distribution curve is often presented with the D_{10}, D_{50}, and D_{90} values which denote that 10%, 50% and 90%, respectively, of the volume of particles in the distribution are smaller than that size (e.g. a D_{50} of 32 µm indicates that 50% of the volume of particles are smaller than 32 µm in diameter). For shape, a range of parameters can be extracted, which are discussed further in Section 6.1. These parameters are used to describe the particles across a distribution and establish the effect of particle shape. A shortfall of most particle measurement techniques is that they rely on 2D measurements of 3D particles, however, this is an accepted simplification which provides satisfactory results. Otherwise, much more complex and expensive techniques such as XCT can be used to analyse particles, but the extra information these provide is generally not worth the extra expense and it is not practical for large scale analysis [94].

The morphology and shape of the particles plays a role in PBF-LB. Particle shape influences the packing of the powders, Figure 2.27 shows the trends of particle shape effects on apparent density of powders (the proportion of the voids between powder particles in a volume, rather than the material density of voids within the powder particles). More spherical particles flow more readily and fill more gaps in the loosely packed bed, this leads to a higher ‘loose’ or apparent density. This is attributed to the solidified part being more likely to have a higher density, and conversely, more irregular particles have been shown to decrease packing density and the final density of components [95–97]. This has led to the use of gas atomised powder being preferred over irregular water atomised powders. It has also been demonstrated that PREP powders are able to produce parts with higher density [98] and superior mechanical properties [99]. Particle shape and surface texture are both factors in the particle morphology, for instance gas atomised powder are often spherical but generally have a proportion of

satellites attached to them. These satellites and other irregularities can impede the flow of particles by becoming entangled with other particles [97].

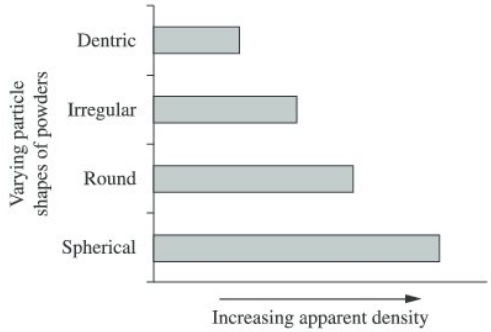

Figure 2.27 Effect of particle shape on apparent density of powders [100,101]

The PSD is the primary factor explored for its effect on packing density and the flowability of powders, which in turn have been investigated for their contribution to part quality in PBF-LB. The flowability influences the packing density and in PBF-LB the crucial factor is the packing density of the powder layer melted by the laser. Spierings *et al.* [66,67] concluded in their study of three SS316L powders with different PSD (average particles sizes D_{50} of 15.12, 25.26, and 37.70 µm building with layer thicknesses of 30 and 45 µm) that powder material feedstock size affects the properties of AM parts. They investigated the effects of PSD on the resulting density, surface quality, and mechanical properties of the parts produced. Their results showed that the smaller size fractions require less energy input to achieve high density, but with optimisation of the parameters all powders reached similar densities. Their mechanical testing showed a reduction in UTS of 20% and yield strength at 0.2% offset of 34% from the powder with the largest size. The authors indicate that the change in properties is not necessarily to do with smaller size fractions of powders but with a PSD that is fit for the powder layer thickness selected. Karaptis *et al.* [83,86] and Spierings *et al.* [67] discussed some important concepts with regards to processing of powders in PBF-LB. The layer thickness defined in the process, which dictates the displacement of the build plate for a new powder layer, is not the thickness of the powder to be melted for a new layer. As depicted in Figure 2.28, the powder bed is consolidated under melting, so when the table is displaced for another layer the powder must fill this displaced amount as well as the reduction in height of the melted section. Therefore, as shown in graphs from Spierings & Levy [66] in Figure 2.29, only for the first layer of the process is the powder layer thickness the same as the layer thickness

which the build plate is displaced. The actual powder layer thickness is related to the packing density, which controls the level of shrinking from this density to the full consolidated solid density of the material. Simulations by Mindt *et al.* [53] estimated a powder bed density of ~50% and other models have predicted a density of 50-55% [10,102], which leads to the powder layer being consolidated to reach a steady state of twice the thickness of the build plate displacement from the 10th layer as shown in Figure 2.29. Measurements by Liu *et al.* [56] of the powder bed density were 61 and 66% for the two powders used in their study, discussed subsequently, which would lead to a reduced change in actual powder layer thickness as also shown in Figure 2.29.

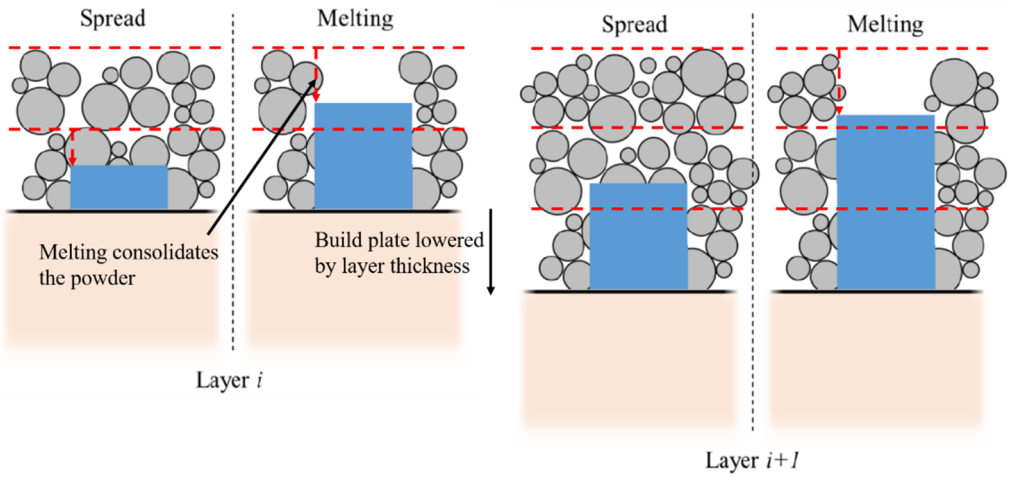

Figure 2.28 Depiction of build plate displacement and powder layer thickness. Modified from Snow [103]

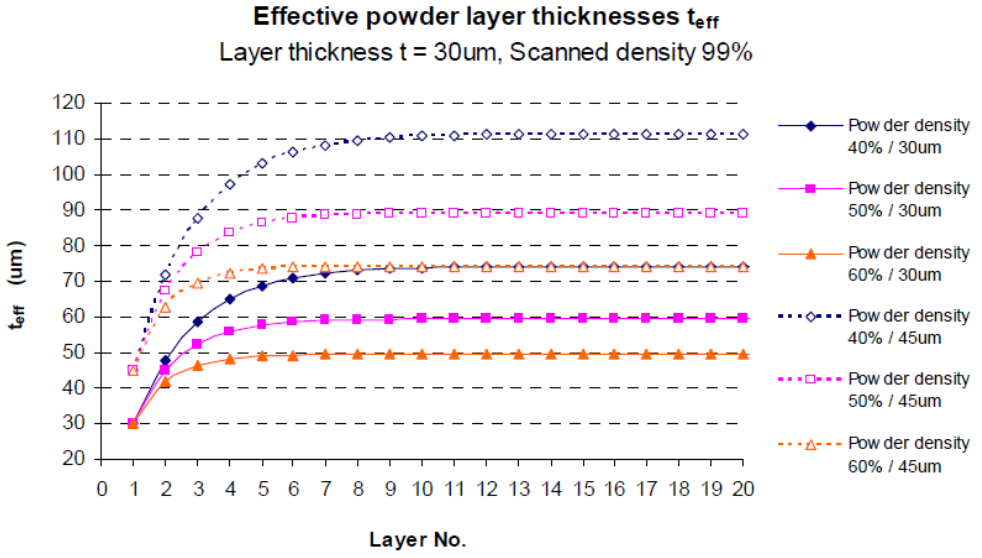

Figure 2.29 Development of the effective powder layer thickness t_{eff} for scanned layer thicknesses of 30µm and 45µm and powder layer densities of 40%, 50% and 60%. From Spierings & Levy [66]

Simulation studies have been conducted to assess the effects of these factors on the powder bed in the process. Mindt *et al.* [53] simulated the spreading of the powder in the recoating of a layer, and demonstrated that interaction of the recoater and the powder can preferentially spread/segregate the particles across the build plate. Notably, this relates to a change in the powder packing density in these regions. This is depicted in Figure 2.30(bottom), where the recoating shows a higher density, and higher proportion of smaller particles, at the beginning of the recoating sequence (highlighted in A), and a lower packing density to the edges of the build plate (highlighted in B). As discussed in Section 2.1.1, Boley *et al.* [30] simulated the absorptivity of the laser by the powder bed using ray tracing scattering models. Their results indicated a variation of the absorption of the laser beam due to the local PSD and subsequent powder packing bed density. For a stainless steel powder with a Gaussian distribution of particles, the absorption of the laser varied from about 0.4 to 0.58. This could contribute to the variation in part properties seen in PBF-LB if this were to be the case. Gürtler *et al.* [54] and Zielinski *et al.* [104,105] simulated the effects of different powder and packing variations and the influence these can play on the melting process and the porosity in the final components. They found that the process parameters need to be optimised for the powder. The ideal powder bed is a stochastic packing of the powder with the PSD distributed evenly across the bed. Whilst variations in this have been simulated, more work is required to understand how this functions in PBF-LB machines. For instance, transference of the powder from storage to the hopper to the recoating mechanism can vary between PBF-LB systems and the standard operating procedures by the users.

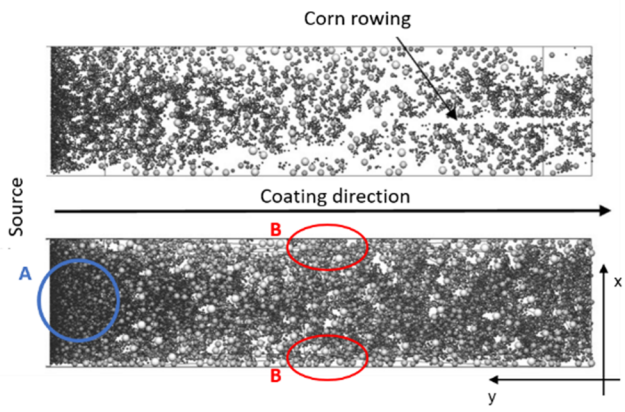

Figure 2.30 Schematic modified from Mindt et al [53]*. Simulation shows the spreading of a 30 µm layer (top) and a 50 µm layer (bottom). On the top the simulation demonstrates the 'corn row' effect when a particle larger than the layer thickness is dragged by the recoater and leaves a streak void of powder. The 50 µm recoating shows a segregation of the particle sizes across the build plate from recoating: with a region of higher packing density at A, at the start of the recoating, and regions of low packing density at B, at the sides of the build plate*

Liu *et al.* [56] investigated the effect of two similar powder size ranges but with different size distributions (0-45 and 14-45 µm with mean sizes of 27.53 and 29.29 µm) and measured the density of the powder bed by building an open top cube sized 30 x 30 x 30 mm. Their results indicated that both powders had their advantages. Despite lower flowability, the powder with the wider size distribution showed higher densities, as shown in Figure 2.31, which made it less sensitive to changes in processing parameters and produced a lower surface roughness. However, the powder with the higher flowability and lower density showed a higher UTS and hardness. An issue with this study, however, is that many of the errors for measurements are not shown and many of the results are within the error ranges, making the trends inconclusive. For example the powder bed measurement technique does not discuss how the powder was extracted and how it was ensured that only, and all, of the powder contained within the box was measured. Also, no correlation of designed volume to actual volume of the box is given and it is known that geometric variations within PBF-LB are an issue [106].

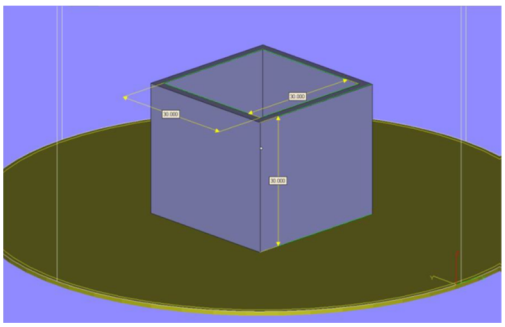

Brand	Apparent density (g/ml)	Powder bed density (g/ml)	Tapped density (g/ml)
Osprey	4.54	5.312	5.54
LPW	4.33	4.88	5.03

Figure 2.31 (Top) Design of container built for powder bed density measurement and (bottom) measured apparent density, powder bed density and tapped density for different SS316L powders. From Liu et al. [56]

Some studies have highlighted the potential effects of the powder surface in the process. With most powder material processing, due to the large surface area of metallic powders, there is a risk of chemical interaction between the powder and the ambient environment [107,108]. Therefore, the ambient environment of the processing facility, and the powder storage containers, can influence the powder properties with higher levels of humidity leading to increased moisture pickup. These gases, or moisture, may interact with the surface of the particles forming oxide and nitride layers which will affect bond forces between powder

particles and flowability. This is a particular issue with regards to the storage and handling of PBF-LB powder and there are many points in the process and supply chain where interaction with these gases or moisture can occur. This is particularly problematic for highly reactive feedstocks such as magnesium, aluminium, and titanium alloys [5,109]. Oxidation hinders the consolidation of the material as oxides have a much lower laser energy absorptivity, down to 3% as shown in Table 2.1. Also increased Oxygen levels leads to instability and breakup of the melt pool, contributing to the balling effects, as discussed in Section 2.1.1. The oxides also hinder surface wetting which subsequently leads to poor adherence between formed layers and produces lack-of-fusion defects and may initiate cracks [110]. Moisture in the powder also leads to agglomeration and poor flowability of metal powders. Powders may often be dried before, and/or, after use to remove moisture present, however, this will not be able to remove any stable oxides which have formed.

2.2.2.1 Powder recycling

The investigations discussed in this section have aimed to understand the effect of particular properties of a powders to the performance in the PBF-LB process. As mentioned previously, an important aspect of PBF-LB is the recycling and reuse of powders, which make the technology economically viable. Whilst it is the 'unprocessed' powders that are collected and reused, these powders have still been processed to some degree through interaction with different environments, thermal cycling, handling, and process by-products have been introduced. Therefore, to achieve predictable and consistent part properties and for quality control it is important to understand the evolution of this powder to understand the change in powder properties and the effect on the final components. The difficulty in making conclusions from the published work, as will be discussed, is that different experimental techniques have been used for the studies or details not disclosed, which can be problematic when studies draw different conclusions.

Seyda *et al.* [111] found in their study of 12 processing cycles that the average particle size increased from 37.4 µm to 51.2 µm, there was a significant decrease in the proportion of particles <20 µm detected, and particles >100 µm were detected which were not in the virgin powder, concluding that fine particles are not recycled and reintroduced in a subsequent production cycle. They commented that the flowability of the powder increased in their

qualitative assessment and concluded this was due to the removal of fine particles and their agglomerative effects on the powder. After 12 cycles the apparent density of their Ti-6Al-4V powder increased from 2.27 $g.cm^{-3}$ to 2.47 $g.cm^{-3}$ which they explained through the coarsening of the powder and improved flowability. They termed these effects the 'aging' of the powder. When processing the Ti-6Al-4V powder, Seyda *et al.* found the part density to increase from 4.408 $g.cm^{-3}$ to 4.421 $g.cm^{-3}$, attributed to a better packing density in the bed. They found the total number of pores decreased but the size of pores increased as powder was recycled, which was likely due to gaps between the larger particles and lack of smaller particles to fill these. An increase in hardness from 364 H_v to 374 H_v was explained by the likely pick up of Oxygen from the powder during its exposure to the atmosphere. Powder oxides form and are transferred to the material during processing. Whilst this may cause an increase in the hardness of the processed material, the detrimental effects, such as a reduction in ductility, was not discussed. Tensile testing showed an initial correlation of increased UTS with an increase in density but this decreased after 6 cycles, at this point it was found that the larger pores acted as stress concentrators, leading to premature failure. There was also an increase in the surface roughness of the parts over the 12 cycles. An issue with the study is that they do not produce details of their recycling process and their methodology with regards to other factors which may affect the results such as with regards to the powder collection, handling, processing environments, build details, etc.

PBF-LB machine manufacturer Renishaw released a white paper investigating the reuse of Ti-6Al-4V in their AM250 machine, this system uses a near-vacuum step before filling with argon to reduce the content of undesirable gases in the chamber for processing. Their study showed a general gradual increase of D_{10}, D_{50}, and D_{90} over the course of 38 builds and a decrease in flowability. There was a clear trend of increase in Oxygen and Nitrogen content over the course of the build, which lead to the powder exceeding the allowable content for these elements for Grade 23 Ti-6Al-4V over the course of the study, as shown in Figure 2.32. A study by O'Leary *et al.* [112] using the same machine showed the powder exceeding the Grade 23 limit much quicker than the Renishaw study, even within the first build, and the Oxygen content exceeding the Grade 5 allowable level, as shown in Figure 2.32. The mechanical performance of parts produced from the builds by Renishaw are summarised in Table 2.3, which shows a general decrease in performance of the parts produced over the recycling of the powder but the highest performance was found in the parts produced in the final build.

This indicates that the changes in the powder, likely to do with the Oxgyen pick up, has a detrimental effect on the properties of the components produced but also that it increases the variability of the specimen, which is an issue already inherent in PBF-LB that inhibits adoption of the technology.

Table 2.3 Tensile analysis from build numbers 1, 12, 18, 24, 31, and 38 for both as-built (AB) and machined (M) surfaces. From Renishaw plc [7]

Build no.	Youngs mod (GPa)		0.2% PS (Mpa)		UTS (MPa)		Plastic elongation (%)		R of A (%)	
	AB	M	AB	M	AB	M	AB	M	AB	M
1	103	113	788	839	925	1012	13	7	24	14
12	103	117	849	934	960	1052	14	12	32	30
18	109	116	863	921	979	1056	15	17	30	42
24	105	116	837	918	951	1051	11	7	21	12
31	104	116	823	897	938	1041	9	10	19	18
38	111	119	916	989	1026	1095	15	17	25	47

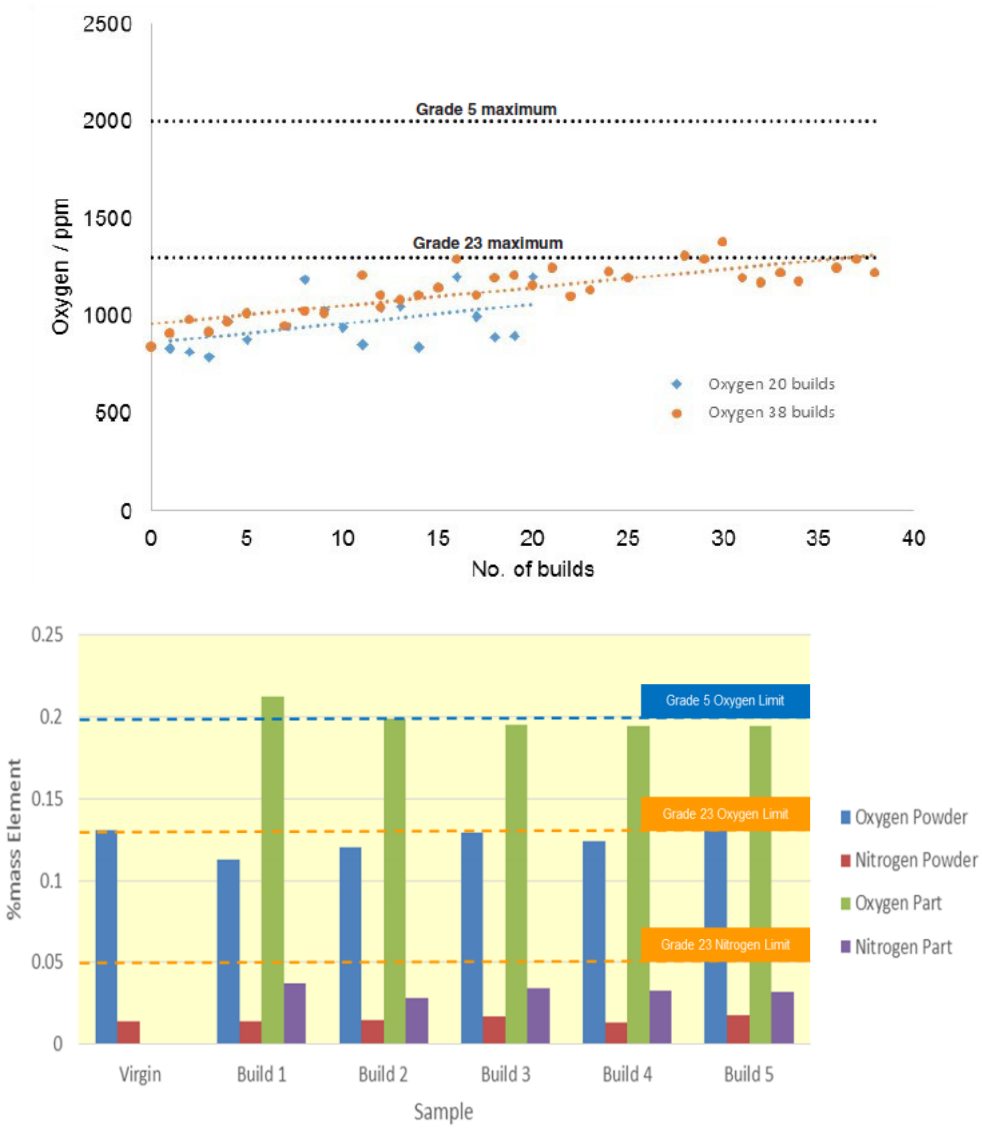

Figure 2.32 (Top) Oxygen analysis over two separate re-use studies shows a gradual increase in concentration from Renishaw plc [7] *and (bottom) LECO analysis results for powder and parts at various stages of recycling from O'Leary et al.* [112]

Strondl *et al.* [113] measured the change in a Nickel-based alloy that had been used once and sieved back to specification (-63 µm) and blended with approximately 5% of new powder. As well as a slight increase of the PSD, they found this improved the flowability of the powder and increased the packing density. In the final parts they found no difference in microstructure but an increase in porosity. With tensile testing, the recycled powder exhibited a similar performance, although figures are not given, but with a decreased ductility and the decrease in ductility was also reflected in a decrease in fracture toughness. The effects on the final part

are attributed to a 58.8% (assumed to be wt% but not stated in study) increase in the Oxygen content compared with the as-received virgin material.

On the other hand, other studies have shown much smaller, or no, effect from the recycling of the powders. Ardila *et al.* [114] investigated the recycling of Inconel 718 powders with a drying and sieving process in between uses of the powder. They found an overall coarsening of the powder over the 14 cycles they conducted, and minimal change in the composition of the powder, with a slight reduction in Nb, Ti, and Al, although they only analysed this via EDS for one spectrum. Their porosity and mechanical testing via Charpy impact testing showed variation across all the builds but no trend, as shown in Figure 2.33. Nguyen *et al.* [115] also investigated the recycling of Inconel 718 after ten uses and found minimal effects, however, they did not describe their recycling process. They found that the PSD and flowability of the powder did not change, and whilst there was a slight decrease in the tensile performance and hardness of the resulting parts, these were within the errors for the measurements. They did measure a decrease in the quantity on Al, Nb, and Mo but did not include how this was measured or the errors in the measurements.

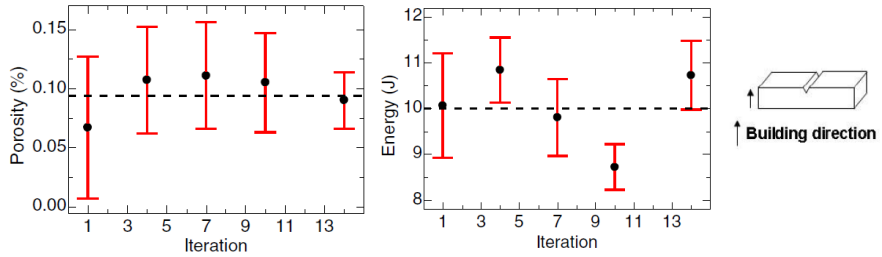

Figure 2.33 (Left) Results from porosity measurements performed over manufactured Inconel 718 samples. Each point represents the average porosity (in percentage) found in 6 samples fabricated in five particular iterations. Red bars indicate standard deviation from this value. The dashed line represents an average porosity obtained from these five values. (Right) Results from Charpy impact tests performed over manufactured samples. Each point represents the average energy needed to fracture 6 samples fabricated in five particular iterations, while red bars indicate standard deviation from this value. The dashed line represents an average energy obtained from these five values. From Ardila et al. [114]

As can be seen from the review above, it is generally agreed that the use and recycling of powders changes and influences them, particularly in increasing the size of the particles and Oxygen content, but it is not conclusive as to what effect this has on the properties of the parts produced. This is an issue that contributes to the uncertainties in the PBF-LB process which is a concern for the technology and a hindrance to its wider adoption. The principal

issue with the studies discussed is that there is a lack of clarity in the design of the recyclability experiments, particularly in terms of what metrics are tracked and the elements that are involved in the recycling process. Figure 2.23 shows the elements of powder output from the system indicating what contributes to recycling. Most of the studies reviewed, however, did not provide details of exactly what the recycling process entailed. All the studies used different powders/materials, built different specimens, used different tests, and different characterisation techniques. Another contributing factor to the range of results is the sampling methods, or lack of, used in the experiments. What powder is analysed, where it is taken from, and the sampling techniques used to ensure a representative sample is used are crucial [116]. A difficulty is that there is no generally accepted process or official standard for assessing the development and changes in the powder and in industry all powders have to be measured to assess them and bring it back to specification if needed, which is impractical and costly. There have been useful reviews/appraisals of good methods for measuring PBF-LB powders and properties to measure and track properties but these need to be integrated with clear design principals for further investigation [65,94]. This is a crucial area for PBF-LB processing; understanding the fundamental influences of the powders' characteristics on the processing, how this changes over reuse of the powder, and what can be implemented to correct these effects. These powder characteristics, which bear a large influence on the processability of a powder through PBF-LB, is very much material and machine specific [117]. Although it would appear that a reasonable amount of research has already been published in the field, the limitations of these studies indicate there is much more that needs to be understood about the change in the powder and material in PBF-LB.

2.3 Nickel-based superalloys

Nickel-based superalloys are predominantly used in high-temperature turbine engine components for power and aerospace applications. Their use in jet engines is shown in Figure 2.34. The major components they are used for are; turbine discs, turbine blades, nozzle guide vanes, and in the combustion chamber. They are used in these applications due to their excellent mechanical properties and oxidation and corrosion resistance at high-temperatures [118]. These properties are key to the performance of components in these very difficult operating environments, especially in industries such as aerospace which have stringent quality standards due to safety critical applications. Applications with high complexity, such

as in turbine engines, provide an ideal opportunity for the exploitation of the advantages of AM. Also, highly profitable industries, such as aerospace and power, are ideal early adopters and drivers of the technology. As one of the most important aerospace materials, Nickel-based superalloys are an important material group for PBF-LB [119]. Another reason for interest in PBF-LB is the difficulty in machining Nickel-based superalloys due to their high hardness. This makes it advantageous to produce them near-net shape.

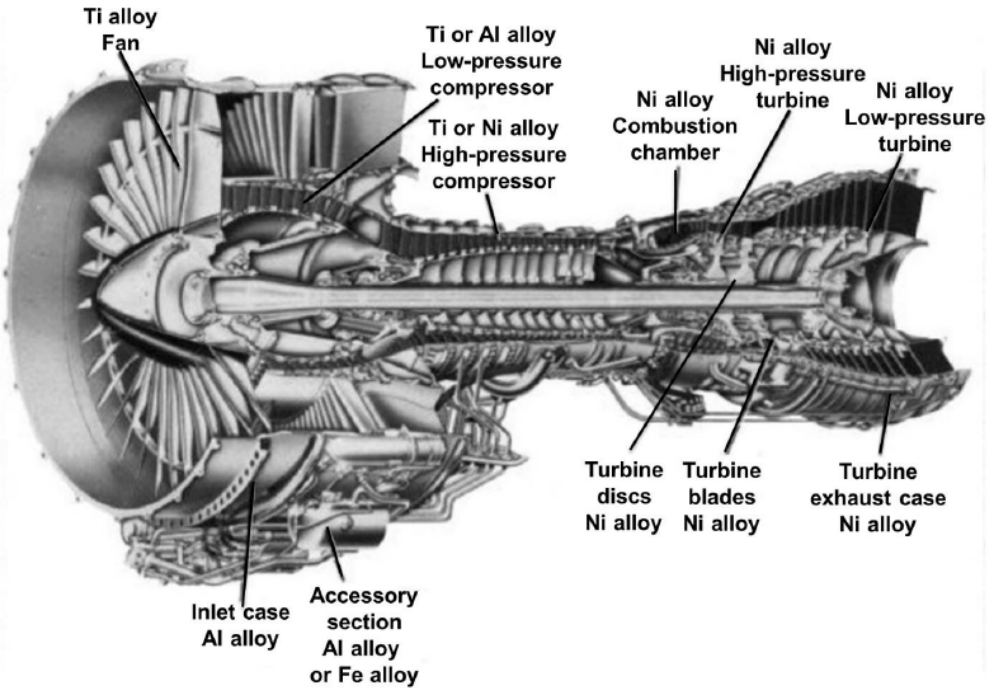

Figure 2.34 Material usage in a turbine engine. From Campbell [118]

The properties exhibited by Nickel-based superalloys are linked to their unique metallurgy. Figure 2.35 highlights many of the particular characteristics found amongst the different Nickel-based superalloys. There are three main categories of the alloys related to the different strengthening mechanisms they employ. These are precipitation hardened, solid-solution strengthened, and oxide dispersion strengthened (ODS) alloys [120].

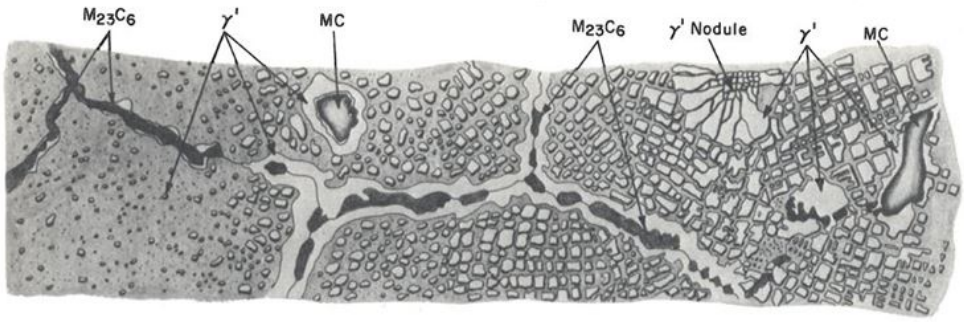

Figure 2.35 Schematic of a typical Nickel-based superalloy microstructure. From Sims and Hagel [121]

2.3.1 Inconel 718

Inconel 718 is a solid-solution strengthened Nickel-based superalloy and the most common superalloy used in aerospace [120]. Many PBF-LB OEMs offer Inconel 718 as a material option for their machines and GE has qualified non-load bearing parts for use in engines [122]. γ' [Ni3 (Al, Ti)] and γ'' [Ni3 (Nb, Ti)] are the two main precipitates which provide Inconel 718's high strength at elevated temperatures. The nominal composition for Inconel 718 according to ASTM B637 is listed in Table 2.4.

Table 2.4 Allowable range for nominal composition for Inconel 718 from ASTM B637 [123]

Element	Wt%	Element	Wt%	Element	Wt%
Ni	50.0 - 55.0	Al	0.20 - 0.80	P	0.015
Cr	17.0 - 21.0	Co	1.00 max	S	0.015
Nb	4.75 - 5.50	C	0.08 max	B	0.006 max
Mo	2.80 - 3.30	Mn	0.35 max	Cu	0.30 max
Ti	0.65 - 1.15	Si	0.35 max	Fe	Balance

Typically, Inconel 718 has been manufactured in wrought, cast, and powder metallurgy routes, however more recently, work has been conducted into its use through PBF-LB. Compared to the conventionally manufactured Inconel 718, PBF-LB has a much finer microstructure due to the high cooling rate in the process. The microstructure has been characterised in many studies [124–127], and a typical example is shown in Figure 2.36. The columnar grain structure can be seen growing over multiple scan tracks and layers in the build direction. Localised changes can be seen with regards to the scan tracks influencing the dendrite growth at the

edge of the melt pool. The high cooling rate in the process inhibits macro-segregation but it has been noted that micro-segregation of elements with high susceptibility, such as Nb in Inconel 718, occurs [124]. Studies have been conducted into improving and tailoring the microstructure through heat treatments [124,128–130]. The heat treatments successfully promoted the formation of γ' and γ'' strengthening precipitates and the development of the needle-like δ phase along the grain boundaries.

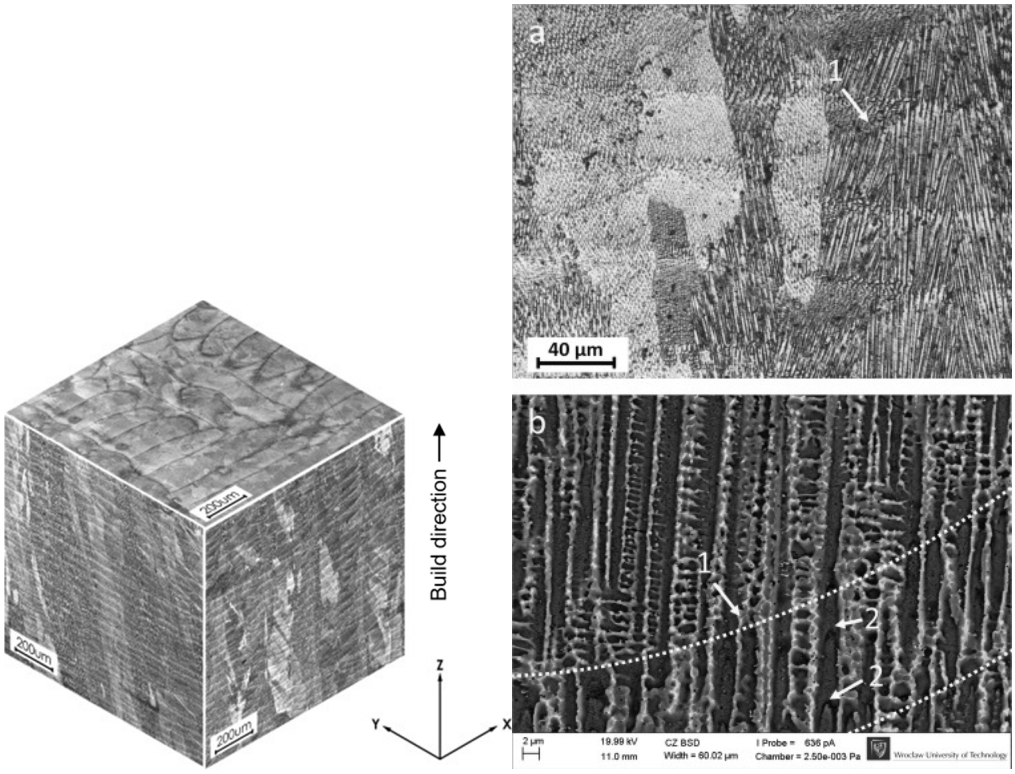

Figure 2.36 (Left) Microstructure of Inconel 718 in as-built condition in three mutually perpendicular planes of the polished section. Columnar architecture and laminar material structure are visible in the yz and xz sections and laser scanning tracks in section xy. (Right) Magnified images of microstructure in the xz plane in as-built condition, showing internal dendritic-cellular grain structure; arrows 1 indicate tracks interface: (a) OM image and (b) SEM image of track interface; arrows 2 indicate segregation traces at dendritic cells tips (see arrows 2). From Chlebus et al. [124]

The mechanical properties exhibited by PBF-LB manufactured Inconel 718 are promising. Studies have shown similar and even better mechanical performance, in terms of tensile and hardness properties, compared to conventionally manufactured components. Even performing to comparable levels at high temperature, as shown by Trosch *et al.* [127] in Table 2.5. Studies have shown heat treatment procedures to improve these properties as summarised in a review by Wang *et al.* [119]. A point to note, however, is the range of properties achieved. Trosch *et al.* [127] showed significant variation due to build direction and

anisotropy. Chlebus *et al.* [124] showed this as well, but also noted variation in properties between parts, their Young's modulus results for five parts with different build orientations were 163±30, 199±15, 188±19, 209±44 GPa. That final orientation, at a 45˚ build angle, having a deviation of ±21% in the Young's modulus. The results, from various studies, summarised by Wang *et al.* [119], show a variation in properties between manufacture from different places, which may involve different powder sources, different PBF-LB systems, different processing parameters, and numerous other potential factors.

This variation is an issue for adoption of the technology for this material for use in critical aerospace applications, as quality control is imperative. Progress has been made, with the properties indicating acceptable static mechanical performance, leading to the use in non-load bearing components. However, to achieve the aim of use in more demanding components more needs to be done to understand factors which can influence the variation in properties and control them.

Table 2.5 Mechanical properties of Inconel 718 at room temperature, 450 °C and 650 °C. From Trosch et al. [127]

UTS[a] (MPa) $R_{p0.2}$[b] (MPa) ε_f[c] (%)	Horizontal	Vertical	45˚	PBF-LB (Average)	Forged	Cast
Room temperature	1440	1400	1450	1430	1380	950
	1186	1180	1190	1185	1192	940
	18.5	20.4	16.9	18.6	19.1	23.1
450 ˚C	1216	1160	1255	1210	1177	766
	1033	1026	1080	1046	1055	750
	12.4	15.9	12.8	13.7	17	10.9
650 ˚C	1011	992	1074	1026	1061	576
	870	860	855	862	955	517
	3.6	14.2	5.8	7.9	13.9	13.7

Note: Each value was determined from an average of 4 measurements.

[a]Ultimate yield strength [b]0.2% yield strength [c]Elongation to failure

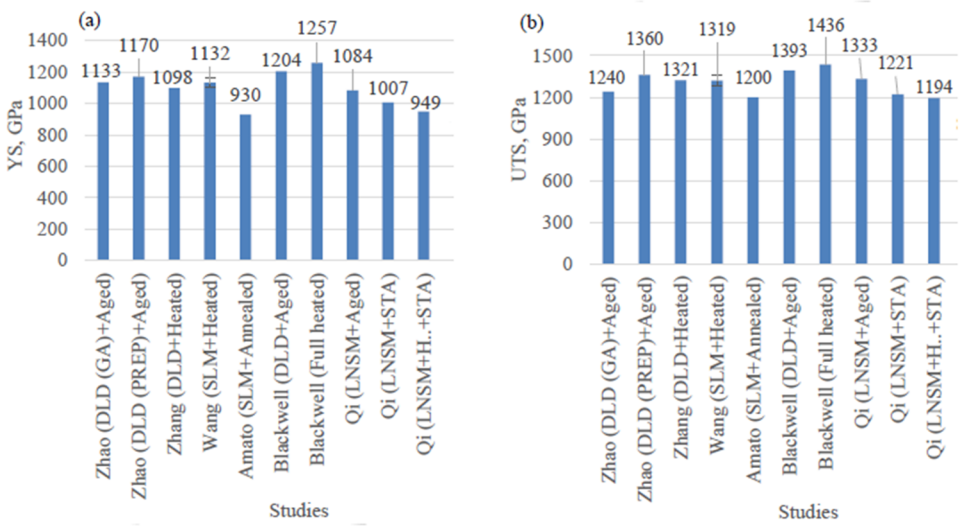

Figure 2.37 Mechanical properties for Inconel 718 after various heat treatments from a range of studies. From Wang et al. [119]

2.3.2 Hastelloy X

Hastelloy X is a solid-solution strengthening Nickel-based superalloy. This mechanism is achieved by the solution of elements, such as Cr, Mo, Co, W and Fe, into the Nickel-based γ matrix [121]. Consequently, Hastelloy X has a lower content of γ' precipitating elements such as Al, Ti, Nb, and Ta, and this lack of γ' precipitation means that Hastelloy X is not one of the strongest Nickel-based superalloys. However, the high content of Cr leads it to being among the most corrosion and oxidation resistant and it is still utilised in applications with high loading and extreme environments [131]. The nominal composition for Hastelloy X alloys according to ASTM B435 is listed in Table 2.6.

Table 2.6 Allowable range for nominal composition for Hastelloy X from ASTM B435 [132]

Element	Wt%	Element	Wt%	Element	Wt%
Ni	remainder	Mo	8.0—10.0	Mn	1.00 max
Fe	17.0—20.0	W	0.2—1.0	P	0.04 max
Cr	20.5—23.0	C	0.05—0.15	S	0.03 max
Co	0.5—2.5	Si	1.00 max		

Much less research has been conducted into the PBF-LB processing of Hastelloy X compared to Inconel 718. However, a large proportion of the published research has been from Siemens

Industrial Turbomachinery [133–135], highlighting the commercial significance and drive for processing this alloy via PBF-LB. It has been shown that cracking is often an issue with PBF-LB processing of Hastelloy X. Tomus *et al.* [136,137] and Harrison *et al.* [138] showed how crack formation occurs and linked this to micro-alloying segregation during solidification. Both studies showed how altering the composition of the alloy, particularly the reduction of Si and Mn, was beneficial in removing cracking from the material, suggesting metallurgical improvements could be made for PBF-LB specific Hastelloy X. Mertens *et al.* [139] investigated the effect of preheating on the processing of four materials including Hastelloy X. They showed that preheating could be used to reduce the crack formation and improve the part quality by reducing the formation of residual stresses, but that the laser processing parameters had a larger effect. Brodin & Saarimaki [134] showed that the PBF-LB processed parts exhibited similar, and in some cases superior, strength to hot-rolled specimens but with less ductility. Brodin *et al.* [133] found worse fatigue and creep performance than the hot-rolled material, but better than cast material for low cycle-low temperature fatigue. These studies, and that by Tomus *et al.* [137], found significant anisotropy in the results of their mechanical testing, as shown in Figure 2.38. Etter *et al*. [140] showed how heat treatment and scanning strategy can reduce the anisotropy in the material however it could not be completely removed. As with for Inconel 718, there is still much work required to achieve acceptable quality and consistency in PBF-LB manufacturing for adoption and use in aero components for Hastelloy X.

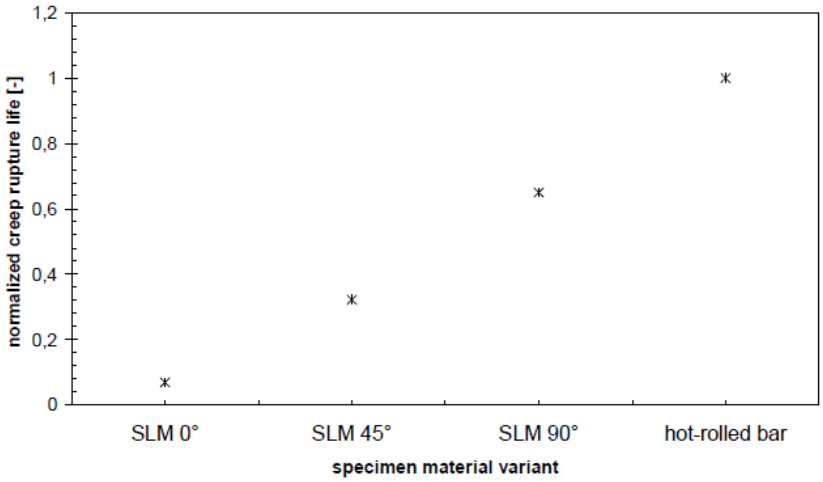

Figure 2.38 Stress rupture testing at 815°C. Comparison of SLM material and hot-rolled Hastelloy X. From Brodin et al. [133]

2.4 Fatigue crack growth in PBF-LB

As previously illustrated, process induced defects and microstructure variations can affect quasi-static mechanical properties of components. However, such defects can potentially have an even larger effect on the dynamic properties, such as in cyclic fatigue and crack growth [64]. Fatigue fracture initiates in regions of stress concentration, such as defects. Therefore most fatigue cracks initiate and grow from these defects in location of high stress, leading to early failure of components, as shown in Figure 2.39. Traditional cyclic fatigue life testing is dominated by surface condition and defects, which are numerous at the surface and sub-surface of as-built PBF-LB components [141]. Many investigations have been conducted to show that the effect of surface defects impacts significantly on the fatigue life of components, the majority for Ti-6Al-4V [142–150] with less work on Nickel-based superalloys, steels, and aluminium alloys [64,151–155]. The stochastic element to defect distribution in the process leads to scatter in fatigue results and may also severely restrict the application of PBF-LB parts. The morphology, size, number, and location of defects all have significant influence on the fatigue life. Generally, spherical defects have a lesser effect than irregular defects. Gong *et al.* [156] found that small spherical defects had little influence when the porosity level in the part was <1%, however the more irregular defects, which are generally larger, had a considerable influence, regardless of the porosity level. Many of the studies also found considerable anisotropy in the fatigue performance, as was also seen in the static mechanical testing. Post-processing through surface treatments and heat treatments have been shown to considerably improve the fatigue performance of PBF-LB specimen.

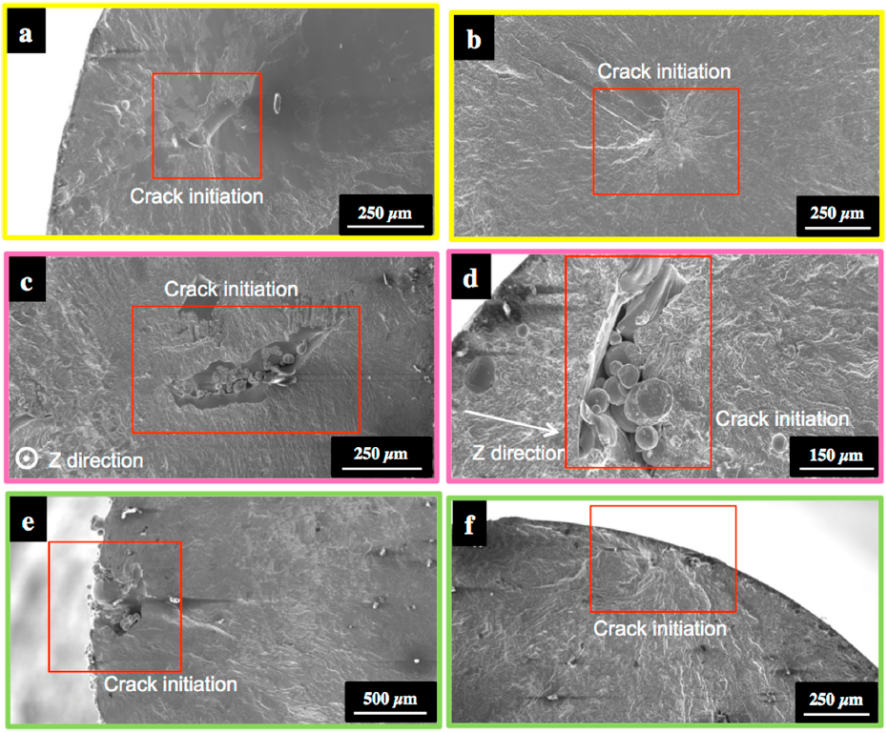

Figure 2.39 Fracture analysis of different types of defects identified to be the crack initiation origin in Ti-6Al-4V PBF-LB high-cycle uniaxial fatigue specimen. From Charkaluk & Chastand [157]

Fatigue crack growth (FCG) testing provides understanding of the growth of cracks in the bulk material and is less influenced by the surface of the specimen. For crack propagation, in contrast to the traditional stress-life and strain-life approaches to fatigue, cracks are assumed to exist in material and structures within the context of fracture mechanics and characteristics of fatigue are gained by relating the rate of crack growth of such cracks to an appropriate fracture mechanic parameter [158]. Crack growth is important for Inconel 718 due to its application in high cyclic loading applications such as turbine engines, as discussed in Section 2.3. These harsh operating environments promote accelerated crack growth which can lead to premature critical failure in components, therefore, a high crack growth resistance is desired. Defects are likely to be present in PBF-LB specimen, which are common crack initiators, and if combined with poor FCG resistance would lead a high crack growth rate and fast rupture of components.

The majority of FCG studies for PBF-LB components has been for Ti-6Al-4V. Hooreweder *et al.* [159] showed similar crack growth performance for PBF-LB manufactured specimens compared to vacuum arc re-melted mill annealed specimens due to the fine grained microstructure with high density of grain boundaries acting as obstacles for crack propagation.

This fine grain structure however lead to an inferior fracture toughness. Leuders *et al.* [148] showed that the fatigue crack growth rate (FCGR) is influenced by residual stresses and the performance can be improved with a suitable heat treatment. Cain *et al.* [160] explored further the improvement of stress relieving and heat treatment on the FCGR, as shown in Figure 2.40(a-c). Their study and that by Vrancken *et al.* [161] found anisotropy in the FCG performance, with orientation of the crack plane parallel with the build direction (XY) providing the highest FCGR, as shown in Figure 2.40(d-f).

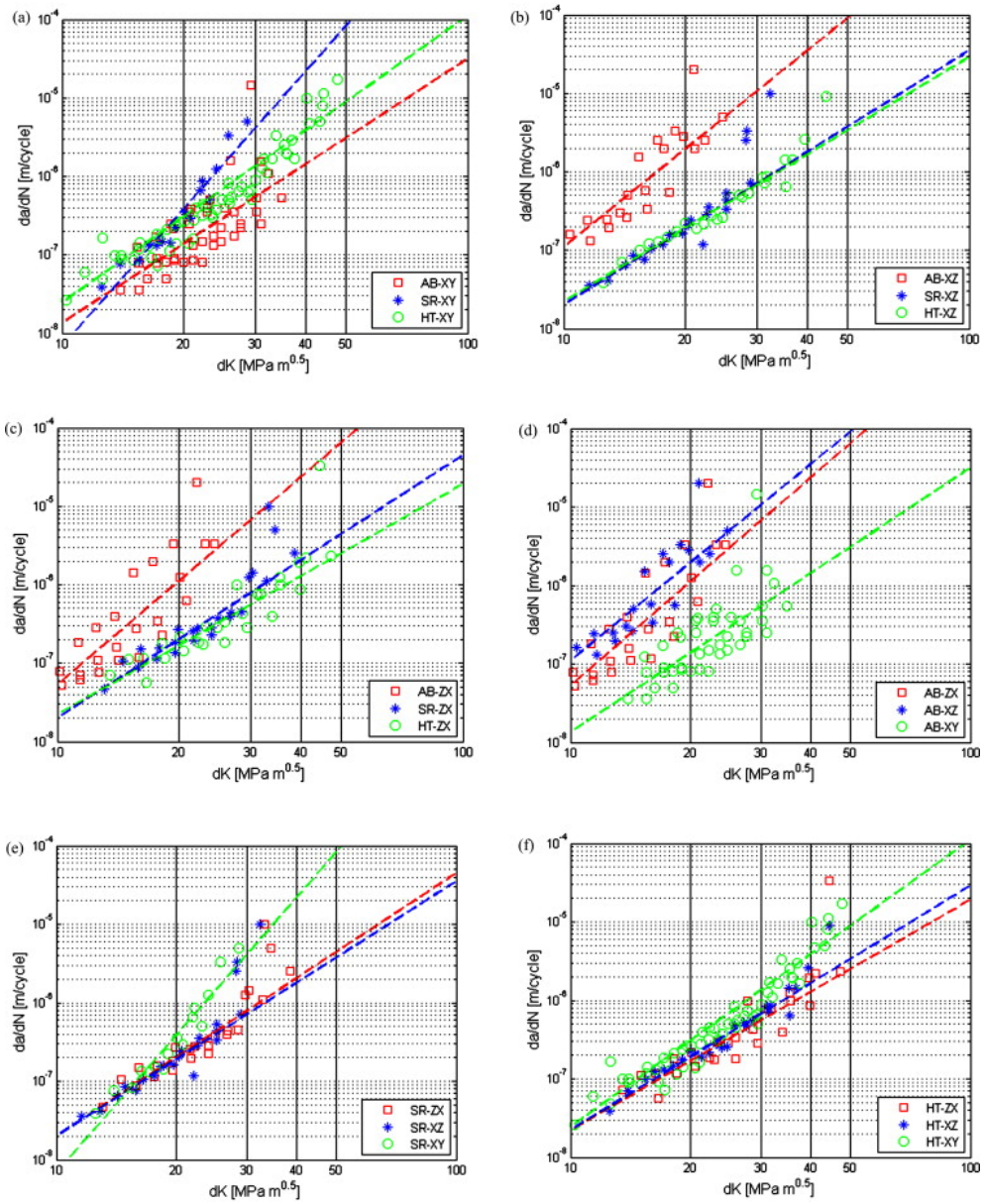

Figure 2.40 Crack growth da/dN versus stress intensity range dK for (a) the XY specimen orientation, (b) the XZ specimen orientation, (c) the ZX specimen orientation, for the different post-heat treatment conditions, and (d) the as-built (AB) condition, (e) the stress relieved (SR) condition and (f) the heat-treated (HT) condition, for the various orientations. From Cain et al. [160]

Investigation of the FCG in PBF-LB manufactured Inconel 718 was conducted by Konečná *et al.* [162,163]. Their tests found that the PBF-LB specimen performed similarly to the conventionally manufactured Inconel 718 at high crack rates (above $5x10^{-5}$ mm/cycle) but had a much lower threshold (K_{th}), as shown in Figure 2.41. They proposed the low threshold value to be due to low boron content, the fine grain structure produced by PBF-LB, and high residual stresses in the specimen. However, they didn't provide further data to assess these factors. Their specimen had the crack initiation notch manufactured as the PBF-LB geometry of the specimen, as opposed to machined, and they discussed how this would likely have had an effect on the residual stresses at the start of the crack growth area. It is clear that further investigation is still required to understand the fatigue performance of PBF-LB manufactured Inconel 718.

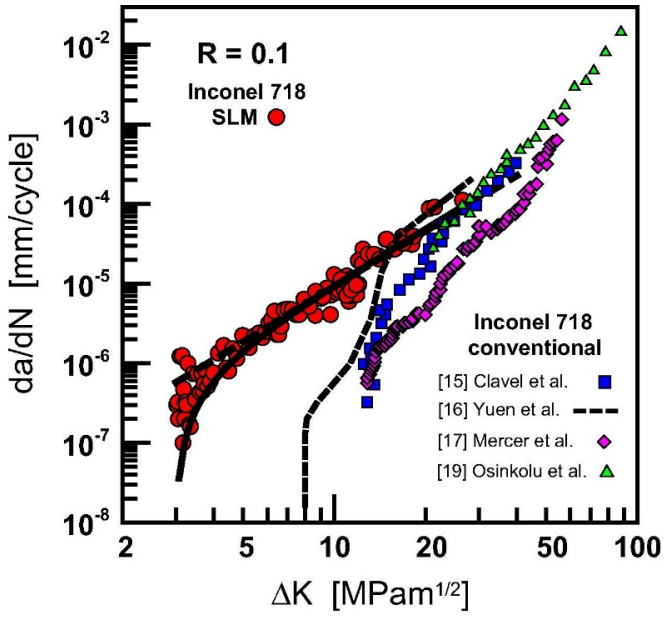

Figure 2.41 Comparison of fatigue crack growth data for conventionally and SLM manufactured Inconel 718. From Konečná et al. [162]

2.5 Summary and research opportunity

PBF-LB technology is developing at a rapid rate and has been qualified for use in non-load bearing components in aerospace turbine engines. However, there are still inherent variabilities and quality issues which arise in the process, as discussed in Section 2.1. Specimens built by different machines use different parameters and produce different

properties. These inconsistencies and flaws hold back the implementation of PBF-LB for high-performance application in the more demanding sections of the engine. The ideal for PBF-LB is to be able to take a digital file of a component and know the process well enough that it could be manufactured anywhere in the world and result in known properties, as with many conventional manufacturing techniques. This relies on defining and understanding of all the factors which can influence part properties in the process.

Vaporisation is an inherent part of the melting regime in welding and is accompanied by the ejection of spatter melt material, as discussed in Section 2.1.2. Much of the research into spatter has been focussed on the physical phenomena that drive it and the different effects which occur in PBF-LB compared to conventional welding, such as the entrainment of particles. A few studies have attempted to explain the material that is produced from the spatter process. They have shown that there are different effects amongst different materials, raising a need to qualify each alloy system. The investigations have been far from exhaustive and more recent advances in understanding of the formation phenomena allow greater insight into the material produced. Analysing the material produced, considering much of it is incorporated into the rest of the powder, makes this a difficult challenge and the studies presented have some shortcomings. Improvements can therefore be made in analysing these particles combined with advancements in understanding of their generation. Understanding of the direct effects the spatter can have on part performance is required too.

The majority of research in PBF-LB has focussed on improving mechanical properties, primarily static properties, through optimisation of the processing parameters. There has been much less focus on the properties of the powders. There have been studies which have started to understand that conventional powder measurements are not always appropriate for the PBF-LB process. They have started to identify the important powder characteristics and correlate these to their effects in the PBF-LB process, as discussed in Section 2.2.2. Conclusions of much of the research is that the powder characteristics affect the deposition and spreading of the powder and laser processing parameters need to be tailored to the powder in the bed.

Investigation into the recycling of the powders in the process has shown that there is change in the powders over reuse cycles, as discussed in Section 2.2.2. Across the research it was unclear what the exact implications of the recycling on the part performance were, as studies

gave conflicting conclusions. This identified that due to the numerous factors that can affect the results of studies there needs to be a greater understanding of the changes in the material, how to track these, and the design of experiments to investigate their effects. An area that was highlighted was the pick-up of Oxygen by materials in the process and the potential negative ramifications this can have on the mechanical properties and the qualifications of parts. There appears to be lacking an understanding of appropriate recycling procedures, and guidelines, based on the properties of the spatter generated. This area also requires further investigation.

Nickel-based superalloys are a crucial material group for the aerospace industry and demanding components in turbine applications. Therefore, considerable research has been conducted into their use for PBF-LB, as discussed in Section 2.3. The research has showed that similar static mechanical properties can be produced in PBF-LB components compared to conventionally manufactured components and that heat treatment procedures can improve these properties. However, the studies also showed that there are issues with greater variability in properties between specimens and a range of properties produced by different studies.

Whilst the performance of PBF-LB specimen with regards to static properties has been promising, their performance with regards to dynamic properties still requires improvement. FCGR testing is highlighted as a good technique for assessing the fatigue properties of the bulk material, as discussed in Section 2.4. The FCG studies conducted so far have predominantly investigated Ti-6Al-4V and shown that residual stresses in the components greatly reduce the performance of as-built PBF-LB specimens and that heat treatments and stress relief can improve the properties. There has been minimal investigation of the FCG performance of Nickel-based superalloys and those conducted have shown a reduced resistance to crack growth compared to conventionally manufactured materials.

Following the review of the literature, the key gaps are outlined below, which have been used to shape the research presented in this thesis:

- Understanding of the particles produced by spatter during processing is required to understand the change in material and powder through the process (Chapter 5 and 6)

- The spatter produced and changes in powders needs to be understood for each material and PBF-LB system as changes will be bespoke to alloys and how they are processed (chapter 5 and 6)
- The change in the powder must be understood for the build in which spatter is generated and for subsequent builds through the recycling of powder (Chapter 6 and 7)
- Methods of understanding the powder bed with regards to the material which the laser interacts with, across the powder bed and between builds, which can cause variation in the properties of parts (Chapter 7)
- Understanding the fatigue properties of PBF-LB manufactured specimens need to be understood, particularly for Nickel-based superalloys, to drive their adoption to more demanding applications (Chapter 8)

The work of this thesis aims at addressing these gaps in order to contribute to developing a comprehensive understanding of the process, in order to advance the technology towards a more reliable and controlled process with wider adoption in industry.

Chapter 3 Experimental tools and methods

This chapter describes the materials and methods involved in the research, including the PBF-LB machines, laser processing parameters, design, and characterisation. Section 3.2 discusses the range of PBF-LB machines used for building specimen and generating spatter across all the chapters and work. The relevant differences between the machines are described, and the processing parameters listed in Section 3.2.5. Section 3.3 describes the specific experiments and characterisation carried out. Section 3.3.1 details the investigation of spatter particles in Chapters 5 and 6, including the investigation of the particles, the parts produced, and other process by-products. Section 3.3.2 introduces a new methodology which is presented in Chapter 7, investigating the contents of the powder bed. Section 3.3.3 introduces the investigation of fatigue crack growth rate of PBF-LB Inconel 718 samples and the influence of spatter powder. The methodologies for Chapters 7 and 8 are presented with the relevant chapters as they are based on findings from Chapters 5 and 6.

3.1 Powder characterisation

A Hitachi TM3030 (Hitachi Ltd., Japan) Scanning Electron Microscope (SEM) was used to image the powder particles and assess their morphology. Back-scattered electron (BSE) imaging was used to identify any compositional differences. Energy-dispersive X-ray spectroscopy (EDS) was used in conjunction with the SEM to characterise and map the composition of the powders. Inductively coupled plasma atomic emission spectroscopy (ICP-OES) was outsourced to analyse the composition of the primary and trace elements of the powders, measured on loose powder samples.

The PSD of the powder was analysed using laser diffraction with a Malvern MasterSizer 3000 (Malvern Instruments Ltd, UK). Samples were measured dry and air was used as the measurement medium. The results were analysed using the ‘General Purpose’ mode which utilises the Mie diffraction theory to estimate particle sizes. Particle sizes between 0.01 – 3500 µm were measured. For each sample measurement, the background was measured for 10 s, each sample was measured for 5 s, and 10 repeat measurements were made. Obscuration limits were set between 0.5% and 6.5%.

Apparent and tapped densities were measured according to ASTM B212 [164]. These values were used to calculate the Hausner ratio for as a measure of the flowability:

$$Hausner\ ratio = \frac{Apparent\ density}{Tapped\ density}$$

To ensure reliability in the results, all powders were handled in the same way prior to use in the investigations. The powders were dried in an oven for at least 3 hours at 125 ˚C to remove any moisture (even if opened for the first time). Sampling methods were used, discussed later in Section 3.3.1.1, for all testing to ensure a representative sample was analysed. The study in Chapter 7 was one of the first conducted in the research, which found handling of the powders having an influence on build results. Therefore, subsequent to this and for the rest of the results, sampling techniques were used for all powders for future PBF-LB builds. Powder was mixed in the container and loaded into the PBF-LB machine or hopper in a piece wise manner (~300 g dose at a time) and the powder container mixed again before the next powder dose was loaded. This ensured a representative dose of the virgin powder was in the machine for each build. To minimise the possibility of cross-contamination, as can occur in the industry and reported by LPW [165], for all experiments, all machines and equipment was cleaned to manufacturer's specification, and/or with Isopropanol. Individual brushes, pans, and sieves were used for the materials in this work.

3.2 PBF-LB apparatus

A range of commercial PBF-LB systems were used in this research to ensure that findings for spatter and oxide generation were generalised and not specific to a single PBF-LB architecture, and to allow comparison between these systems.

Each PBF-LB system has a different laser system and operates with different processing parameters to produce specimen with high density. There are over 130 parameters that can manipulated within the machine to alter what is produced [16]. These factors will affect the spatter produced and oxides that form. With so many influencing factors that cannot be set to be the same between machines, the machines must be used as best as they can individually to produce components and then compared as separate systems. This is acceptable as this is

how the systems would be used in industry. The layer thickness of the builds were kept consistent at 40 µm across the machines to ensure that at least the volume of powder melted across the systems was comparable. The relevant details of each machine and the location of spatter powder collection is labelled in the following descriptions.

The systems used are:

- ReaLizer SLM50
- Renishaw AM125
- SLM Solutions 125
- Trumpf TruPrint 1000

Comparison of the main aspects for the system are shown in Table 3.1 and further details of the architecture are presented in Sections 3.2.1-3.2.4. Section 3.2.5 then details the processing parameters and scan strategies used for the manufacture of specimen.

Table 3.1 Comparison of PBF-LB systems used

PBF-LB system	Laser power (W)	Laser spot size (µm)	Build volume (mm)	O_2 level (%)
SLM50	100	40	70 Ø x 40	0.2
AM125	200	40	125 x 125 x 125	0.1 (Pre-vacuum)
SLM125	400	85	125 x 125 x 125	0.1
LMF1000	200	55	100 Ø x 100	0.1

All machines were thoroughly cleaned before material changes and builds according to manufacturer's recommendations to minimise potential for cross-contamination. New filters were not used for each build and were changed when required according to the manufacturer's guidelines.

3.2.1 ReaLizer SLM50

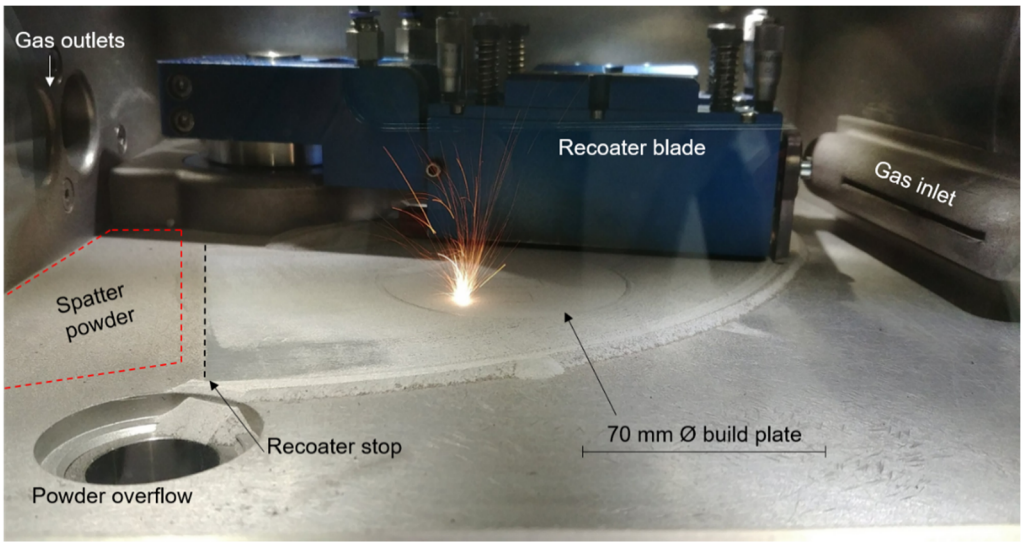

Figure 3.1 Realizer SLM50 chamber. The hopper feeds up between the two blades where the recoater is currently positioned. The recoater moves up to the black dashed line and virgin material is not spread beyond this

The ReaLizer SLM50 (referred to as the SLM50) is a PBF-LB system produced by ReaLizer GmbH (Germany). The system operates a double blade (rubber) recoating system to spread the powder over the build plate. The recoater system passes back and forth over the powder bed for a single recoat, with each blade spreading the powder in one direction, and generally a double recoat is used each layer to ensure a level powder bed. The recoater blade recoats in an arc as seen in Figure 3.1 by the recoater stop point and the trail of powder. The build plate lowers after the scanning of a layer and remains at the same height during recoating. The system uses a hopper feed system connected to the top of the machine which then feeds from underneath the machine using a stepper motor system. The inside of the build chamber can be seen in Figure 3.1. The SLM50 operates at O_2 levels <0.2%. The gas inlet and outlet are shown in Figure 3.1, which produce a flow of argon across the build plate.

3.2.2 Renishaw AM125

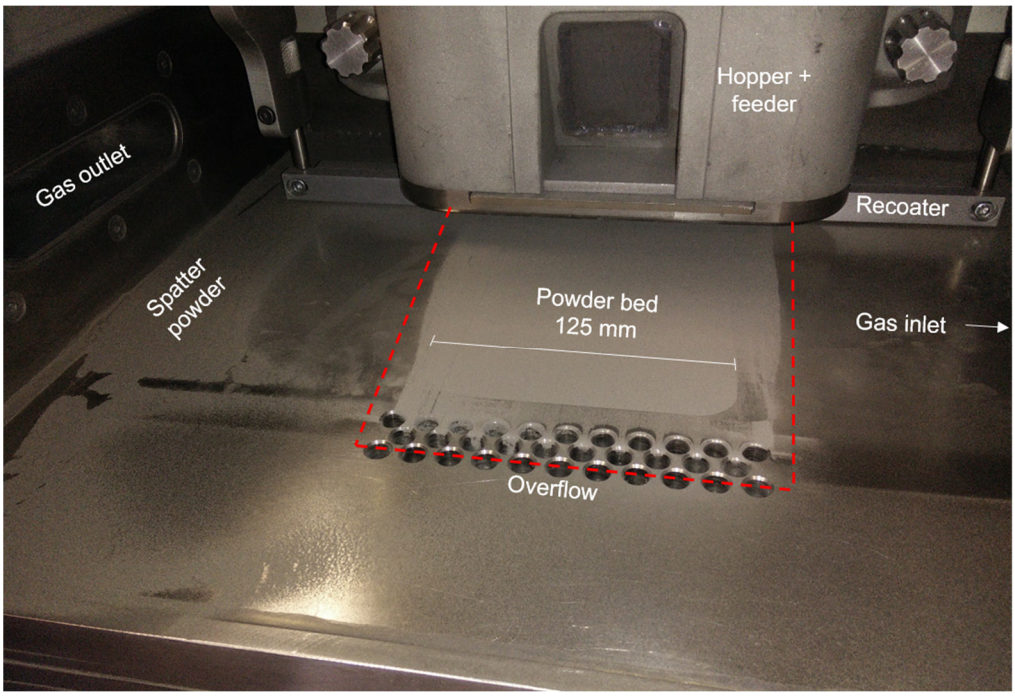

Figure 3.2 Renishaw AM125 chamber after a build – the feedstock material is only spread within the boundaries of the red line

The Renishaw AM125 (referred to as the AM125) is a PBF-LB system produced by Renishaw plc (UK). The powder is spread over the build plate by a uni-directional rubber re-coater blade with one pass. The recoater returns to the home position, when the build plate is lowered, before more powder is dosed and the next layer spread. The powder is stored in an internal hopper within the chamber that doses directly in front of the recoater. A dosing factor of 150% was used for recoating each layer. The Renishaw systems are unique to other PBF-LB systems as they bring the chamber to a near-vacuum (a pressure differential of -964 Mbar from atmosphere) before filling with argon to remove as much O_2 present in the chamber before processing. The AM125 therefore has the best O_2 control and can reach lower levels, important for assessing the oxidation of materials in PBF-LB. The AM125 has O_2 levels <0.1%. The processing chamber of the AM 125 is depicted in Figure 3.2. It is important to note, that although the majority of redistributed material and spatter is by the gas outlet, with the gas flowing perpendicular to the recoating direction, there is material spread throughout the chamber.

3.2.3 SLM Solutions 125HL

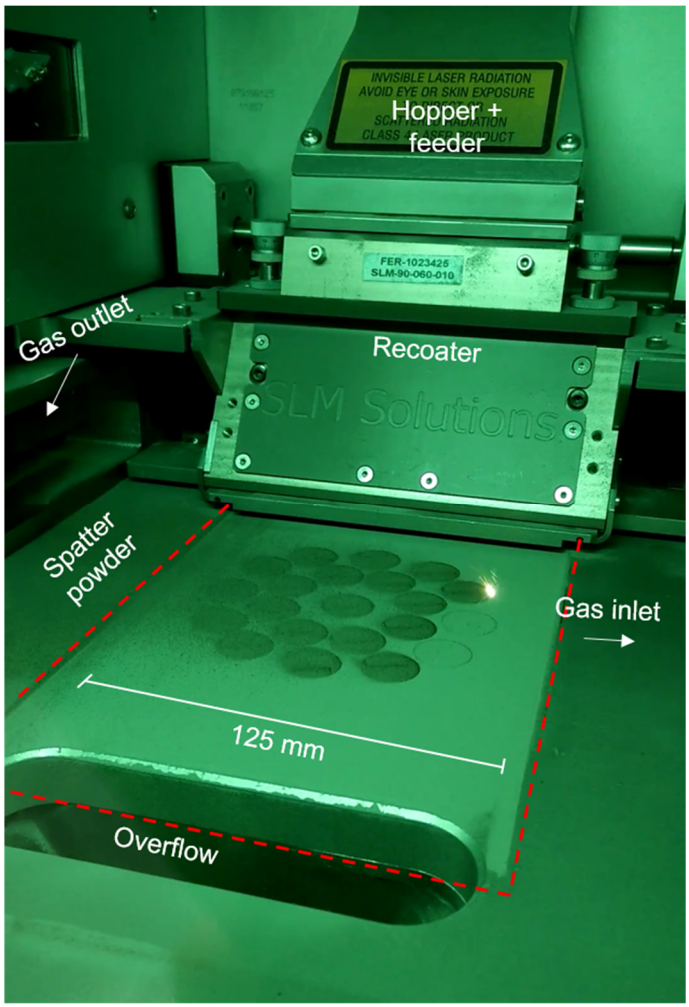

Figure 3.3 SLM Solutions 125 build chamber. The hopper feeds powder into the recoater, which doses half the powder in the position it is pictured in before spreading across to the opposite side. The layer is processed and then the recoater doses the second half and spreads a layer back to return to the home position.

The SLM Solutions 125 HL (referred to as the SLM125) is the smallest system developed by SLM Solutions Group AG (Germany). The SLM125 has an external hopper system that feeds down into the recoater system. The recoater stores powder for two layers and recoats in both directions to improve build speed and efficiency. Powder for two layers is fed into the recoater system in the home position, it spreads one layer to be in the 'out' position, the layer is then processed by the laser, then the recoater dispenses and recoats another layer back into the home position, before that powder layer is processed. The SLM125 is back-filled from air with argon and processes at an O_2 level of <0.1%. The gas flows perpendicular to the recoating

direction. The build chamber can be seen in Figure 3.3. This system was used to test the methodology for assessing the powder bed content presented in Chapter 7. The recoating mechanism is relevant to how the powder is spread to produce the powder bed for this study.

3.2.4 Trumpf TruPrint 1000

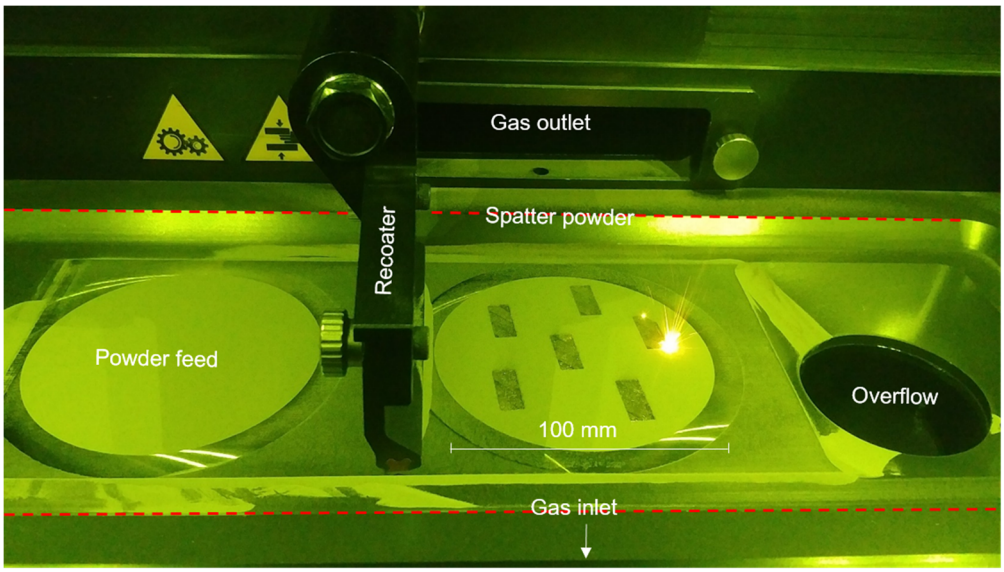

Figure 3.4 Trumpf TruPrint1000 build chamber

The Trumpf TruPrint 1000 (referred to as the LMF1000) was used to produce the fatigue samples with incorporated spatter in Chapter 8. The build volume is a cylinder of diameter 100 mm x 100 mm height. The powder feeder is a paired 100 x 100 mm (Ø,z) piston feed, as seen in Figure 3.4, which raises the required powder to be spread by the rubber blade recoater each layer. This architecture allowed the smallest proportion of powder used for a build and greatest control over the powder in the build due to easy access to the chamber, simple loading and unloading of powder, the lack of powder having to travel through the hopper/feeder, and accurate dosing of the powder producing minimal wastage. The recoating was performed with a 110% dosing. This was imperative for the manufacture of specimen for Chapter 8 and is discussed further in the chapter's methodology. The system operates at O_2 levels below 0.1%.

3.2.5 Processing parameters

Processing parameters used in each machine were specific to those machines and were parameters that have been previously used to produce dense components (>99% density). The parameters used for the LMF1000 were proprietary parameters developed for the system which were not accessible. The relevant parameters for used in the experiments for the other machines are shown in Table 3.2.

Table 3.2 Processing parameters used for each machine for builds where spatter was generated

	ReaLizer SLM50	Renishaw AM125	SLM Solutions SLM125
Scan speed ($mm.s^{-1}$)	560	1300	680
Laser power (W)	100	200	225
Hatch distance (µm)	60	90	90
Energy density (J/mm^2)	0.57	0.49	0.50
Substrate temperature (°C)	250	180	200

The scanning strategy for each machine was the same. A back-and-forth raster scan with a stripe width of 10 mm (overlap of 0.5 mm), followed by a border scan, for each layer. Each subsequent layer was rotated 67˚ as depicted in Figure 3.5. This 67˚ rotation maximises the number of rotations before a repeat orientation of a previous layer, which reduces the build-up of residual stress.

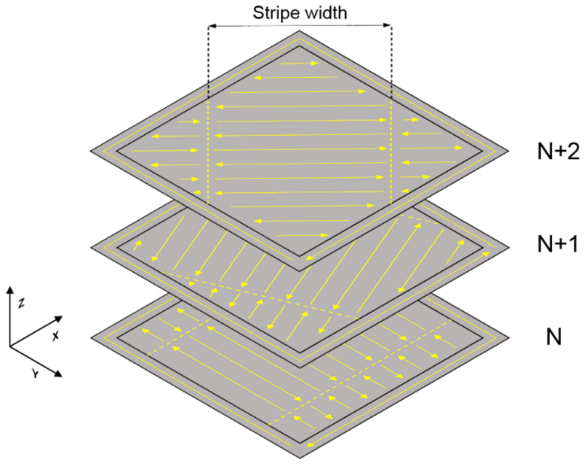

Figure 3.5 Schematic of scanning strategy shows the scanning of the part border and infill meander raster strategy. Every subsequent layer (N+i) the infill raster scan rotates 67˚

The processing strategy for each system scans the specimen located next to the gas outlet first before scanning parts in sequential order to the nearest to the gas inlet. This processing strategy ensures that, whilst scanning a part, minimal spatter is relocated onto areas of the powder bed yet to be scanned in that layer.

3.3 Experimental methods

All systems were used to process Inconel 718 for spatter investigation and only the SLM50 was used to process Hastelloy X. The SLM50, being the smallest system, allowed the easiest and most effective capture of small amounts of spatter which was required for the investigation of Hastelloy X. All four systems were used to characterise the spatter particles produced in processing Inconel 718 for Chapters 5 and 6. The SLM125 was used to investigate a capsule method for assessing powder bed metrics in Chapter 7. The SLM125 was used due to its square build plate, which is common for larger industrial machines as opposed to the circular build plates on the smaller SLM50 and LMF1000 systems, to ensure the methodology is more relevant for these systems. The LMF1000 was used for the investigation into spatter effects on fatigue properties in Chapter 8 due to its ease of changing the powder and its material efficiency due to the scarcity of spatter powder available for processing.

3.3.1 Spatter and oxide investigation (Chapter 5 and 6)

All of the PBF-LB machines were used to investigate the spatter particles produced from processing of Inconel 718 on these machines. Chapter 5 focusses on the spatter produced across the range of machines for characterising and understanding of spatter and oxide generation. It also studies oxide formations in another Nickel-based superalloy, Hastelloy X, processed on the SLM50. These two alloys are Ni-Fe-Cr based superalloys and this allows understanding of the alloy constituent elements influence on oxide formation. To produce the spatter for the investigation a range of builds, with varied components, were conducted. This gave a spatter representation for common use and builds on the PBF-LB systems as would be conducted in industrial applications. The effect of different builds and geometries on the spatter produced was not within the scope of the investigations.

Vaporisation plays an important role in the generation of spatter and the vaporisation of the alloy is another by product from the process. To provide a more complete picture of the by-products from the spatter process, the vaporised material was collected, via the use of 3 mm copper TEM grids strategically placed throughout the build chamber of the SLM50, as shown in Figure 3.6. More detail is provided in Section 5.1.1.

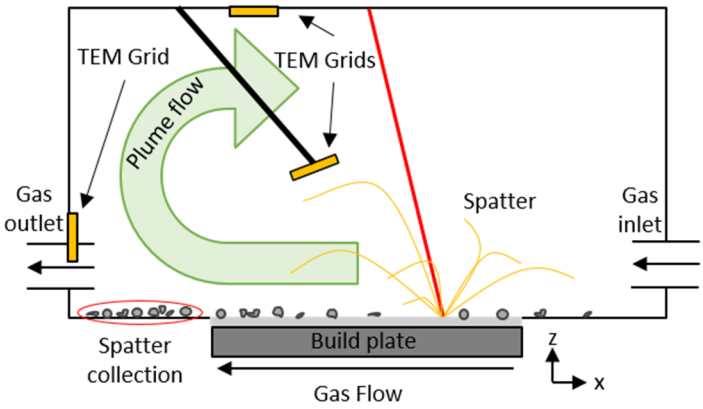

Figure 3.6 General arrangement of experiments intended to capture spatter and nano-particles formed during PBF-LB

Chapter 5 shows variation between virgin material and spatter material for Inconel 718 and this is different from what occurs in Hastelloy X. In Chapter 6 spatter is collected for Inconel 718 from multiple PBF-LB systems and a secondary Hastelloy X composition is tested for the effect of composition on the oxide formation. The powders are analysed and compared for their size, size distribution, morphology, shape, and proportion of oxidised particles. This is achieved via an automated particle shape and size analyser and through image analysis of SEM images. The characteristics the powders are analysed for are based on the results from Chapter 5 and the details of the methods are presented in Chapter 6.

For each PBF-LB system, the spatter for assessment was collected from the processing of a set of 10 x 10 x 10 mm cubes with 3 mm of support structure for easy removal. For each machine (details for LMF1000 not available as stated), the scanning strategy shown in Figure 3.5 was used and the processing parameters detailed in Table 3.2.

3.3.1.1 Spatter collection (All chapters)

During the processing of each layer, spatter is continuously ejected upwards from the melt pool and away from the powder bed. This is common across all PBF-LB systems and accepted as part of the process. A proportion of the spatter landed back on the bed, however, due to the gas flow across the powder bed for each system, a proportion of spatter is redistributed away from the powder bed and built up to the side of the chamber, and these locations are depicted in Section 3.2. The distance between the manufactured specimen locations and the spatter collection location for each machine was not considered in the experiments.

The spatter particles can be found on all sides of the chamber, as they are ejected at high speeds in all directions, however, the largest collection is by the gas outlet where the gas flow across the bed blows them. It can be verified that these particles are just spatter as there are no particles in this section of the chamber when the gas flows across the powder bed prior to processing or during spreading of a layer. This was tested with the machine recoating with the gas flow but no scanning and no powder was found in the region. Material only ends up in this section when the laser is melting powder and the material is redistributed during this process. This allowed a collection of pure spatter for analysis that was separate from the original powder in the bed and a depiction can be seen in Figure 3.6. For analysis of the spatter particles, at least three samples (depending on the quantity required for analysis) were extracted from different sections of the collected powder, and the powder was mixed prior to each extraction. The sample for analysis was then made up of the multiple samples to ensure a representative sample was analysed. Unless otherwise stated, all spatter samples referenced and analysed in this research were spatter collected from these regions. This method applies to all chapters of this work.

A Hitachi TM3030 SEM was used to image the powder particles. BSE imaging was used to identify compositional and morphological differences. A FEI Quanta200 3D DualBeam FIB/SEM (Thermo Fisher Scientific, USA) system was used to perform in situ focussed ion beam (FIB) milling and analysis of particle cross sections. EDS was used in conjunction with the SEM to characterise and map the composition of the powders to identify surface oxides and their constituents. The PSD of the powder was analysed using laser diffraction with a Malvern MasterSizer 3000 as detailed in Section 3.1.

3.3.2 Powder bed assessment investigation (Chapter 7)

In this study a new method is proposed which uses a capsule based approach to directly assess the powder spread across the build plate and that the laser interacts with. Study of the capsules allows analysis of the powder bed density (PBD) and PSD across the bed. The analysis of the PSD allows assessment of the level of spatter in the powder bed. The aim of the method is to understand the correlation between the powder feedstock input and what powder the laser interacts with in the powder bed, particularly assessing the PBD and the distribution of spatter. X-ray computer tomography (XCT) was used to analyse the defects within the capsules to understand and correlate the effect of the powder in the bed to the quality of the specimen produced. The results are specific for the PBF-LB system used, in this case the SLM125, however the methodology is designed to be applicable to any PBF-LB system. The details of the method and the results are discussed in Chapter 7 and from these findings improvements to the methodology are proposed.

3.3.3 Fatigue crack growth rate (Chapter 8)

To assess the effect of spatter on the performance of PBF-LB specimen a study was designed to establish the performance of different levels of spatter used to manufacture fatigue specimen. Fatigue testing is most suited to explore the effect of the defects as the cracks propagate from defect to defect and fatigue crack growth has a lower dependence on the surface condition compared with conventional fatigue life testing used to produce S-N curves, therefore providing better understanding regarding the bulk material. Compact tension (CT) specimen were manufactured to test the fatigue crack growth of the specimen produced. To assess the effect of spatter incorporated into the build, specimen were built with three different levels of spatter powder to assess the fatigue crack growth rate (FCGR) produced in the each specimen. This was made possible using the LMF1000 PBF-LB system. Wrought specimen were produced for comparison with conventionally manufactured Inconel 718. It is important to understand what effect the spatter particles have on the performance of specimen to understand safe levels of these particles in builds and how they contribute to changes in part performance. Details of the methods and testing and the results are detailed and discussed in Chapter 8.

Chapter 4 Characterisation of feedstock powders

A range of gas atomised powders designed for PBF-LB were used throughout this research. Much of the following research relates to changes in the powder due to PBF-LB processing, therefore, it is important to understand the material used to show and understand the change in the powders. In this chapter, the relevant properties for each powder have been characterised for the subsequent research. Particularly, with the identification and investigation of oxides, it is shown what, if any, potential contaminants are present in the virgin material. This chapter also discusses features in these conventional gas atomised PBF-LB powders that may cause quality issues.

The powders used are commercially available gas atomised PBF-LB powders. A powder was also sourced from a secondary supplier to ensure findings are generalised and not specific to one manufacturer. The powders used in the subsequent studies are characterised in Chapter 4. The characterisation of the virgin material in Chapter 4 provides the basis for the investigation and characterisation of spatter powder for PBF-LB in Chapters 5 and 6 and their effect on the process in Chapters 7 and 8.

4.1 Inconel 718

Three Inconel 718 powders were used in this research. The majority of investigations were undertaken using a PBF-LB gas atomised powder which is denoted as Supplier 1 Inconel 718 and was used in virgin condition for all experiments except Chapter 7, therefore the powder used for the experiment in Chapter 7 has been characterised separately. A second commercial powder was sourced, and is known as Supplier 2 Inconel 718, and investigated in the same manner to ensure that the results from the investigations were generic results and not specific to one powder or supplier.

Figure 4.1 shows the PSD of the Inconel 718 powders used. This shows a similar PSD for the two Supplier 1 Inconel 718 powders, with a slight shift for the powder used for Chapter 7 that was used once and sieved -53 µm. It can be seen that the two virgin powders, sized +15-45 µm, show a greater variation with the Supplier 1 powder showing a slightly wider and larger

span. These results can be seen in the changes in the D_{10}, D_{50}, and D_{90} of the powders, shown in Table 4.1.

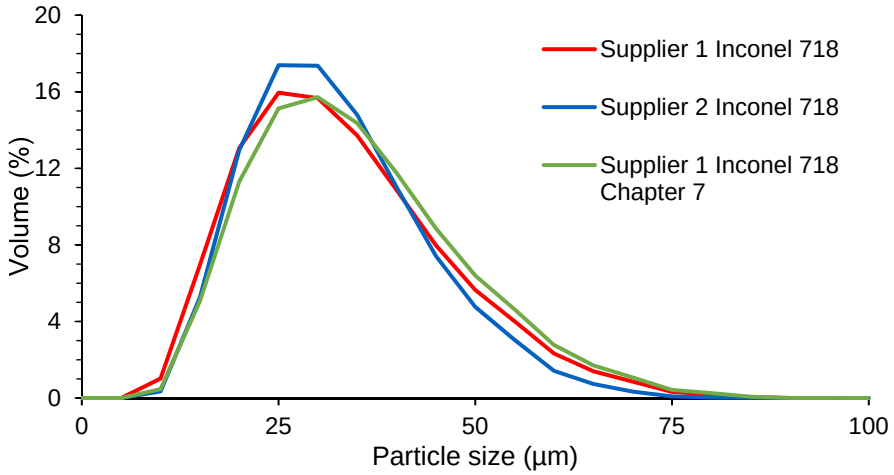

Figure 4.1 PSD of the Inconel 718 powders used in this study measured via laser diffraction techniques on the Malvern Mastersizer 3000

Table 4.1 The D_{10}, D_{50}, and D_{90} for the Inconel 718 powders

(µm)	Supplier 1	Supplier 1 Chapter 7	Supplier 2
D_{10}	21.02	22.27	21.84
D_{50}	34.12	35.77	33.55
D_{90}	54.09	55.90	50.73
Span	0.97	0.94	0.86

4.1.1 Supplier 1 Inconel 718

Supplier 1 Inconel 718 was the most used powder in this research, all reference to processing Inconel 718 refers to using this powder and if otherwise, for Chapter 7 and for Supplier 2 Inconel 718 powder, that will be stated.

BSE-SEM analysis, in Figure 4.2, shows the powder is a typical gas atomised powder. It is mostly spherical, with some elongated particles, splat-caps, and satellite particles present. The BSE-SEM was used to ensure there was no major cross contamination or defects within the powder system.

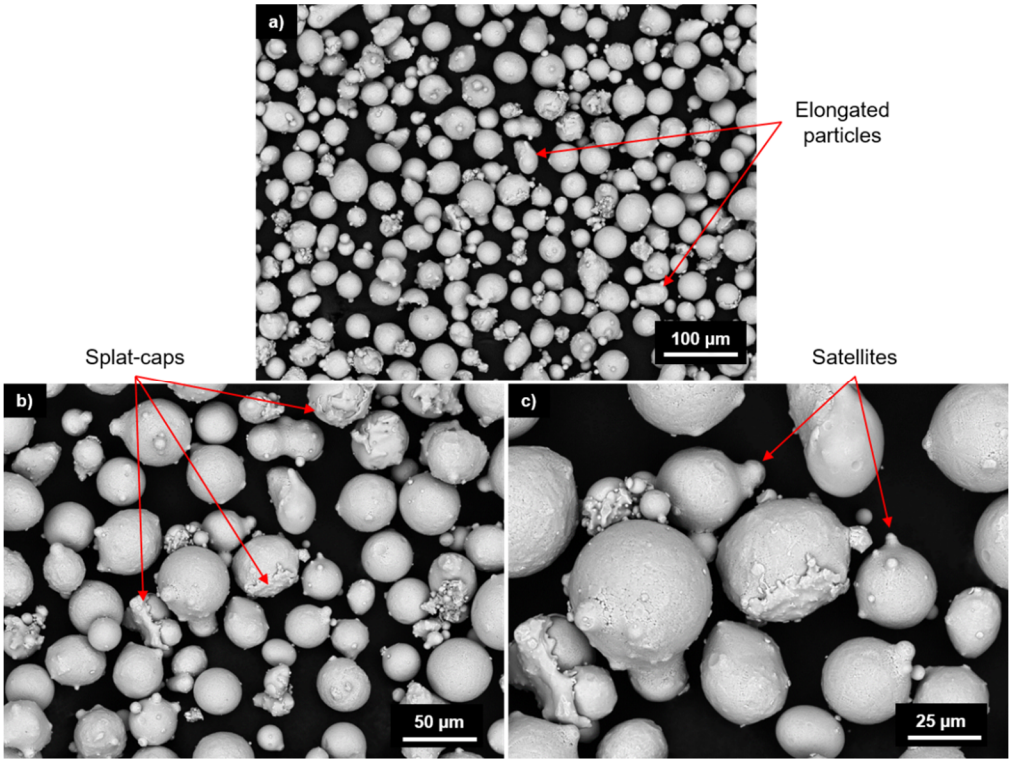

Figure 4.2 BSE-SEM micrograph of the virgin Supplier 1 Inconel 718 with different magnifications and typical features in gas atomised powders

Titanium nitride particles were found within a proportion of the particles. Which could be seen at the surface of some particles and within the bulk of the particles, as seen in Figure 4.3 and Figure 4.4. These particles ranged in size from approximately 1-25 µm. As seen, the nitrides are a range of angular and cubic shapes and some of the nitrides clump, or agglomerate, together. These nitrides must be present in the feedstock for the powder or produced during the gas atomisation process. The inclusions are not unique to this powder however, they were also present in the second supplier's Inconel 718 powder and a study by Smith *et al.* [166] into the Inconel 718 supply chain found the presence of titanium nitride inclusions in powder from 8 different commercial suppliers, showing it to be an industry wide issue.

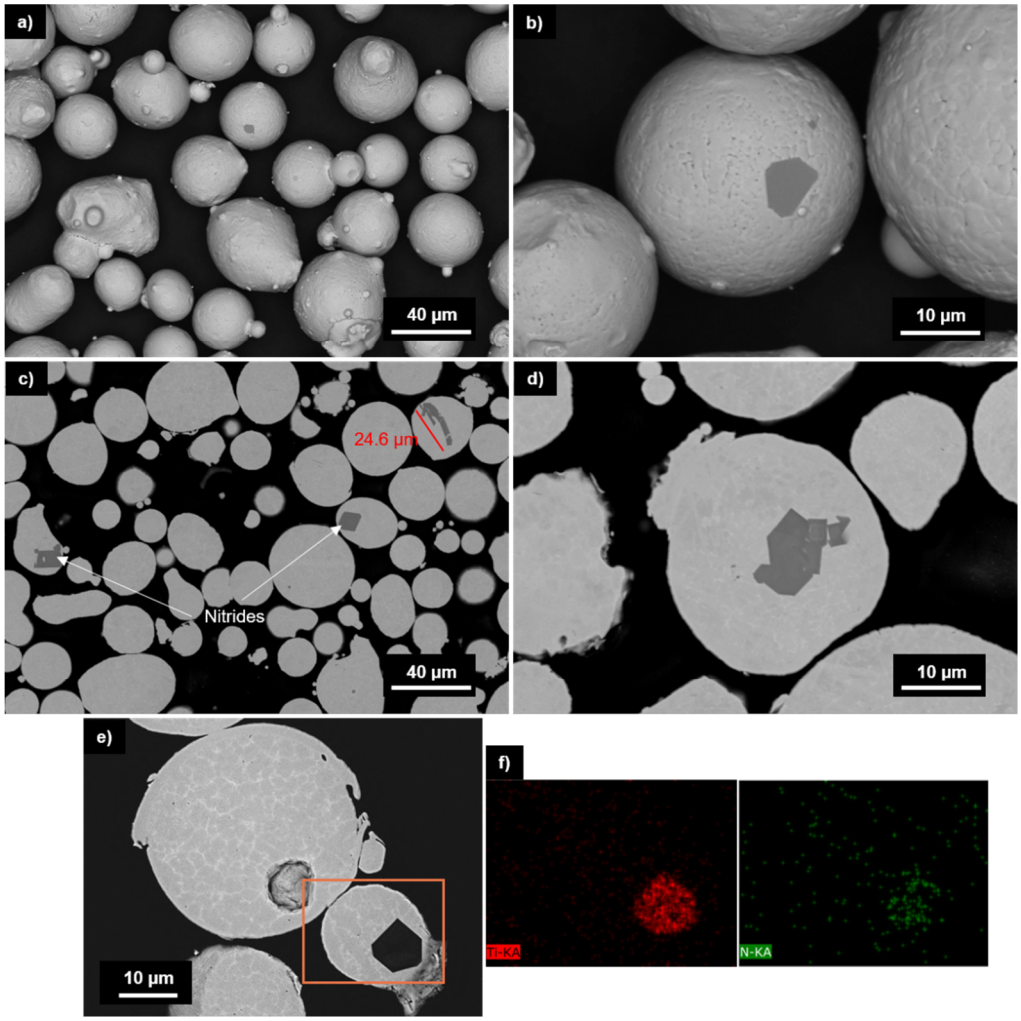

Figure 4.3 a-d) BSE-SEM images showing titanium nitride inclusions in the virgin Supplier 1 Inconel 718 material at the surface and within the particles, e&f) EDS mapping showing titanium nitride within particle

The gas atomisation process produces a fine bi-phasic γ/γ″ microdendritic or equiaxed structure [128]. Figure 4.4 shows the range of microstructures present in the powder. The microstructure is dependent upon the cooling rate of each particle, primarily dictated by its mass.

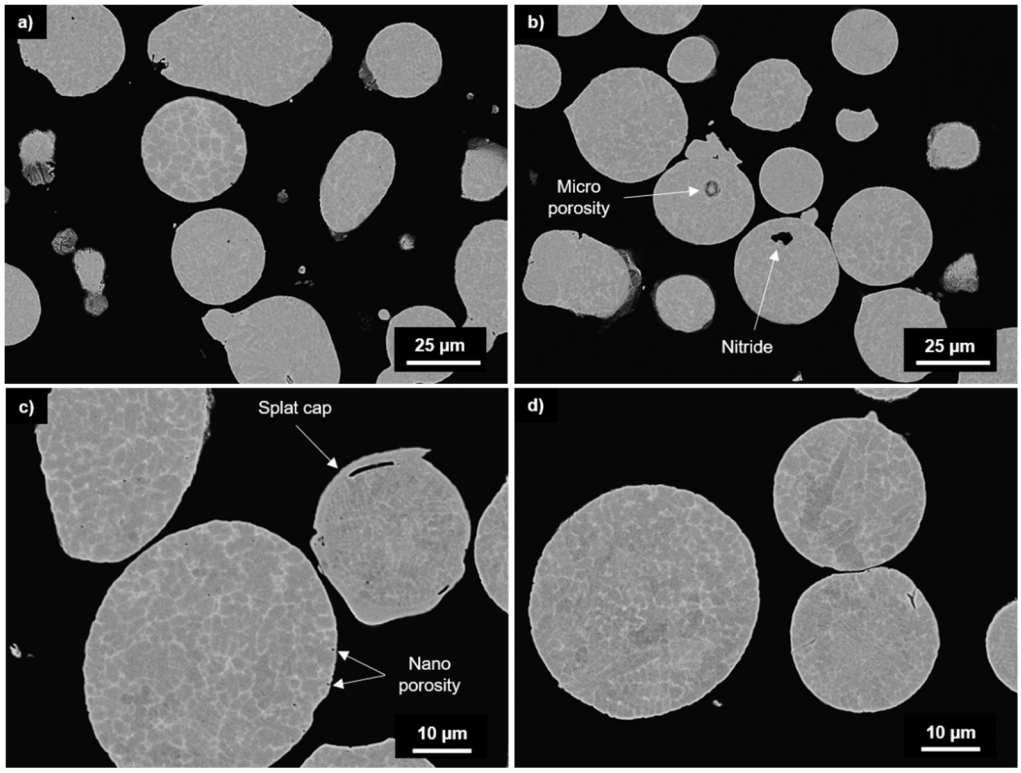

Figure 4.4 BSE-SEM micrograph of cross section of virgin Supplier 1 Inconel 718 powder showing the range of microstructures and produced from the gas atomisation process. Highlighted are also internal nano and micro-porosity and splat cap features that are produced during gas atomisation

Table 4.2 shows the composition of the Supplier 1 Inconel 718 powder used. The elements of most interest in this research are the Al at 0.44 wt% and Ti at 0.9 wt%.

Table 4.2 Nominal composition ofASTM F3055-14a Inconel 718, Supplier 1, and Supplier 2 Inconel 718 powder used in this study (wt%)

	ASTM F3055-14A		Supplier 1	Supplier 2
Element	min	max		
Al	0.2	0.8	0.44	0.46
B	–	0.006	<0.01	<0.01
C	–	0.08	0.04	-
Co	–	1	0.03	0.05
Cr	17	21	19.04	19.33
Cu	–	0.3	0.02	0.02
Fe	Bal.		17.17	18.42
Mn	–	0.35	0.08	0.09
Mo	2.8	3.3	3.07	3.11
Nb	4.75	5.5	5.12	5.16
Ni	50	55	Bal.	Bal.
O	–	–	0.01	-
P	–	0.015	<0.01	<0.01
Si	–	0.35	0.04	0.03
S	–	0.015	<0.01	-
Ti	0.65	1.15	0.9	0.88

4.1.2 Supplier 2 Inconel 718

A secondary source for Inconel 718 PBF-LB powder was used to ensure the findings of the research were not specific to a single source. This powder was characterised to ensure the quality and that findings were comparable to those from the Supplier 1 Inconel 718. Figure 4.5 shows that the powder is a similar gas atomised powder and Figure 4.1 showed they had a similar PSD.

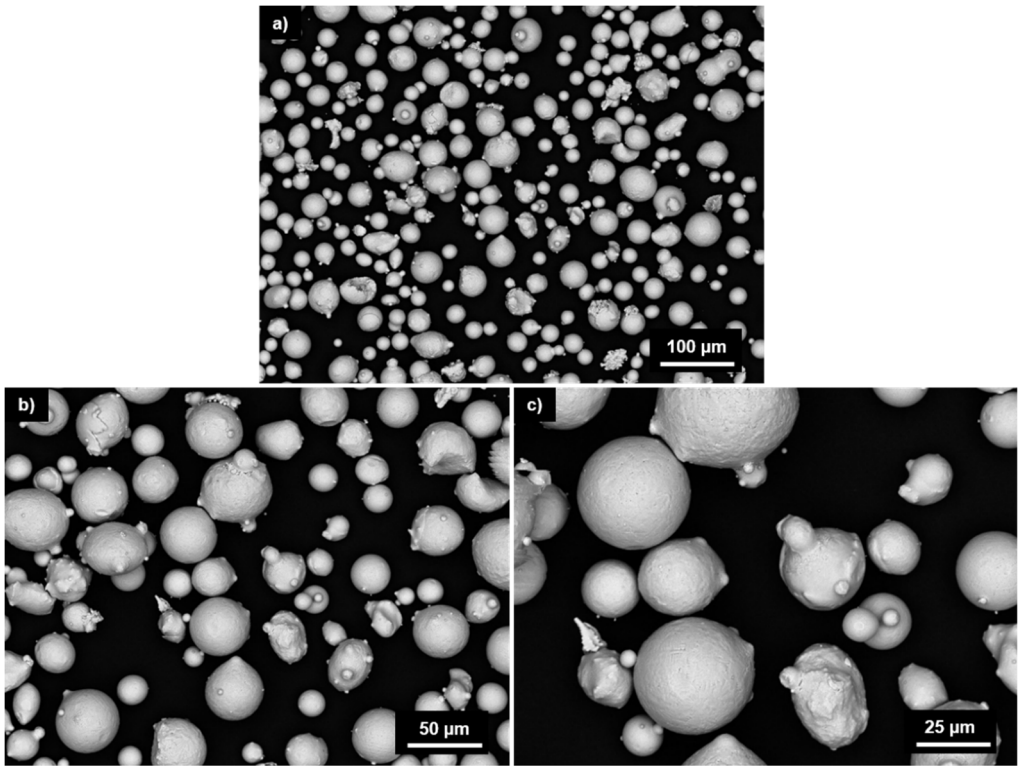

Figure 4.5 BSE-SEM micrograph of the virgin Inconel 718 powder from Supplier 2

Figure 4.6 shows the Inconel 718 powder from a secondary source also contains titanium nitride inclusions, which were present on the surface and in the bulk of the particles. This further emphasises an industry-wide issue with the formation or transfer of these inclusions in the powder feedstock. The nitrides were of the same size range as in the Supplier 1 Inconel 718, and Figure 4.6c also shows some nitrides <1 µm.

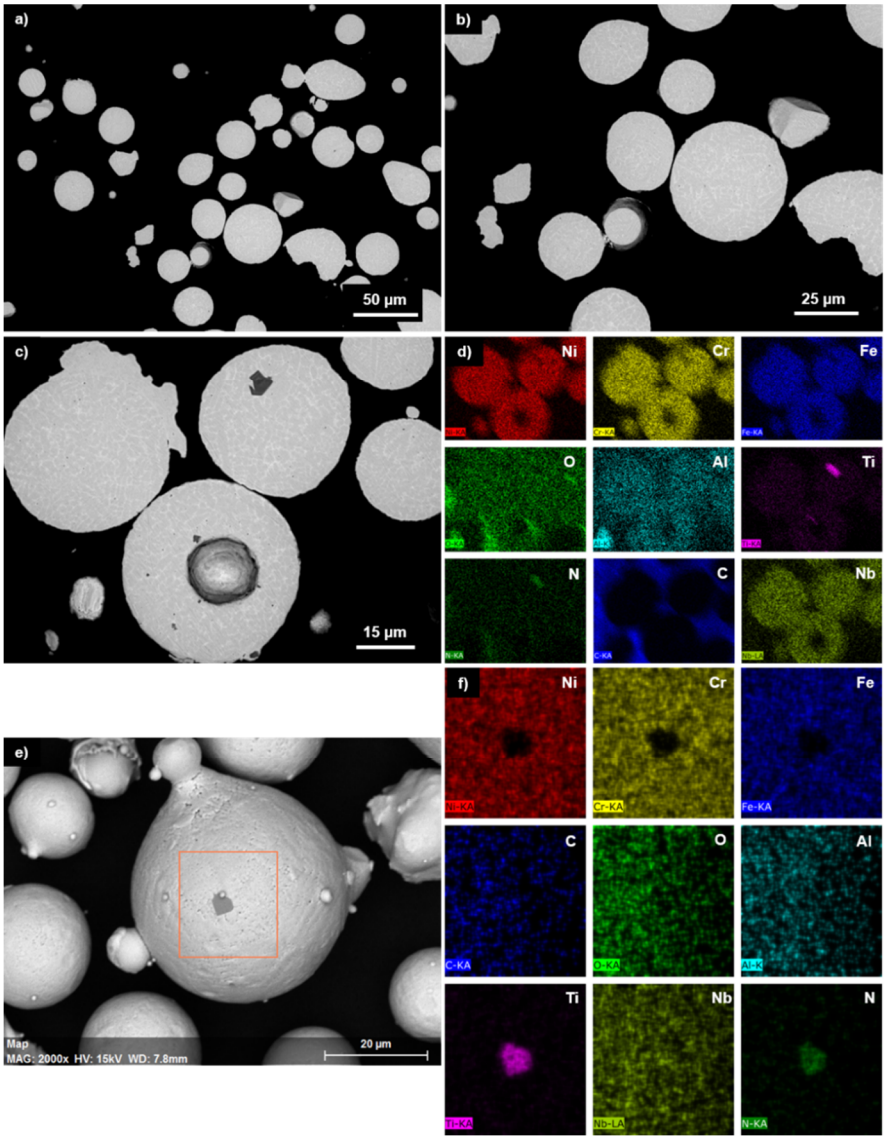

Figure 4.6 a&b) BSE-SEM micrographs of the cross section of virgin Supplier 2 Inconel 718 powder microstructure, and c&d) showing the presence of titanium nitrides within the particles as well as on the surface. The EDS scan shows some image drift during the scan but the concentration of Ti and N can be seen

The composition of the Supplier 2 Inconel 718 powder was very similar to the composition of the Supplier 1 Inconel 718 powder as shown in Table 4.2. The largest variation was in the Iron content which was 1.25 wt% higher in the Supplier 2 powder. Important to the subsequent investigations the content of Al and Ti were both only 0.02 wt% in difference.

4.1.3 Supplier 1 Inconel 718 used for Chapter 7

For the study in Chapter 7, a 100 Kg batch of powder was used. Due to limitations in using all virgin material for this, the powder used was material that had been used and sieved once previously. The material was Supplier 1 Inconel 718 +15-45 µm, as described previously, which was sieved to -53 µm after use. Figure 4.1 shows that the PSD has a slight shift from the virgin material, and a slight increase in the D_{10}, D_{50}, and D_{90} seen in Table 4.1. An independent samples t-test was conducted on the repeat laser diffraction measurements for the mean particle size, D_{50}, between the virgin Supplier 1 and the Supplier 1 powder used of Chapter 7. There was a significant difference between Supplier 1 (M=34.13, SD=0.08) and Supplier 1 Chapter 7 (M=35.78, SD=0.34); conditions t(9)=-11.76; p=0.000; for a 95% confidence interval. These results suggest that there is a statistically significant difference between the D_{50} for the two powders, however, the shift in average particle size was 1.5 µm. The change in the PSD and D_{10}, D_{50}, and D_{90} from the virgin Supplier 1 Inconel 718 to the one used in this study, was less than the change in these characteristics for the virgin powder from Supplier 2 listed as the same +15-45 µm specification. Therefore, it is deemed that the powder used in this study is equivalent to using another batch of the same Supplier 1 Inconel 718. The powder used in the study has been characterised independently however to ensure the results in the study are relatable to the powder used. Figure 4.7 shows that the powder is a similar gas atomised powder and no discernible difference was found from that in Section 4.1.1. Figure 4.8 showed that the powder still contained the titanium nitride inclusions.

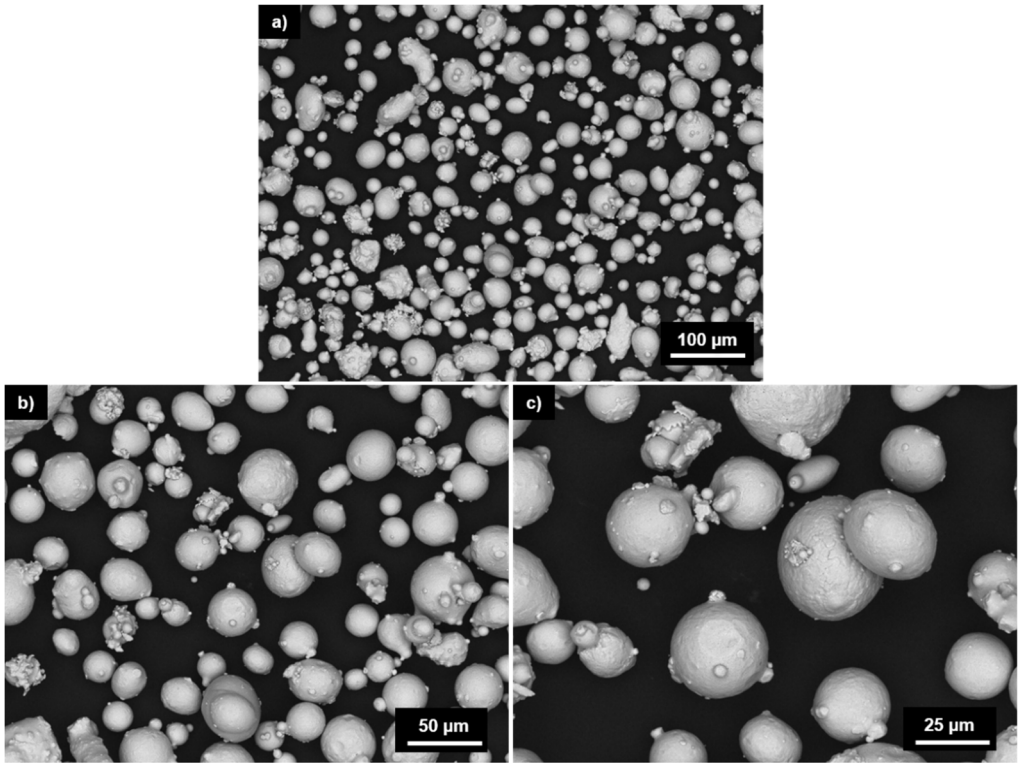

Figure 4.7 BSE-SEM micrograph of the Supplier 1 Inconel 718 powder used for the work in Chapter 7 which was used once and sieved once (-53 µm) prior to use

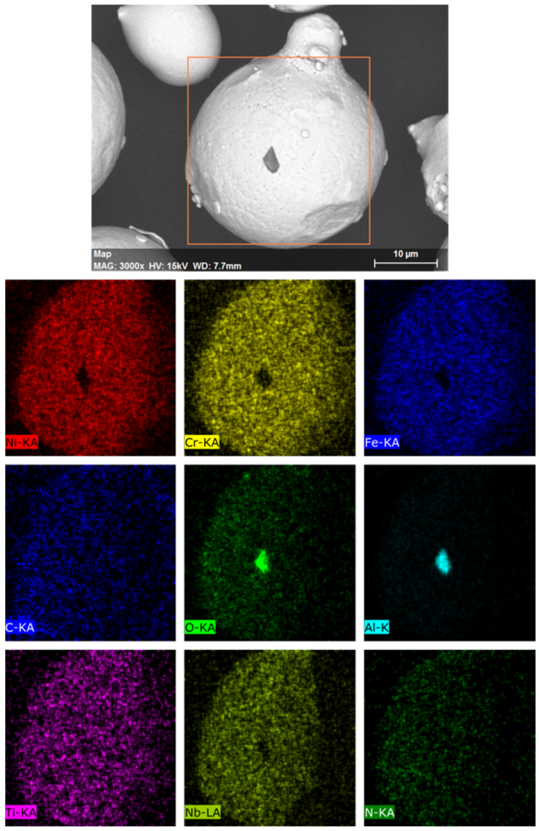

Figure 4.8 BSE-SEM micrograph and EDS mapping showing the presence of oxide in the Supplier 1 Inconel 718 used once and sieved once (-53 µm) prior to use

The apparent and tapped densities of the powder were 4.41 g/cm^3 and 4.91 g/cm^3, respectively, which correlate to relative densities of 53.62% and 59.77%, respectively. These standard packing density values allow comparison of packing density in the powder bed which is investigated in Chapter 7. The Hasuner ratio for the powder was 1.11. Which considers the powder as flowable.

4.2 Hastelloy X

Hastelloy X was investigated for spatter and oxide generation alongside Inconel 718. Two virgin Hastelloy X alloys were investigated, Supplier 1 Hastelloy X and Supplier 2 Hastelloy X are conventional Hastelloy X alloys sized for PBF-LB with nominal composition in line with AMS 5390 nominal ranges for the alloy [167]. The second Hastelloy X alloy from Supplier 2 was sourced as a Hastelloy X with reduced Si content, but both Hastelloy X alloys are within the AMS standard tolerance for Si.

Figure 4.9 shows the PSD of the Hastelloy X powders used. This shows a similar PSD for the two virgin powders both sized +15-45 µm and is corroborated by the D_{10}, D_{50}, D_{90}, and Spans in Table 4.3.

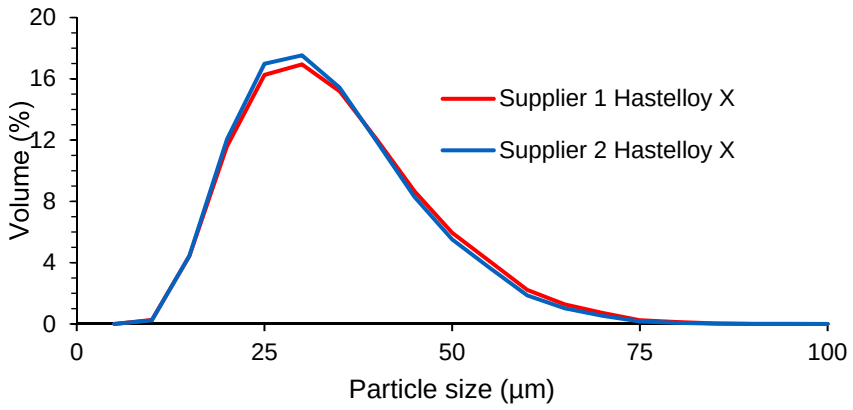

Figure 4.9 PSD of the Hastelloy X powders used in this study measured via laser diffraction techniques on the Malvern Mastersizer 3000

Table 4.3 The D_{10}, D_{50}, and D_{90} for the Hastelloy X powders

(µm)	Supplier 1	Supplier 2
D_{10}	22.62	22.55
D_{50}	35.16	34.63
D_{90}	53.67	52.33
Span	0.88	0.86

4.2.1 Supplier 1 Hastelloy X

BSE-SEM analysis, in Figure 4.10, shows the powder is a typical gas atomised powder. It is mostly spherical, with some elongated particles, splat-caps, and satellite particles present. The BSE-SEM was used to ensure there was no major cross contamination or defects within the powder system.

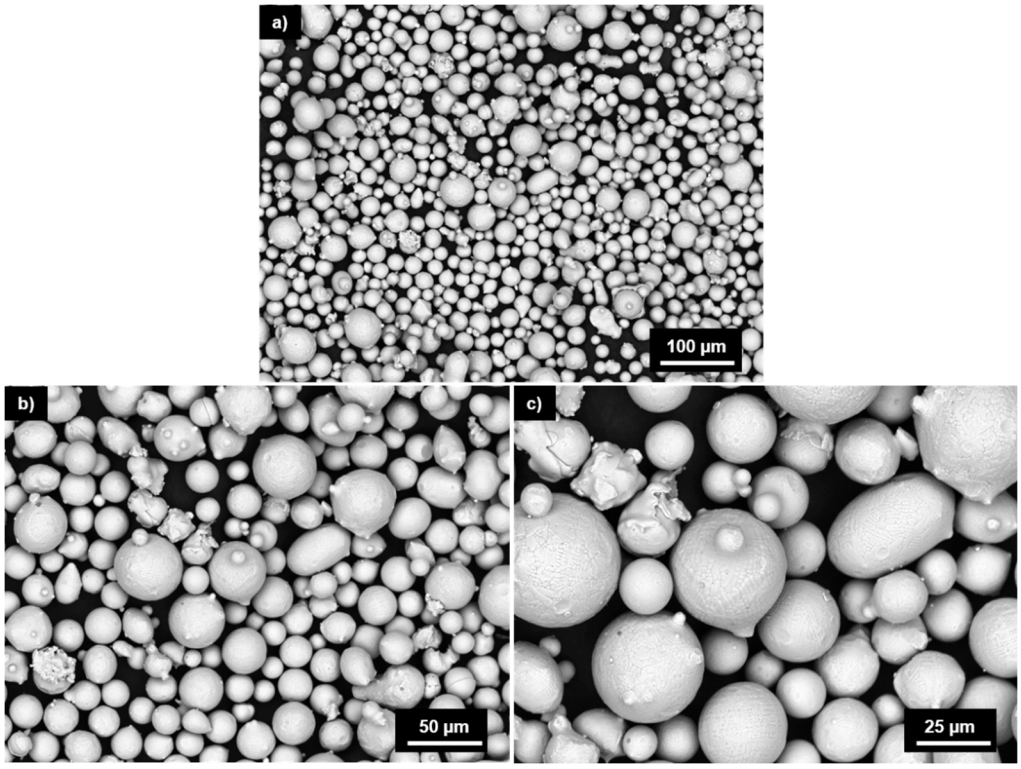

Figure 4.10 BSE-SEM micrograph of the virgin Supplier 1 Hastelloy X powder with different magnifications

The gas atomisation process produces a fine bi-phasic γ/γ˝ microdendritic or equiaxed structure [128]. Figure 4.11 shows the range of microstructures present in the Hastelloy X powder, dependent upon the cooling rate of each particle and primarily dictated by its mass.

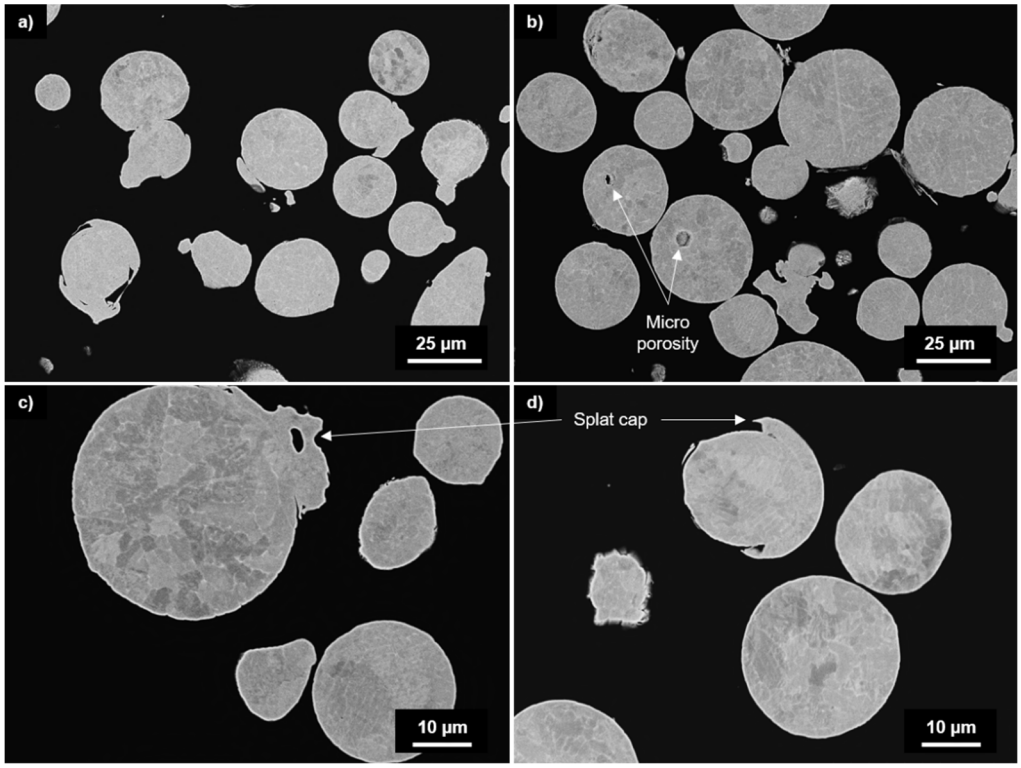

Figure 4.11 BSE-SEM micrograph of cross section of virgin Supplier 1 Hastelloy X powder showing the range of microstructures and produced from the gas atomisation process. Highlighted are also internal micro-porosity and splat cap features that are produced during gas atomisation

Table 4.4 shows the composition of the Supplier 1 Hastelloy X powder used. The elements of most interest in this research are the Al at 0.1 wt%, Si at 0.5 wt%, and Cr at 21.5 wt%.

Table 4.4 Nominal range for composition for Hastelloy X (UNS N06002) according to AMS 5390 [167] *and the composition of Supplier 1 Hastelloy X-1 (HX1) provided by the manufacturer*

	Ni	Fe	Cr	Co	Mo	W
ASM 5390	Bal	17.0-20.0	20.5-23.0	0.5-2.5	8.0-10.0	0.2-1.0
HX-1	Bal	18.2	21.5	2.1	9.4	0.9
	C	Si	Mn	Al	Ti	O
ASM 5390	0.10 max	1.00 max	1.00 max	-	-	-
HX-1	0.04	0.5	0.1	0.1	0.1	0.02

4.2.2 Supplier 2 Hastelloy X

Supplier 2 Hastelloy X was sourced as a secondary Hastelloy X gas atomised PBF-LB powder with +15-45 µm with reduced Si content. The exact details of the powder and composition cannot be disclosed but it can be confirmed that the composition of major elements is very similar and reduction in Si content is the only major difference, with all elements within the AMS 5390 specification. Figure 4.12 shows that Supplier 2 Hastelloy X has a similar gas atomised morphology as well as PSD shown in Figure 4.9.

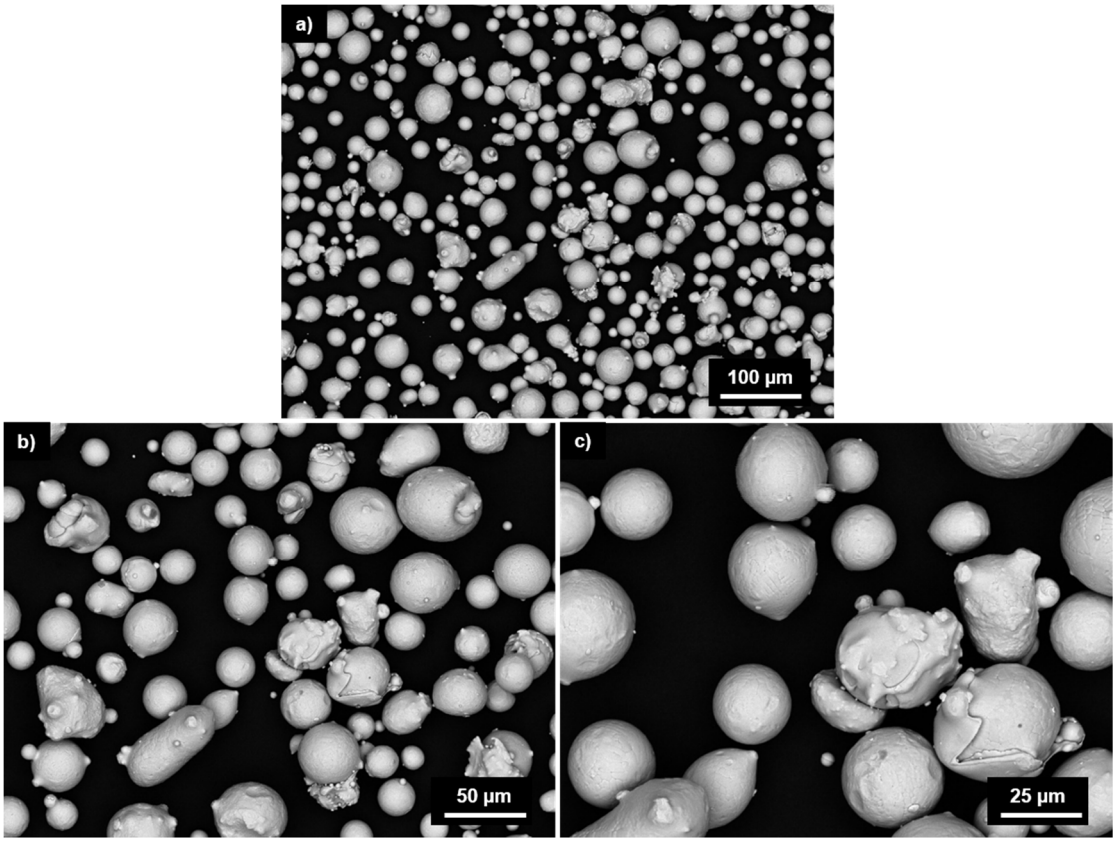

Figure 4.12 BSE-SEM micrograph of virgin Supplier 2 Hastelloy X powder with different magnifications

4.3 Summary

The powders used for this work are typical gas atomised powders, commercially available for PBF-LB, and commonly used in industry. The particles show an appropriate mono-modal size distribution appropriate for PBF-LB processing. The particles contain a proportion of satellites and irregularities, which are commonplace with gas atomisation, however, the powders are

flowable and suitable for the process. The Inconel 718 powders, from both supplier 1 and 2, have TiN inclusions present within the particles which must be incorporated somewhere earlier in the manufacturing of these materials and corroborates with findings in literature of this issue present across the industry. The laser diffraction measurements of the PSD highlight the difficulty of comparing these measurements with sieve sizing. The powders are sized as 15-45 µm, however, the laser diffraction PSD measurements show the distribution tails exceeding these sieve cut offs and having a D10 of ~ 20-25 µm and D90 of ~50-55 µm. As discussed in Section 2.2.2, this is a known issue in literature and is due to a combination of the measurement approximations and irregularities in the particles or any deviations from a spherical particle. These materials and characterisation in this chapter provide a basis for investigating the change in the powder through PBF-LB and the spatter which is generated.

Chapter 5 Characterisation and classification of spatter in PBF-LB

Spatter is generally considered detrimental to the PBF-LB process, but little is understood about the nature of the particles produced and their effect when incorporated into parts. The first step of this, is understanding the by-products from the laser melting of the powder and the spatter particles themselves. As discussed in Chapter 2, there has been much research previously into the physics of the generation of spatter in conventional welding techniques, and more recently in PBF-LB with the additional complexity the powder bed creates. This has led to the understanding that what is typically described as spatter is a collection of by-products with different mechanisms. The vaporisation of some of the material, the ejection of material from the melt pool, the entrainment of particles in the bed close to the melt pool, which are either heated as they pass through or by the laser, or entrained behind the laser with minimal heating. These spatter particles are distributed throughout the chamber and a proportion back into the powder bed. A proportion of these particles redistributed back into the powder bed will be melted and incorporated into the parts produced.

This chapter investigates these spatter particles produced and establishes their variation from the feedstock material. The particles are assessed for their size, morphology, and compositional differences, particularly regarding the presence of oxides in the material. The oxides are shown to form at and transfer from the surface of the melt pool, where a proportion remain as a part of the manufactured material. The vaporised material is collected to analyse the nano-particles produced and complete the picture of the by-products from the laser melting of the powder bed.

Inconel 718 was the primary material investigated. The findings from the investigation of Inconel 718 were used to understand spatter generally and link the resulting by-products to the generation mechanisms established by others in Chapter 2. Inconel 718 was investigated across four different PBF-LB machines detailed in Chapter 3, the SLM50, AM125, SLM125, and LMF1000, to compare the material generated from different systems. The findings from Inconel 718 were used as the basis to investigate Hastelloy X for the generation of spatter

particles and their oxidation in another Nickel-based superalloy with a different composition. For Hastelloy X the effect of change in the composition of the virgin powder is explored for the oxide formation in the spatter and PBF-LB produced material.

5.1 Methods

The spatter collection method and analysis for this chapter and the subsequent chapters was detailed in Section 3.3.1.1. As part of the investigation into the spatter generation this chapter also includes analysis of vaporised material, which was deposited on the walls of the build chamber, and of the PBF-LB scan tracks.

5.1.1 Collection of deposition material from vaporisation

During laser melting of the powder some of the material is vaporised. The vaporised material is deposited on the inside of the processing chamber. To collect this vaporised material, 3 mm copper TEM grids with a Carbon film back were used to capture the material in a similar setup to that employed by Louvis *et al.* [4]. This was undertaken in the ReaLizer SLM50 system. During processing, the plume can be seen to circle around the chamber as depicted in Figure 3.6, due to the circulation of the gas flow. Therefore, the grids were placed by the gas outlets, the ceiling of the chamber, and suspended above the melt pool to allow the best opportunity to collect the vaporised material.

The copper grids were analysed using the JEOL 7100F FEG-SEM (JEOL Ltd., Japan), and a JEOL JEM-2100PlusTransmission Electron Microscope (TEM). This system was equipped with TEM-EDS to characterise the composition of these particles and EDS spectra were taken from six large clusters of nano particles. The Carbon film back to the TEM grids contributed to an increase in the C reading for the vapour particles.

5.1.2 Analysis of scan tracks

The scan tracks are analysed on the build surface of specimen produced in the builds that spatter was collected and single scan tracks were also assessed. These were analysed using

the Hitachi TM3030 BSE-SEM with EDS to characterise the morphology and composition in the tracks and identify oxides. The micrographs presented are from the surface of 10 x 10 x 10 mm cubes manufactured in the SLM50. The surfaces of specimen with different geometry and the surfaces of specimen from each of the machines were also analysed and confirmed the findings were general across systems.

The SLM50 was used to investigate oxide formation on the melt pool. A 10 mm long single scan track of 10 layers was fabricated with the Oxygen level kept <0.15%. The chance of spatter generated from melting of this track landing in the bed and being incorporated into the part was highly unlikely, and if so, would have a minimal effect relative to the quantity of oxides being investigated. The study of this track allowed the investigation of whether oxides on spatter particles and in parts are due to powder-to-part or part-to-powder transfer.

5.1.3 Investigation of composition change on spatter and oxidation for Hastelloy X

In this chapter, the oxidation and spatter formation between different PBF-LB systems and different alloy systems is investigated. This chapter also investigates the effect of the quantity of micro-alloying elements on spatter and oxide generation. This is investigated for Hastelloy X, which is shown to produce predominantly Cr and Si oxides. As discussed in Section 2.3.2, studies by Tomus *et al.* [136,137] and Harrison *et al.* [138] showed that a reduction in Si and Mn content in Hastelloy X could reduce the micro-cracking and improve performance of the alloy in PBF-LB.

The Supplier 1 Hastelloy X used, has a composition within the allowable range according to AMS 5390 specification for the nominal composition and tolerances for each element, this will be referred to as Hastelloy X-1 (HX-1). The compositions for HX-1 and the standard are shown in Table 4.4. A second Hastelloy X alloy was sourced with a reduced Si content to investigate the effect of the reduction on the oxide and spatter formations in the PBF-LB processed material. The exact composition of the material cannot be disclosed but it can be confirmed that the composition of major elements is very similar and reduction in Si content is the only major difference. This alloy is referred to as Hastelloy X-2 (HX-2).

For comparison with the findings for HX-1, the HX-2 was processed in the same manner using the SLM50. Spatter was collected from processing 10 x 10 x 10 mm cubes with the same processing parameters. The single track investigation was also conducted to assess the oxide formation at the melt pool and the part surface.

5.2 Inconel 718

5.2.1 From virgin to spatter particles

5.2.1.1 Size and morphological characterisation of spatter

Analysis of the spatter particles collected at the side of the chamber for each PBF-LB system showed that the spatter powder was dissimilar from the virgin material characterised in Chapter 4. The BSE-SEM micrographs in Figure 5.1 shows that the particles differ by size, shape, morphology, and the presence of oxides. Oxides were evident as the dark spots present on a proportion of particles, with the dark contrast indicating a lighter elemental composition in BSE-SEM. The four images show a range of different particle types were found within the spatter across the different PBF-LB systems. Each machine produced a different profile of spatter (with regards to morphology, size distribution, and oxide presence) but all produced similar types of particles. The difference between spatter from different systems is explored further in Chapter 6.

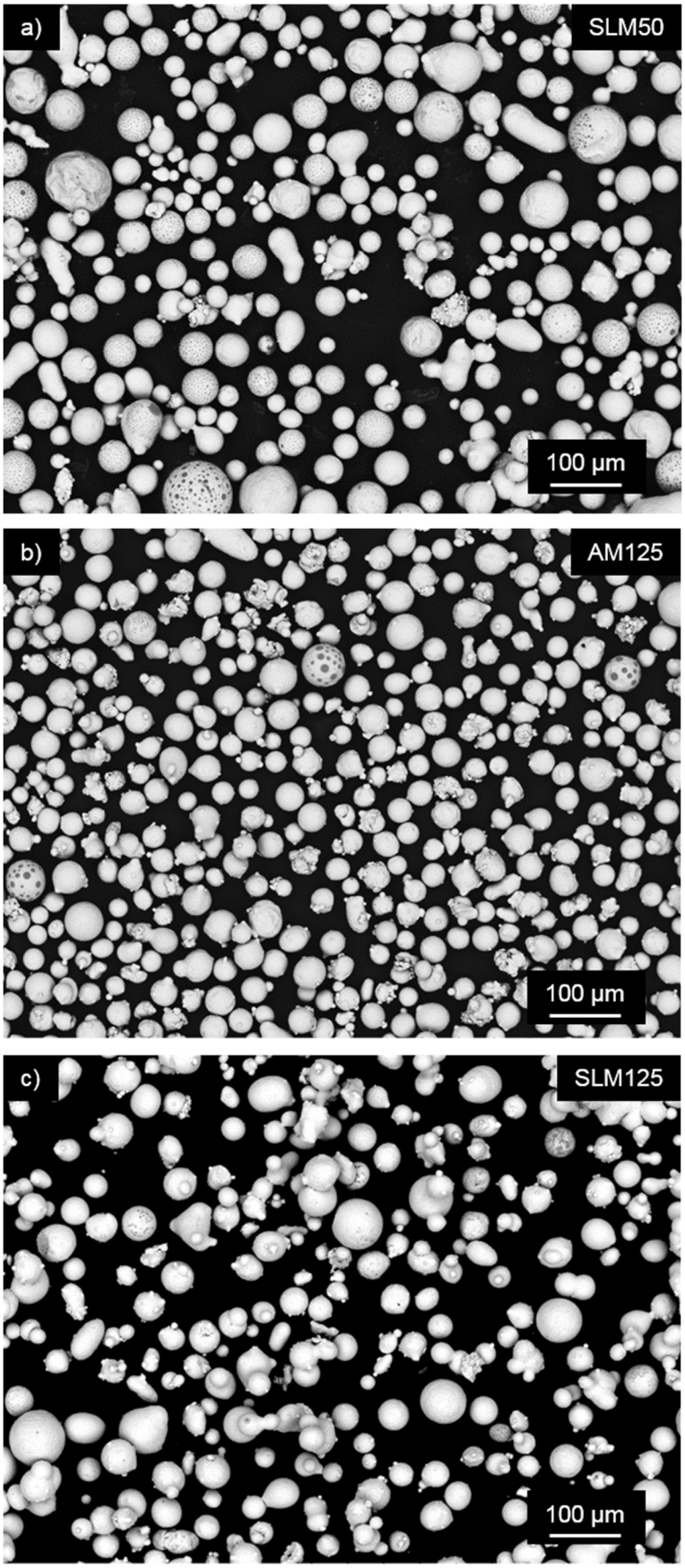
a)
SLM50
100 µm
b)
AM125
100 µm
c)
SLM125
100 µm

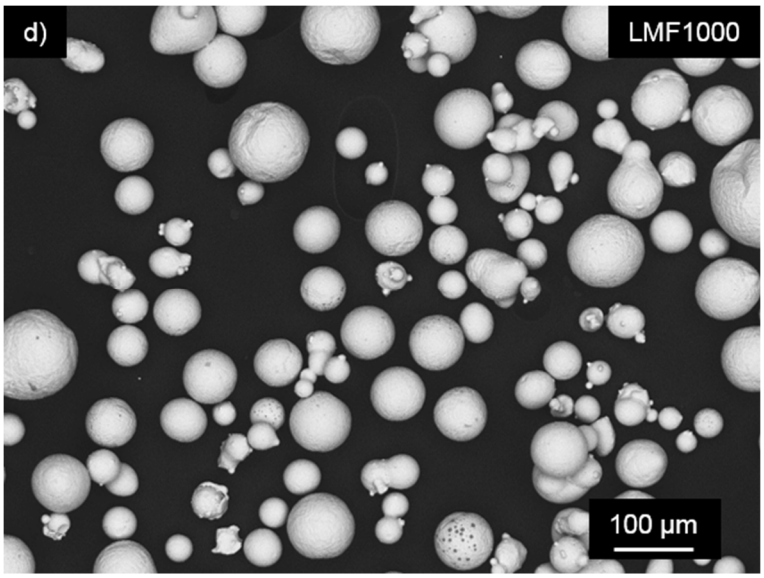

Figure 5.1 BSE-SEM micrographs of Inconel 718 spatter powder collected from the: a) the ReaLizer SLM50 system, b) Renishaw AM125, c) SLM Solutions SLM125, and d) Trumpf TruPrint 1000. All images to the same scale

The range of spatter particles found have been grouped into different classifications in Table 5.1, with the particles classified by size, morphology, and other descriptors such as oxides and agglomeration derived from SEM analysis. Examples of the classifications are provided in Figure 5.2 but are not exhaustive in terms of the range of particles in these classifications. The classifications cover the range of particles found in the powder analysed and provide general descriptors for the particles. Further, or different classifications could be made, however, the ones presented help link the types of particles to the different mechanisms by which they are generated and to understand the formation of the oxides. The generation mechanisms and their link to the particle classifications are discussed in Section 5.2.2.

Table 5.1 Classification of spatter particles

Particle Classification	Features	Size (µm)	Example in Figure 5.2	Generation Mechanism (Section 5.2.2)
I	Particles similar to virgin gas atomised particles	15-45	a1	Cold entrained (Type 3)
II	Particles with morphology different to gas atomised	15-45	a4	Hot entrained or melt eject (Type 2 or 1)
III	Larger singular particles with different morphology	45-111	a3	Melt eject (Type 1)
IV	Particles with oxide spots	23-567	a2, d-i	Melt eject (Type 1)
V	Particles covered with oxide	31-128	b, c	Melt eject (Type 1)
VI	Small particles	<15	j	Melt eject (and explosion) (Type 1)
VII	Agglomerates	<273	k, l	All mechanisms (Type 1-3)

The particles can be classified due to their difference from the virgin material input. The virgin material had a size range of 15 - 45 µm, a reasonably consistent morphology, and no presence of oxides. From the spatter particles found in the study, the particles can then be separated as those that fit the description of the virgin material (type I) and are of the same size. Those that are the same size as the virgin material but have an altered morphology (type II). Particles that are larger than the virgin material but are a singular particle (not an agglomerate) are classified as type III. Particles identified to have oxides, either as spots or films, are classified as type IV and V respectively. Type VI particles are those smaller than the virgin material and type VII are large agglomerates which are not present in the virgin material. Examples of particles depicting the different classifications are in Figure 5.2 and Figure 5.1, with Table 5.1 identifying specific examples. It is possible for a particle to come under two categories, particularly categories I and II, however, by far the majority of particles only come under a

single category and the categories help to identify the generation mechanisms for these particles.

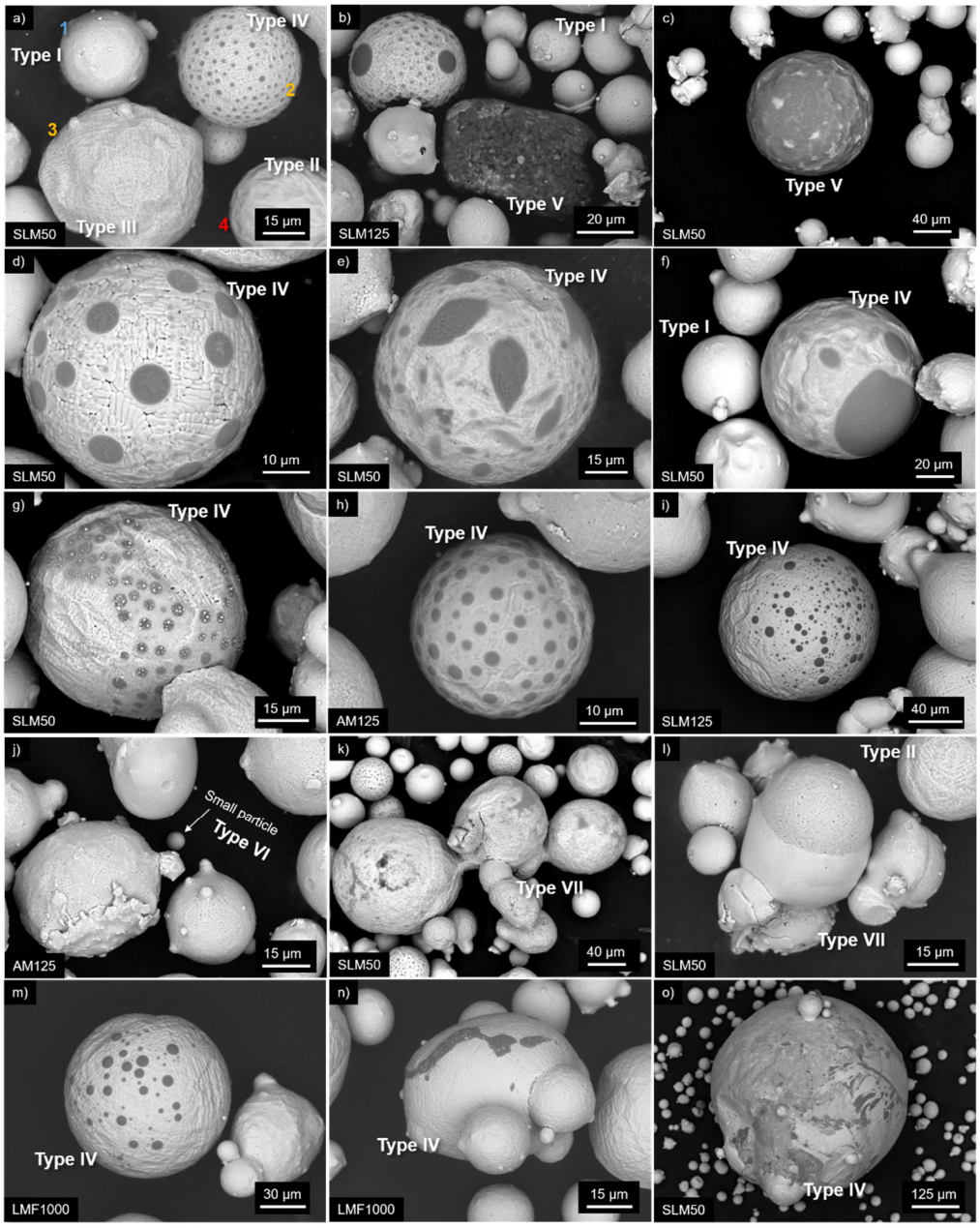

Figure 5.2 BSE-SEM micrograph with examples of different types of spatter particles highlighting the range and variety within the classification proposed in Table 5.1. The machines the particles were produced from are indicated, however, these are just examples of the types of particle classifications and the whole range of particles were witnessed in the particles produced by each machine

Laser diffraction analysis of the spatter collected at the side of the chamber for each PBF-LB machine showed that spatter generated is larger than the starting powder and has a wider

distribution, as shown by the shift in D_{10}, D_{50}, and D_{90}, shown in Figure 5.3. This is in agreement with previous studies [5,44,45], however, the size distribution for the spatter showed by Liu *et al*. [44] and Wang *et al.* [45] were attained by sieving used powder +75 µm. Therefore, their results did not account for spatter being smaller than 75 µm, and hence, their distributions were skewed with respect to the actual spatter size distribution. The PSD results in Figure 5.3 show that some spatter is of a similar size to the virgin feedstock. This is also evidenced by the particles of type II, IV, and V from Table 5.1 that have particles of the same size as, but are not, virgin material. The results presented here represent the distribution of just spatter particles, redistributed to the side of the build chamber where no virgin material from the powder bed is present. It is assumed that these are representative of the spatter that is redistributed inside the powder bed too, which it is not possible to analyse separate from the rest of the powder in the bed.

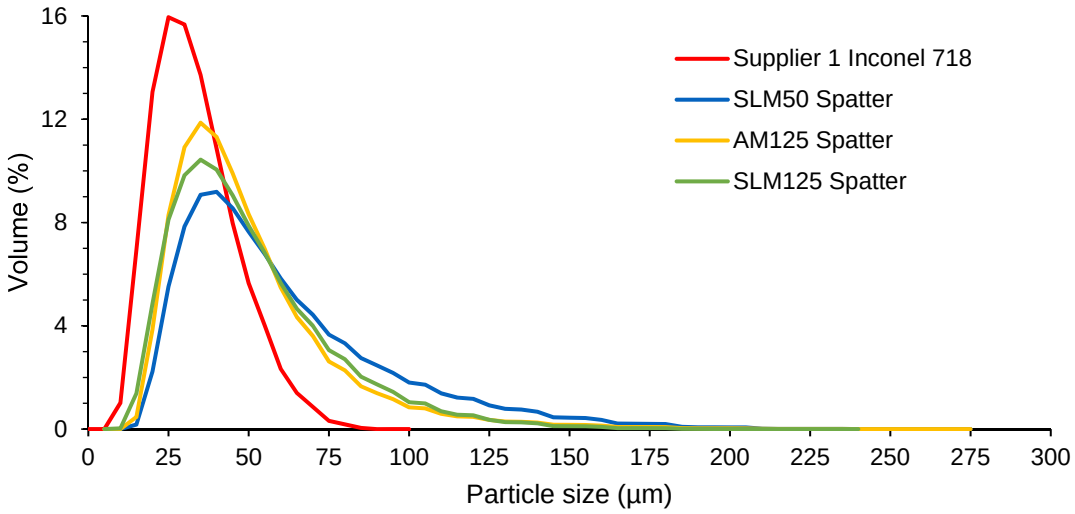

Figure 5.3 PSD for virgin Inconel 718 powder and collected spatter from each machine analysed through laser diffraction

Table 5.2 D_{10}, D_{50}, and D_{90} for virgin Inconel 718 and spatter produced by the SLM50, SLM25 and AM125

(µm)	Virgin Supplier 1 Inconel 718	SLM125 Spatter	AM125 Spatter	SLM50 Spatter
D_{10}	21.02	27.59	28.64	31.53
D_{50}	34.12	47.87	46.61	54.88
D_{90}	54.09	88.43	85.04	112.28

The spatter powder's PSD shows that a proportion of the spatter powder is generated within the size range of the virgin material. The proportion of the spatter particles generated within the size specification of the virgin material, based on the equivalent sieve size from laser diffraction, were 45.5, 56.8, and 56.9% for the SLM50, SLM125, and AM125 respectively. This proportion of spatter powder generated cannot be removed from the unprocessed powder by sieving for the purpose of recycling as it would sieve identically to virgin material. The powder size distributions shown in Figure 5.3 and the D_{10}, D_{50}, and D_{90} in Table 5.2, highlights that different PBF-LB machines produce different PSDs of spatter under recommended process parameters.

The spatter collected for this experiment was spatter that had been redistributed away from the powder bed. A proportion of the spatter landed back into the powder bed and then had the potential to be incorporated into the part. Through this, the oxides found on the spatter particles can be transferred to the bulk of the part, or the oxides could be melted into the rest of the consolidated material and increase the Oxygen content. Some of the spatter was much larger than the virgin powder particles, with particles like that in Figure 5.2o, up to 567 µm. It is often assumed that the recoater will remove these larger, problematic particles. However, they may land in an area of the powder bed yet to be irradiated by the laser, or they may cause issues such as corn rowing in the powder bed which themselves lead to defects [53,104]. When these larger particles are incorporated into parts they may not be fully melted, causing discontinuity and porosity in parts. These quality issues are important consideration for the processing of Inconel 718, and in likelihood many other alloys and, hence, warrants further investigation.

5.2.1.2 Compositional characterisation of spatter

SEM-EDS was used to evaluate the composition of the oxides of the spatter particles classified IV and V. Figure 5.4a-c shows that the dark spots shown in BSE-SEM mostly contain Al and O, and that the larger dark spots also contain Ti. EDS quantification results indicated that the oxides were a combination of Al_2O_3 and TiO_2. The lack of Al and O in the right hand side of Figure 5.4c is due to the EDS measurements lack of signal, for the lower energy lighter elements combined with the curvature of the particle and position of the EDS detector, rather

than a separation of Al and Ti in the oxide. All machines produced spatter particles with similar characteristic oxides.

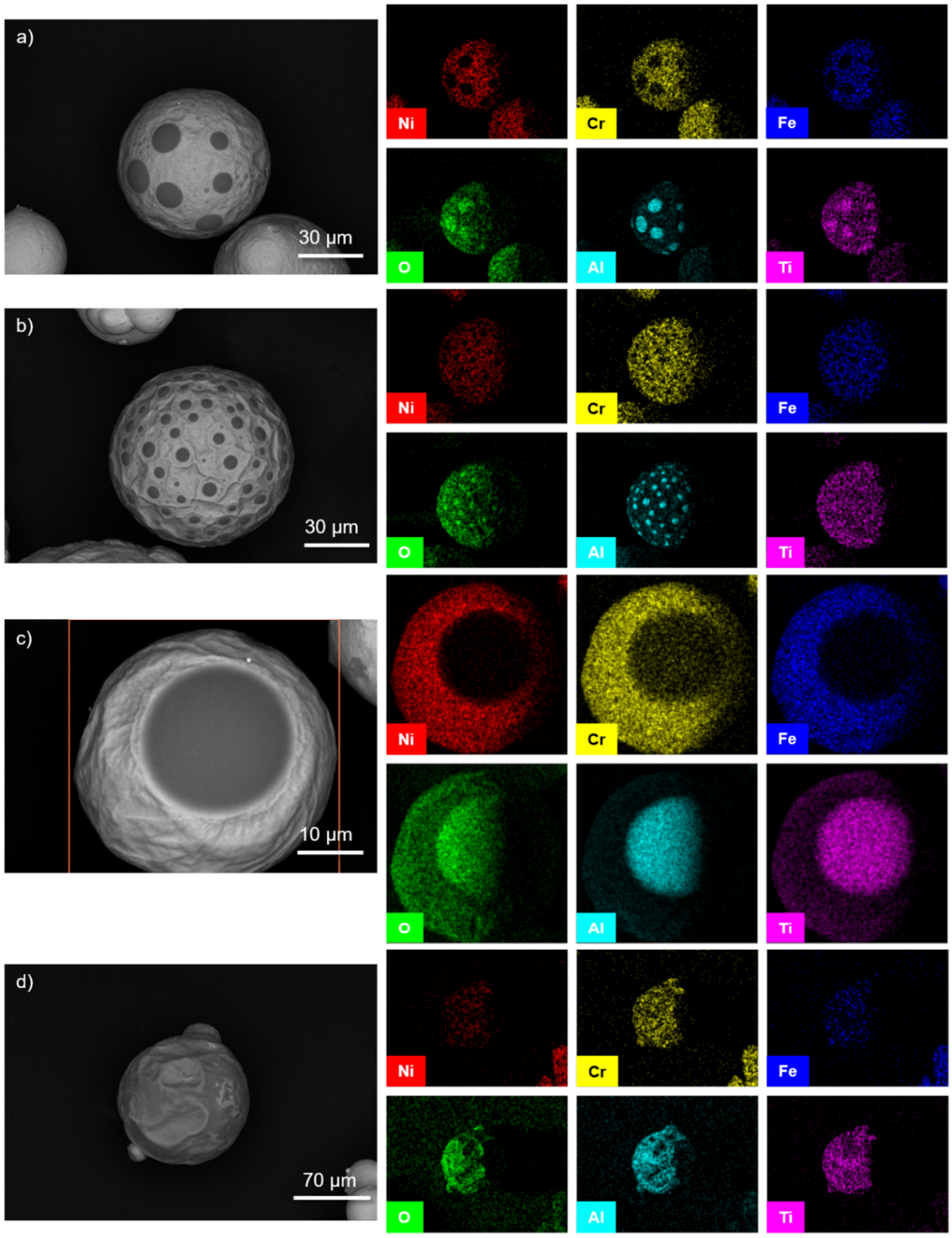

Figure 5.4 Left) BSE-SEM micrograph, and right) EDS mapping of elements of Inconel 718 Spatter collected from the ReaLizer SLM50

The majority of the dark spots were circular in shape, as seen in Figure 5.4, indicating that they experienced conditions conducive to forming a minimum psotential energy shape. However more irregular shaped or patches were also found, such as in Figure 5.2e and f, which is closer

to those found in other studies [5,44,45]. It can also be seen that the spots are not level with the surface of the particle and are raised, as seen in Figure 5.2d. Compared to oxides found in the other studies [5,44,45], the oxides for this Inconel 718 powder were generally more regular, circular, and numerous in their covering of the particles.

As well as the particles with oxide spots and patches, particles were found that were completely oxidised. Figure 5.4d shows that this oxide coating was again a combination of Al and Ti oxides. These particles were found in the spatter from all the systems. Across the machines, the particles with oxide spots were mostly found in particles ranging in sizes from 23 – 118 µm, and the spots themselves were found to range from 0.7 – 30 µm in diameter, however some very large particles with oxides were found. Figure 5.2o shows a 567 µm wide spatter particle with oxides. The fully oxidised particles were found in the range of 31 – 128 µm.

To establish the extent of the oxidation of the spatter particles, a particle with oxide spots and a fully oxidised particle were analysed using SEM-EDS with in situ FIB to mill a section of the particle away, as seen in Figure 5.5. The cross section shows that the oxidation is only a surface phenomenon and does not continue further into the bulk of the particle. From the cross section, the oxide spots were found to have widths of 1890 – 2210 nm and heights of 470 – 780 nm, the particle had a width of 34 µm. The spots analysed had an aspect ratio (Width:Height) of 2.43 – 4.68, hence it is predicted that that largest spots found, at 30 µm width, had a height of between 6.4 – 12.3 µm. The oxide layer on the 65 µm diameter oxide coated particle in Figure 5.5b had an average depth of 216 nm.

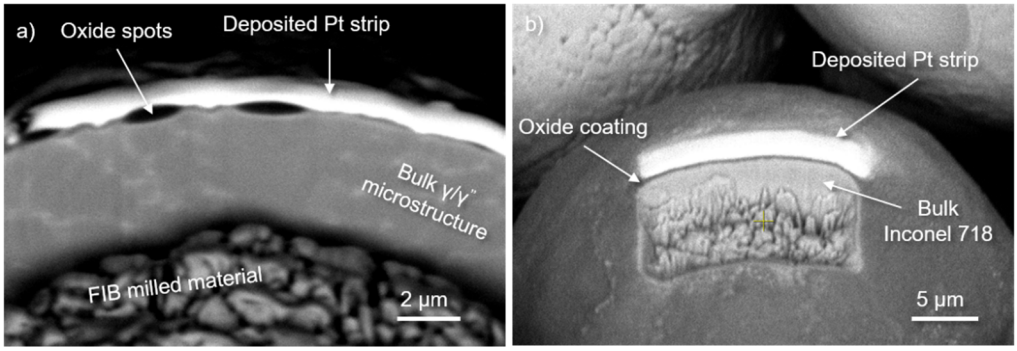

Figure 5.5 BSE-SEM micrograph of particle with FIB sectioning to reveal microstructure and surface oxides (darker material) for particle a) with oxide spots and b) with oxide coating. The bright section is the sacrificial platinum strip deposited prior to ion milling

The microstructure of the spatter particles compared to the virgin material was initially assessed by mounting and cross sectioning the spatter. However, the particles with oxides were not discernible from the cross sections and, other than size and shape, there was no clear difference in microstructure as the microstructural variation of the spatter particles were the same witnessed in the virgin gas atomised material. FIB-SEM was then used to interrogate particles with oxides directly. Figure 5.5a showed a microstructure similar to the virgin gas atomised microstructure, as shown in Chapter 4, therefore with no contradicting evidence it is assumed to be a bi-phasic γ/γ″ microdendritic structure as seen previously [128]. This indicates that the spatter ejected from the melt pool goes through a similar cooling regime as gas atomised powder. This is consistent with the observations of Simonelli *et al.* [5], who proposed that spatter forms a similar microstructure to the gas atomised powder as they solidify in a similar room temperature and inert environment, but may differ slightly due to a slightly higher thermal mass as the spatter particles are generally larger.

5.2.1.3 Origin of oxides on spatter particles

Oxides are present on the top surface (X-Y plane) of Inconel 718 parts produced by PBF-LB, as can be seen by the dark spots in Figure 5.6a. As these spots are similar to the oxides we find in the spatter particles, the question raised is whether: the oxides transfer from the spatter powder to the part, from landing back in the powder bed; or, as the spatter particles are ejections from the melt pool, whether the oxides are present at the melt pool level and transferred to the spatter. Figure 5.6b shows the 10 mm 10 layer single scan track which revealed oxides present on the surface. This shows that the oxides formed at the melt pool surface despite the gas flow across the bed. The oxide formed on the melt pool, and as spatter is ejected from this melt pool, the oxides remain on the surface of the spatter particle. A full part, as in Figure 5.6a, will have oxides formed at the surface as well as oxides incorporated from spatter particles landing in the powder bed and being melted into the part. The single scan track did not produce enough spatter for those particles to land in the area of yet un-melted track and create the quantity of oxides seen in Figure 5.6b. Hence, the oxides formed during the solidification of that track.

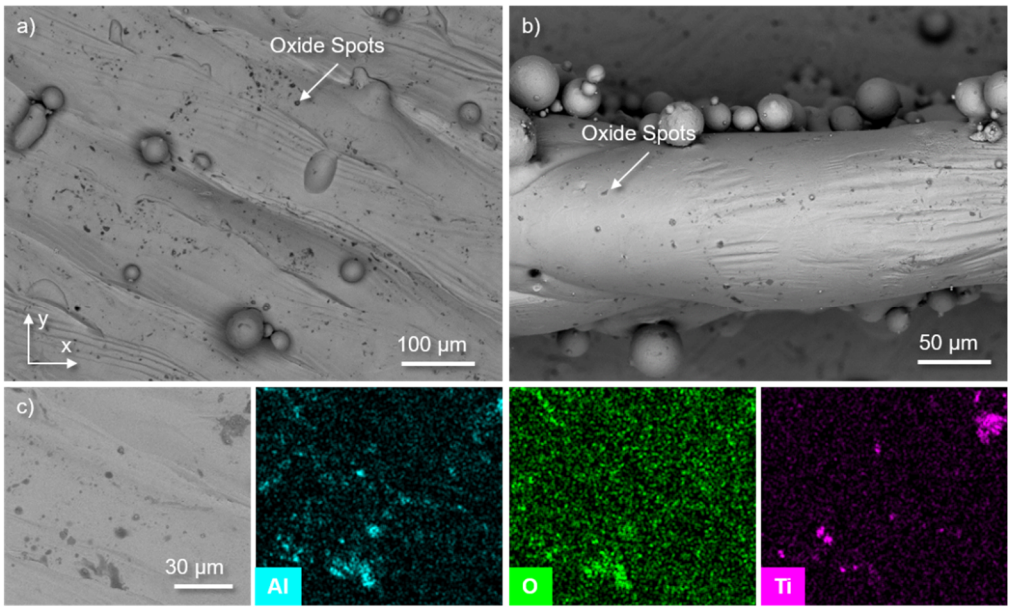

Figure 5.6 BSE-SEM micrographs showing: a) the surface of a cube with the presence of oxides, b) a single 10 layer scan track also showing the presence of oxides, and c) EDS map of the surface in (a) showing the dark sections are Al and Ti oxides

5.2.1.4 Vapour plume and nano particulates

Cu TEM grids were placed in the chamber of the SLM50 machine, as depicted in Figure 3.6 in Section 3.3.1.1 and discussed in Section 5.1.1. Figure 5.7b shows that the deposited material which adhered to these grids was nano-scale vaporised particles sized between 10 – 100 nm that create chain-like clusters, spanning up to 9 µm. Micro-sized particles, such as those shown in Figure 5.7d, were found on the grid suspended above the build plate. These particles are of a similar size to the oxides spots found on the spatter, however, EDS results showed they were of the same composition as the starting material. These particles were distinct from the vaporised nano-particles and are classification type IV particles from Table 5.1. This showed spatter can produce particles of 1 µm diameter.

The TEM-EDS spectrum showed that the vaporised deposition was comprised of the primary constituents of the Inconel 718, Ni-Fe-Cr, with an increased O content and a small detection of Al. The average composition of the nano-particles is shown in Table 5.3. From comparison with the composition of the virgin material it can be seen that the relative level of Cr, Al, Si and C in the vapour has increased. The increase in C and Si can likely be attributed to the C film backing on the Cu TEM grid, with the Si content likely due to its exposure to air before the experiment. The relative increase in Cr and Al is a likely indication of preferential vaporisation

of it from the melt pool. This is could be explained by the lower boiling point and enthalpy of vaporisation for Cr and Al compared to the other elements, as seen in Table 5.3.

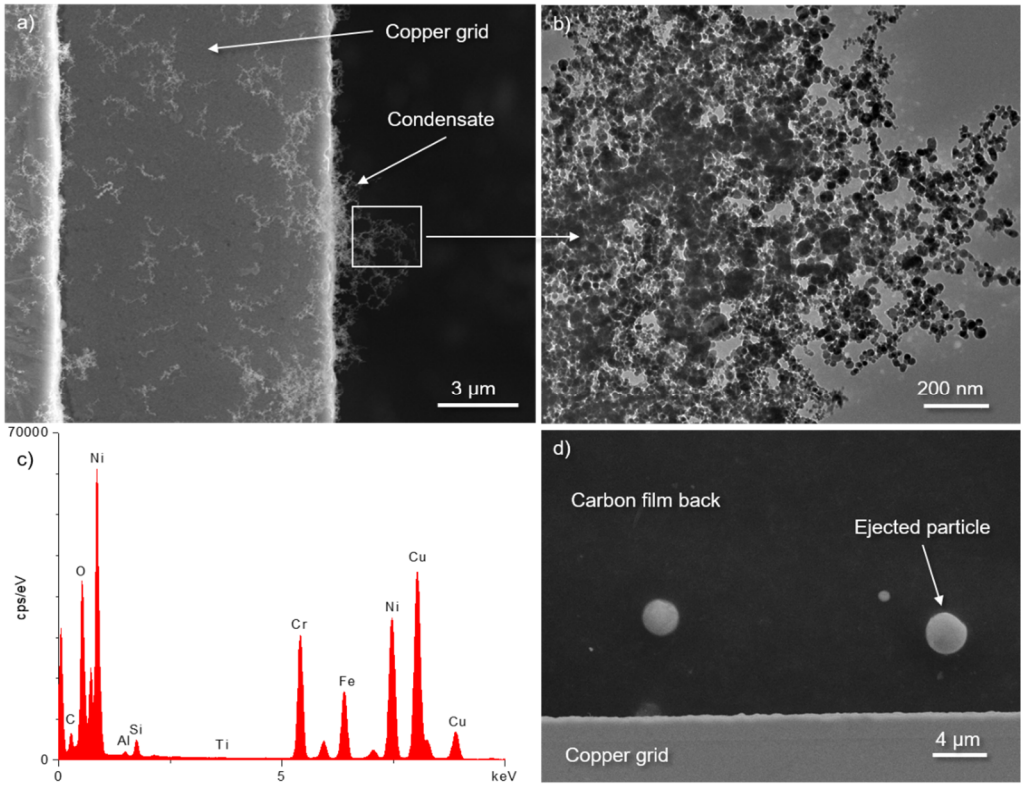

Figure 5.7 a) Secondary electron SEM micrograph showing condensate on copper TEM grid, b) TEM micrograph of the condensate, c) TEM-EDS spectrum of the condensate, and d) Secondary electron SEM micrograph showing ejected or detonated particle adhered to C film

Table 5.3 Average composition of vapour nano particles and the virgin material, and the boiling point and enthalpy of vaporisation for the respective elements [168]

Element	C	O	Al	Si	Cr	Fe	Ni
Vapour particles (wt%)	5.0	31.9	0.3	1.7	19.6	12.1	29.2
Virgin material (wt%)	0.04	0.01	0.44	0.04	19.04	17.17	54
Boiling point (K)			2743	3533	2755	3273	3003
Enthalpy of vaporisation ($kJ.mol^{-1}$)			284	383	347	354	379

5.2.1.5 Second supplier powder

A second commercial Inconel 718 PBF-LB powder was sourced to ensure the findings were generalised and not due to a particular powder source. Figure 5.8a shows the formation of Al and Ti oxides on the part surface, and (c&d) show the oxides form and transfer to the spatter particles the same as in the Supplier 1 Inconel 718. Figure 5.8b shows an example of either a spatter particle with oxides that has landed back into the powder bed and been partially melted and incorporated into the surface, or is part of the melt pool that didn't have sufficient energy to completely eject from the melt pool. Examples of this occurrence of part of the melt pool not escaping can be seen in high-speed videos of the laser melting process by Matthews *et al.* [39] and Bidare *et al.* [40]. This kind of particle inclusion can lead to lack-of-fusion defects and porosity surrounding it.

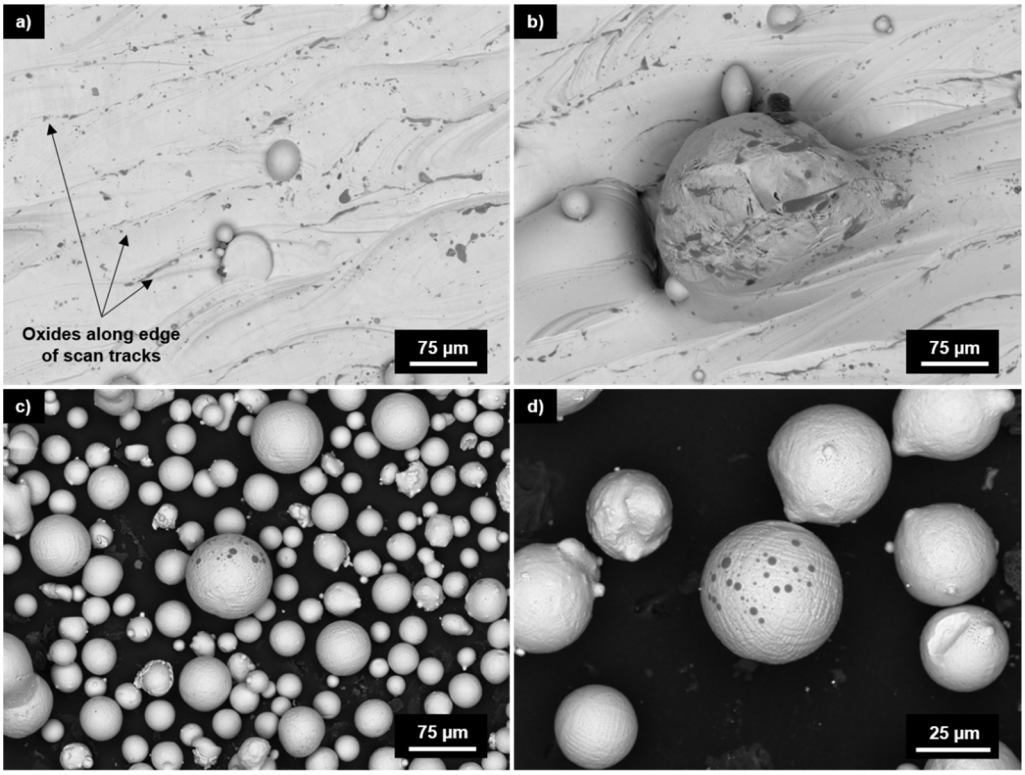

Figure 5.8 BSE-SEM micrographs of Supplier 2 Inconel 718 powder. a) cube surface with oxides along scan tracks, b) large particle with oxides in the part surface, c&d) spatter particles with oxide spots

5.2.1.6 Oxidation in 'inert' PBF-LB systems

Simonelli *et al.* [5] first demonstrated the formation of oxide patches on spatter produced from Stainless Steel 316L powder, however, it appeared to a much lesser degree than found

in this investigation. Particles covered in oxide spots and fully coated with an oxide film were not encountered in their study. They assumed that the oxide was formed on the particle during its solidification, however, our results show that the formation of the oxides occurs at the surface of the melt pool. Some oxidation of the melt pool, which remains on the top surface of parts produced, was found by Louvis *et al.* [4] in Al alloys. Thijs *et al*. [169] also demonstrated oxidation on the surface of maraging steel parts produced by PBF-LB. In both these studies the oxide layer formed less as spots and patches on the surface but more as a continuous film. We predict that for the Al alloys [4] this is due to the much higher content of Al and other elements with high oxygen potential, and for the maraging steel [169] due to the chamber oxygen content being much higher (up to 2% in some instances) in the study. We would assume that the spatter produced in the processing of both those materials would also exhibit the oxides found in our study. These other studies performed with different alloys, from different powder suppliers, and in different PBF-LB machines demonstrate this to be a generic issue for some alloys being processed by PBF-LB.

Inconel 718 consists mainly of Ni, Cr, Ti, Al, Nb, and Mo. From the Ellingham diagram [170] in Figure 5.9, in order of oxidation potential based on the Gibbs free energy (from low to high): Ni, Fe, Cr, Ti, and Al have the potential to produce NiO, FeO, Cr_2O_3, TiO_2, and Al_2O_3 in the presence of O_2. The formations of these oxides is in agreement with Rao *et al.* [171] who reported elements Al and Ti forming their stable oxides, Al_2O_3 and TiO_2, when O_2 is absorbed during powder metallurgy Hot Isostatic Pressing (HIP) of Inconel 718. The oxides in this study are a combination of Al_2O_3 and TiO_2 and each oxide had a different ratio the two. This is likely due to the O_2 content that the area comes in contact with in the chamber environment, which varies due to the gas flow at a given time and will fluctuate, and the localised concentration of Al and Ti. It is envisioned that there is a higher composition of TiO_2 in the larger oxide spots and films as more of the available Al had already formed Al_2O_3 allowing the oxidation of available Ti in the spatter particle.

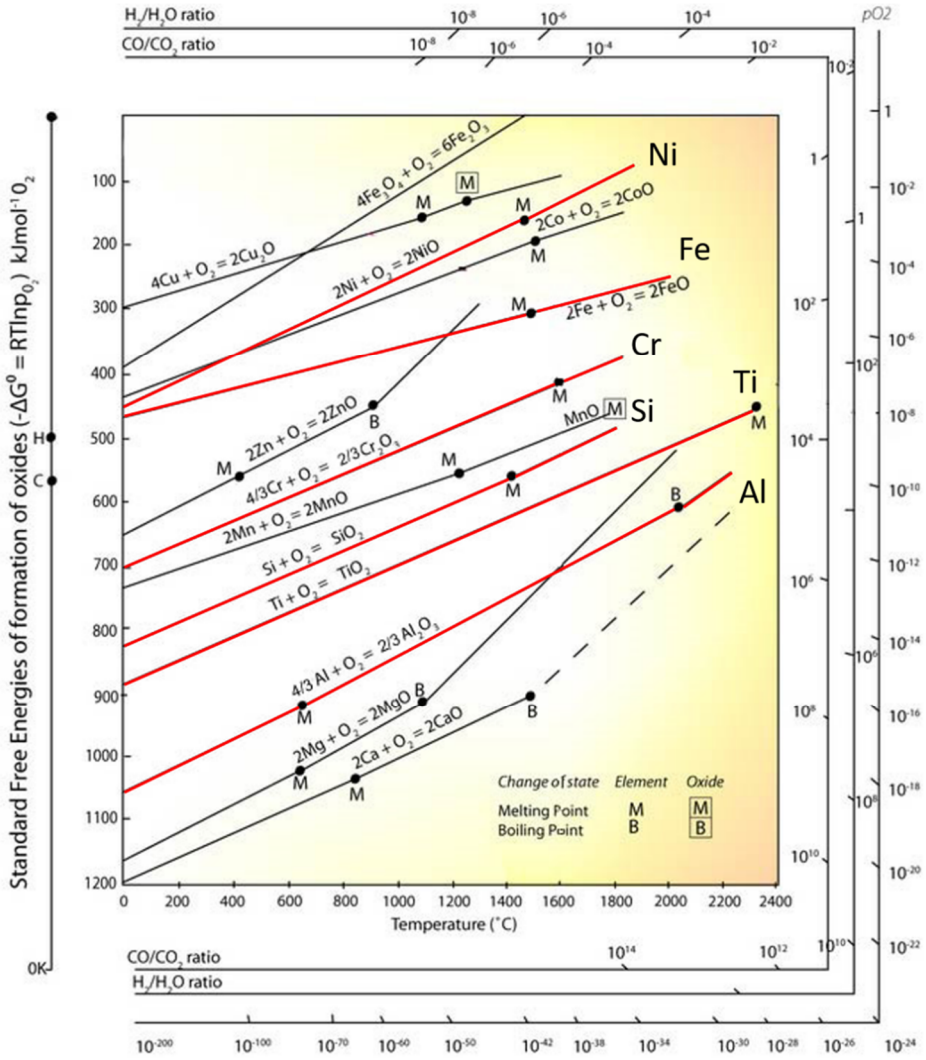

Figure 5.9 Ellingham diagram depicting the oxidaiton potential of different elements with regards to temperature and partical pressure of Oxygen. The relevenat constituent elements of Inconel 718 and Hastelloy X are highlighted in red. [170]

Avoiding this oxidation may not be possible and is a major consideration for use of this, and similar alloys, in PBF-LB. Zhang *et al.* [172] encountered Al_2O_3 and Cr_2O_3 films during DED of Inconel 718 and discussed the unavoidability of oxidation of these elements. Based on the equilibrium partial pressure of oxygen threshold below which oxidation of Al should not occur (10^{-58} atm from the Ellingham diagram), even industrial grade 1 Ar gas with a 99.9999 % purity still has the potential to oxidise Al. Further, even at near vacuum pressures used in vacuum casting and electron beam welding, their corresponding oxygen partial pressures (2×10^{-8} – 2×10^{-9} atm) [173] were still higher than the oxidation thresholds for Al, Cr, Fe, and Ti in Inconel 718 [172]. Wang *et al.* [45] suggested that the oxidation they found in PBF-LB could be reduced by evacuating the chamber before flooding with high purity Ar. However, the AM125 system

used in this study initially reaches near-vacuum and oxidised particles were still produced in that system, indicating that this is not an easily avoided problem. Improving the dynamics of the gas flow across the powder bed may help to reduce the levels of oxidation and reduce the quantity of spatter re-incorporated into the part.

5.2.2 Overview of spatter and process by-products with generation mechanisms

To produce the different types of particles shown in Figure 5.1 and Figure 5.2, requires a number of different formation mechanisms, hence, spatter cannot be regarded as one entity. It would also be expected that each type of spatter would have a different effect if incorporated into a part. It is proposed that the different spatter particles types identified in this work can be correlated to the spatter generation mechanisms proposed by Ly *et al.* [2] and demonstrated by Leung *et al.* [41], as depicted in Figure 5.10.

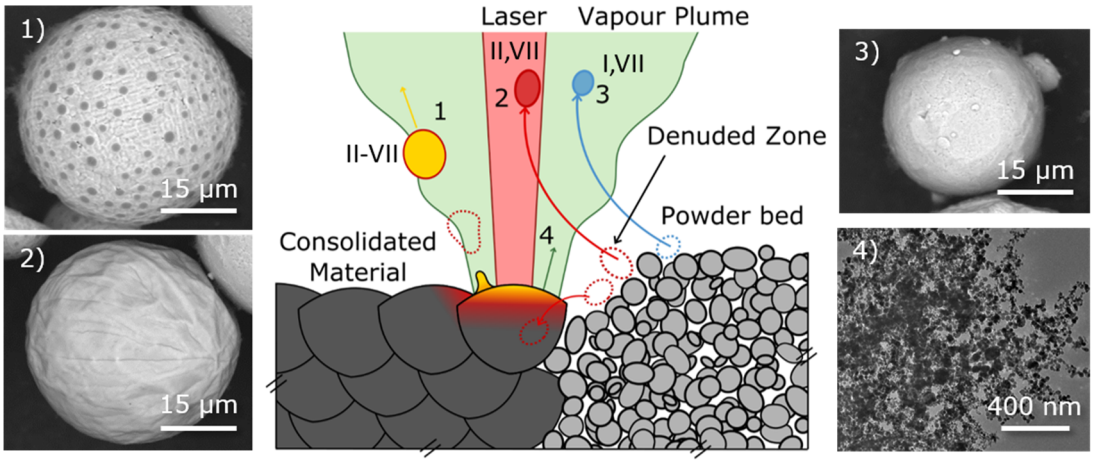

Figure 5.10 Updated schematic of laser material interaction in Fig 2.7, laser scanning direction out of page: the schematic depicts the generation of (1) melt ejection spatter, (2) hot entrained spatter, (3) cold entrained spatter, and (4) metal vapour ejection and vapour plume, with relevant examples from Fig 5.2 and classes from Table 5.1

(1) Melt ejection spatter (shown as a yellow particle in Figure 5.10) produces the particles classified as II-VI in Table 5.1. This melt ejection is a gas atomisation process occurring during the PBF-LB process: a molten particle is ejected and solidifies in an inert gas atmosphere. In our study, singular particles correlating to this type were found ranging in size from 23 – 136 µm, identified by their singularity (not agglomerates) and presence of oxides. This is in good agreement with the size of melt ejection particles simulated by Ly *et al.* [2] of ~25 – 100 µm.

The melt ejection spatter typically had a different morphology, compared to the virgin material, due to their different formation conditions, which is unique for each particle. The particles, which are of a range of sizes, may interact with different gases, vapours, and particles during its travel and solidification through the chamber, which will produce a unique formation condition and particle. The particles with oxide spots are melt ejected spatter where oxides on the surface of the melt pool remain on the surface of the material that is ejected and these are classified as type IV particles. Some particles may be ejected from regions that do not contain oxides, these may be the same size as the virgin material and classified as type II, or larger than the virgin material and classified as type III.

The formation mechanism of the spatter particles which are completely coated by oxide (type V), were harder to identify. It may be that the surface oxides on the melt pool were sufficiently large enough to cover the spatter particle when ejected. Based on the lesser thickness of the oxide coating to the spot in Figure 5.5, the coating could be an oxide film that forms on the spatter particle mid-flight. However, if this were the case it would be assumed that these particles would be much more numerous. The type VI particles which are smaller than the virgin material are formed by detonation or explosion of spatter particles which occurs mid-flight. This has been witnessed through the use of high speed cameras in this investigation and by Bidare *et al.* [40]. Some of these smaller particles may also just be smaller melt ejected particles as like other gas atomisation processes there is a large range of particle sizes produced. Melt ejection spatter can also cause agglomerates (type VII), through collision with other particles mid-flight, or if they land on the powder bed whilst they are still molten.

(2) Hot entrained spatter (shown as red particle in Figure 5.10) produces particles of type II from Table 5.1. Virgin powder particles are entrained from the powder bed and are partially or fully melted, as they pass through the laser, which may produce morphological changes as they solidify. These particles remain the same size as the virgin material. However, as these particles are entrained in the laser's wake they have a greater potential to collide with other entrained particles, producing agglomerates, sometimes larger than the virgin material. These particles would be identifiably different from the larger singular particles produced by melt ejection, as the combined hot entrained particles would not produce spherical singular droplets. However, the hot entrained particles may not be distinguishable from melt pool ejected particles which don't have oxides and are of the same size as virgin material, therefore

particles of type II are classified as being produce by both hot entrained and melt ejected spatter.

There may be some oxidation of these hot particles during flight, but it is likely to be different to the melt ejection spatter. The higher thermal mass of the melt pool allows for the larger oxides to form, as seen on the part and single scan track surface, over a longer period. These oxides then form the surface of the melt ejected spatter. Ly *et al.* [2] estimated that hot entrained spatter accounts for 60% of spatter formation, if these produced the characteristic oxides found then we would expect a much higher proportion of the spatter particles to have the oxides spots and coatings, however, as seen in Figure 5.1, the proportion found was low.

(3) Cold entrained spatter redistributes entrained particles near the laser's path and would correlate to type I spatter. These are particles of a similar size range to the virgin material and have endured only minimal or no apparent morphological change. This shows that a large proportion of what is typically considered spatter, and what was collected on the chamber side, is likely to be redistributed material from the powder bed that has gone through little change. This highlights the challenge of distinguishing between spatter and used powder when their sizes overlap, and what is actually defined as 'used' powder when it comes to recycling and powder management. Cold entrained particles will also create agglomerates if they collide with melt ejected or hot entrained spatter mid-flight, however, they are unlikely to be heated enough to create agglomerates with other cold entrained particles or the powder bed.

(4) Vaporisation of material plays a role in the ejection of spatter from the melt pool and also drives the entrainment of particles behind the laser [2]. The vaporised material forms nano-particle clusters, as shown in Figure 5.7, which coat the inside of the build chamber. These nano-particles are important in terms of health and safety surrounding PBF-LB and the use of the machines. These particles can be deposited on the optical lens and attenuate the laser, providing unwanted variations in the processing characteristics. TEM-EDS analysis of the vapour nano-particles showed vaporisation of the bulk Inconel 718 with preferential vaporisation of Cr, as can be seen in Table 5.3. This preferential vaporisation of Cr was found in PBF-EB of Inconel 718, where vaporisation rates were higher due to processing in a vacuum

[174], and confirms the hypothesis of preferential vaporisation of elements in PBF-LB proposed previously [175,176].

The spatter particle characterisation and the oxides present in the particles in this study allowed new and improved connection between the generation mechanisms of spatter and the particles produced. This was aligned with and found agreement with the simulations and high-speed videos (up to 1Mfps) conducted by Ly *et al.* [2] and Matthews *et al.* [39]. This made improvements to the characterisation of spatter types by Wang *et al.* [45] which had some drawbacks and limitations based on the spatter collection method and the high-speed camera analysis having too low frames per second (500 fps) to provide suitable detail of the formation mechanisms. As critiqued in Section 2.1.2, Wang *et al.* [45] defined spatter as the particles sieved out in the recycling of the powder (+75 µm), however, in this study it has been shown that an important proportion of spatter particles for characterisation are within the same size as the feedstock material. The four types of process by-product and spatter particles characterised here are the current best understanding of the output of the spatter process and can be used to feedback experimental data to the simulations which have been conducted for the spatter generation. As new and better techniques for simulating and analysing the melt pool are created, this proposed model will likely be improved and updated.

Although this study has helped to connect investigations into spatter generation and the particles produced, there is still much that needs to be understood with this connection. The processing parameters, and machine architecture, will affect the melt pool behaviour, vaporisation and local pressure conditions, and thermal cycling of the material which will influence the generation of spatter. Changes to the parameters could influence the proportion of the different types of spatter produced as well as the quantity of spatter. These could be used to mitigate the potential effect of spatter by reducing the quantity of detrimental particles. An area of future investigation would be to link the effect of each parameter to the melt pool formation and subsequently to the spatter formation. This could be used to produce better processing windows for material to ensure quality whilst mitigating the formation of spatter, or at least more detrimental spatter.

5.2.3 Spatter in parts

It has been discussed that these spatter particles are known, and can be seen in any build, to land back into the powder bed, where they have a chance to be incorporated into the part. Figure 5.11 shows evidence of the incorporation of these particles, particularly the effect of large particles, on the resulting parts. Figure 5.11a shows an Al and Ti oxide spot present within the part below the surface. The size and shape show the oxide spot to be similar to what was found on the surface of the spotty oxide particles classed V in Table 5.1 and Figure 5.11b shows that the oxide is comprised of Al and Ti as seen on the Inconel 718 parts and spatter. This could be an oxide spot which is remnant from one of these spatter particles being incorporated into the melt pool, and due to the higher melting point, lower absorption to infrared laser, and lower thermal conductivity, it has not been melted during processing. The oxide also may have formed at the surface of the melt pool, where it could have been ejected with a melt ejection spatter, but instead flowed deeper into the melt pool during the Marangoni convection. Either way, the inclusion is present within the part and represents a potential weakness or stress concentrator within the final component.

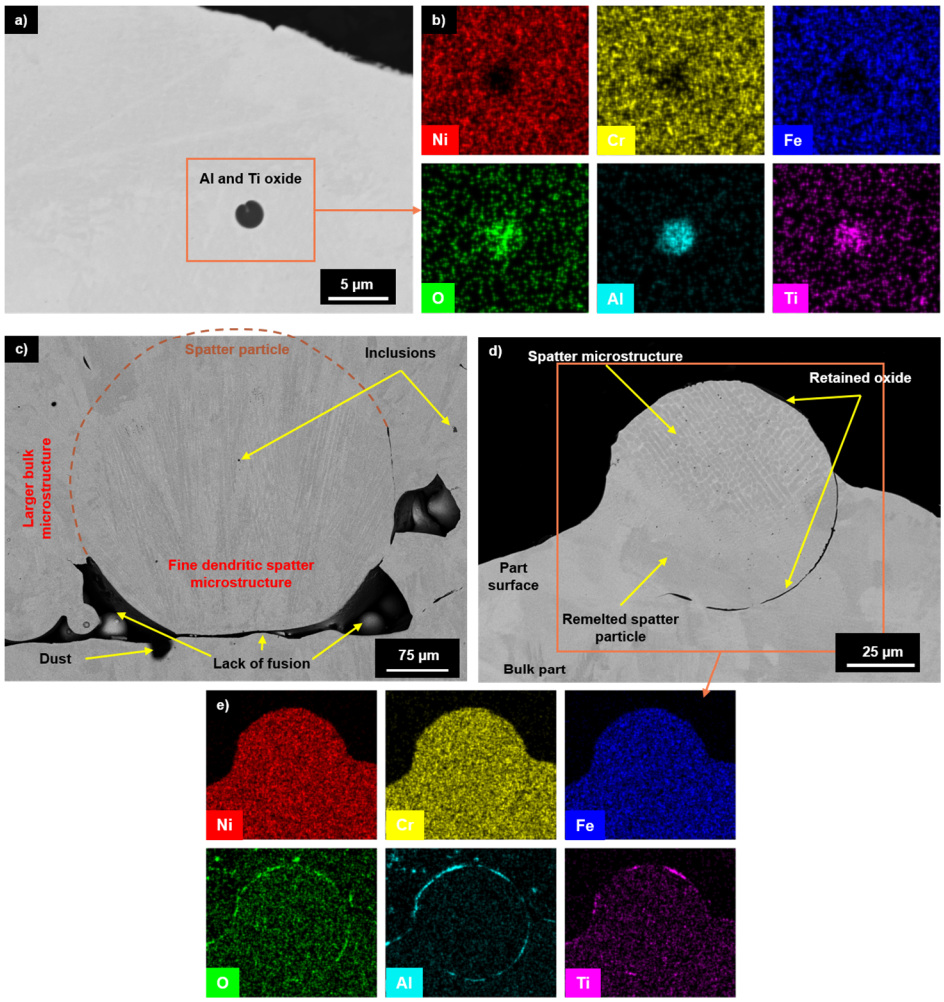

Figure 5.11 Examples of spatter particles incorporation in parts: a) Al and Ti oxide spot remaining within solidified part, b) EDS map for oxide spot, c) lack of fusion defect due to large spatter particle (estimated as 393 µm width), d) large spatter particle (87 µm width) partially fused to build surface with oxide layer retained within part, and e) EDS map showing oxide layer of spatter particle

It has been discussed about the possibility of large particles causing lack-of-fusion defects in parts as the laser is not able to penetrate or fully melt the particle, either directly or through conduction from adjacent tracks. Nguyen *et al.* [52] found evidence of these lack-of-fusion defects occurring form large spatter particles shown in . Figure 5.11c shows an example of a large spatter particle causing connected lack-of-fusion porosity in the part. The dotted orange line shows the predicted size of the large spatter particle, estimated to be 393 µm in width, and the lack-of-fusion defect beneath it 452 µm in width. It is not possible to tell how far through the particle the cross section is, based on the curvature seen in the voids beneath then it is not quite halfway through the particle, indicating the particle and void could be larger still at the widest point. Fine dendritic, directionally solidified grains can be seen within the

spatter particle, distinctly different from the larger grain texture in the bulk material, and it can be seen within the estimated boundary of the spatter particle that some remelting has occurred. The large defect caused by this particle could pose a significant issue for the performance and qualification of this part. This demonstrates that large spatter particles, likely to be less significantly affected by the gas flow, will land back in the powder bed and can cause quality issues for the build.

Figure 5.11d shows a smaller, but still large spatter particle, with a width of 87 µm partially fused to the surface. This particle could have landed and attached to the surface whilst partially molten, or more likely, was present within the surrounding powder to the melt pool and entrained into the melt pool. This mechanism was shown to occur by Matthews et al. [39], Ly et al. [2], and Bidare et al. [40] in both simulations and high speed videos of the process. As seen in Figure 5.11c, the finer, dendritic grain structure of the spatter particle can be seen in the top part of the particle and the remelted section beneath which has formed with the bulk material. Of interest within this particle is the oxide layer, seen in Figure 5.11e, which shows that the particle was likely an oxide covered particle (class V in Table 5.1) which has retained the majority of its oxide layer, even within the remelted section. This further highlights the issues these particles can cause with their inclusion in parts and difficulty in fully melting them. The particle causes a potential range of issues, the particle clearly causes a discontinuity in material and microstructure within the part, but the protrusion of a large particle can also cause streaking or ‘corn-rowing’ with recoating of subsequent layers of the powder bed as discussed in Section 2.2.2 and shown in Figure 2.30, the particle could also damage the recoater and potentially lead to failure of the build. These particles evidence a few of the issues that these spatter particles can cause within a build but are not exhaustive.

5.3 Hastelloy X

5.3.1 Spatter characteristics (HX-1)

5.3.1.1 Size and morphological characterisation of spatter

Figure 5.12 shows that the spatter particles produced from processing Hastelloy X are dissimilar to the virgin Hastelloy X particles. Like in Inconel 718, they differ in size, shape, morphology, and the presence of oxides. The BSE-SEM images show oxide formations on the surface of the particles, but formations that are quite different from that found in Inconel 718.

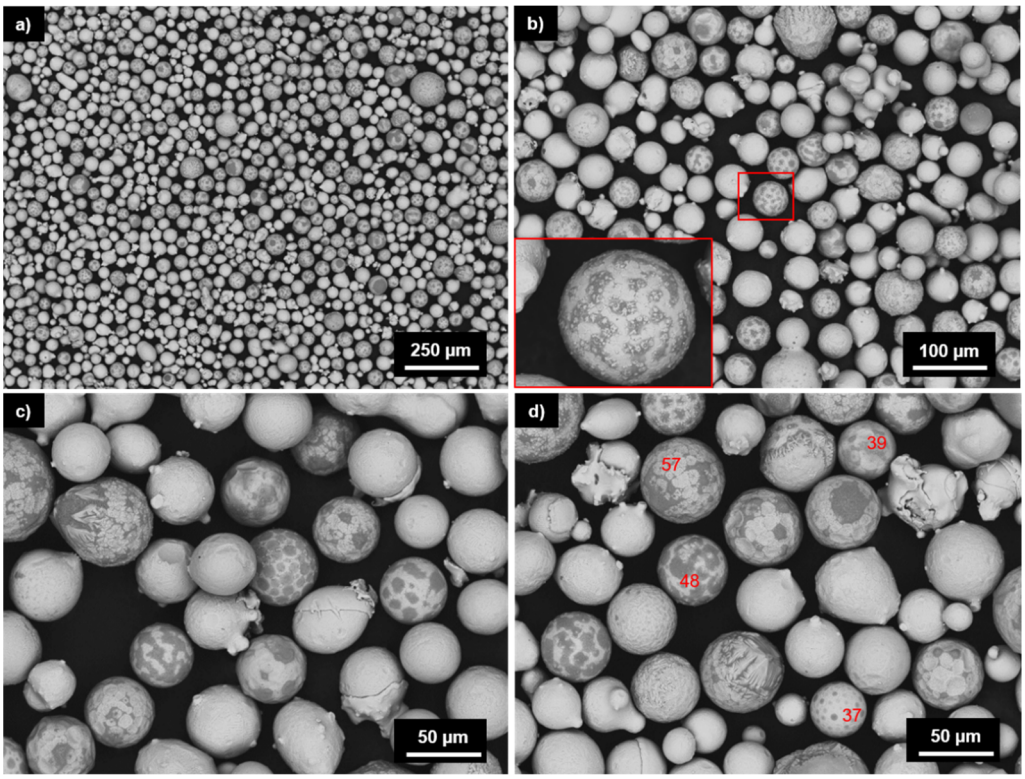

Figure 5.12 BSE-SEM micrograph of Hastelloy X spatter produced on the SLM50. d) some particles have their diameter (µm) overlaid for reference

5.3.1.2 Compositional characterisation of spatter

The spatter contained examples of the different classifications from Table 5.1. It was evident, however, that there was a different oxide regime. The Al oxide spots that comprised the majority of the oxidised particles in Inconel 718 were present, as seen in Figure 5.13, but as a

minority. No Ti was detected in the oxide spots in Hastelloy X. The quantities of these particles are explored further in Chapter 6.

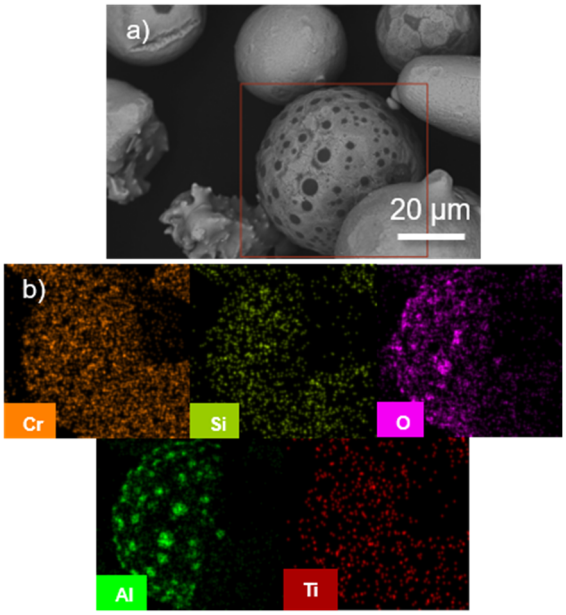

Figure 5.13 BSE-SEM and EDS map showing spatter particle with Al oxide spots

The majority of the oxidised particles were Cr and Si oxides, as shown in Figure 5.14. The Cr and Si oxide formations demonstrated a much larger range of formations compared to the Al and Ti oxide spots in Inconel 718. Most of the oxide formations appeared to have formed in situ with the bulk Hastelloy X material, creating complex surface structures. Particles such as that in Figure 5.14r-t showed an oxide that was mostly distinct from the bulk material but still had peaks and faceted features that appeared to have formed with the bulk. The formation of the particles such as Figure 5.14g could not be understood as to the mechanisms which lead to the structure formed. Particles with a full oxide coating were witnessed also, as seen in Figure 5.14k. Figure 5.14 shows in detail the range oxide formations at the surface of the particles.

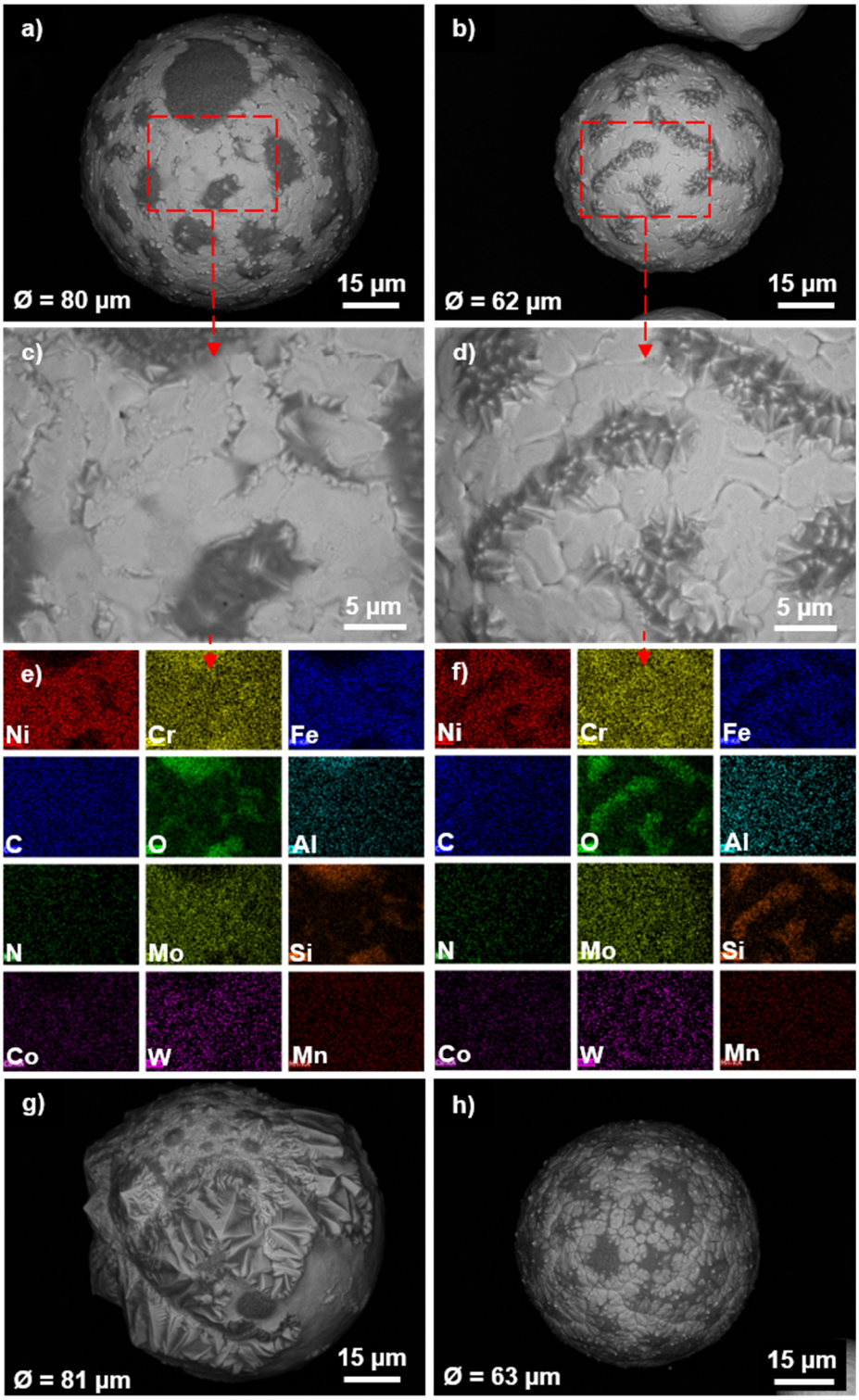

Figure 5.14-1 Range of surface oxide formations in Hastelloy X spatter from the SLM50

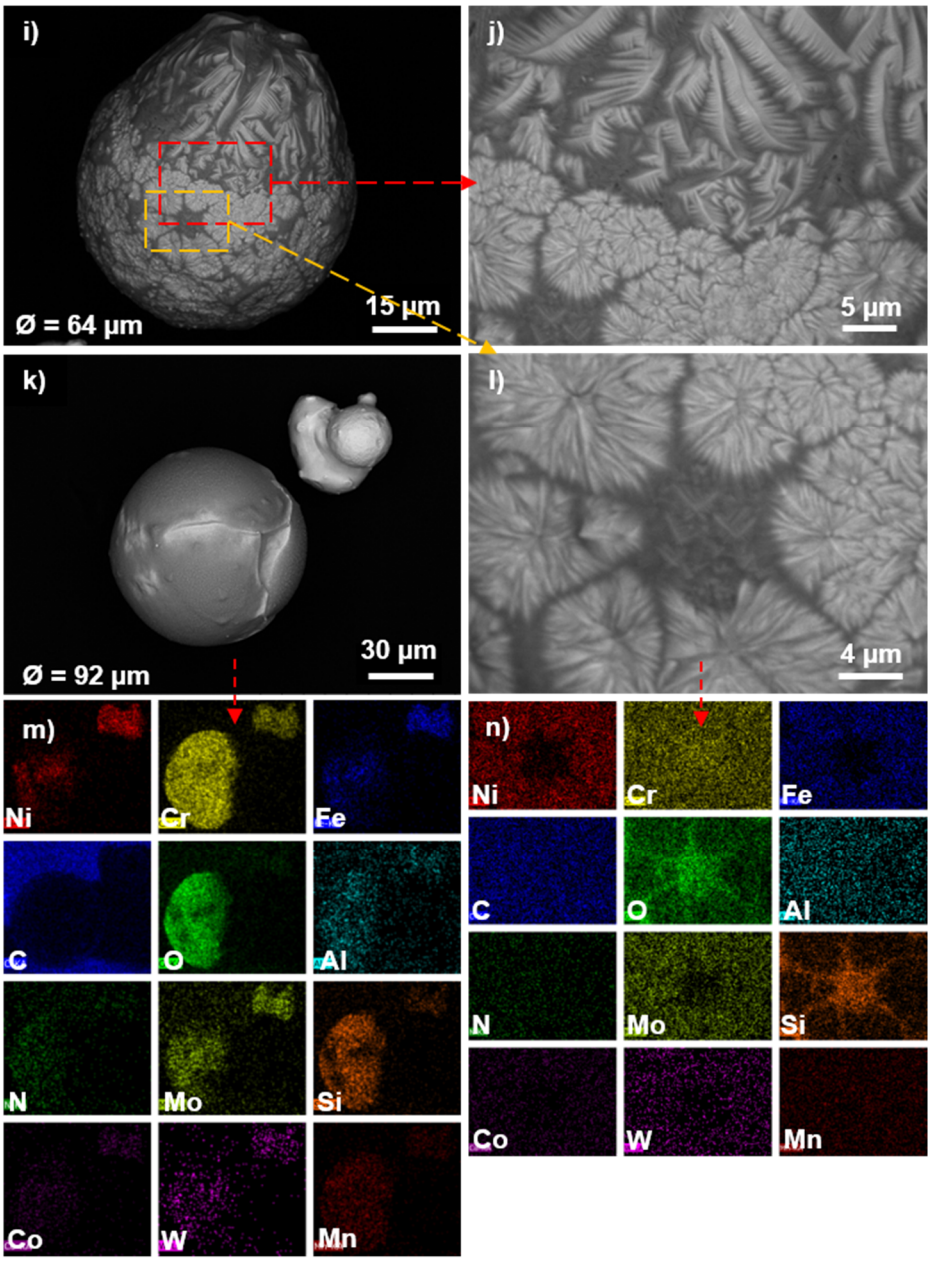

Figure 5.14-2 Range of surface oxide formations in Hastelloy X spatter from the SLM50

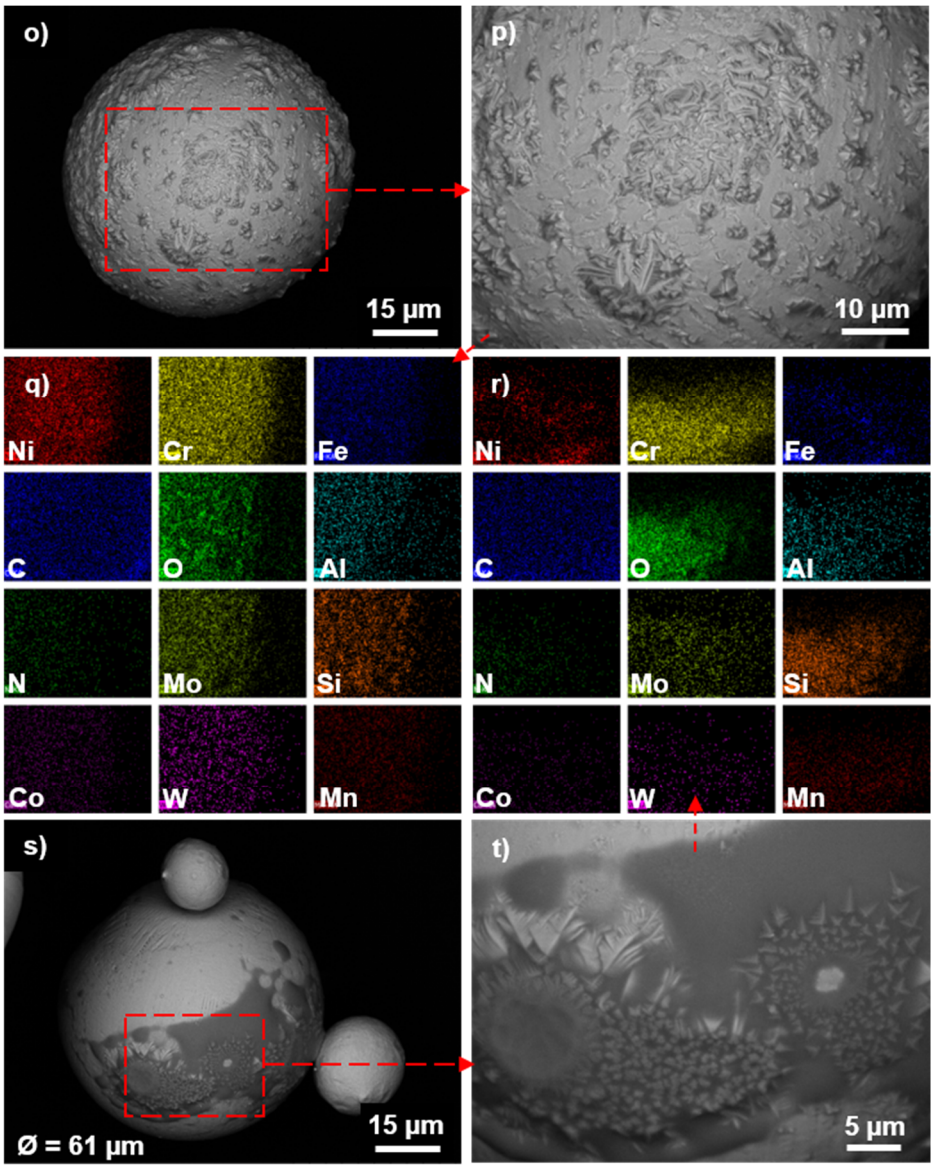

Figure 5.14-3 Range of surface oxide formations in Hastelloy X spatter from the SLM50

In situ FIB cross sectioning, shown in Figure 5.15, showed that the oxide was again a surface formation and did not form deeper within the particle. The cross section showed the region where the bulk oxide formed between oxides, in this complex surface formation. The sectioned oxide was 810 nm at its thickest for a particle with diameter 41 µm. It is envisioned that the different formations of surface oxide shown in Figure 5.14 will have different depths.

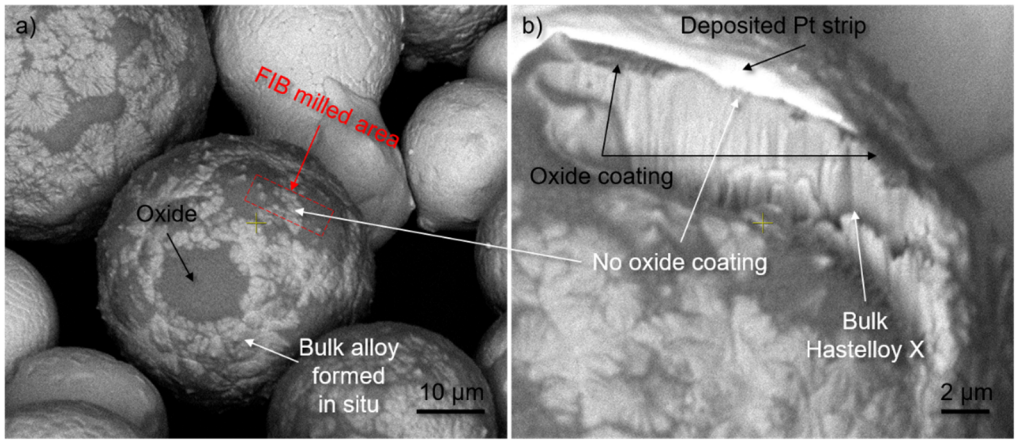

Figure 5.15 BSE-SEM micrograph of FIB milled section of oxidised Hastelloy X particle showing oxide layer above bulk Hastelloy X alloy

5.3.1.3 Origin of oxides on spatter particles

Oxides were present on the top surface of Hastelloy X cubes produced, as can be seen in Figure 5.16a. The large oxide formation in Figure 5.16c&d was 207 µm long and 47 µm wide. EDS mapping in Figure 5.16d shows the large oxide formation was mainly Cr and Si oxides and the smaller oxides were Al oxides. The cube surfaces showed a range of oxide streaks, comprised of Cr and Si, and oxide spots comprising of Al and Si, with the large Al oxides present on the surface being up to 29 µm in diameter.

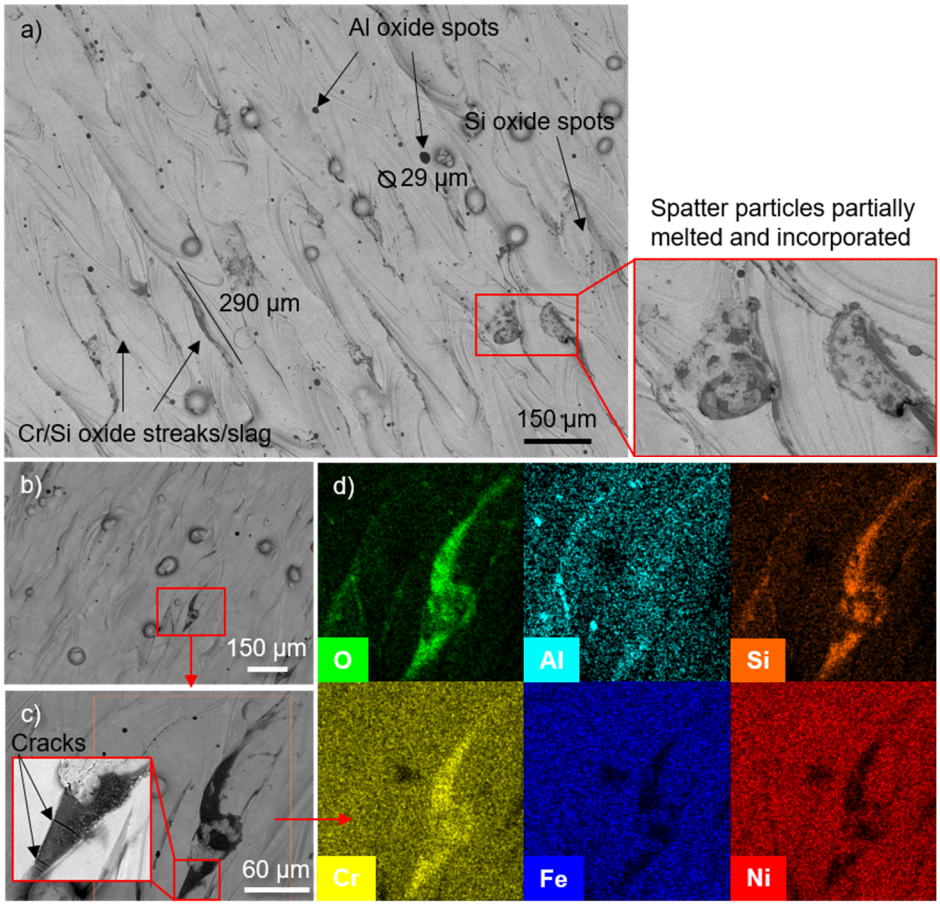

Figure 5.16 a) Stitched BSE-SEM micrographs of cube surface showing different oxide formations found on the part surface including oxides from spatter particle incorporation, b-d) surface of finished part showing large oxide with cracks, and d) EDS map showing large oxide is comprised of Cr and Si and smaller oxides are predominantly Al

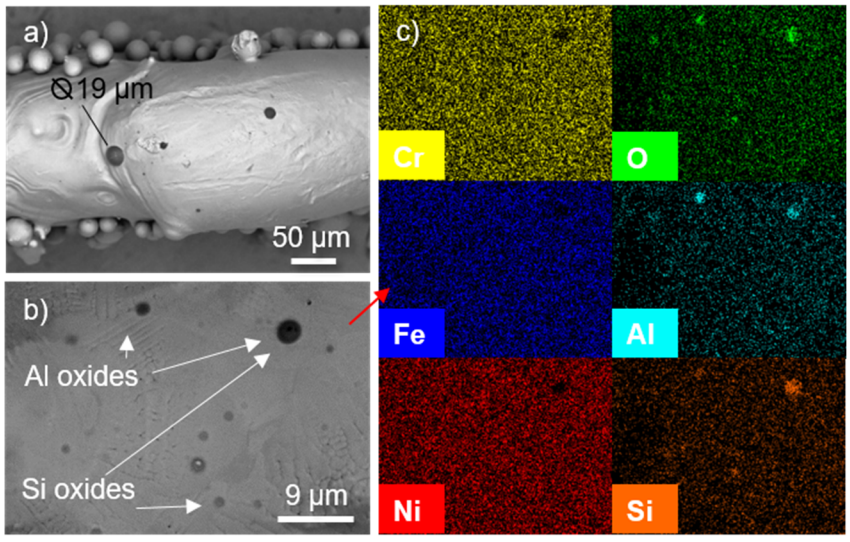

Figure 5.17 BSE-SEM micrographs and EDS maps of oxide formations on single track showing the formations of Al and Si oxides at the melt pool surface

In the single tracks, as shown in Figure 5.17, Al and Si oxides were evident but there was no clear indication of Cr oxides. The oxides formed as spots, the largest spot on the 10 mm track was 19 µm in diameter, however, oxide streaks or larger formations were not observed.

5.3.2 Oxidation in another Nickel-based superalloy (HX-1)

For Inconel 718, oxide formation was established to occur at the melt pool. Only Al and Ti oxides were present and remained at the surface of the part and weld tracks. These would have been mixed into the part during solidification due to Marangoni effects, or ejected as spatter where they then remained on the surface of the spatter particle; these spatter particles could then be incorporated back into the part if landing on an unmelted section of the powder bed. For Hastelloy X, the oxidation witnessed at the single track, cube surface, and spatter particles had separate characteristics. The single track showed Al and Si oxide spots along its length indicating, again, that oxidation initiated at the melt pool level. The larger oxide formations on the cube surface, with larger Si and Cr oxides formed as a slag, indicated the initial oxides may have acted as nucleation for larger oxides to develop over many rasters and layers, as the one witnessed in Figure 5.16c. The presence of Al and Si oxides at the single track, and lack of Cr oxides, was likely due to the higher affinity of Al and then Si for Oxygen, as indicated in the Ellingham diagram [170], shown in Figure 5.9. The difference between the oxide species on the single track and cube surface may be due to lower Al and Si concentrations in the alloy, 0.1 and 0.5 wt% respectively, and higher affinity for Oxygen meaning they were depleted preferentially, followed by the development of more Cr rich oxides. The Inconel 718 contained 0.44 and 0.9 wt% Al and Ti respectively, and Al_2O_3 formed preferentially in oxides with TiO_2 forming in greater concentration in larger oxides. With Hastelloy X, the 0.1 wt% Al oxidised preferentially at the melt pool surface, after this the 0.5 wt% Si and then the 21.5 wt% Cr dominate oxide formation. This shows that even small concentrations of these elements with high oxidation potential can play an important role and will oxidise in O_2 concentrations <0.2% during PBF-LB processing.

The oxide formation in the spatter particles appears to be of a different nature to that observed in the melt pool and on the surface of parts. There were some oxides on the cube surface that appear similar to those from the spatter particle, however, these were likely

attributable to spatter particle inclusion, as evidenced by Figure 5.16a inset. The spatter particles were covered by unique oxide formations that appeared different to those generally observed on the tracks and cubes. Oxides, formed on the tracks and cubes, tended to appear in isolation. These appeared in the form of spots or slag, or occasionally as a streak through the material, with a small amount of mixing, but were mostly separate from the bulk matrix material. The oxide formation on the spatter particles, however, appeared to form in situ with the bulk matrix of the particle, as evidenced by the formations seen in Figure 5.14, and seemed to be a more complex mechanism in the formation of the particle surface. The oxide formations in the spatter were of a wide variety of shape, size, structure, and covering, which may have been due to the unique thermal history of each particle, and potentially, factors such as inhomogeneous chemical composition in the melt pool [177]. The difference between the spatter and melt pool oxides could have been due to the higher cooling rate of the spatter particles from their lower mass and high surface area, leading to the formation of more crystalline and faceted features. As they mostly formed as single spherical particles larger than the input powder particles, these were most likely produced via melt ejection [178], with the elements with high oxygen affinity bonding with Oxygen present in the chamber atmosphere and shielding gas. However, further investigation is required to fully understand the mechanisms of oxide formation in spatter, particularly the conditions which allow the variety of structures produced that are so different to those formed in the melt pool.

It could be possible, that in some alloy systems or applications the oxide formations could be beneficial. If the distribution and sizes of the oxides could be controlled they could be processed as an integral part of the system. With the additive nature of the process the oxides could possibly controlled throughout the part [179]. These could be used to create oxide dispersion strengthened alloys, which are applied to some Nickel-based superalloys, to increase the mechanical performance of the parts produced. Alternatively, in some alloy systems, such as some Al alloys, the oxides could possibly be used as seed crystals to manipulate the microstructure in components. Much more would need to be understood about the formation of the oxides in the PBF-LB process to establish if they could be controlled before this could be usefully investigated.

5.3.3 The effect of micro-alloying elements on oxide formation – HX-2 vs HX-1

The reduction in Si content in the HX-2 was found to cause different oxide formation compared to the HX-1 composition presented in Section 5.3. The spatter particles produced can be seen in Figure 5.18. The reduction in Si content lead the oxide formation to be driven by Ti and Al instead of Si and Cr. The oxide formations in the spatter resembled the oxide spots observed in the Inconel 718 spatter, and the EDS results showed that they were also predominantly Ti and Al spots. The highly featured and faceted Si and Cr oxides, depicted in Figure 5.10 and Figure 5.12, which were characteristic of the HX-1 alloy composition were not present in the spatter from the HX-2 composition. Evidence of spatter particles with Al and Ti spots were found in the HX-1 spatter, however, these were of a significantly lower proportion compared to the Si and Cr oxidised particles. In comparison with the oxidised particles in Inconel 718, the number of Ti and Al oxide spots per particle were visually less numerous in the HX-2 material.

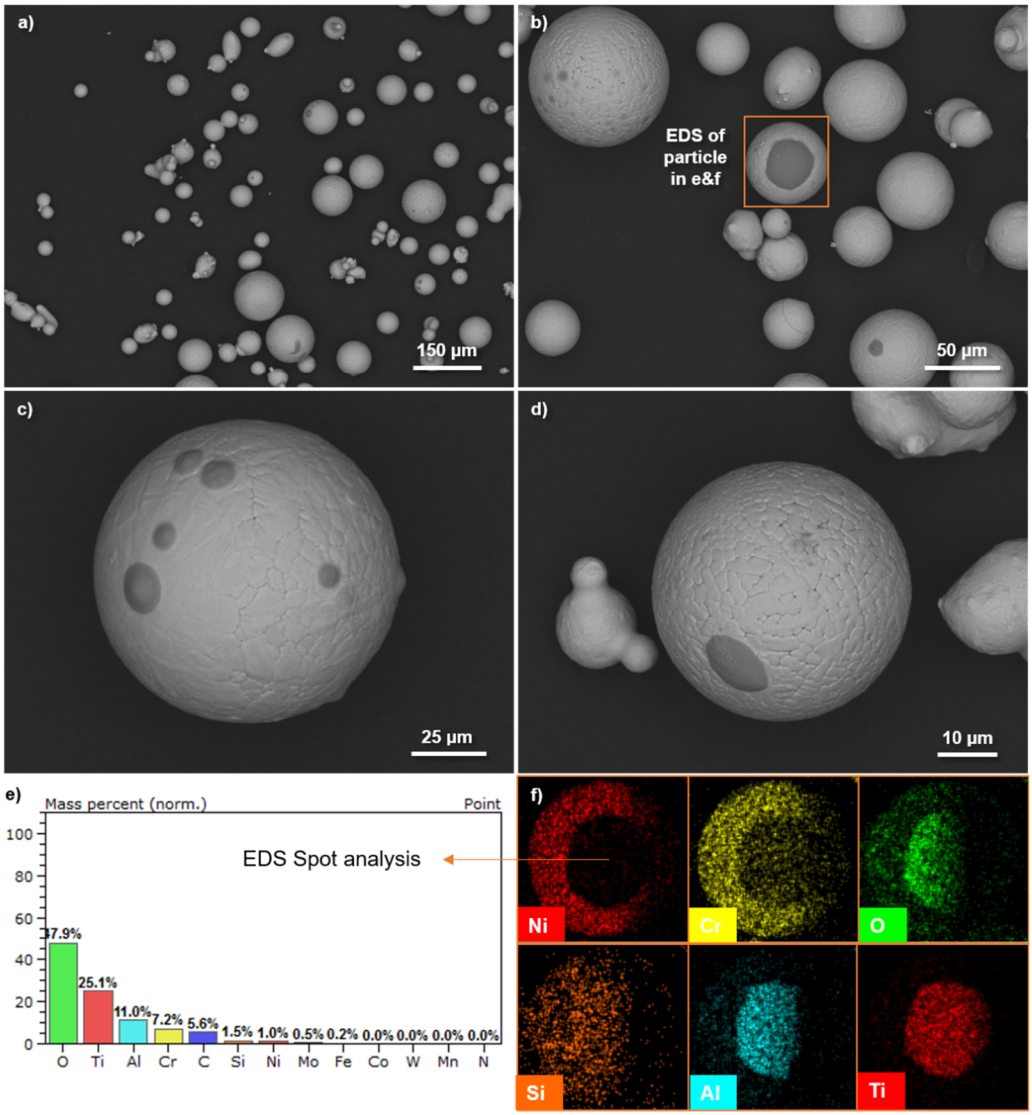

Figure 5.18 Ti and Al oxide formation in the spatter produced from the Hastelloy X-2 alloy with reduced Si content

The Ti and Al oxides were present at the top surface of the parts, as seen in Figure 5.19a&b. The oxides were formed at the melt pool from the single track investigation as found in Chapter 5. Figure 5.19c-f shows the oxide formation at the melt pool appears to be the same oxide formations present on the spatter particle. This is important in comparison with the HX-1 oxide formation where Al and Si oxides were found at the melt pool and larger Cr and Si and smaller Al oxides at the part surface. The HX-1 also had different oxide formations at the spatter particle surface compared to the part surface. For HX-2 the oxide formation appeared to be dominated by the Ti and Al content with the oxide formation on all of the spatter, part, and single track material being of the same nature. As found in the Inconel 718 and HX-1

materials, the change from the single track oxides to the oxides at the part surface indicated continued growth of a proportion of the oxides forming as slag over progressive layers and re-melting in the PBF-LB process. The development of these appears linked to the Maragoni flows in the melt pool and the larger oxides can be seen as high aspect ratio streaks along the boundaries between adjacent scan tracks, as shown in Figure 5.8a for Inconel 718, Figure 5.16a for HX-1, Figure 5.19a for HX-2.

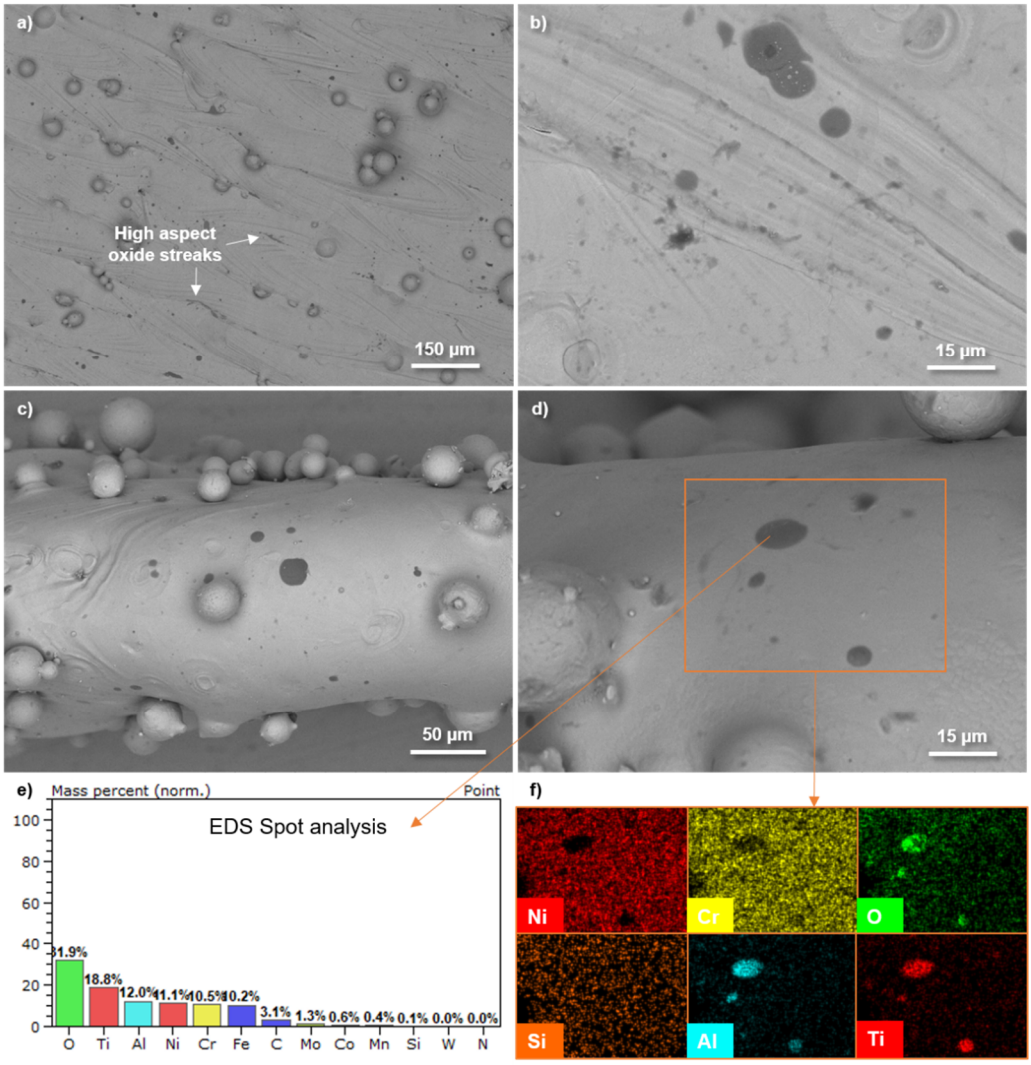

Figure 5.19 Ti and Al oxide formation on the part surface (a&b) and single track (c-f) produced from the Hastelloy X-2 alloy with reduced Si content

From the investigations of oxide formation in PBF-LB processed Inconel 718, HX-1, and HX-2 it appears that the content of micro-alloying elements influences the oxide formation in PBF-LB. The higher content of Al and Ti in Inconel 718 produced a greater quantity of Al and Ti

oxides compared to Hastelloy X. As far as could be established, for Hastelloy X the content of Si played an important role in the oxide formation and it appears there is a threshold for the Si content with which the oxidation is dominated by a particularly element. Ti has a similar but slightly higher oxidation potential compared to Si, as shown in the Ellingham diagram in Figure 5.9, and it is presumed that as the Si content nears the Ti content there is a transition in the dominant oxide formation in the process. The significantly higher oxidation potential of Al leads to its oxide formation preferentially before the other elements, as seen in Inconel 718 with Al forming ahead of the Ti, despite almost twice the quantity of Ti. With the smaller quantity of Al in the Hastelloy X alloys it allows the greater oxidation of other elements. So whilst Al oxides were present in the HX-1, the greater proportion of oxidation occurred from Si and Cr, and importantly the larger oxides (<160 µm) which will likely have a more significant detrimental effect on part performance, and in HX-2 the Ti in the alloy dominates. The processing of HX-2 showed that the Si oxidation can be avoided, however, the formation of oxides could not be completely avoided with the current alloys and processing.

It is important to note that both compositions HX-1 and HX-2 are within the tolerances for Hastelloy X, according to AMS 5390 [167] for investment casting for high-performance applications, shown in Table 4.4. This shows that these conventional standards may not be suitable to the PBF-LB process, and for Hastelloy X tighter tolerances are required in the alloy composition. The results of the oxide formation in all the alloys investigated also indicates the need for alloy design specifically for AM. In their reviews of the state-of-the-art, Sames *et al.* [62] and Collins *et al.* [180] suggested that tailored alloys are required for the future of PBF-LB as the solidification mechanisms due to the very high cooling rate and successive re-melting are not appropriate for many conventional alloys which were designed for different processes. For instance, the investment casting which the AMS 5390 standard relates to may typically have cooling rates in the order of 10s of ˚C/min compared to the $>10^6$ ˚C/s which occurs in the PBF-LB process [181]. Another indicator that new alloys are required are that many of these alloys and standards were designed long before AM and PBF-LB were recognised manufacturing techniques. The Inconel family of alloys were developed to support the original jet engine, the Whittle engine, in the 1940s and the original AMS 5390 standard for Hastelloy X was published in 1955 [182].

5.4 Summary

This chapter aimed to characterise the spatter and oxide formations in PBF-LB of Inconel 718 and Hastelloy X and link them to their generation mechanisms. This was achieved through classification of the particles by their size, shape, morphology, and presence of oxides in comparison with the virgin material. The classifications found agreement with the spatter generation mechanisms proposed in literature. The oxide formations in the material were shown to initiate at the melt pool in the single track investigations and formed as spots and larger slag formations at the surface of the final parts which formed the surface of some spatter particles. Oxidation in parts and spatter was found to occur in Hastelloy X, driven by the Si content in the alloy instead of the Al and Ti in Inconel 718. The Hastelloy X found unique oxide formations in the spatter particles in comparison to the single tracks and the part surface. The reduction in Si content in HX-2 showed that the oxide formations on the part and spatter transitioned from being predominantly Si and Cr to being driven by Ti and Al, identifying the significance of the micro-alloying elements for oxide formation in PBF-LB processing. This established that the spatter and oxidation is unique to each alloy in PBF-LB. The key findings from the chapter are:

- Spatter particles were characterised and shown to be dissimilar to the virgin material in size, shape, morphology, and the presence of oxides
- Spatter particles were classified based on identifiers from their size, shape, morphology, and the presence of oxides which allow them to be linked to cold-entrainment, hot-entrainment, and melt ejection generation mechanisms and provide a greater understanding of spatter in PBF-LB
- Spatter was analysed from four different PBF-LB systems and two different powder suppliers to ensure findings for spatter and oxidation are general. The general characteristics of spatter are that it is of a larger size range (span and particle size), different morphology, and increased proportion of agglomerates compared to the virgin material, and that for these Nickel-based superalloys, oxide formations are present within a proportion of the spatter
- The spatter shown had a size range of 1 - 567 µm, with oxidised particles ranging from 23 - 567 µm. The larger particles have the potential to cause issues within the build,

whilst a proportion of the spatter is within the size specification for PBF-LB powders and cannot be removed from the powder during recycling, potentially causing issues for future builds

- It was shown that some spatter particles generated from the melt pool included oxides which formed at the melt pool surface, and for Inconel 718 the oxides formed are Al_2O_3 and TiO_2
- Vaporisation of Inconel 718 produced nano-particle clusters which had evidence of preferential vaporisation of Cr
- Evidence of the effect of spatter particles on the part were shown with lack-of-fusion defects, part discontinuity, oxide inclusions, and potential effects on the recoater and spreading of subsequent powder layers
- A standard commercial PBF-LB Hastelloy X (HX-1) with composition within AMS 5390 standards was processed and the spatter was shown to produce different oxides to Inconel 718 due to different constituent elements
- HX-1 showed initial oxidation of Al and Si from the alloy in single tracks, before Si and Cr dominate oxide formation in production of cubes, due to their higher wt% in the alloy
- HX-1 oxide formation in melt ejection spatter particles was mostly Si and Cr oxides but was different to that seen on the part surface, whereas in Inconel 718 the oxides appear to be the same as oxides on the surface. The Hastelloy X spatter particles formed a range of complex surface oxides in situ with the bulk alloy
- The processing of HX-2 alloy, and comparison with HX-1, found that the oxide formation in PBF-LB processing of Hastelloy X is influenced by the Si content. The reduction in Si content in HX-2 lead to Ti dominating the oxide formation and producing similar formations to that observed in Inconel 718 but in lower levels. The results indicated the importance of micro-alloying elements on the oxide regimes and the need for tighter tolerance and new standards for PBF-LB alloys

It has been established that spatter generated during processing produces particles which can vary significantly from the virgin powder input to the process. Due to the large mass and/or presence of oxides, many of these particles have the potential to cause defects in the parts from these particles landing on sections of the powder bed yet to be scanned and causing

lack-of-fusion or inclusions from oxides. Therefore, it is important to understand what proportion of these particles have detrimental qualities to the process. It also cannot be assumed that the spatter from each PBF-LB system and alloy is the same and variations between machines are important quality considerations for the process. Chapter 6 furthers the understanding of the spatter produced through characterisation and analysis of the spatter produced from the four PBF-LB systems and for Hastelloy X, with further investigation into alloy composition effects on the formation of oxides and spatter in Hastelloy X.

Chapter 6 Oxide and spatter generation between different machines and materials

Chapter 5 showed that the spatter generated in Inconel 718 and Hastelloy X was different from the virgin material. It was established that the oxidation of these alloys is a material issue that occurs across PBF-LB systems and different powders. The changes in the particles of the spatter material make a proportion of the distribution out-of-specification from the virgin material. This is important to understand for quality control in the PBF-LB process. In this chapter the change in the powder is analysed in greater detail using optical particle metrics to compare the spatter generated in different PBF-LB architecture, between alloys, and for reprocessing of the spatter powder. The powders are compared for their particle shape and size, their chemical composition, and for the proportion of oxidised particles. The shape and size is measured using a commercial automated particle shape and size analyser and the oxidised particles are identified using a combination of SEM and image analysis techniques. For Inconel 718, spatter which is generated by processing spatter powder is analysed to understand the evolution of the material through re-processing. The results from the chapter are important for understanding the change in powder produced in the spatter powder, the variation due to machine architecture, and the ramifications that spatter and oxidised powder can have for recycling of powders in the PBF-LB process.

6.1 Methods

The spatter collection method and analysis for this chapter are the same as for Chapter 5, and the subsequent chapters, that was detailed in Section 3.3.1.1. Further methods specific to this chapter are detailed in this section. Spatter was collected from all the machines discussed in Chapter 5: the SLM50, AM125, SLM125, and LMF1000, which were presented in Section 3.2.

A proportion of spatter particles generated during processing land back in the powder bed and are reprocessed or are recycled for subsequent uses in the system. In both these scenarios the spatter powder may be processed and used to generate more spatter powder. To assess the evolution of the powder and spatter through reuse, spatter powder was used as feedstock

for a PBF-LB build and the spatter from this collected and analysed. For convenience, this spatter generated from spatter feedstock powder is referred to as spatter^2.To achieve the quantity of powder required for a build, the spatter powder used for the build was a blend of spatter from each of the machines obtained over a number of builds. All of the spatter powder collected had been generated from the processing of virgin material, therefore the build was only the second use of the powder and represented the worst case scenario of powder evolution in two uses.

6.1.1 Shape and size analysis

The PSD of the spatter and virgin material presented in Chapter 5 were obtained using the Mastersizer 3000 laser diffraction system. The laser diffraction system is particularly useful for producing size information for large numbers of particles, as discussed in Section 2.2.2, with the merits of different particle measurement systems. However, laser diffraction provides only approximated 2D size information (and subsequent approximated 3D volume) about the particles. The laser diffraction 2D measurements are an approximation to a circular equivalent (CE), the equivalent diameter of a circle with the same area as the measured particle, and it provides information for the powder as a whole entity. In this study, static optical imaging techniques are used. In the static optical imaging method, the size and shape parameters of each individual particle are provided and these parameters can then be assessed for the whole or sub-sections of the powder. As an alternative, static optical imaging still only provides 2D information for the particles (and approximated 3D volume), but each particle is individually captured and more data, with regards to shape parameters and filtering capabilities, can be extracted from them.

Figure 6.1a shows the capture of particles and parameters obtained from static optical imaging of particles. The particle size can be described by the particles minimum and maximum width, the CE diameter, and the spherical equivalent (SE) volume which can be seen for an example particle in Figure 6.1a. The SE is the equivalent volume for a sphere with the diameter of the CE. As discussed in Section 2.2.2, the CE is commonly used and accepted in industry, as laser diffraction is most commonly used to establish the PSD of powders. However, the accuracy of the technique is reduced as the particles become less spherical.

Such as for elongated particles, where the minimum width may allow the particle to pass through a sieve mesh, however, the CE classes the particle larger than this. A variety of shape parameters can be used to describe the particles including the circularity, elongation, aspect ratio, and convexity. Malvern Instruments, in a white paper, analysed multiple powder feedstocks for PBF-EB from different suppliers and manufacturing processes to assess their shape characteristics on their suitability for PBF processes [71]. They used dynamic powder flow properties of basic flow energy and packing density on the FT4 Rheometer, which Clayton and Deffley found to be the current best metrics for powder quality for AM processes [183]. The white paper showed that across the shape parameters the circularity of the particles and the proportion of highly spherical particles (compared to slightly and non-spherical particles) in the powder, along with the particle size, had the greatest effect on powder performance. They showed a strong correlation (R^2 = 0.9885) between the circularity and the basic flow energy and packing density. Therefore, for the study of the spatter particles in this investigation the circularity shape parameter was investigated for the three levels used in the white paper: highly-spherical (Circularity ≥ 0.95), slightly-spherical (0.95 > Circularity ≥ 0.85), and non-spherical (0.85 > Circularity). Examples of the particles classified by these parameters from the spatter powder can be seen in Figure 6.1b-d. The effect of the shape in the powder system is a result of irregular particles leading to increased particle friction and mechanical interlocking, which both decrease flowability, and consequently, packing density [81].

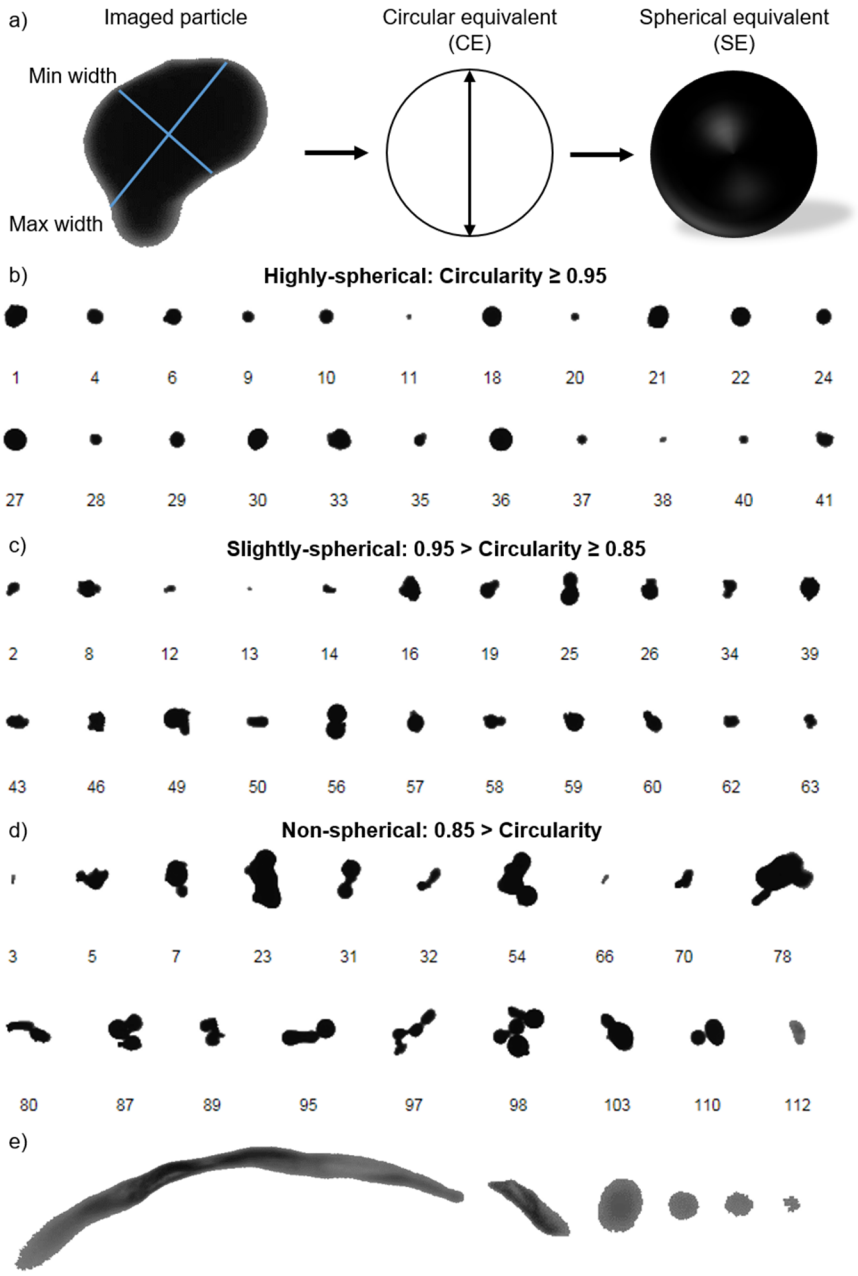

Figure 6.1 a) Particle capture and parameters from optical particle imaging, and SLM125 Inconel 718 spatter particles representing particles identified and classified as b) highly-spherical, c) slightly-spherical, and d) non-spherical, based on the circularity of the particles, and e) fibre and dust particles filtered out from the analysis

The Malvern Morphologi G3 was used for the static optical imaging of the particles. This system used compressed air to disperse a sample of particles over a glass plate. The glass plate was under lit to produce a silhouette of the particles and then the microscope scanned over the area, imaging and measuring the particles. Filters were used in the software to exclude artefacts which were not the intended powder particles and improve the quality of the data

obtained from the machine. These are commonly fibres and dust which may be in the air and land on the glass plate. As the particles are backlit, the fibre and dust can be distinguished as the light passes through these light particles and not through the metal particles as can be seen from the example of these particles in Figure 6.1e. Because of this they produced a different mean intensity. The mean intensity is the average grey value for all pixels in a particle, where 0 is black and 255 is white. These dust particles were excluded using a filter for mean intensity of particles >100. Particles below 5 µm CE were also excluded as due to their low intensity they were difficult to distinguish from artefacts. The Standard Operating Procedure (SOP) parameters used for the Morphologi G3 for this study are included in Appendix A1.4.

An advantage of using an automated static optical image analyser such as the Morphologi G3 the analysis of larger quantities of particles which reduced the effect of anomalies which may be detected. For the samples analysed for this investigation the average number of particles measured for each sample was 3284, with a minimum of 2045 and maximum of 5221. To provide the best measurement accuracy, the microscope was focussed on a particle of 40 µm and all samples imaged with the same focus. This will lead to some error in particle dimensions of particles much smaller and much larger than this size, however, this is minor and is a compromise of particle analysis techniques. This focus level allows best results for the size categories used for analysis of 15, 30, 45, 53, and 63 µm which is the focus of the study. It must also be noted that the proportions categorised for the sizes, in comparison with sieving, are indicative and not absolute as there is no guarantee that a particle with a min width or CE within a size range will actually pass through a sieve, as discussed previously. The Morphologi G3 system was used to analyse the spatter produced from the SLM50, AM125, and SLM125 machines and for the virgin Inconel 718 powder to allow comparison of the change in the powder and generated by the machines. The Morphologi G3 was no longer accessible when the spatter was collected from the LMF1000 and therefore was not analysed. The particles were assessed for their size and shape based on circularity as discussed.

6.1.2 Oxidised powder analysis

The chemical composition of the powders was assessed to detect any change in the constituent elements of the alloys and the pickup of Oxygen and Nitrogen. This was achieved using ICP-OES for the constituent elements of the alloys and the pickup of Oxygen and Nitrogen was measured using Inert Gas Fusion Infrared and Thermal Conductivity Detection on a LECO ONH836 (LECO Corporation, USA). These measurements were outsourced and analysis conducted by the author.

Chapter 5 identified that a proportion of the spatter particles produced during processing have a level of oxides present on the surface. To investigate the quantity of these particles containing oxides (referred to hereon as 'oxidised particles') a combination of BSE-SEM and image analysis was developed in order to identify oxidised particles, determine their size, and count them. This was not possible via other methods as only BSE-SEM imaging produces different contrast for elemental composition which makes the oxides detectable.

A MATLAB script was developed for this study with the aid of Duncan Hickman at the Centre for Additive Manufacturing, University of Nottingham. The script is provided in Appendix A.1.1. A flowchart of the process is shown in Figure 6.2. There are three key sections to the program, firstly the auto identification of all the particles in the image, secondly the auto identification of the 'spotty' particles, and finally manual correction of the spotty particles and disqualified particles.

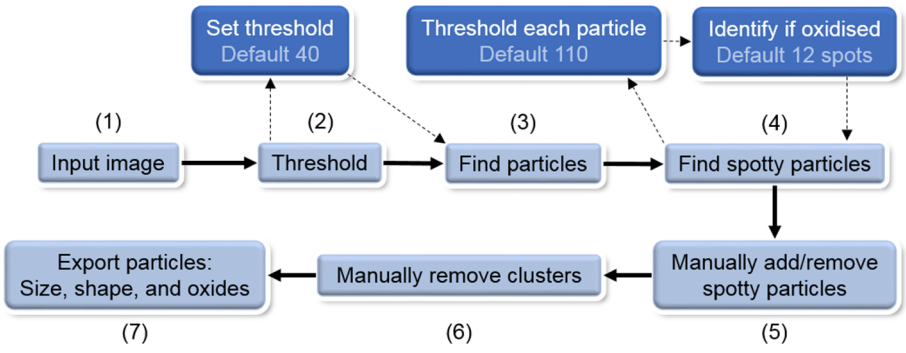

Figure 6.2 Flow chart of the process undertaken in the image analysis for oxidised particles

For imaging in the SEM, the sampling techniques from Section 3.3.1.1 were used to ensure the most representative sample possible was investigated. The particles were dispersed on a Carbon tab for imaging by dropping them from height (~10 cm) which allowed the particles to scatter over the tab. This was the most effective way to produce a random distribution of particles with appropriate spacing between particles for effective image analysis. 10 random sections were imaged at 150x magnification, which produced an average of 1809 particles assessed per sample. Best measures were taken to reduce errors from sampling and by using as much sample as possible, however, only a limited quantity of spatter was produced to be used for a range of analysis. Therefore, the results provide the best representation of the sample possible but must be taken with appreciation of the limitations.

In order to identify particles, a threshold was applied to the image. Images were loaded individually and the threshold parameters (default setting 40) were used to threshold the greyscale image between the Carbon tab (to black) and the spatter particles (to white), seen in Figure 6.3a&b. The identification of all the particles was done using the in-built MATLAB function *regionprops* which identified each separate region, in this case particle, in the image and properties for each region are returned [184]. Properties returned included a unique region number and the major and minor axis lengths of the particle contained within that region.

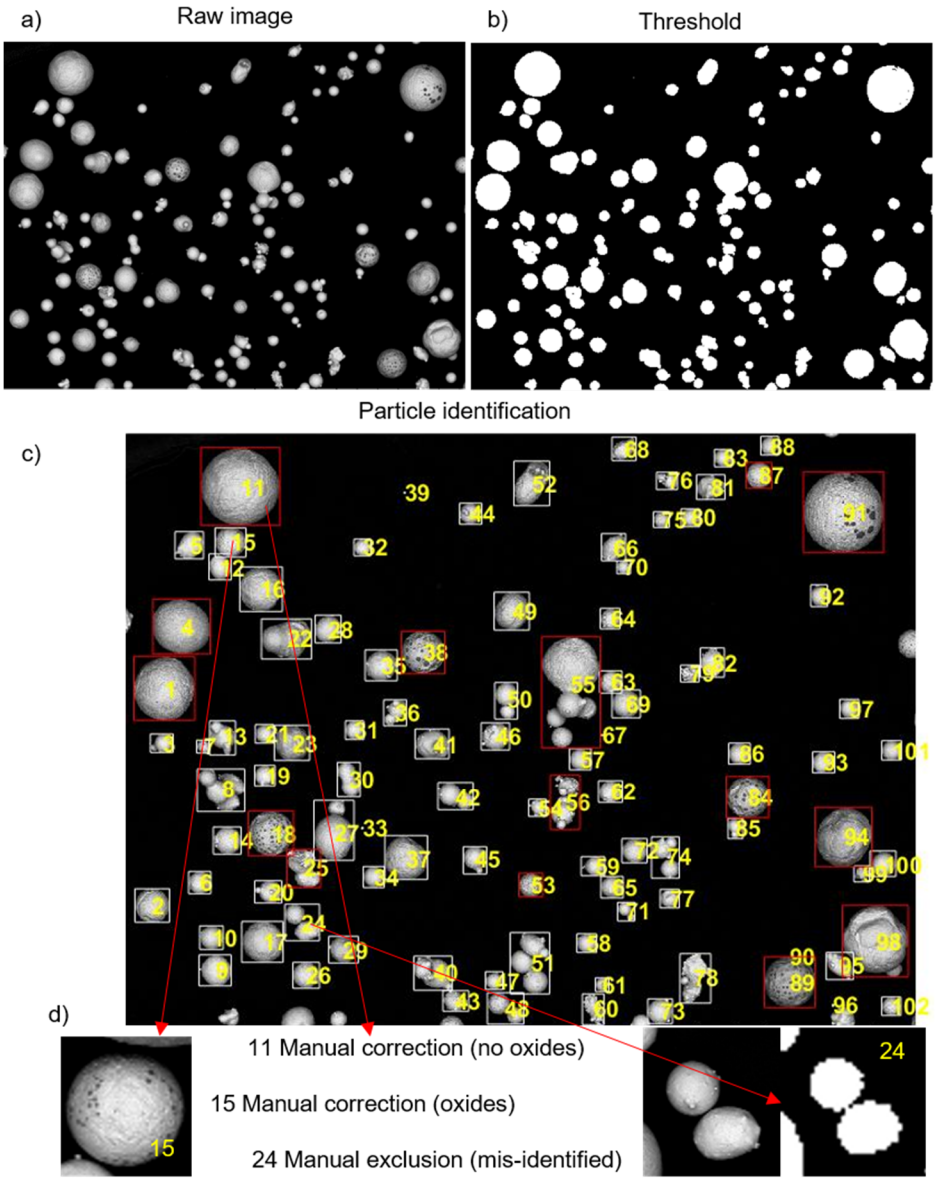

Figure 6.3 Summary of the image analysis from: (a) raw image, (b) thresholding with the default setting of 40, and (c) auto particle identification and classification using the default setting of 110, with identified oxidised particles given a red box. (d) Demonstrates examples of correction of the particle classification estimation and threshold anomalies

Next, each particle was assessed to estimate if it contained oxides or not. In the previous step, r*egionprops* effectively created an individual image for each particle identified, with the original grayscale and the threshold version available. For each particle, the original grayscale image of the particle was thresholded at a higher level (default setting 110), which revealed the oxides spots (as black) on the particle. The *regionprops* function was used for each particle image to assess the quantity of objects, or oxide spots, detected. If the particle contained

more than the defined number of spots (default 12) then it was classified as an oxidised or 'spotty' (as described in script in Appendix A.1.1) particle.

Particles could then be manually identified or corrected if the program had misidentified it. Examples of these can be seen in Figure 6.3d. This could occur if the particle had less than the defined minimum number of spots; or if other factors like the morphology or clustering caused the thresholding to produce objects in the particle which were not due to oxide spots. Particles which had not been separated by the thresholding process and would skew the results, were also manually removed. Noise in the greyscale image was occasionally misidentified as small particles due to the thresholding process. To remove the noise, particles were excluded with ≤25 pixels, which equated to a CE diameter of 5 µm and allowed greater comparison with the Morphologi G3 results. The thresholding was set by the user for each image as the brightness and contrast from the SEM images varied between imaging of samples. This introduces some user bias and error in the results however this is minimal in effecting the results and is explored in Appendix A1.2. The default settings were set for the SLM50 set of images which were first analysed and then adjusted for each subsequent set of images.

The result of the MATLAB process was a table containing a range of information about the particles in the image included in the quantification process. This included the number of particles present, the size of all particles, and which of those particles were oxidised. A summary of the process is shown in Figure 6.3.

6.2 Comparison of spatter generation between different PBF-LB systems

As with the results from the Mastersizer 3000 in Figure 5.3, the size analysis from the Morphologi G3 showed the spatter produced from each machine was larger than the virgin powder but showed a proportion of overlap within the original size specification of the powder. The data from the Morphologi is not fitted to a distribution and therefore the data looks more irregular, as seen in Figure 6.4a. The virgin material specification is 15 - 45 µm, but it can be seen that there is a proportion of the powder sized larger than this from the Morphologi G3 measurements. The table in Figure 6.4 shows the proportion of each powder larger than specified common sieve sizes (45, 53, and 63 µm) with the particles measured for

their CE and minimum width for number and volume distributions. The CE diameter produces an overestimation of the particle size (unless purely spherical), the advantage of the optical imaging and image analysis techniques is that they provide more information about the particle size, particularly the particle width. As discussed in Section 2.2.2, the particle width can be a more useful measure of the particle size, especially for comparison with sieving, as more elongated particles will be classed over size by the CE estimated diameter whilst the minimum width of the particle may allow it to pass through the sieve mesh if the orientation aligns. This can be seen in the difference between the CE and minimum width results in the table in Figure 6.4b. Despite this, the minimum width of the virgin powder still shows a proportion of the particle sized over 45 µm. This could be due to agglomeration of the particles which remained despite the compressed gas dispersion, or particles in contact in the image, which are identified as a single particle. This shows that the Morphologi G3 results may still oversize particles in comparison with sieving, again demonstrating the difficulty with comparing particle measurement techniques, and the results must be taken with this consideration. For the basis of the rest of the analysis the particles are measured by minimum width to allow the analysis to be more relevant for sieving and recycling in the PBF-LB process.

a)

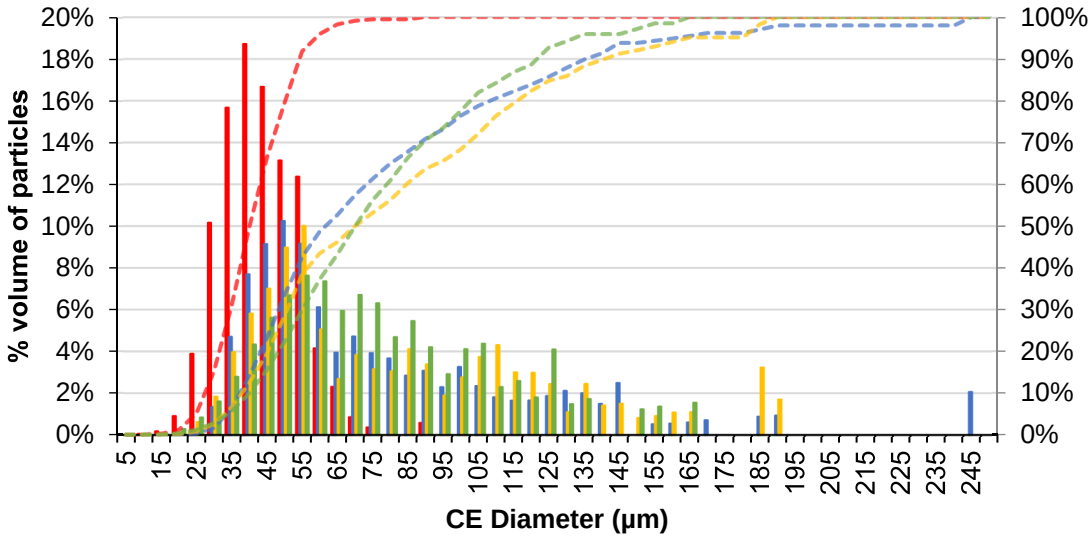

b)

	CE	By number		→ SE	By volume	
	>45 µm	>53 µm	>63 µm	>45 µm	>53 µm	>63 µm
Virgin powder	10.0%	2.4%	0.3%	33.7%	11.6%	2.8%
SLM50 spatter	35.4%	17.1%	8.8%	76.9%	60.6%	49.1%
AM125 spatter	33.4%	16.3%	8.5%	80.6%	65.4%	54.7%
SLM125 spatter	35.1%	22.2%	12.3%	84.5%	73.0%	58.7%

	Min width	By number		→ SE	By volume	
	>45 µm	>53 µm	>63 µm	>45 µm	>53 µm	>63 µm
Virgin powder	6.8%	0.9%	0.0%	23.8%	4.9%	0.6%
SLM50 spatter	27.1%	11.3%	5.8%	69.0%	51.5%	41.4%
AM125 spatter	27.2%	12.1%	7.2%	74.8%	59.3%	51.2%
SLM125 spatter	28.9%	16.5%	8.9%	78.3%	63.6%	49.5%

Figure 6.4 a) Volume based PSD of particles in virgin Supplier 1 Inconel 718 powder and spatter powder from different PBF-LB systems and b) table of the proportion of particles out-of-specification for different sieve sizes measured for CE and minimum width and their volumetric equivalents

The table in Figure 6.4b shows the proportion of the spatter from each machine, showing the SLM50 to have the smallest proportion of large particles greater than 45, 53, and 63 µm and 8-12% less than the SLM125, by volume. The AM125 spatter generally had lower proportions than the SLM125. This is perhaps due to the larger laser spot size, 80 µm for the LSM125 compared to 40 µm for the AM125 and SLM50, although as this parameter is doubled it may

be expected that it would have a larger affect. Assessing the shape characteristics of the powder, Figure 6.5a shows the proportion of particles from each powder that are highly-spherical, slightly-spherical, and undesirable non-spherical particles. This showed a major difference between the virgin material and spatter particles, with over 51.1% of the spatter on average being non-spherical compared to the virgin material with 16.4%. Similarly the spatter had a lower proportion of highly and slightly-spherical particles. This indicates the detrimental properties and contribution the spatter particles make to the powder system inside PBF-LB machines.

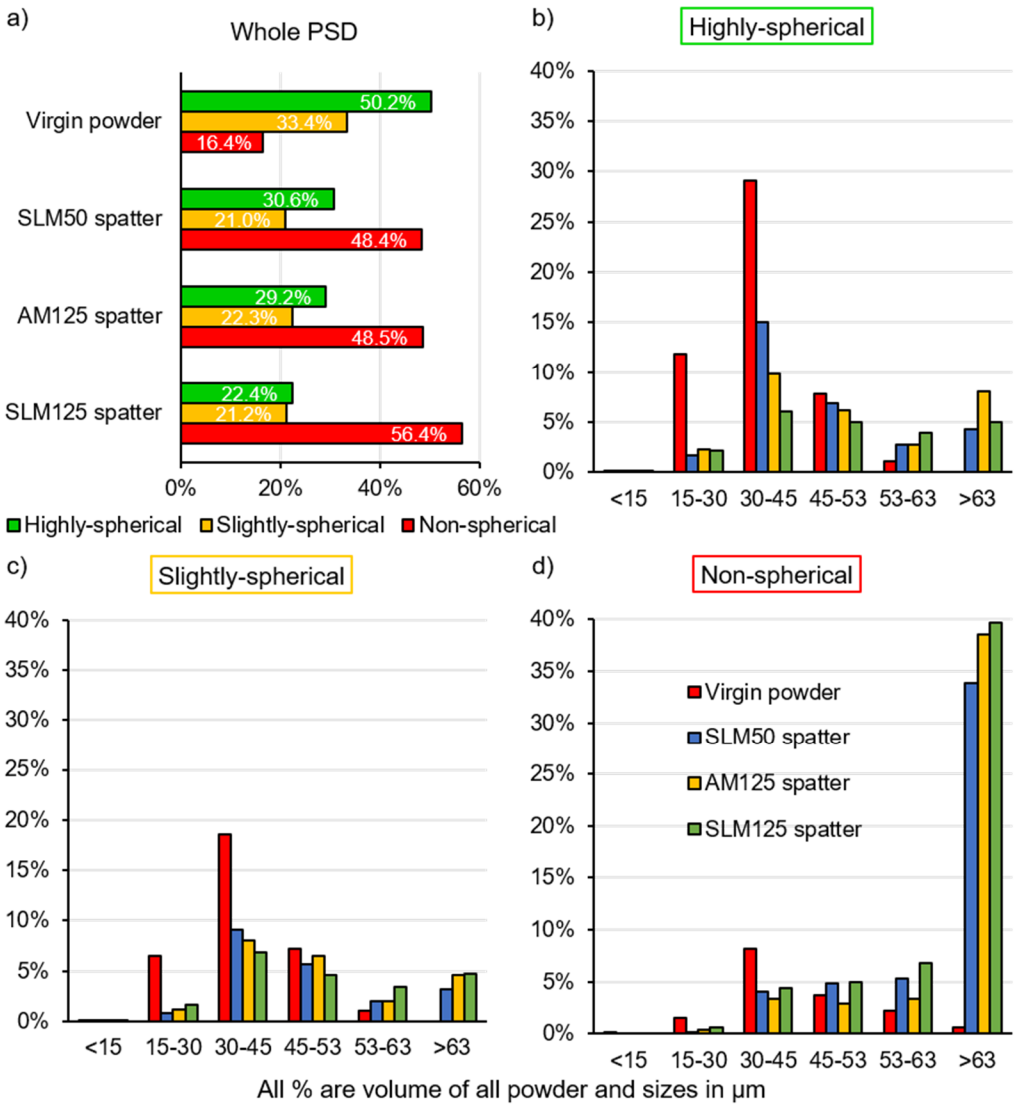

Figure 6.5 Comparisons of the circularities of the virgin and spatter powder and the circularity related to the size of the powder, assessed for the 15 µm bins up to 45 µm and then for sieve sizes 53 µm and 63 µm. The legend in (d) relates also to (b) and (c)

Analysing the shape characteristics of the powder with regards to the particles size provides useful understanding for the recycling of the powders. Figure 6.5b-d separates the particle circularity into size bins which shows the proportion of particles for different sieve sizes and for within the 0 - 45 µm range. This shows that by far the largest proportion of the spatter powder, which were non-spherical, was larger than 63 µm. Importantly, this indicates that the majority of the most detrimental powder is sieved out when the powder is sieved to this size or below. From the trends in the data, the virgin material shows a normal distribution for all three shape categories over the size distribution, indicating a greater consistency in powder particle shape. In comparison, the spatter particles show the same trend with highly and slightly-spherical particles over the size range but with a second peak in the over 63 µm category. This is due to this size bin covering a much larger size range and these particles having a much greater proportion of the overall volume of the powder. This is in agreement with findings of large spherical particles from Chapter 5 which were linked to be the melt ejection spatter and often containing oxides. However, the increase in the proportion for these highly and slightly-spherical particles are substantially less than found in the non-spherical spatter particle greater than 63 µm, indicating a significant proportion of irregular and agglomerated spatter.

Between the spatter produced in the different systems the SLM50 shows the highest proportion of highly-spherical particles with 30.6%, particularly between 30 - 45 µm, and also with the lowest proportion of non-spherical particles with 48.4%, along with the AM125. However, despite the same proportion of non-spherical particles overall, the AM125 had the lowest proportion in each bin size below 63 µm indicating a lower inclusion with recycling. The results indicated that for recycling at each of the three sizes the SLM50 spatter would have the least detriment to the powder characteristics with a higher proportion of spherical particles overall, followed by spatter from the AM125, and both of these would have less effect than the spatter produced from the SLM125. The SLM125 produced 8% more non-spherical particles than the AM125 and SLM50, and had a higher level in each size category, indicating it could have the greatest detrimental effect to recycling at each sieve size. As with all machines however, by far the largest proportion (39.7%) was >63 µm so would not be so detrimental for subsequent builds when sieved to conventional sieve sizes. It is important to note that 33 - 40% of the non-spherical spatter, and an additional 7 - 12% of spherical and slightly-spherical spatter, was >63 µm and so would be removed in the recycling step.

6.2.1 Discussion

The combined size/shape results could have ramifications for acceptable levels of how much spatter could be generated and recycled in a build, the number of times the powder could be recycled from a build, and the size to which the powder should be sieved for recycling, which have not yet been defined for the process. Combining the effect of the levels of these particles produced in a build and remaining in the powder could allow these results to be used to design quality control metrics for powder systems in PBF-LB. For instance, the results shown indicate that the greatest reduction in particle shape effects occur from sieving the powder at 63 µm and the particles in the 45 and 53 µm range could be acceptable to the process. This could influence the sieve size for recycling, increasing the yield in the recycling process and reducing costs. It could be established that for the large scale manufacture of a component it would be more cost effective to use the AM125 over the same sized SLM125 as more builds could be completed before there are any potential negative effects on part quality due to powder. The results could also influence the proportion of virgin powder that could be mixed with the recycled powder to bring the used powder back to specification. However, Clayton and Deffley [183] found that the blending of the powder did not always improve the dynamic flow properties of AM powders. Implications of practices such as blending require further investigation.

The spatter generated and collected was influenced by the architecture in the PBF-LB systems. The smaller and less irregular spatter in the SLM50 and AM125 is likely due to the smaller laser spot size in these systems. The smaller spots size would have produced a smaller melt pool. This smaller melt pool has less molten material to eject and likely a higher surface tension to reduce the size and quantity of spatter ejected. However, the change between the spatter profiles is not that pronounced considering the SLM125 spot size is twice as large. The energy density for the SLM125 was 0.50 $J.mm^{-2}$, less than the SLM50 of 0.57 $J.mm^{-2}$ and similar to the AM125 with 0.49 $J.mm^{-2}$. The majority of the large non-spherical particles could be agglomerations caused by the hot particle entrainment spatter as opposed to the melt ejection spatter. The profile of the AM125 spatter could be influence by the pulsed laser used in this system, compared to the continuous lasers used in the SLM50 and SLM125. Mumtaz and Hopkinson [58] showed that the recoil pressure and spatter ejection could be influenced

by the pulse shaping of the laser but comparison between the different laser systems for spatter ejection has not been established.

The gas flow may also influence the results presented. Whilst the gas flow is unlikely to have a major effect on the generation of spatter in the system it has a significant effect on the redistribution of the spatter throughout the chamber as shown by Anwar & Pham [50] and Ferrar *et al.* [185]. As the spatter for the study is collected by the side of the powder bed by the gas outlet it will be influenced by what spatter is redistributed there by the gas flow. Anwar & Pham [50] showed that the gas flow does not blow the large particles as far at the smaller spatter particles and Ferrar *et al.* [185] showed that optimisation of the gas flow can clear more spatter from the powder bed zone. Therefore, if one PBF-LB system has a more optimised gas flow system it may have redistributed a different size fraction to this area, or, it may have redistributed the same size distribution, but in higher quantities. This aspect of the process needs further investigation. As the rest of the spatter lands in the powder bed, it would require an experimental setup, such as that used by Lutter-Günther *et al.* [46], and discussed in Section 2.2.2, which lays a mask over the powder bed to collect the spatter which lands on it.

6.3 Spatter composition and quantity of oxidised particles

The results in Section 5.2 observed that preferential vaporisation of Cr occurred in PBF-LB processing of Inconel 718, as concluded in PBF-EB [174] and proposed by previous studies [175,176]. Whilst an increase of Cr content in the deposited metal vapour suggested that this may lead to a change in the composition of the alloy through processing, this was not indicated in the compositional analysis of the spatter produced. The Cr content was found to increase from the virgin material to the spatter, as shown in Table 6.1. The largest differences in the major elements were an increase in Fe and decrease in Ni, the source of which was not found. For the oxidising elements, Al and Ti, no trend was observed across the spatter produced from different machines, or from the spatter[2]. However, it is worth noting that the ICP-OES method measures the Al and Ti content contained within the oxide present at the surface of the spatter powder. Therefore, it may still be the case that there is less present in the bulk alloy. The greatest change was noted in the Ti content of the AM125 spatter with an

increase from 0.9 to 1.31%. From noting that the oxide content is included in the measurement it could be that a greater proportion of Ti in the alloy formed as oxide which was transferred to the surface of the spatter. However, this was not particularly noticed in the investigation of this powder and there was nothing else to indicate why this would be.

Table 6.1 Chemistry of Inconel 718 as virgin powder and from the spatter powder produced from different machines. All values are in wt % and all composition are measured via ICP-OES apart from O and N which are measure via LECO inert gas fusion

Element	Virgin 718	SLM50	AM125	SLM125	LMF1000	Spatter^2
Ni	54.25	51.89	52.0199	52.62	52.10	52.01
Cr	19.04	19.75	19.54	19.12	19.55	19.56
Fe	17.17	18.62	18.36	18.61	18.61	18.67
Nb+Ta	5.13	5.26	5.18	5.20	5.24	5.26
Mo	3.07	3.15	3.1	3.13	3.13	3.13
Ti	0.90	0.86	1.31	0.92	0.91	0.90
Al	0.44	0.47	0.49	0.40	0.46	0.47
O	0.0124	0.0594	0.0309	0.0296	0.0682	0.1025
N	0.0060	0.0244	0.0149	0.0317	0.0220	0.0382

With regards to the Oxygen and Nitrogen content it was found that pickup of these interstitial elements occurs through processing in PBF-LB and there is variation depending on the system used. Figure 6.6 plots the O and N content for the spatter produced in each system in relation to the virgin material. The LMF1000 produced the greatest O pickup along with the SLM50, with almost twice the O content of the powder produced in the AM125 and SLM125. This is despite the SLM50 rated to operate at <0.2% O_2 and the LMF1000 to <0.1%. The O pickup in the SLM125 was slightly lower than in the AM125, despite the AM125 having a pre-vacuum step designed to minimise the O content in the build chamber. This indicates that this step may be unnecessary in consideration of time and cost for the process.

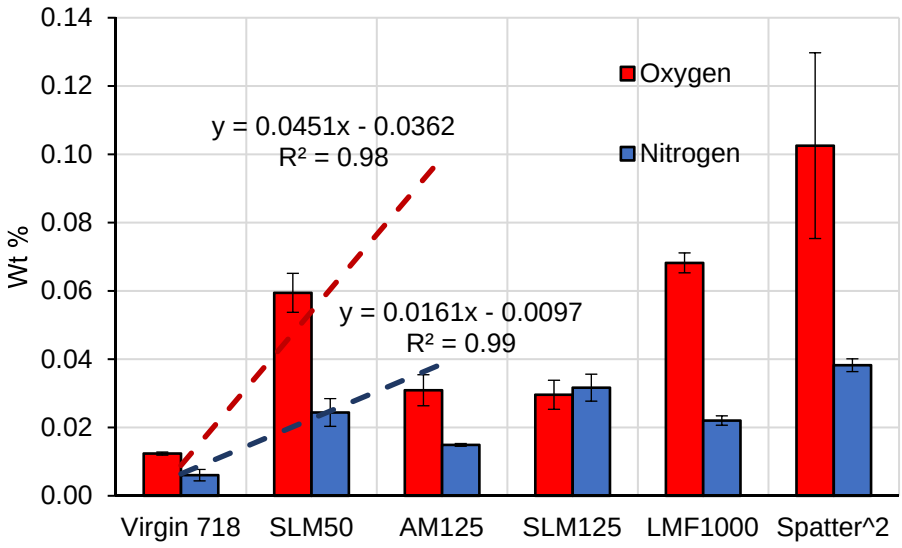

Figure 6.6 Plot of the Oxygen and Nitrogen content in the spatter powder produced in each PBF-LB system and for the re-processed spatter with error bars representing the standard error. The dotted lines represent the linear trend of O and N pickup from subsequent processing of the spatter based on the spatter^2 representing two process cycles and the average across the machines representing one process cycle. Therefore, the x-variable represents number of processing cycle sand the y-variable the O and N content

The pickup of N appeared to show a correlation with the pickup of O. However, the SLM125 which produced the lowest O pick-up also produced the highest N pickup. Whereas for all the other systems the N content remained at least half of the O content. Re-processing the material lead to continued increase in the pickup of these elements as shown by the spatter^2 result. It is also shown that there was good fit (R^2 = 0.98 and 0.99) for the linear trends for O and N pickup from virgin to the spatter^2 powder, using the average O and N across each machine (this was used as the powder processed for spatter^2 was a blend of the spatter powders). This trend is plotted by the dashed line from the virgin material. This indicated a continued trend of increased O and N pickup over repeated processing of the spatter powder.

As discussed in Chapter 5, the oxidised spatter particles produced during a build are likely to be detrimental to the parts produced and would certainly not be desired in any virgin material. Using the combined BSE-SEM and image analysis technique allowed an assessment of the proportion and size of these oxidised particles. Figure 6.7 shows the number and volume proportion of oxidised particles, overlaid with the O content of the powder, across each machine and for Hastelloy X. The plot appears to show a trend between the O content and the proportion of oxidised particles produced in each machine. It was expected that the O

content should correlate with the proportion of oxidised particles and gives more confidence in the analysis. The trend does not correlate as well with the volume proportion of the oxidised particles, with the AM125 and LMF1000 machines showing minimal difference between the volume proportions compared to the O content. The pronounced difference between the number and volume proportions, for example in the AM125, suggests that the oxidised particles in these systems are much larger than in the other systems. The oxidised particles in the Hastelloy X show an even greater increase from the number to volume distribution which will be important for the sieving and recycling of these particles.

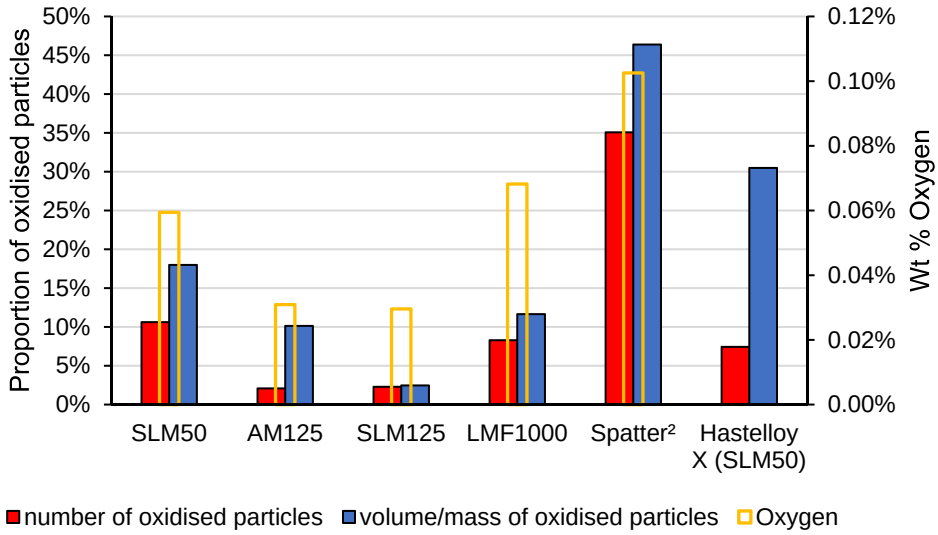

Figure 6.7 The proportion of oxidised particles in the spatter produced by different PBF-LB systems, in reprocessed spatter, and in Hastelloy X. The Oxygen content of the powders are overlaid, however, there is no Oxygen content data for Hastelloy X

From Figure 6.5 we know that sieving to 45, 53, and 63 µm removes most of the undesirable non-spherical particles from each machine, Figure 6.8a provides results for the proportion of undesirable oxidised particles which would likely be removed using different sieve sizes. This shows, as indicated by the difference with the number and volume proportions in Figure 6.7, that the majority of the AM125 oxidised particles are larger and would be sieved out in the recycling process (maximum of <3.5% retained by the 63 µm). The spatter[2] and Hastelloy X spatter showed a similar high proportion of oxidised particles removed from all sieve sizes. The spatter from the LMF1000, SLM50, and SLM125 showed lower proportions of the oxidised particles removed via the sieve sizes and a more pronounced change in the proportions between each size. This implies that the oxidised particles were across a wider size distribution

in these systems. These large particles are still relevant for inclusion in the powder bed and part during the build. The large size of these particles combined with the oxides increase the likelihood of the particles not being melted by the laser and causing lack-of-fusion defects.

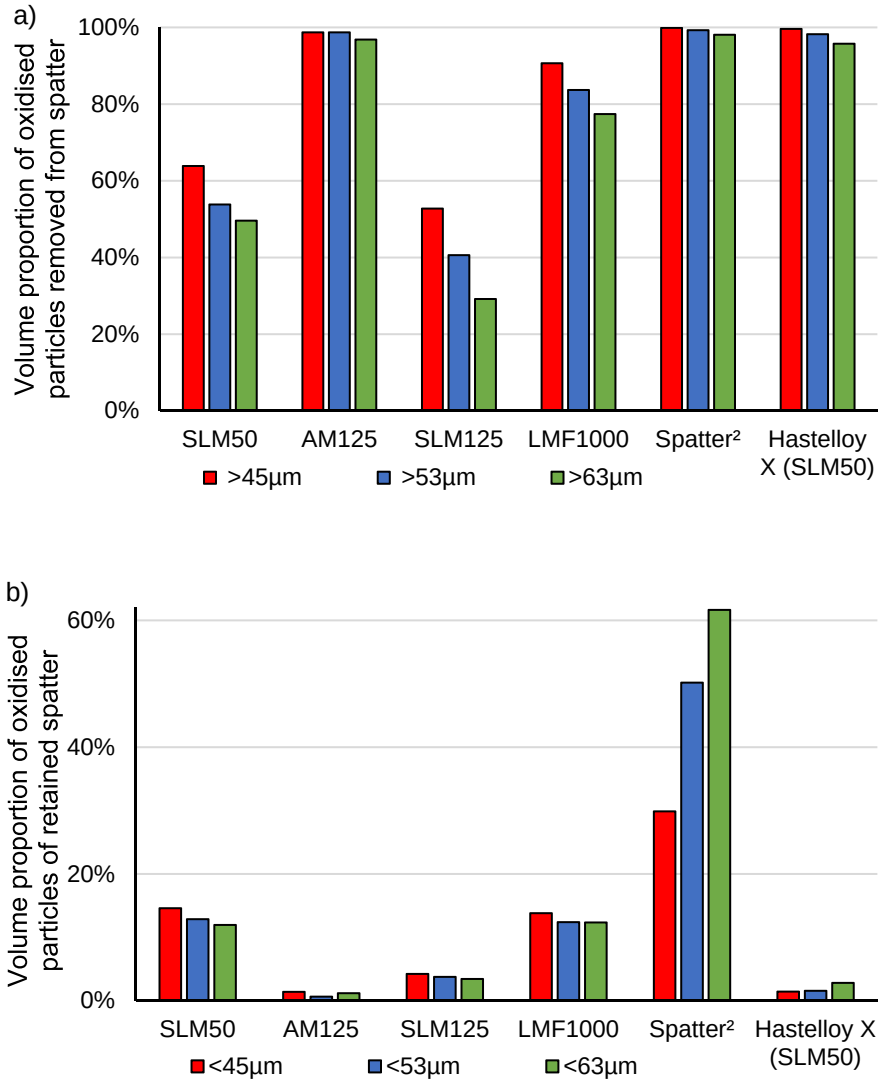

Figure 6.8 Plots of a) the % of oxides particles removed via different sieve sizes and b) the % of spatter particles retained in sieve which are oxidised

The proportion of oxidised particles sieved out is one side of the analysis in terms of what is removed, more crucial to recycling is the proportion of these particles which are retained. Figure 6.8b shows the proportion of the oxidised particles as a total of the powder retained by the different sieve sizes. Whereas the proportion of oxidised particles sieved out of the material increased with smaller sieve size across all samples, this was not the trend for the proportion of oxidised particles in the retained powder. For the Inconel 718 spatter from the

four machines, the proportion increased for the smaller sieve sizes indicating it could be advantageous to sieve at a higher size. This would retain more oxidised material as a quantity, but as a proportion more powder without oxides would be included. The spatter[2] and Hastelloy X spatter showed the expected trend that removal of a higher proportion of the oxidised particles with a smaller sieve size correlated to a decreased proportion of oxidised particles in the retained material.

6.3.1 Discussion

The size distribution of these particles provided useful information for recycling of the powders again. For example, Figure 6.7 shows that the SLM125 includes the lowest proportion of oxidised particles, useful in comparison to the AM125 which contained a similar O level. Analysing these particles for their size in Figure 6.8b showed that despite a larger proportion overall in the AM125, there is a lower proportion of these particles retained in the powder for all sieve sizes. This gives the AM125 an advantage over the SLM125 in the recycling of the powder from the machine. Comparing the oxidation of Hastelloy X and Inconel 718 with both processed in the SLM50 provides similar results. Overall the proportion of oxidised particles in the Hastelloy X is 53% more than in Inconel 718. However, at the highest difference (for <45 µm) the Hastelloy X has only 10% of the proportion of oxidised particles retained through sieving.

Whilst it is shown that the sieving process will remove the majority of the oxidised particles from the spatter, the smaller particles which are retained should not be ignored. Lutter-Gunther *et al.* [46] analysed the O content of Al-10Si-Mg spatter above and below their sieve size, of 75 µm, and there was negligible difference between the two size fractions. It follows then that the rest of the spatter powder within the sieve size, which was not classified as oxidised, may still contribute to an increase in O content in the recycled powder. The oxides found are predominantly surface oxides and the smaller particles have a higher surface area to volume ratio. It could be the case that the smaller particles consequently have a higher proportion of oxides for a given volume than the larger particles. However, it was not possible to analyse the level of oxides on the particles. Part of this is the consideration that oxidised particles were only identified for oxides visible in the SEM images. Because of this, it is likely

that the level of oxidised particles in this analysis is conservative. This is a limitation of 2D analysis of particles but currently better methods are not available.

Based on the combination of analysis for particle shape from the Morphologi system and the oxidised particles from the combined SEM and image analysis it could be recommended that the recycling of the spatter from the AM125 system would be the least detrimental for reused powder. It was also indicated that sieving at either 45, 53, or 63 µm would not particularly change the effect of the powder and so a larger sieve size could be used for higher yield and cost savings. For the other machines, such as the SLM50, considerations would need to be made for the sieving level as a smaller sieve size increased the proportion of highly-spherical particles but also increased the proportion of oxidised particles. These would need further analysis into the effects that these particles play on the build quality to then establish appropriate recycling strategies for the powders. For serial manufacture via PBF-LB a customised recycling plan could developed for any machine and powder combination using similar analysis with the level of spatter generated in the build and the quantity of unused powder in each build. This analysis would be relatively simple and inexpensive and could optimise the efficiency and cost of the manufacture of a component, making it more viable as a business case. This could be highly beneficial given the cost of PBF-LB is a barrier for its adoption for serial production [186].

Assessing the AM industry with regards to manufacture and recycling of powders, oxidation during processing shown in Chapters 5 and 6 present an issue for the industry. The results shown here found that up to 70% of the oxidised spatter particles could remain in the recycled powder after sieving and currently cannot be removed. Spatter particles have also been observed landing on the powder bed during processing indicating that even if only virgin powder is used spatter may still be incorporated into parts. There is a drive by the industry for tight tolerance and control in powder specifications and quality [94,187]. This is leading to the use of even more advanced powder manufacturing methods introduced in Section 2.2.1, such as EIGA, VIGA, and PREP, which are more expensive than the conventional gas atomisation process most commonly used in AM, which is still prohibitively expensive for many applications [68]. These more advanced processes are being used for the most critical applications and reactive alloys, mainly Ti based alloys and Nickel-based superalloys presented here. However, melt ejection spatter is a gas atomisation process within the PBF-LB process,

generating a secondary powder system, which we have established is dissimilar to the virgin powder, and may enter recycled feedstock or land on the powder bed during processing. These more advanced and expensive powder-manufacturing processes are, hence, possibly made redundant if the PBF-LB processing is not to the same standards or O_2 control. If we are to control the powders used in the system, then understanding the spatter powder generated for each material and the effect of micro-alloying elements is crucial to help design bespoke PBF-LB alloys.

6.4 Summary

The aim of this chapter was to quantify the size, shape, and oxide presence differences between the spatter and virgin particles, to assess these for the spatter generated by different PBF-LB architecture. This was achieved through analysis of the spatter powder from four PBF-LB systems for their size, shape, composition, and proportion of oxidised particles. The use of the Morphologi G3 showed distinct differences between the virgin and spatter material and smaller differences between the spatter from different systems. The use of a purpose built image analysis showed differences in the proportion of oxidised particle between each system related to the Oxygen pickup in each system. The analysis of these metrics over the size of the particles showed that a proportion of the undesirable irregular and oxidised remain in the powder for commonly used sieve sizes but most would be removed by the recycling. The key findings from the chapter are:

- The size, shape, and level of oxides in the spatter powder varies from the virgin material, is influenced by the PBF-LB system architecture, and varies for different alloys
- It was established that with current particle measurement technique a range of techniques are required to understand the characteristics of the powders in the system
- Particle shape and size analysis via the Morphologi G3 showed that the spatter particles contained a large proportion (average of 51.1%) of undesirable non-spherical particles but that the majority of these particles can be removed by sieving using a 63 µm mesh

- Combined BSE-SEM imaging and a semi-automated image analysis program was used to assess the level and size of oxidised powders in the spatter. This found a good correlation with the level of Oxygen pickup in the powders
- It was found that whilst the overall proportion of oxidised particles was important, and would play an important role in inclusion during a build, the size distribution showed that some powders with higher levels of oxidised particles would retain lower proportions through recycling
- The detrimental change from virgin to spatter powder was found to continue with the processing of spatter powder. The spatter[2] increased the size, proportion of non-spherical particles, the Oxygen content, and the proportion of oxidised particles
- It was found that Inconel 718 and Hastelloy X produced different proportions and sizes of oxidised particles and highlights that the spatter powder and its effect needs to be assess for each material
- The combined analysis techniques indicated that the spatter from the AM125 system would have the least detrimental impact on the recycled powder and was the least susceptible to change in sieve size for recycling. This proposed that higher efficiency in recycling could be achieved with this system producing cost improvements for manufacture with the system

It has been established that much of the spatter which is generated varies considerably and is out-of-specification from the virgin powder. It was shown that most of the undesirable and out-of-specification powder can be removed during sieving and recycling processes for subsequent builds. However, these particles are still present in the powder bed for the build they are generated in. Therefore, it is important to understand their proportion in the powder bed which forms the final material and may impact on the part properties. Chapter 7 investigates this as part of a new method for assessing the powder bed contents and its variations across the build plate.

Chapter 7 A new method for investigating the powder bed

The quality and characteristics of the powder bed that the laser interacts with has a direct effect formation and behaviour of the melt pool, as discussed in Section 2.1.1. Variations in the powder bed can then lead to variations in the quality and properties of the parts produced. Therefore, it is important to measure and understand the powder bed and variations within it. The characteristics of the powder bed measured in this chapter are the powder bed density (PBD), the PSD, and the spatter content. Previous work has indicated that the recoating of the powder can introduce variations in the powder bed, with regard to the PSD and PBD across the build plate, and that these correlate to variations in the laser-material interaction, such as the absorptivity of the incident laser energy. It is known that spatter is produced and distributed throughout the build chamber. In Chapters 5 and 6 these spatter particles have been shown to vary significantly from the virgin material in shape, size, morphology, and in the presence of oxides. The spatter particles have been shown to introduce defects into parts and therefore it is important to understand the quantity and distribution of these particles in the powder bed and correlate these factors to part quality.

In this chapter, the capsule methodology for investigating the powder introduced in Section 3.3.2 is tested over three builds. The study is conducted on the SLM125 using Supplier 1 Inconel 718 powder as described in Section 3.2.3. The powder bed is investigated for the PBD variation across the build plate and between builds, which provides inference about powder handling and usage in larger scale manufacturing. The powder inside the capsules is analysed via sieve analysis to assess the large fraction and out-of-specification powder. The distribution of spatter across the powder bed is established with the out-of-specification powder and the spatter which is collected beside the build plate. A series of capsules across the three builds are analysed via XCT to assess the porosity and the quality of the part produced to correlate the powder bed characteristics to the final part. Finally, the shortfalls of this methodology for powder bed assessment are discussed and potential improvements and wider applications of the method.

To achieve industrialisation of the PBF-LB process, a method needs to be developed to measure the powder bed metrics to qualify and control the process as currently a standard

does not currently exist. To achieve this aim, and make it applicable for industry, the method proposed here aims to:

- Accurately measure the powder bed quality parameters – PSD, PBD, and spatter content
- Measure these powder bed metrics across the powder bed
- Be quick and easy to replicate
- Be applicable to any PBF-LB system
- Be reliable and repeatable

In this chapter the initial method is presented and detailed in Section 7.1. This method is tested and the results are presented in Section 7.2. In Section 7.3, the results from the exemplar study are discussed and improvements to the method proposed.

7.1 Method development

The method is described in three sections. First, the capsule and build design are presented, then the analysis of the capsule to provide the powder bed metrics, and finally the XCT methods for porosity analysis are detailed. The initial design was for the SLM125 PBF-LB system, but allowances are made for application in other systems. The study is conducted on the SLM125 described in Section 3.2.3 using Supplier 1 Inconel 718 powder as described in Section 4.1.3. Three builds were conducted on this system to test the methodology.

7.1.1 Capsule and build design to assess powder bed content

The method was designed to provide PSD, PBD, and spatter content for the powder bed across the build plate. To achieve this, a capsule was designed, shown in Figure 7.1a, to collect the powder spread each layer over the length of a build. The capsule was designed to have a volume of 12.5 cm^3, half that of the ASTM standard B212 for density measurements [164] of metal powders and referenced by the ASTM Standard F3049 for characterising metal powders for AM. Designing a capsule to contain the full 25 cm^3 as used in the standards would have made the capsule dimensions too large to provide sufficient resolution to measurements of the powder bed to allow a spatial assessment. The capsule had a 20 mm internal diameter,

where spread powder was collected, contained within a 1 mm thick wall. The hemi-sphere top ensured that the powder was contained and separate from the rest of the powder in the bed. The issue with an open top container, as used by Liu *et al.* [56] and shown in Figure 2.31, is difficulty in not affecting the powder in the container when trying to remove the rest of the powder in the bed. This can occur either by removing or adding more powder, or in losing powder when extracting the build plates and removing the parts from the build plate. The issue with a completely closed capsule is that a hole would need to be created afterwards to extract the powder, likely by drilling, which will remove powder in the process or introduce swarf to the powder contents. Both of these will contribute to the errors in the measurement. Using a 2 mm hole in the top allowed easy sealing of the capsule at the end of the build to ensure no loss of powder and the capsules being built on 3 mm supports allowed for easy removal of the build plate and parts from the build plate, further details of this are provided subsequently. However, the hemi-sphere top also presents drawbacks. This introduces overhangs to the manufacture of this section which produce different processing conditions which will likely produce different spatter and this region also introduces a different internal diameter for the powder collection which will likely influence the powder collected in this region. Therefore, it is ensured that this region is a minority (10 mm of capsule height) compared to the 20 mm diameter capsule wall (35 mm of capsule height).

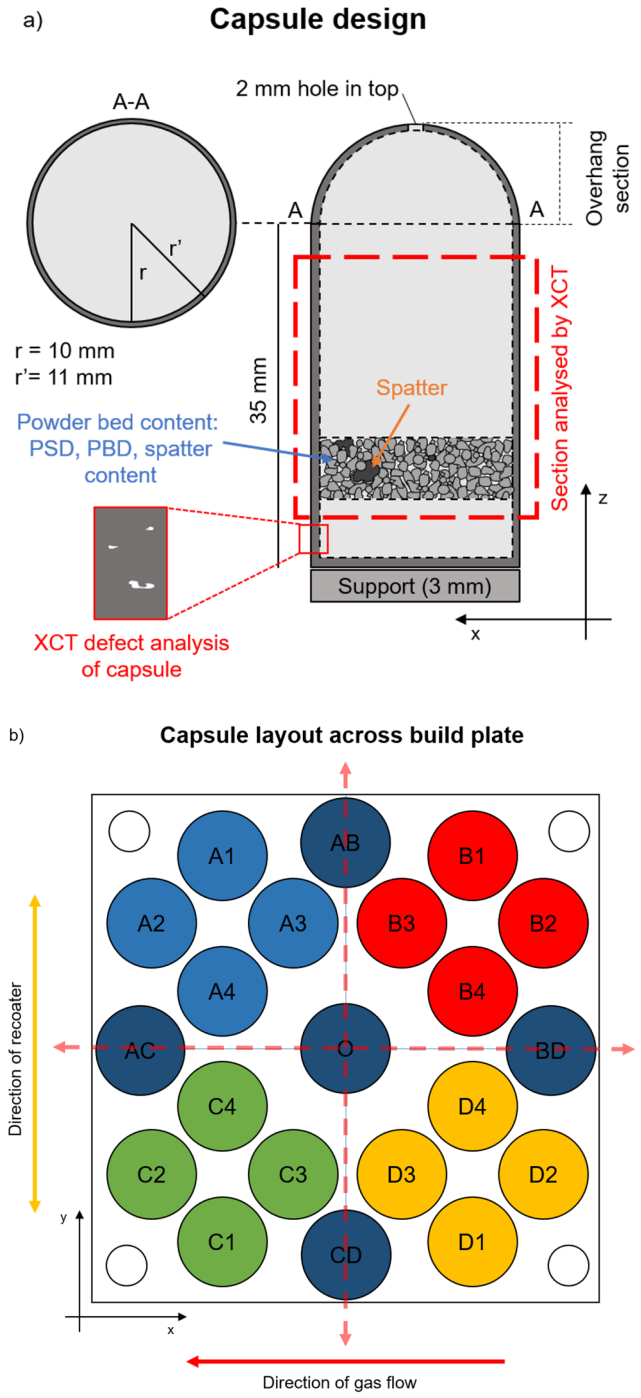

Figure 7.1 a) Design of hollow capsule with volume of 12.5 cm^3, the section of the capsule analysed by XCT is indicated by the red box, and b) schematic of the layout of the capsules dividing the grid into four quadrants and along the central axes

The capsule dimensions were designed to achieve a compromise between volume of powder tested and quantity of capsules across the build plate to provide spatial assessment. The capsules could be designed to be taller with a thinner internal diameter which would allow

more capsules to fit in the build plate. However, there is potential for some interaction between the capsule wall and the powder during recoating and in particles fused to the walls, therefore, it is preferable to have a lower surface area to volume ratio of the capsule wall to powder.

To achieve assessment of the distribution of the powder bed quality metrics the build plate was divided into four quadrants (A – D), each with four capsules, numbered to mirror the opposite side of the build plate, depicted in Figure 7.1b. A key consideration in the layout was for a capsule (O) positioned at the centre of the build plate, and capsules positioned at the end of each dividing axis. This layout gives information along the central axis of the build plate and spatially for each quadrant and the whole build plate. This also allowed an optimal covering of the build plate over a grid system due to the areas of the build plate lost due to curvature and the corner holes for securing the build plate, which can be seen in Figure 7.2b. These are common on most PBF-LB systems.

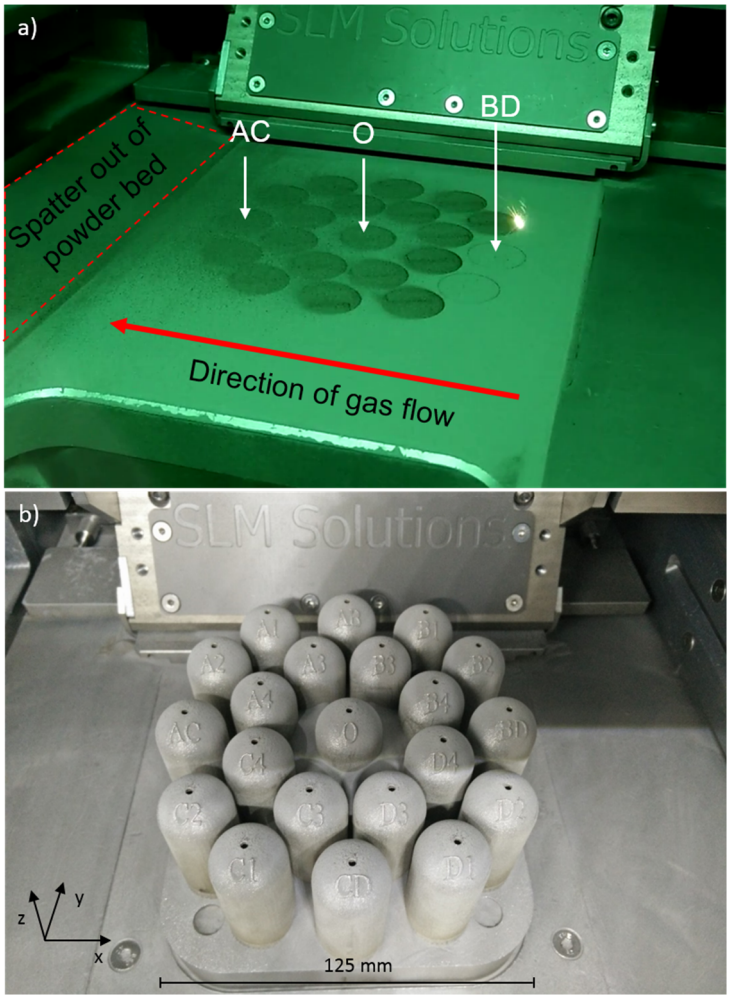

Figure 7.2 a) Image of the powder bed during processing of the base of the capsules. Spatter and process by-products can be seen distributed preferentially to one side due to the gas flow across the bed. This processing represents 52.4% of the build area be being processed, during the processing of the walls when the powder bed contents was captured, 9.1% of the bed was processed. The area contained by the dotted red line is where the pure spatter sample was collected as in previous experiments. b) Capsules at the end of build before removal from the machine for analysis

The 125 x 125 mm build plate in the SLM125 allowed 21 capsules arranged across the bed for the layout. This produced a build utilisation of 9.1% for the manufacture of the capsule walls. The distribution of the capsules across the powder bed allowed investigation of the possible change in PBD across the bed due to preferential recoating of the powder PSD as predicted in simulations by Mindt *et al.* [53], depicted in Figure 2.30, which correlated to different PBD and has been attributed to varying absorptivity and part properties. The simulations conducted by Mindt *et al.* [53] showed higher PBD at the centre of the start of the recoated layer, position A in Figure 2.30, and lower PBD at the edges of the mid-point of the recoated layer, positions B. It is important to note, as described in Section 3.2.3, that the SLM125 used for this

experiment recoats in both directions which will influence the correlation between these simulations and the experiment results.

The spatial assessment of the powder bed also allows investigation of the redistribution of spatter during processing, as investigated by Anwar & Pham [50] using image analysis, but the capsule method provides other metrics to analyse the powder bed. Evidence of the spatter distribution can be seen with the eye, as shown in Figure 7.2a which shows the manufacture of the base of the capsules for this study, but it is important to understand the quantity of these particles in the powder bed.

The order in which the parts in the build are scanned has an effect on the amount of spatter on the powder bed when a certain part is scanned. To reduce the amount of spatter when processing, the parts should be scanned in order from the gas outlet side to the gas inlet side of the build plate, the x direction shown in Figure 7.1b and Figure 7.2b with capsule AC scanned first and capsule BD scanned last. This is the strategy that was used in the builds to test the methodology, as can be seen in Figure 7.2a, B2 is currently being scanned, before D2, and then finally BD. This ensures that all the other capsules have been scanned before the spatter from scanning BD is blown across the powder bed due to the gas flow. Spatter from the previous capsules will still end up in the area of BD as spatter is distributed throughout the chamber by all parts, but less than what is distributed 'downwind' due to gas flow.

A collection of 'pure' spatter was taken from the area by the gas outlet, depicted by the red line in Figure 7.2a, and as previously for Chapter 5 and 6. This collection of spatter allows for comparison with the feedstock material and the powder and spatter contained in the powder bed. The PSD of the powders was analysed using laser diffraction with a Malvern MasterSizer 3000, as previously.

To demonstrate applicability for other systems and scale up for larger powder bed systems the capsule layout has been adapted for other common PBF-LB architectures. Figure 7.3 shows the layout scaled and adapted for a 250 x 250 mm PBF-LB system, offered by many manufacturers, and the same scaling could be used for any rectangular system. This would allow it to produce the same data and format with corresponding grids of four capsules mirrored across the build plate, shown in the same colour scheme. The layout is also shown

adapted for a circular build plate, in this case the 100 mm diameter build plate for the LMF1000 used for Chapter 8. The circular build plates are most commonly used in smaller PBF-LB systems which would be expected to have less variation in powder across the bed. This layout is proposed as suitable for addressing the aims of the method and allowing comparison with different architecture, but, as long as the capsules provide the relevant data then any layout could be adopted for different aims or in improvement to the method.

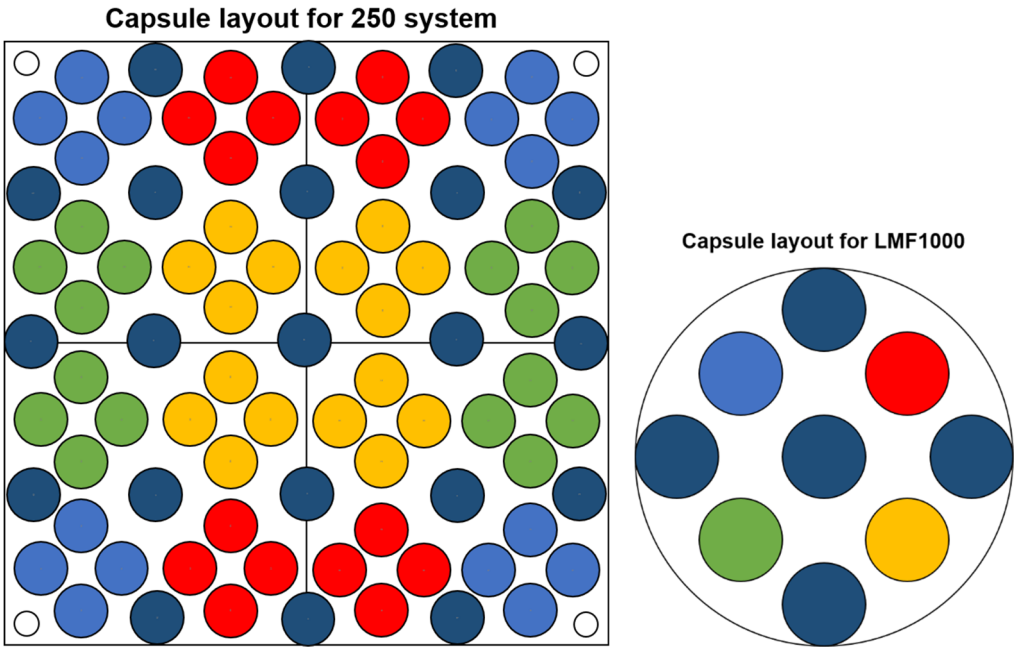

Figure 7.3 Capsule layout for method adapted to a 250 x 250 mm build plate and for the LMF1000 circular 100 mm build plate used in Chapter 8

7.1.2 Analysis of capsules

At the end of the build (Figure 7.2b), the build plate was raised, during which the powder level inside the capsule consolidated below the top of the extraction hole due to the vibrations. During the raising of the build plate the powder not contained by the capsules freely flowed away. The capsules were then capped using tape, so no powder could escape, and carefully removed from the machine. The parts were then manually broken off the support structures without any loss of powder. For the analysis, each capsule was emptied into a glass container via a simple bespoke rig (details can be seen in Appendix A2). A pneumatic ball vibrator was used to ensure that all powder was emptied from the capsule into the glass container. Each glass container was weighed before (*EV*) and after filling with powder (*FV*) to give an accurate

powder weight. The empty capsules were weighed (*EC*) then filled with de-ionised water (*FC*) to establish the volume of each capsule (*V*), this was conducted at room temperature using the density of de-ionised water, with ρ_{water} at 20 °C of 0.9982 g.cm^{-3} [188]. The advantage of this method is that it allows for variation in specimen dimensions, as the internal volume of the capsule which the powder bed occupies is measured and allows each capsule to provide an accurate and specific packing density. The density of material for each capsule (ρ_{pow}) was then calculated by the powder weight over the capsule volume. The PBD is then this density divided by the density of the Inconel 718 material, 8.22 g.cm^{-3}.

Errors in this process are in the weighing of the powder and water, which was measured to four decimal places with an error of ±0.00005 g. There was also potential errors in ensuring that all powder was removed from the capsules, which was minimised with the powder extraction rig utilising the pneumatic ball vibrator. The capsules were flushed with water after emptying to ensure that all powder had been removed. Any trace powder which was flushed via the water was too small to measure. This produced a low uncertainty to the density measurements of 0.0005% PBD, with the error calculated due to the errors from the weight measurements as shown in Equation *7-1* (further details in Appendix A2):

$$\frac{\Delta\rho}{\rho} = \sqrt{\left(\frac{\Delta EV}{EV}\right)^2 + \left(\frac{\Delta FV}{FV}\right)^2 + \left(\frac{\Delta EC}{EC}\right)^2 + \left(\frac{\Delta FC}{FC}\right)^2} \quad \text{7-1}$$

The capsule powder, and thus the powder bed, was analysed via sieve analysis to investigate the contents of powder and the distribution of the spatter. The powder was sieved through a 270 mesh (53 µm) and 325 mesh (45 µm) using a Retsch AS200 (Retsch GmbH, Germany) automatic sieve shaker. All capsules were sieved using the same parameters (amplitude 5 for 3 minutes, alternating 5 seconds on-3 seconds off). These parameters were established from trial tests that allowed all powder to pass through these sieve sizes using virgin material. After passing the capsule powder through, the sieve residues were then weighed using digital scales with an accuracy of ±0.005 g and this was the error in the analysis. The powder used in the study was sieved to 270 mesh (-53 µm) before use, therefore, it is known that sieve residue from this sieve analysis is a by-product and produced during the PBF-LB process, what is

considered spatter. The data is presented for each sieve fraction as percentages of all powder in the capsule to provide relative proportions of these sieve fractions in the powder bed. For each build, capsules AC, O, and BD, which represent the central x-axis of the build plate and parallel to the gas flow direction, as seen in Figure 7.1 and Figure 7.2, were analysed via sieve analysis. This provides the most useful information for the distribution of spatter generated during processing in analysing the capsules closest to the gas inlet, outlet, and centre which will have higher proportions of spatter being central to the build and therefore finding more measurable differences. The other capsules in the builds were used to test the best method to assess the spatter distribution from sieve analysis, laser diffraction or SEM plus image analysis. Therefore, a full sieve analysis could not be performed on all capsules as many had been compromised in other tests. The PSD of the powder from capsule C2 from build 1 and 3 was analysed using laser diffraction to check the findings from the sieve analysis.

7.1.3 X-ray computer tomography

To relate the powder bed metrics to the part quality XCT was used to analyse the porosity in capsule. The capsules AC, O, and BD assessed via sieve analysis for the spatter content across the bed were measured once, for all three builds.

A Nikon MCT 225 (Nikon Corporation, Japan) was used to perform the XCT measurements on the capsules from each build. A central 24 mm section of the cylindrical part of the capsule was measured, depicted in Figure 7.1a and Figure 7.4a. The scans were conducted in a controlled metrology lab and the same scan parameters were used for each capsule, as follows: source voltage 110kV, source current 136 µA, exposure 3142 ms, and a 0.25 mm Cu filter. This produced a voxel size of 12.9 µm. X-ray imaging and volumetric reconstruction were performed by the technician using Nikon software (Inspect-X and CT-Pro, respectively), to produce an image stack of raw, unfiltered XCT images in the x-y plane.

Analysis of the XCT image stack was performed by the author using the public domain image processing software ImageJ [189,190]. 1 mm worth of the image stack, from the top and bottom of the scanned area, was discarded and a stack of 1706 images (22 mm) was used for the analysis. IsoData thresholding was applied to each image of each stack using ImageJ [191]. The thresholding binarised the images to display solid material as white and voids or pores as

black. This threshold was chosen as the threshold setting which gave a suitable representation of the voids as seen in the raw XCT images whilst having minimal noise, this process is depicted in Figure 7.4. To further reduce the noise, the analysis was performed for pores larger than 20 pixels in area. This therefore provided information for pores which have a circular equivalent diameter of >65 µm. Consequently, the porosity values represented here are lower than the actual porosity of the part. However, the reduced noise is beneficial in being able to compare the specimen fairly and the larger pores are more critical for part performance and allowing assessment of part quality. The standard deviations presented were established by segmenting the stack into five sections along the z plane, in a similar method to Slotwinski *et al.* [192], using all slices in the z plane. Whilst different thresholding or processing techniques may give different levels of porosity, fair comparison is made by using the raw XCT slices scanned with the same parameters and processed in the same way for porosity analysis.

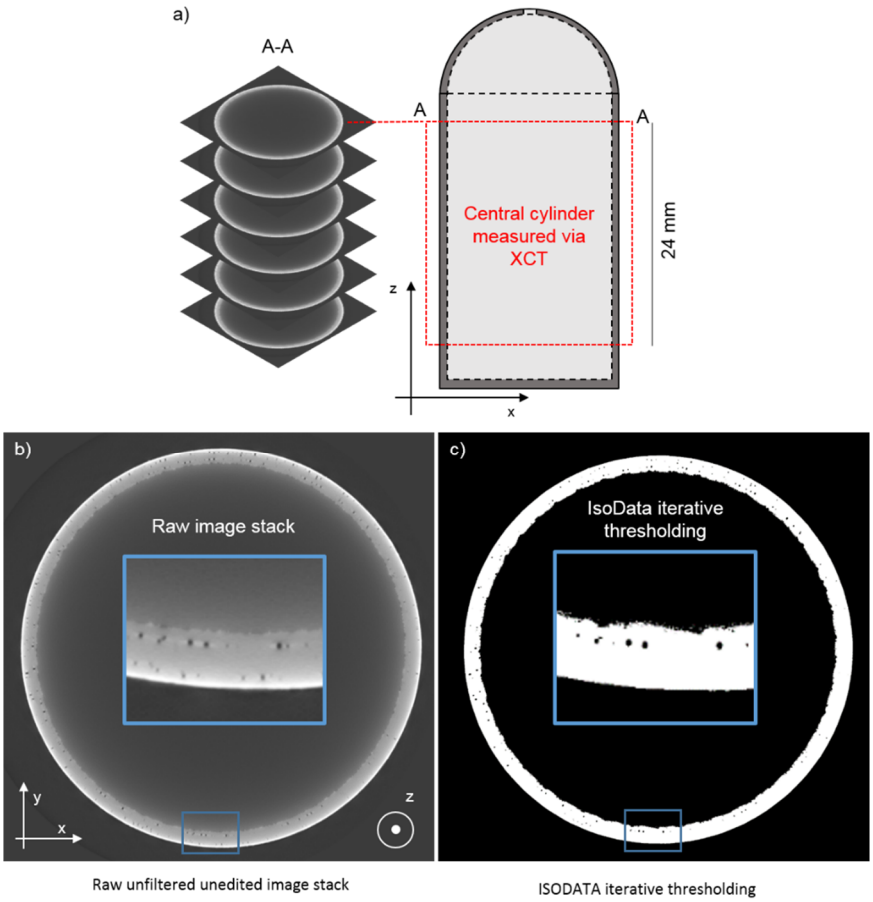

Figure 7.4 a) Schematic of area of capsule measured and the corresponding image stack and b&c) depiction of the IsoData thresholding process applied to the image stack. Noise can be seen due to the gradient of the grayscale on the inside wall of the capsule

7.2 Exemplar results

7.2.1 Powder bed density

Analysis of the powder collected in the 21 capsules allowed assessment of the PBD across the build plate. The results showed that the average PBD of the powder bed across the three builds in order were 61.10 ±0.24%, 60.53 ±0.23%, and 59.20 ±0.25%, with an overall average PBD of 60.27 ±0.98%. The PBD results for each experiment are summarised in Figure 7.5 and detailed in Table 7.1. This is compared to the relative apparent density of the powder of 53.26% and showed a similar density to the relative tapped density of 59.77% for the feedstock powder reported in Section 4.1.3. This indicates that the powder goes through rearrangement over the repetitive recoating process, compacting the powder closer to the tapped density of the powder rather than the loose density. Figure 7.5 shows that the spread of PBD across the 21 capsules was low, and that the difference between the subsequent builds was larger than the difference within a single build. This can be seen by the average standard deviation of PBD within the capsules of the builds being 0.24% compared to the average PBD standard deviation of capsules between builds being 0.98% (represented by the red error bar in Figure 7.5). A one-way between subjects ANOVA was conducted to compare the mean PBD between builds 1-3 (mean and standard deviation listed above). The results showed there was a significant difference between the mean PBD at the $p<.05$ level for the three builds [$F(2, 59) = 334.26$, $p = 0.000$].

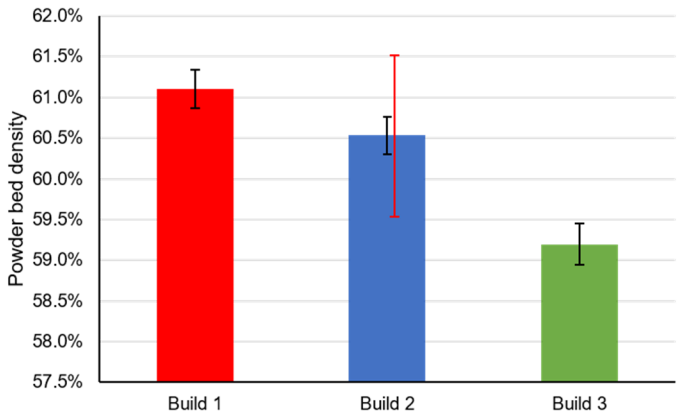

Figure 7.5 The average PBD of the 21 capsules in each build. The black error bars represent the standard deviation of PBD for the capsules in each build and the red error bar represents the standard deviation for average PBD between builds. This shows that the variation in PBD across each build is less than the variation between builds.

Table 7.1 Summary of the PBD (%) for the capsules from each build. The capsule highlighted orange had some powder spilled during measuring and was excluded from the results

	Build 1	Build 2	Build 3	Average	Std Dev
A1	61.19%	60.62%	59.27%	60.36%	0.99%
A2	60.90%	60.31%	58.82%	60.01%	1.07%
A3	60.81%	60.30%	58.87%	59.99%	1.01%
A4	61.44%	60.33%	59.02%	60.26%	1.21%
AB	61.46%	60.86%	59.57%	60.63%	0.96%
B1	61.36%	60.77%	59.59%	60.57%	0.90%
B2	61.20%	60.64%	59.31%	60.39%	0.97%
B3	60.80%	60.36%	59.05%	60.07%	0.91%
B4	61.02%	61.00%	59.20%	60.41%	1.05%
BD	61.22%	60.48%	59.36%	60.35%	0.94%
C1	61.21%	60.62%	59.22%	60.35%	1.02%
C2	60.92%	60.32%	59.45%	60.23%	0.74%
C3	60.80%	60.34%	58.91%	60.02%	0.98%
C4	60.83%	60.32%	58.90%	60.02%	1.00%
AC	61.07%	60.27%	58.95%	60.10%	1.07%
D1	61.30%	60.74%	59.46%	60.50%	0.94%
D2	61.22%	60.57%	59.27%	60.35%	0.99%
D3	60.81%	60.36%	59.06%	60.08%	0.91%
D4	61.06%	60.50%	59.14%	60.23%	0.99%
CD	61.57%	60.96%	59.70%	60.75%	0.96%
O	60.91%	60.29%	59.00%	60.07%	0.97%
Average	61.10%	60.53%	59.20%	60.27%	0.98%
Std Dev	0.24%	0.23%	0.25%	0.24%	
Range	0.78%	0.73%	0.88%	0.75%	

Figure 7.6 depicts the variation of the PBD across the build plate. This is presented as the deviation for each capsule from the mean of the build, averaged across the three builds. It can be seen that the main trend was the increase of PBD seen in the positions of capsules AB and CD. These were the positions at the start of the spread layer, as each subsequent layer is recoated in the opposite direction to the previous layer. However, a deviation of 0.47% points in PBD as the largest deviation demonstrated that the recoater spread an even layer. This is also shown by the maximum range of the three builds of 0.88% points. There also appears to be a trend of decreasing PBD in the –x direction indicating some effect form the gas flow. However, this influence was not conclusive and varied over the three builds.

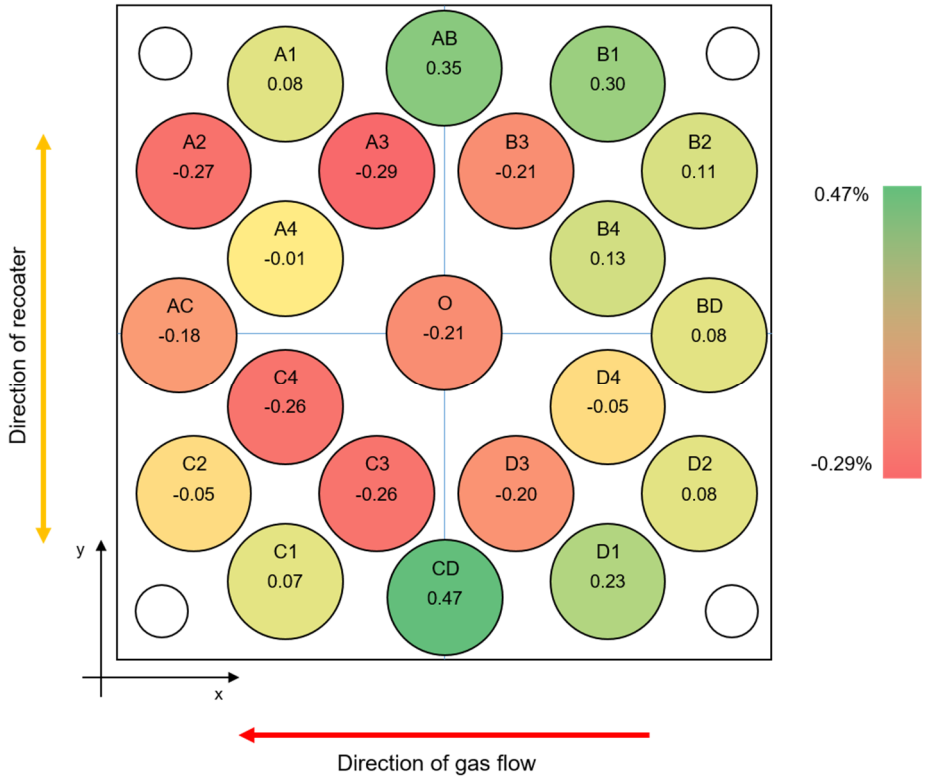

Figure 7.6 Variation of PBD from the average PBD across the build plate. The value is the average over the three builds for the difference of that capsule from the PBD average for the build. The colour map depicts areas with a PBD higher than the average in green and lower than the average in red. Values give the change in % points.

7.2.2 Powder bed contents

To assess the local content of the powder bed across the build plate, particularly for spatter distribution, the powder from the capsules were analysed by sieving through a 270 mesh (53 µm) and 325 mesh (45 µm) sieve. As the powder was sieved to 270 mesh before use in the machine, the sieve residue from this step can be classified as spatter that is produced during processing and is out-of-specification. Sieving to 325 mesh provided additional information of the PSD of the powder in the bed.

Table 7.2 Percentage (by mass) of capsule powder retained by 270 mesh (53 µm) and 325 mesh (45 µm) sieves for capsules AC, O, and BD

Out-of-specification > 53 um

	AC	O	BD	Avg	Std Dev
Build 1	1.05%	0.61%	0.56%	0.74%	0.22%
Build 2	0.98%	0.62%	0.37%	0.66%	0.25%
Build 3	0.95%	0.43%	0.45%	0.61%	0.24%
Avg	0.99%	0.55%	0.46%	0.67%	0.23%
Std Dev	0.04%	0.09%	0.08%		

Large particle fraction 45 – 53 um

	AC	O	BD	Avg	Std Dev
Build 1	9.69%	8.78%	12.22%	10.23%	1.45%
Build 2	6.90%	7.20%	5.06%	6.39%	0.95%
Build 3	3.40%	3.13%	4.91%	3.81%	0.78%
Avg	6.67%	6.37%	7.39%	6.81%	0.43%
Std Dev	2.57%	2.38%	3.41%		

The results of the sieve analysis are presented as percentages, summarised in Table 7.2, with the 270 mesh residue showing that across the three builds and capsules 0.67% of the powder bed was out-of-specification, which was generated during processing. Of this, there was approximately double the quantity of this out-of-specification spatter powder in capsule AC by the gas outlet, with 0.99% of the powder in that location compared to 0.55% in O and 0.46% in BD. Figure 7.7a shows the trend with average quantity per capsule overlaid.

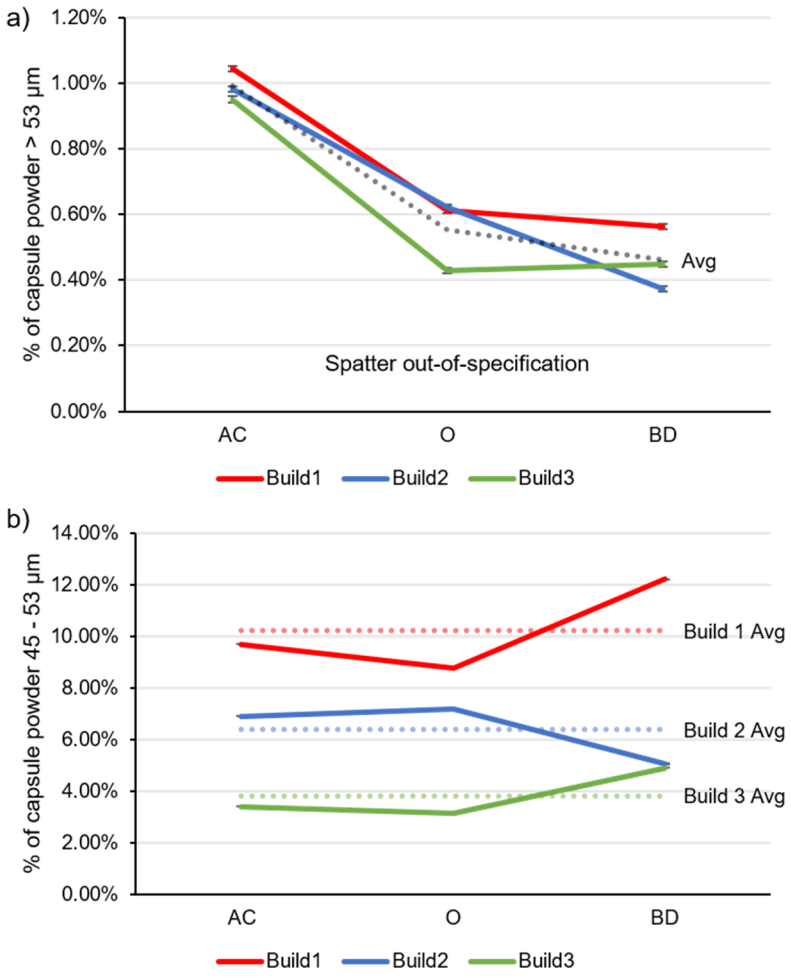

Figure 7.7 Percentage of powder in the capsules AC, O, and BD across builds 1-3 a) particles >53 µm, spatter produced during processing, showing a higher proportion in capsule AC by the gas outlet for all builds, and b) particles sized between 45 - 53 µm showing that the powder size distribution in each build was different; both graphs contain error bars

Figure 7.7b shows the proportion of the powder in the bed/capsules sized between 45-53 µm and shows that this was different for different builds. Unlike the out-of-specification spatter particles in Figure 7.7a, this larger sized 45-53 µm powder fraction did not appear to show a particular trend across the x-axis over the three builds. The sieve analysis did indicate a decreasing trend over subsequent builds with build 1, 2, and 3, averaging 10.23%, 6.89%, and 3.81% of the capsule powder respectively. Error bars are shown in Figure 7.7, however, the advantage of using sieve analysis for all the capsule powder was that error was that inherent to the scales for weighing, which as a proportion of all the powder in the capsule was small.

The trend was further confirmed by laser diffraction of powder from capsules from build 1 and 3. As shown in Figure 7.8 and in the D_{90} in

Table 7.3, the powder from build 1 has a longer right tail showing a higher proportion of larger particles. . An independent samples t-test was conducted on the repeat laser diffraction measurements for the mean particle size, D_{50} , between the powder in the C2 capsules from Build 1 and Build 3. This found that there was a significant difference between Build 1 (M=31.04, SD=0.11) and Build 3 (M=30.70, SD=0.29); conditions t(8)=2.43; p=0.041; for a 95% confidence interval. These results suggest that there is a statistically significant difference between the D_{50} for the two powders, however, the shift in average particle size is very slight and the p value was near the 0.05 interval. A more pronounced difference is seen in the change of D_{90} from 51.06 µm in Build 1 to 46.76 µm in Build 3. This shows how in subsequent builds with the 'same' input powder there was different PSD produced in the powder bed. However, it is not certain why the powder in the bed for both build was finer than the Supplier 1 Inconel 718 Chapter 7 powder batch they were from. It is suggested that this could be due to the some of the larger size fraction being swept into the overflow. This may occur as the percentage of the build area scanned is low for the capsule walls, at 9.1%, and the layer depth for the unscanned areas is 40 µm compared with the scanned real layer depth of ~80 µm.

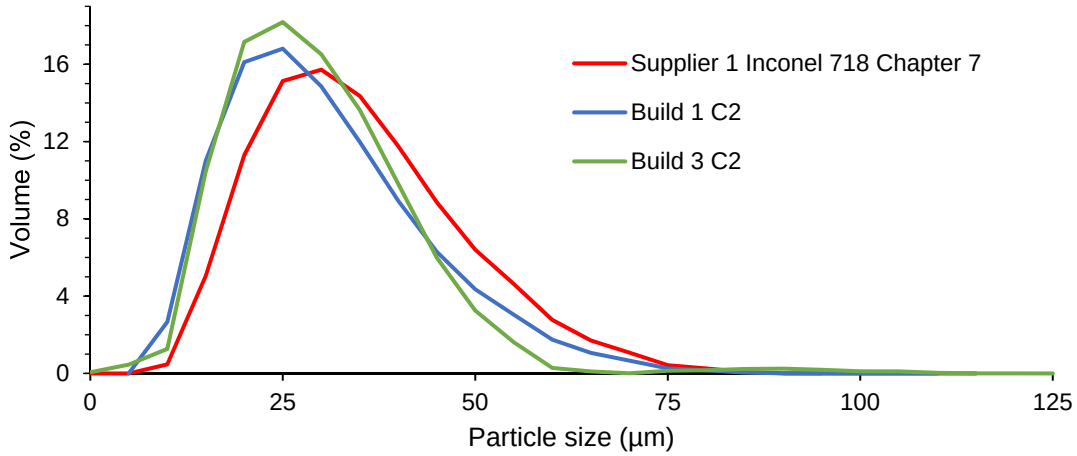

Figure 7.8 Comparison of PSD of powder in capsules on the edge of the build plate for builds 1 and 3 and the starting powder, measured via laser diffraction

Table 7.3 The D_{10}, D_{50}, and D_{90} for the powders in Figure 7.8

(µm)	Supplier 1 Chapter 7	Build 1 C2	Build 3 C2
D_{10}	22.27	18.78	19.28
D_{50}	35.77	31.04	30.70
D_{90}	55.90	51.06	46.76
Span	0.94	1.04	0.895

As shown in Chapter 5 and 6, spatter produced during processing had a much wider PSD than the feedstock powder with a proportion in the same size range and a proportion outside the starting specification. The size of the spatter produced over the three builds and an average was characterised via laser diffraction and is shown in Figure 7.9e, overlaid with the feedstock material. This is the spatter which lands outside of the powder bed and provides a measurement of the 'pure' spatter separate from the powder bed. From the PSD in Figure 7.9e and the D_{10}, D_{50}, and D_{90} shown in Figure 7.9f, it can be seen that there was little variation in the spatter PSD between each of the builds, despite Figure 7.7b showing that the powder size was different between the three builds. This could indicate that the PSD of spatter produced has a higher relation to the processing parameters rather than the powder it is generated from, or that the powder variation in this instance is not large enough to play a predominant role.

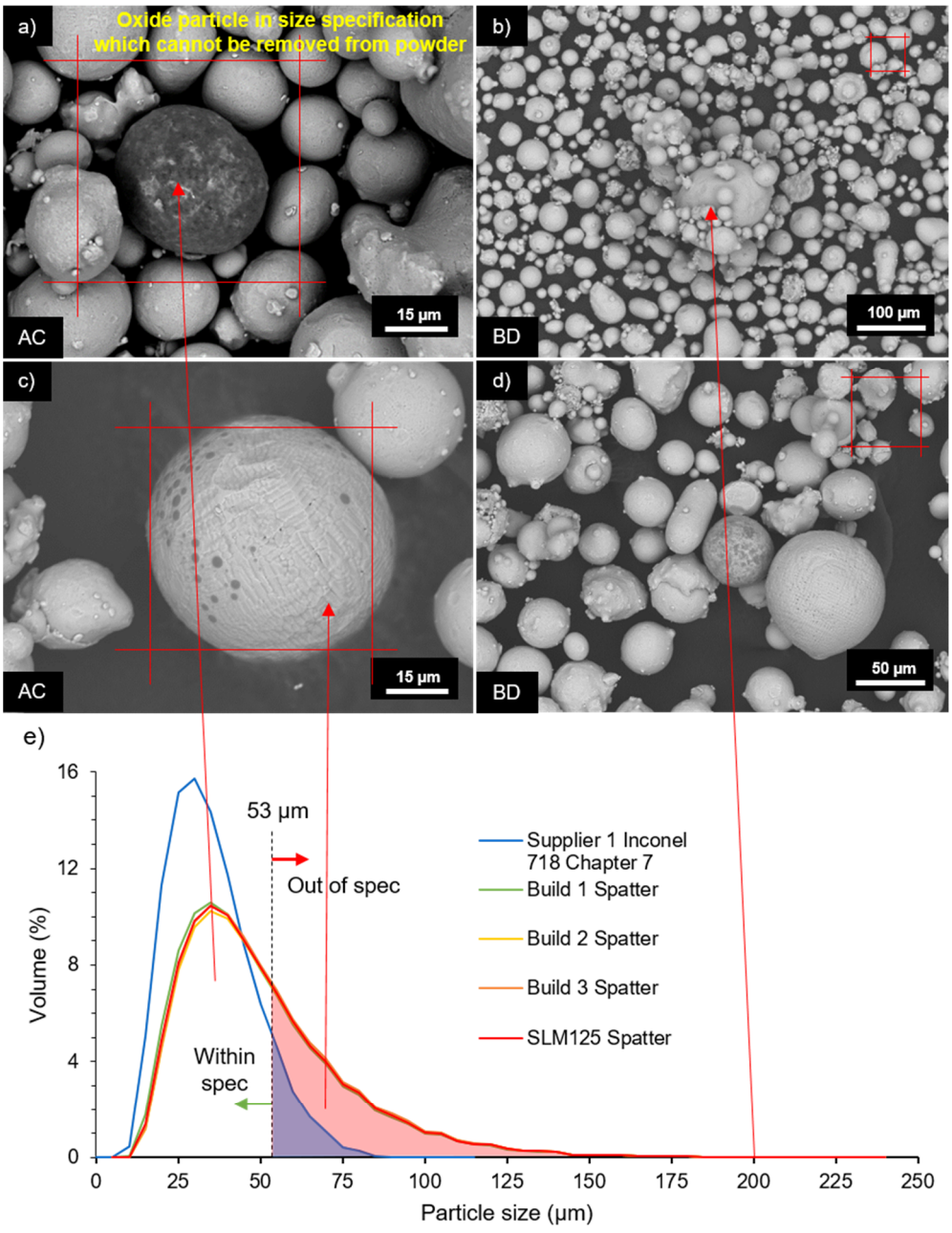

f)

	Feedstock powder	Build 1 Spatter	Build 2 Spatter	Build 3 Spatter	SLM125 Spatter
D_{10} (µm)	22.27	26.79	28.01	27.86	27.59
D_{50} (µm)	35.77	46.76	48.73	48.13	47.87
D_{90} (µm)	55.90	85.38	92.92	87.43	88.43

Figure 7.9 a-d) BSE-SEM micrographs of powder and spatter particles found within capsules AC and BD showing oxidised and large spatter particles with the potential to cause defects. The red square on each image depicts a 53 µm mesh e) PSD of the feedstock powder, the spatter from each build, and the average of the spatter across the three builds. The 53 µm sieve cut-off is indicated for powder which is out of and in specification. f) Summarises the D_{10}, D_{50}, and D_{90} from the laser diffraction measurements for each of the PSDs in (a)

The sieve fraction >53 µm shows how much out-of-specification spatter powder in the powder bed was produced during processing, and the laser diffraction measurements of the collection of pure spatter produced shows the distribution of all the spatter produced from processing. Therefore, from this it is possible to infer how much spatter overall is in the bed, including that which is the same size as the feedstock powder (<53 µm) and can't be separated. From the laser diffraction measurement of the PSD of the spatter it is estimated that 41.07% of the spatter produced is >53 µm (58.93% <53 µm). This was then used to estimate the total proportion of spatter expected to comprise the powder bed in positions AC, O, and BD, which was 2.41%, 1.34%, and 1.12% respectively. This includes the smaller spatter particles within the specification of the feedstock material which can also be problematic, for instance, Figure 7.9a shows an oxidised particle in the powder bed which cannot be separated from the un-processed powder. From the combined SEM and image analysis in Section 6.3, it was estimated that 59.4% of the oxidised particles were <53 µm, however, only 2.5% of the SLM125 spatter was estimated to be oxidised.

7.2.3 Capsule porosity and part quality

The spatter produced and collected from beside the powder bed from the SLM125 and other PBF-LB machines have been characterised previously, in Chapter 5, Chapter 6, and earlier in this chapter. The particles shown in Figure 7.9a-d are particles taken from capsules AC and BD and confirm that oxidised spatter particles, including large particles, were found within the powder bed. These are the particles which can cause random defects in parts produced from oxide inclusions or voids. Figure 7.7a shows that there was a higher proportion of these particles in the powder bed closer to the gas outlet. Finding these particles in the capsule, and therefore the powder bed, demonstrated that these particles are not completely removed by the gas flow, or larger particles removed by the recoater. It is important to note the particles found in the capsule BD, which was located by the gas inlet. These showed that spatter is ejected in all directions, and although the gas flow influences their redistribution, it does not stop spatter particles being redistributed all over the powder bed. The large particle in Figure 7.9b, which is approximately 200 µm, is not necessarily represented in the laser diffraction measurements of the spatter.

XCT analysis of the capsules was designed to assess the correlation between powder and part quality, given by a porosity level. The spatter particles are capable of introducing defects into components. In particular, large spatter particles incorporated into the powder bed can form lack-of-fusion and porosity defects. XCT measurements of the capsules AC, O, and BD, were taken to analyse the porosity within the capsules related to the powder content. The average porosity of these capsules from the XCT measurements are shown in Figure 7.10. Capsule AC in build 2 and 3 had porosity greater than one standard deviation higher than capsules O and BD, indicating a potential effect due to higher proportions of spatter shown, but this trend was not found in build 1 AC. The average porosity measured for builds 1-3 were 0.032 ±0.01%, 0.025 ±0.02%, and 0.017 ±0.02% respectively, displaying a trend of decreasing porosity from build 1 to build 3. This had a similar trend to the average proportion of larger powder in the build and to the average PBD in the builds, as shown in Figure 7.10. Whilst the trend matched the average PBD in each build, it did not match the specific PBD for each capsule. However, it is important to note that the standard deviation presented here are a standard deviation of the porosity within the sample, not for the measurement. This is an issue with the XCT measurements performed. With the XCT available it was opted to scan each of the three capsules from all three builds instead of perform three repeat measurements for one set of capsules. Therefore, the repeatability and accuracy of these measurements is not known, and makes confidence in the results low, particularly for the low porosity levels measured.

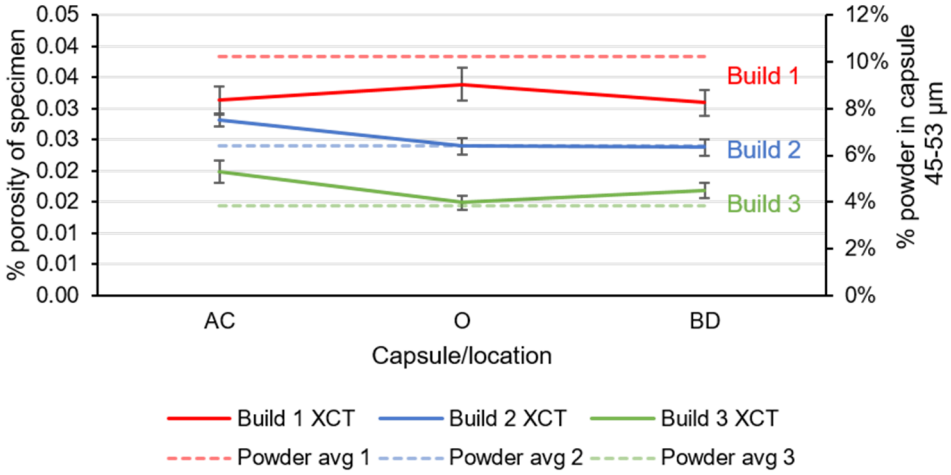

Figure 7.10 XCT analysis of porosity in capsules AC, O, and BD across the three builds for pores >65 µm overlaid with the average % of powder in the capsule comprising 45-53 µm from Figure 7.7b. The errors bars show the standard deviation in the porosity measurement

Another element which could be assessed for build quality was the geometric accuracy of the builds. Each capsule had a designed volume of 12.5 cm^3 and had its actual volume measured. All capsules produced volumes smaller than the designed volume from a minimum of -0.59% and a maximum of -1.72%. This was likely due to fused particles which adhere to wall surfaces and are known to increase geometric tolerances in PBF-LB. The difference from the designed volume showed a range of 1.13% and standard deviation of 0.20% across all the capsules built. No trend was found between the volume of the capsule and the powder bed characteristics analysed but validates measuring the individual capsule volume for PBD.

Table 7.4 Percentage volume deviation from the designed 12.5 cm^3 for each capsule

Capsule	Build 1	Build 2	Build 3	Average	Std. Dev.
A1	-0.73%	-0.76%	-0.82%	-0.77%	0.03%
A2	-0.73%	-0.83%	-0.87%	-0.81%	0.06%
A3	-0.81%	-0.79%	-0.82%	-0.81%	0.01%
A4	-1.59%	-0.59%	-0.81%	-1.00%	0.43%
AB	-0.91%	-0.92%	-0.88%	-0.90%	0.01%
B1	-0.82%	-0.90%	-1.11%	-0.94%	0.12%
B2	-0.82%	-0.98%	-1.01%	-0.93%	0.08%
B3	-0.80%	-0.86%	-0.91%	-0.86%	0.05%
B4	-0.75%	-1.64%	-0.89%	-1.10%	0.39%
BD	-0.75%	-0.73%	-0.88%	-0.78%	0.07%
C1	-0.78%	-0.80%	-0.84%	-0.81%	0.03%
C2	-0.70%	-0.71%	-1.72%	-1.04%	0.48%
C3	-0.75%	-0.74%	-0.75%	-0.75%	0.01%
C4	-0.80%	-0.74%	-0.79%	-0.78%	0.03%
AC	-0.96%	-0.88%	-0.98%	-0.94%	0.05%
D1	-0.88%	-0.97%	-0.93%	-0.93%	0.04%
D2	-0.76%	-0.88%	-0.88%	-0.84%	0.06%
D3	-0.84%	-0.88%	-0.87%	-0.86%	0.02%
D4	-0.91%	-0.96%	-0.90%	-0.92%	0.03%
CD	-0.96%	-0.86%	-0.86%	-0.89%	0.05%
O	-0.87%	-1.35%	-0.76%	-0.99%	0.26%
Average	-0.85%	-0.87%	-0.93%	-0.89%	
Std. Dev.	0.18%	0.20%	0.20%	0.19%	
Range	0.89%	1.06%	0.96%	0.35%	

7.3 Discussion

The capsules allowed the analysis of the powder which the laser interacts with to produce parts in the PBF-LB process. The results from the study allow the evaluation of the considerations for how the material input to the system is translated to the powder bed, the subsidiary material or spatter produced during the process, and quality of the parts produced. The consistency of the process and the parts produced is a key factor for the industrialization and greater adoption of the technology, of which, the powder bed is an integral component of this. The study highlighted shortcomings of the methodology and areas for improvement which will be discussed.

7.3.1 Variation in powder bed density

One of the first aspects the methodology assessed was the spatial assessment of the PBD. The simulations by Mindt *et al.* [53] predicted that there would be an increased PBD at the centre of the beginning of the recoated layer, the region labelled A in Figure 2.30. Figure 7.6 showed that on average the highest PBD was at the start of the recoated regions, in capsules AB and CD, which agrees with the simulations reported by Mindt *et al*. The increased PBD occurs at both sides of the build plate as the recoater in the SLM125 recoats in alternating directions each subsequent layer. The lowest PBD was generally in the centre of the build plate, and there appeared to be a slight decrease from the right hand side to the left. However, the variations in the PBD across the plate had a range of 0.75% points, with a standard deviation of 0.22% and a maximum of 0.47% points from the average PBD for whole build volume. This could be indicative of a stable recoating mechanism as even a 0.47% as the highest variation may not have a large effect on the quality of the parts produced, or other factors may have more significant effects. However, this would require further analysis, ensuring the same input powder over repeat builds to then assess the statistical significance of the recoating spread and stability. Although the porosity showed a decreasing correlation with the average PBD between builds it did not show a correlating trend between the individual PBD of the capsules and the capsule porosity, indicating the PBD may not be the major factor in the porosity change. Liu *et al.* [193] found two powders with a 8.9% difference in PBD produced similar properties with optimal processing parameters. It is important to note that this study is

conducted on a 125 x 125 mm build plate, as the industry moves to processing larger PBF-LB volumes the variation in powder bed content across the bed may become larger and a more important issue.

In the methodology test, the designed build was repeated three times to establish the repeatability of the powder bed content. With regards to the PBD, it was shown that each build produce a similar standard deviation and range (0.24%, 0.23%, 0.25% and 0.78%, 0.73%, 0.88% for builds 1, 2, and 3 respectively). However, the change between mean PBD in each build was larger than the variation from the mean in any single build. As all the processing was kept the same for each build, it was established that the powder in each build must be different, despite each build coming from the same 100 kg batch of powder. This was shown to be the case in the 45 - 53 µm sieve fraction, which from build 1 - 3 changed from 10.23% to 6.89% to 3.81%. This is likely due to a combination of the materials handling and the hopper system in the SLM125 system. Larger particles have a higher flowability, so when dispensing from a container or loading in a hopper/moving through the hopper system, these particles flow first [94]. It is proposed that due to this preferential flow, the first build had a higher proportion of these large particles, with subsequent builds having reduced proportions. The skewed PSDs with a higher proportion of large particles correlated to a higher PBD produced in the builds. This change in powder from build to build, although seemingly using the same powder from the same batch, highlights the difficulty of working with powders and, therefore, producing consistent quality in PBF-LB as it is possible to be processing different powder in the bed to the feedstock specification. This could be avoided with the implementation of appropriate standardised operating procedures for powder handling and processing. The industry is starting to move towards integrating the powder handling into the machines so that these operations are carried out mechanically which may further mitigate these powder processing issues.

The build quality of the capsules was analysed using XCT to evaluate the level of porosity, or voids, in the material. The trend in the porosity of the capsules showed a step change between builds however the porosity levels measured were low (<0.1%). As only one measurement was taken for each sample there was no indication of the repeatability or accuracy of the measurements, and therefore, it was not possible to assess if the results are statistically significant. The porosity had an inverse relationship with the PBD level for each build. This

seems to be different to findings from Liu *et al.* [56], where an increase in PBD correlated with a slight increase in density of parts. However, in Liu *et al.*'s study, the increase in PBD was much more significant and the powders were more dissimilar, so there may have been other more influencing factors such as the higher proportion of small particles (<15 µm) in the powder with higher PBD. Spierings *et al.* [67] used three different powders in their study of the role of powder characteristics, their results indicated that a larger span of the PSD correlated with a higher apparent density and the powder with the smallest size fraction (D_{50} = 15.12 µm compared to the other powder's 28.26 and 37.7 µm) produced the most dense parts for identical processing parameters. The results from this test study showed that the build with the highest PBD produced the highest porosity, which may seem counter intuitive. However, the XCT analysis measured only larger voids (>65 µm circular equivalent diameter) to reduce noise and error in the measurement. This is another indication that the measurement technique was not appropriate. Whilst build 1 had the highest PBD, it had the highest 45 - 53 µm powder fraction. Therefore, it is possible that what voids there were in the powder bed packing were larger but overall less numerous, or there were sections where a couple of large particles prevented full melting or penetration of the laser, as is caused by large spatter particles. The powder with higher apparent density and PBD in Liu *et al.* and Spiering *et al.'*s studies had a larger span of PSD, this allowed those larger voids between large particles to be filled by smaller particle. Whereas in this study the powder has a skewed PSD and not a wider PSD so this void filling would not have occurred. However, this was not conclusive. Whilst there was a trend in the XCT analysis of the capsules, the test run predominantly highlighted opportunities for improvement with the methodology which are discussed subsequently.

7.3.2 Spatter generation and distribution during PBF-LB processing

The proportion of spatter found in the powder bed is important for quality control in the process. As these particles can produce detrimental effects, it can provide considerations for placement of critical parts in the build chamber. Ladewig *et al.* [47], Anwar & Pham [48,50], and Philo *et al.* [194] showed that the gas flow in the system plays a crucial role in how much spatter is carried across the build plate towards the gas outlet or off the build plate. The methodology in this chapter allowed an assessment of the quantity of spatter in the powder

bed and confirmed the higher proportion of spatter particles found in the powder bed by the gas outlet.

Whilst the gas flow plays a role, the proportion of spatter in the powder bed is related to how much material is processed. This could be measured as the surface area processed each layer, or a total volume of final material as a proportion of the build volume, but will be specific to each build. For the majority of the powder collection in the capsules (building the 21, 1 mm thick walls, for 875 layers) the build utilisation was 9.1%, which produced an average 0.67% out-of-specification spatter, and estimated 1.63% total spatter, comprising the powder bed. The schematic in Figure 7.11 shows the build utilisation. Figure 7.11c shows the processing of the layer which corresponds to the base of the capsules, which related to a build utilisation of 52.4%. The darker, oxidised spatter powder can be seen spread across the build plate and would contribute a higher proportion of the total powder bed, which can contribute to greater detriment to the parts. This is important for consideration for the industrialisation of PBF-LB and in the mass manufacture of components as utilisation of the build volume is important for the economies of the technology to be viable [80,195]. As the industry moves towards larger build volumes and multiple lasers, the issue of spatter distribution across the bed will become more important. One laser may distribute spatter into the unprocessed sections of another laser and gas flows will be less able to remove the process by-products from the processing zone.

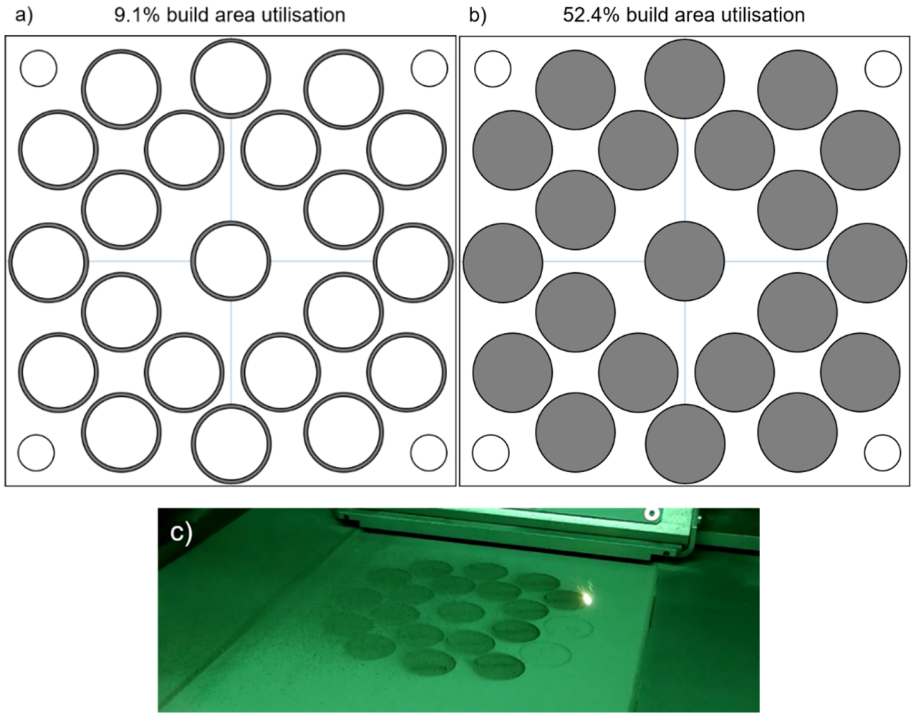

Figure 7.11 Schematic of processing a) the capsule wall, for which the spatter was collected, in which 9.1% of the build area is utilised and b) the base of the capsules, for which the spatter produced is much higher and can be seen in (c), where 52.4% of the build area is processed. c) Image of the processing of the base of the capsules inside the SLM125

Build utilisation also plays a role in the recycling of powders. As discussed, as more of the powder bed is processed, more spatter is generated. However, more of the in-specification powder is also used up. Therefore, from the material removed from the system at the end of the build, the ratio of spatter (and processed/affected powder) to 'unused' powder is greatly increased. In the builds in this study, it was estimated that 0.96% of the powder bed was spatter powder (58.93% of spatter) that is in specification (<53 µm) and would be retained if sieved back to this size. If the powder was sieved at other common size fractions used in industry, such as 45 or 63 µm, this would relate to a retained fraction of 0.71 or 1% (43.67 or 61.12% of the spatter) respectively. This is just for the powder in the bed and does not include other powder in the system such as in the overflows. However, this is for one build and powder is expected to be used multiple times in the PBF-LB system to make the technology sufficiently economic.

The methodology proposed has the potential to be used to predict the proportion of spatter in the powder bed. Further work would be required to establish a true relationship but the principles can be demonstrated using the results presented, given a few assumptions. In the

laser scanning of a part, if the average 10 mm scan track produces *x* g of spatter then it is proposed that two 10 mm scans produces *2x* g of spatter and a 15 mm scan produces *1.5x* g of spatter. Therefore, it could be assumed that the quantity of spatter (which will be denoted as spatter quantity *SQ* and would be measured in grams) produced in a build is linearly related to the area of powder bed processed, or the build utilisation (*BU*), using a scaling factor *C*, as shown in Equation *7-1*. (The quantity of spatter generated will be influenced by the processing strategy, however, this is beyond the scope of this study.)

$$SQ = BU \times C \tag{7-2}$$

The scaling factor *C* would be set from the ratio of *SQ/BU*. This data is provided from the test build. Which, for the average *SQ* over the builds, *C* is 16.28. This can also be determined for the variation across the bed by using the *SQ* for the capsules AC, O, and BD which would produce a *C* of 24.14, 13.49, and 11.2 respectively. Next, it was discussed that the proportion of spatter in the powder bed is related to how much spatter is generated and how much virgin/feedstock material is used up. The quantity of virgin material (*V*), or un-processed powder, in the powder bed is assumed to decrease linearly with the proportion of the powder bed processed and consolidated into the parts, again the build utilisation. To relate to *BU* as a percentage, *V* and *SQ* are scaled so *V* + 100*BU* = 100. For example, for the average from the test build with *BU* = 9.1%, the measured *V* and *SQ* are 61.25 g and 0.41 g respectively, which for the calculation are scaled to *V* = 90.9 g and *SQ* = 1.48 g. Therefore, the quantity of un-processed powder in the bed is expressed by:

$$V = 100 \times (1 - BU) \tag{7-3}$$

The spatter content (*SC*) can then be estimated as the ratio of *SQ/V* and both *SQ* and *V* are calculated in relation to the build utilisation *BU*. Figure 7.12 shows the relationship between the build utilisation and the spatter content in the powder bed using the data from the test

for the average spatter and spatter across the build plate. The BU is plotted up to 70% which typically wouldn't be exceeded for manufacturing.

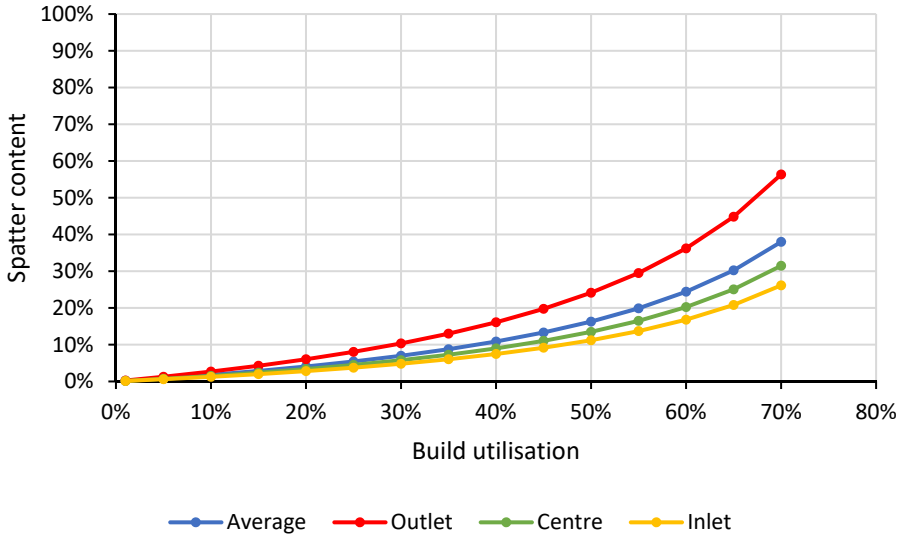

Figure 7.12 Proposed estimation of spatter content in the powder bed related to proportion of the powder bed processed (Build Utilisation) as an average for the build and across the build plate

As stated this is a proposed method of estimating the spatter content in the powder bed using one data point of *BU* to *SC* and the assumptions discussed. The methodology could be further used to vary the *BU* and establish the relationships between the *BU* and the *SQ* and *V* in the powder bed. Using a method like this to be able to establish and predict the level of spatter in the powder bed could be used to further correlate this to part performance. This could then be used as part of design principles for PBF-LB and for qualifying parts and builds.

The majority of studies are conducted with virgin material, however, the majority of manufacturing with PBF-LB in industry will be conducted with recycled powder in order to make this an economically viable technique. The cost and the variability of the process are two key barriers for wider adoption and industrialisation of the technology. Both of these are influenced by how well powder in the process can be recycled. The recycled powder is a combination of the un-melted powder input to the system and the spatter generated during processing. As the input powder is generally considered a known factor and manufactured to a designed specification, which may go through some change due to thermal cycling and handling in processing, the spatter is the major consideration for the change in the powder. The studies conducted in the literature [7,112–115,196] for the effect of powder recycling are

often lacking in detail of the builds conducted, recycling process, powder handling, sampling techniques, and many other parameters required for an understanding of the recyclability of the powders and testing conducted. The most common metric to assess the recycling of the powder is the number of builds a powder has been used. This falls short in qualifying the change in the powder. A build could contain any number of parts of different sizes and simply using a number of builds a powder has been used for equates the powder from the building of one 10 x 10 x 10 mm tall part to the powder from building 30 10 x 10 x 100 mm parts. The change in powder needs to be assessed at a more fundamental level. It has been discussed how the BU could be used to predict the quantity of spatter generated and the proportion of un-processed powder remaining. If the model was developed as stated and combined with the characterisation of spatter powder, as in Chapter 5 and 6, this could potentially provide a more accurate way of assessing and predicting the recycling of the powders and the quality of this powder for future builds.

7.3.3 Improvements to the methodology

The test run of the methodology provided results and insights into the particles which comprise the powder bed and also highlighted some shortfalls in the methodology and areas which can be improved. One aspect which is not considered is the effect of the capsule on the powder which is collected within it. It is not known if due to features like the denudation zone and the volume of consolidated material from the capsule wall has an effect on the powder spreading and therefore whether the thickness of the wall and the geometry of the capsule may influence the results. This is depicted in Figure 7.13. For the methodology the wall thickness is kept to a minimum in an attempt to reduce the possible effects. The methodology could be used to initially assess the powder characteristics in the capsule and then the capsule design modified and the test repeated to assess if the geometry affects the results.

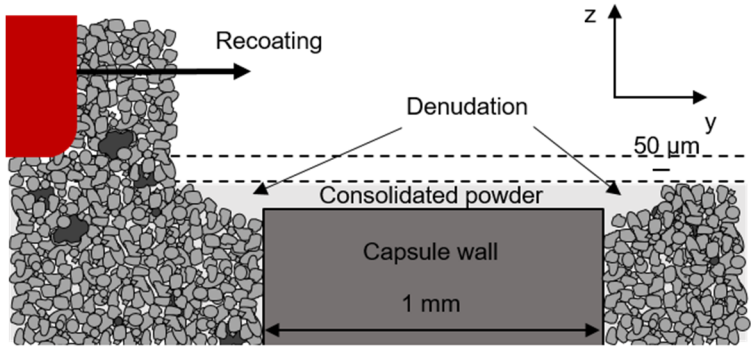

Figure 7.13 Recoating of the next layer of powder by the capsule wall. With denudation zone. The dotted lines represent the layer heights and dark particles the spatter

One assumption in the methodology is that the powder that the laser interacts with can be related to the powder metrics assessed. The laser interacts with a volume of approximately $1x10^6$ µm^3 (100 x 100 x 100 µm height x width x depth) whereas the capsule is measuring a volume of $1.4x10^{13}$ µm^3 (20000 x 45000 µm diameter x depth). Whilst the capsule can provide an overall average across the volume it is difficult to ascertain the correlation of the metrics between these volumes. The capsule also cannot assess the more localised variations of the powder bed which the laser interacts with. This is a limitation of the capsule methodology, the powder in the capsule is measuring the build-up of recoated powder onto previously recoated powder, whereas most powder processed is spread onto consolidated material. This consolidated material has a different layer height as shown in Figure 2.28. This may also make it more difficult to correlate the powder bed metrics with porosity formation and a supplementary analysis of the 'real layer density' could advance these investigations.

Phuc & Seita [197] integrated a contact image sensor from a paper document scanner into the recoater system of an SLM500 PBF-LB system which was able to image/measure the powder bed with a spatial resolution of ~5 µm. This allowed them to detect variations and defects in the powder bed, although with resolution issues in depth and difficulty in calibrating the system with the powder bed contents. If this system was installed in the recoater to be used with the methodology presented, it could work as an in situ verification of the powder bed and the results from the capsules could be used to calibrate the scanned data. The combined method could then be used to further investigate powder bed variations and spatter distribution which lands on the powder bed and what remains in the powder. The incorporation of this scanner could also aid in investigating the preferential distribution of the

PSD across the build plate providing higher resolution of the change in particles across the bed.

A difficulty in powder analysis is the comparison between sieve analysis and laser diffraction for particle size analysis [72,92]. As discussed in Section 2.2.2 both techniques have their advantages and disadvantages. For laser diffraction, due to the approximation of a circular equivalent and fitting to a distribution it produces a tail at either end of the distribution, and so for a powder sieve to a certain size the laser diffraction measurements will show a proportion of the particles over this size. The effects of this can be seen in Figure 7.9, where the feedstock material which has been sieved to 53 µm has a section above this size (highlighted under the line in blue). This means in analysing the 'pure' spatter powder collected via laser diffraction and measuring the fraction above and below 53 µm may not give the same size fractions as if it were sieved. In the methodology we use the size fraction from the laser diffraction measurement to infer the remaining size fraction of spatter <53 µm which cannot be separated from the powder bed. This may therefore have errors with using different distributions which couldn't be reported. Greater analysis needs to be conducted to assess the discrepancy between these methods of measurement for these powders, which could be achieved in establishing sieve equivalent sizes in the laser diffraction measurements between the powders.

An alternative method for analysing the spatter separate from the powder bed was explored by Lutter-Günther *et al.* [46] as discussed in Section 2.1.2 and depicted in Figure 2.12. They used a 'sheet mask', a thin sheet of metal which was placed directly on top of the powder bed to collect the generated spatter. Their sheet mask modification was applied to an SLM125 system as used in this study. The sheet mask could be adapted to the capsule layout in this methodology, a schematic is shown in Figure 7.14. The additional holes for the capsule walls across the sheet mask will make it difficult to collect the spatter by tipping the sheet, instead the internal section of the capsule where the spatter lands could have a sticky Carbon tabs commonly used for SEM placed on it. This would collect the exact spatter which lands in the capsule area which can then be analysed at the end of the build to provide accurate metrics for the spatter via image analysis. This data can then be correlated with the out-of-specification powder measured at the end of the build to produce a more accurate measure of the spatter content in the powder bed. This data could also be analysed with the spatter

collected by the side of the powder bed to mitigate any shortfalls which may occur from only analysing this spatter. As discussed before, this spatter by the side could contain a higher proportion of the smaller spatter particles as these will be redistributed further by the gas flow.

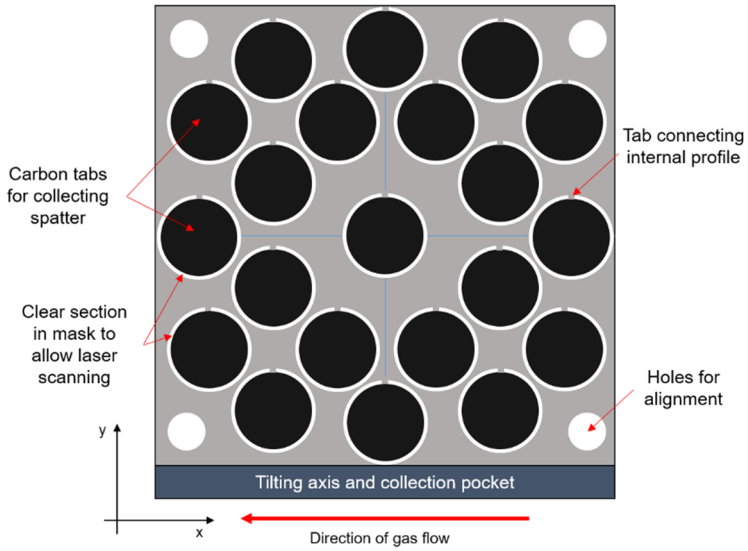

Figure 7.14 Sheet mask spatter collection technique adapted from study by Lutter-Günther et al. [46] *to improve the methodology in the SLM125*

The XCT analysis of the capsule in the exemplar builds make it difficult to find conclusions with the effect of the powder characteristics. Only the 1 mm wall section was analysed which causes limitations. In the processing of this area there is a large ratio of border compared to infill hatching, which may be suitable for lattice strut processing, but for most builds there will be larger geometries and this infill hatching will be the majority of processing which will be the most relevant to the final material and the defects which may form. XCT produces an edge effect, as can be seen in Figure 7.4 in Section 7.1.3 with the high contrast outside edge and lack of definition on the inside edge. This also contributes to issues with defining the edge via thresholding and contributes to noise. Whilst there is ongoing work to improve issues with the XCT of AM components [198–200], to avoid the effect of these in the test study results a large cut-off for minimum feature analysed (>20 pixels) was defined, however this removes a lot of possible data which could improve the analysis and give greater confidence in the results and trends. Therefore, it is proposed to incorporate a designed volume for quality analysis of the part, as shown in Figure 7.15, which can be removed from the capsule after analysis of the powder to assess the part quality with greater confidence. Using this larger volume, the edges

can be avoided and only the internal section of the volume assessed for porosity. The results of the study showed that repeat XCT measurements need to be incorporated into the experiment to establish the repeatability and accuracy of the results. An important consideration with this however, is the length of time that each XCT scan takes; particularly with a trade-off between time and resolution. Repeat measurements for multiple samples in an experiment can be prohibitively expensive and time consuming, particularly for an already expensive process for industry.

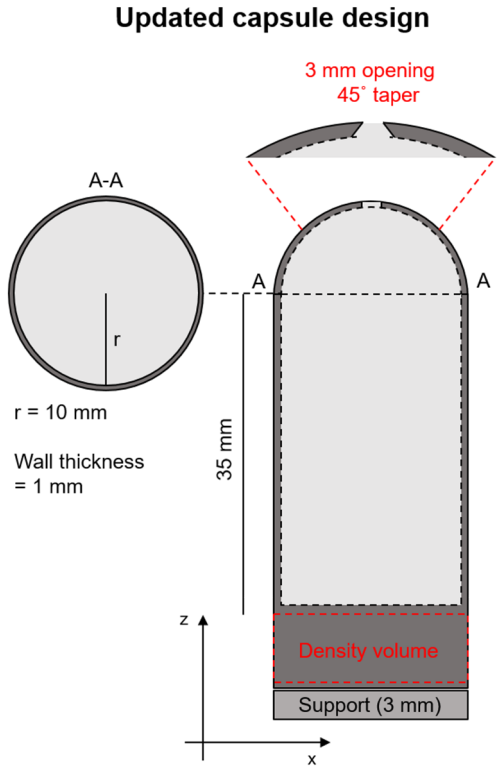

Figure 7.15 Schematic of design improvements to capsule including a modified opening for powder extraction and a solid base for improved porosity and part quality measurements

Another method to assess the part quality could be to analyse the surface quality of the capsules. The capsules contain a side wall, top surface (the top side of the base), and underhang/overhang (the dome top). These regions could be analysed using a surface measurement technique, such as confocal microscopy, to assess the effect of spatter particles in producing anomalies from large incorporated spatter particles which can cause defects. The overall roughness of the surface and large particular particles per area could form the quality metrics across the build plate.

Additionally, improvements can be made in the extraction of the powder from the capsule. The 2 mm hole at the top of the capsule allows the powder to exit the capsule completely but does so slowly, which can be problematic for processing large numbers of capsules. Subsequent to the testing study presented, a modified capsule opening was designed. As depicted in Figure 7.15, the new opening had a 3 mm diameter and a 45˚ chamfer inside and allowed better flow of the powder for removal.

The findings of the methodology test show how the powder in the powder bed can be different from the input feedstock powder and can vary across the bed. The variations are small and require further explanation but can contribute to the variations in parts commonly found to be an issue with PBF-LB. The test found trends in the variation across the powder bed and preferential spreading of the PSD, however, the change in the input powder between each build limits the conclusions that can be drawn for these. Nevertheless, it gives justification that these variations are present, could cause issues, and warrant further investigation. The methodology could also be adapted for future investigations for aspects of the process such as recyclability of powders, or to verify recoater or gas flow designs.

7.4 Summary

This chapter was aimed to meet the objective in this work of assessing the redistribution of material across the powder bed and the powder bed contents. It achieved this through the exploration of a capsule based methodology which allowed the analysis of samples of the powder bed from across the build plate. The exemplar run of the methodology demonstrated that the capsule method could assess the PBD, PSD, and spatter content and that this could be linked to the part quality. The results demonstrated that improvements could be made to the methodology and the method could be applied to a range of investigations of the powder bed. With these improvements the methodology would achieve its aims of being an accurate method of measuring the powder bed content (PBD, PSD, and spatter), to measure these over the powder bed, be simple and easy to replicate, and be applicable to other PBF-LB systems and investigations. The key findings from the chapter are:

- A methodology for assessing the powder bed contents was proposed and tested with three repeated builds which found a difference between the characterised feedstock powder and the powder in the powder bed
- The spreading of the powder showed signs of increased PBD at the centre of the start of the recoated layer, but the variation across the build plate is small and considered to be stable with a standard deviation <0.25% for each build, despite producing different average PBD. The changes in PBD were small but the capsule method proved accurate enough to measure these within error margins
- Variation in average PBD between builds (standard deviation of 0.98%) was greater than the variation within the builds. The cause of variation between builds is attributed to a change in the powder used between each build, likely due to powder handling or related to the hopper system. This produced a skewed PSD for the powder in each build with a decreasing fraction of large particles from build 1 to 3
- The amount of spatter in the powder bed varied across the build plate, up to 2.41% of the total powder content found in our investigation, with the gas flow distributing a larger proportion on the side of the gas outlet. There is still a proportion of out-of-specification powder found on the side of the gas inlet, showing there will always be spatter the gas flow can't remove. Still up to 1.12% of the total powder content and particles >200 µm found in capsule BD. It was suggested improvements could be made in collecting and measuring the spatter for comparison and estimation of the proportion in the bed
- During this investigation, only 9.1% of the build area was processed, to produce an average of 1.63% spatter powder in the build. A method is proposed to estimate the proportion of spatter which would be produced with an increase in the build utilisation. The increase of spatter content in the powder has implications within the build and for the recycling of the powder
- Large porosity (>65 µm) analysed by XCT showed a decrease corresponding with increased PBD and percentage proportion of large particles in the powder bed. It is proposed that this may be from a PSD skewed towards large particles which may allow larger voids between particles. 2/3 of the builds showed a trend in higher porosity related to the higher proportion of spatter but this was not conclusive. The XCT measurements were just of the 1 mm capsule walls which provided limited data, this

lead to the design of an integrated volume for part quality analysis for the new capsule design

- The exemplar results provided important information for the processing of powders in PBF-LB and identified areas for improvement for the method. Modification to aspects of the capsule design and the in situ methods were discussed to improve the data and results produced and to mitigate the shortfalls found in the exemplar run

It has been established that spatter particles are present in the powder bed and that the quantity of these particles are dependent on the location in the powder bed and also by the utilisation of the build volume. With current processing methods it is inevitable that these particles will be in the powder bed and therefore it is important to establish if and what effect these will have on the mechanical performance. Chapter 8 investigates the effect that spatter particles in the powder bed may have on the fatigue crack growth performance of Inconel 718 specimen.

Chapter 8 Effects of spatter on fatigue performance

It was shown in Chapter 5 and 6 that the spatter produced during PBF-LB processing is different from the virgin material and a significant proportion is out-of-specification. Chapter 7 demonstrated that there is a proportion of spatter particles in the powder bed, with certain distribution across the build plate, and the quantity is related to the build area processed by the laser. It was established that spatter particles can form defects in PBF-LB specimen due to lack-of-fusion from large particles and oxides which do not allow the full melting and penetration of the laser, and from oxides and nitrides that can remain in manufactured parts in the form of inclusions. If these materials are to be used to manufacture structural components it is important to understand the effect these particles, and subsequent defects, have on the mechanical properties of parts. To achieve this a set of specimens were manufactured with different levels of spatter powder incorporated as feedstock material. The different material levels were tested for fatigue crack growth (FCG). FCG testing, using fracture mechanics principles, represents the material fatigue resistance and allows greater consideration of defects and flaws present in a material. The testing measures the crack development in each cyclic loading, as a function of a fracture mechanic parameter, compared to measuring overall cycles to failure as in many common fatigue tests. Once the crack growth curve of a material of interest is known, the fatigue life of a component of this material can be determined for applications. This is crucial, and is common practice, in industries with high cyclic loading such as aerospace, that Nickel-based superalloy PBF-LB parts are targeted for. Specimens were also manufactured from wrought Inconel 718 to provide a base comparison of conventionally manufactured Inconel 718. The results of the FCGR testing are used to compare the performance of the PBF-LB material with wrought material and to establish the effect of spatter content.

8.1 Bespoke methodology

The spatter collection technique was the same as that used in previous chapters, described in Section 3.3.1. The powder used for the study was described in Section 4.1.3. The rest of the details of the methods, testing, and analysis relating to this chapter are described below.

8.1.1 Specimen manufacture

In order to test the effect of spatter particles on the fatigue performance of PBF-LB Inconel 718 parts, parts were manufactured using powder with three different proportions of spatter powder incorporated. The three levels investigated were: 0% spatter powder (100% virgin material), 50% spatter powder (a 50:50 mix of virgin and spatter powder), and 100% spatter powder. It was envisioned that the effect of the spatter particles may be small, therefore, the selected range of spatter powder content would provide the full spectrum of data for any effects that may be caused by the spatter. If 100% spatter did not have an effect on the part then it could be confirmed that it is not an issue for PBF-LB process.

The 'pure' spatter, which includes cold entrained, hot entrained and melt ejection spatter, powder was collected from beside the powder bed over numerous builds, in the same way as detailed in Section 3.3.1, to then be used as the powder feedstock for the parts. It is important to note that the spatter used for this investigation is the spatter 'as generated', with no sieving. Therefore, the testing was for the effect of spatter produced during the processing/build which lands in the powder bed and not representative of recycled powder. In the recycling operation the fraction of large particles out-of-specification, which will likely contribute to defects, would be removed. This would be an important future investigation, and is discussed with the results of this investigation.

The quantity of spatter produced during processing is small (in the order of tens of grams) compared to that used for a full build (kilograms) in PBF-LB as powder is required to fill the whole build plate, and considerable extra powder is required in the system for the build to be successful, regardless of specimen size. Therefore, spatter was collected over many builds to collect a reasonable (~1 kilogram) quantity of powder. Even so, this quantity of powder was less than that required to build CT specimens and adaption was required for the specimen and manufacturing. The CT specimen size for FCGR testing is defined in ASTM E647 [201] and BS ISO 12108 [202] standards for fatigue crack propagation testing. To adapt for the manufacturing constraints, with regards to spatter powder quantity, the specimen size was halved from commonly used dimensions (W = 32 mm). The dimensions used for the CT specimen in this study still satisfied the requirements in the standards, as described in section

A1.2.2 and A.1.2.6 in ASTM E647 [201]. The specimen size used is illustrated in Figure 8.1, where W = 16 mm and B = 8 mm. The manufacture was adapted also so that the investigated powder was only used to manufacture the central section of the CT specimen, through which the crack propagates as shown by the dark section in Figure 8.1. From this it can be seen the crack propagates perpendicular to the build direction (z), i.e. along the x-y plane.

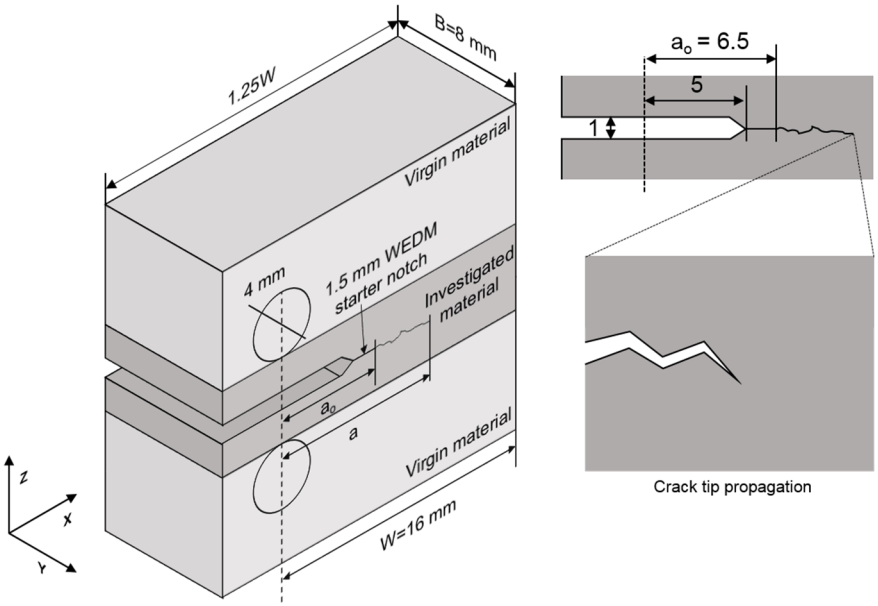

Figure 8.1 Schematic of CT specimen. The darker section depicts the central portion of the CT specimen which was manufactured with the investigated powder and where the crack propagates through. a_o is the starting crack length and a is the crack length measured at any moment.

The 0% spatter sample was manufactured as would be standard using virgin powder. To build the 50% and 100% spatter specimens, the build was conducted as three sections. The bottom section built with virgin powder, the powder was then changed and the middle section built with the investigated spatter powder, then the powder was changed back to virgin material to build the top section of the part. This could be achieved due to the setup of the LMF1000, which uses a bottom up powder feeder and has good access inside the chamber, as shown in Section 3.2.4 and in Figure 8.2. This allowed an easy change of the powder feeder and only the investigated powder required for the central section. The change in powder is illustrated in Figure 8.2, where it can be seen that the spatter powder is of a darker colour to the virgin material, indicative of oxidation. The powder bed was not disturbed during powder change but all powder outside of the powder bed was cleared during powder change to ensure the powder used for manufacture was known and controlled. The manufactured specimen can be

seen in Figure 8.2c. In the as-built specimens, the spatter powder section is visible by its darker colour compared the virgin material, but it is not in the final polished sample in Figure 8.2d.

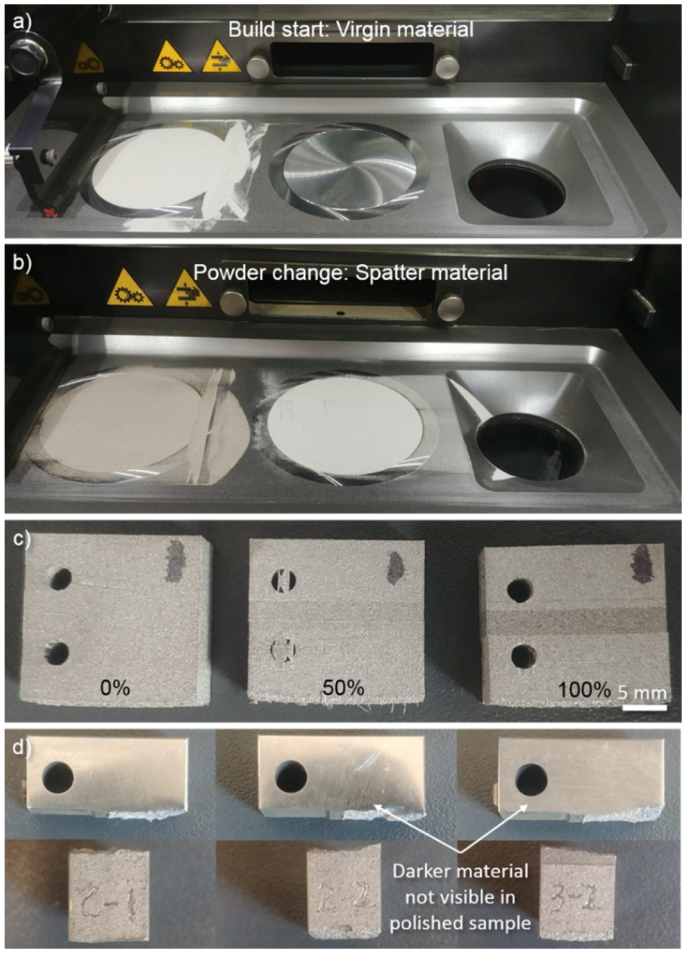

Figure 8.2 LMF1000 build chamber at a) start of build using virgin material and b) powder change using spatter material

The specimens were manufactured using the LMF1000 machine described in Section 3.2.4 using the proprietary processing parameters for Inconel 718, with a 40 µm layer thickness as in all other testing, and the specimen layout of the build can be seen in Figure 3.4 The virgin powder used was Supplier 1 Inconel 718, characterised in Section 4.1.1, and the spatter powder is characterised in Chapters 5 and 6. The change in powder for each build may warrant that the processing parameters are no longer optimised and decrease the quality of the parts produced, this provides additional factor of the effect of spatter incorporation into the feedstock powder. Heat treatments were not performed on the specimen to assess the direct effects of the spatter particles on the PBF-LB specimen. It was believed the specimen with

different spatter levels may be affected differently by the heat treatments and, therefore, influence the comparison between them.

Six specimens were produced in a build, for each powder mix investigated. The wrought material was a 1.25" diameter AMS 5663 wrought bar from DynamicMetals Ltd (Leighton Buzzard, UK) corresponding to ASTM B637 [123] and three specimens were produced. The specimens were manufactured oversized (1 mm extra on all faces) and wire electrical discharge machining (WEDM) was used to cut all specimens to the required size according to the standards, ensuring the samples were in the same condition. A thin, 1.5 mm long cut was included from the notch tip to produce a starting crack length a_o = 6.5 mm. WEDM is the preferred method for machining the specimens as it generates minimal residual stress in the sample and can be used as the final finish according to the standards. To further reduce any surface finish effects the x-z faces (shown in Figure 8.1) were polished with P800 SiC paper by hand.

8.1.2 Fatigue testing

The FCG experiments were carried out according to the ASTM E647 [201] and BS ISO 12108 [202] standards. The testing was conducted on an Instron 8810 (Instron, Norwood, MA, US), at a constant frequency of 10 Hz, in load control and with a load ratio $R = P_{min}/P_{max} = 0.1$, so that the sample was always in tension. The testing was conducted at ambient laboratory conditions. The crack length was measured via a potential drop (PD) method as detailed in section A6 of ASTM E647 [201], with a time step of $1x10^{-3}$ seconds and a voltage resolution of $1x10^{-9}$ V. Often a secondary crack growth measurement is used in FCGR testing such as a crack opening displacement gauge or side mounted cameras, however, this was not possible in this case as the experimental setup for the smaller specimen size made application of these techniques impossible. An issue was encountered with the welds of the PD wires to the samples, which during the testing of some specimens, broke under cyclic loading. This made the data for these samples unusable and lead to five usable data sets for the 0% material, four usable data sets for the 50% material, and three usable data sets for the 100% material. The PD data from these specimens still produced FCGR data and sufficient repeats according to the standards. The load conditions for the testing were conducted so that crack initiation

occurred after some thousands of cycles to ensure stage I slow crack growth occurred and testing continued to failure of the specimen. The crack length was measured via the PD measurements as it propagated through the specimens and was correlated to the final fatigue crack length measured from the fracture surface, defined from the fast fracture region, with crack curvature compensated for by averaging five points across the crack front according to ASTM E399 [203].

Fatigue crack propagation testing is used to produce complete or partial FCGR curves which aim to relate the crack growth rate (*da/dN*) to a suitable fracture mechanic parameter e.g. stress intensity factor (*ΔK*). The stress intensity factor *K* describes the stress state near a crack tip or notch due to a remote load and related to the specimen geometry. *K* is generally described by Equation 8-1:

$$K = \sigma\sqrt{a\pi} \qquad 8\text{-}1$$

Where σ is the applied stress and *a* is the crack length (or width for centre cracks) and the equation modified for the specimen and crack conditions. A schematic of a full fatigue curve is shown in Figure 8.3. The curve is characterised by three sections. Stage I is the near-threshold region with slow crack growth and a characteristic 'knee' into the linear stage. Stage I includes the crack threshold K_{th}, which theoretically, is the stress intensity amplitude below which a crack will have a negligible propagation rate. In stage II, linear crack growth rate occurs on the log-log plot, i.e. a power law relationship between the crack growth rate and fracture mechanic parameter, defined by the Paris law [204]. In stage III the crack growth rate accelerates rapidly to K_{IC} which denotes the stress intensity amplitude at which catastrophic failure occurs.

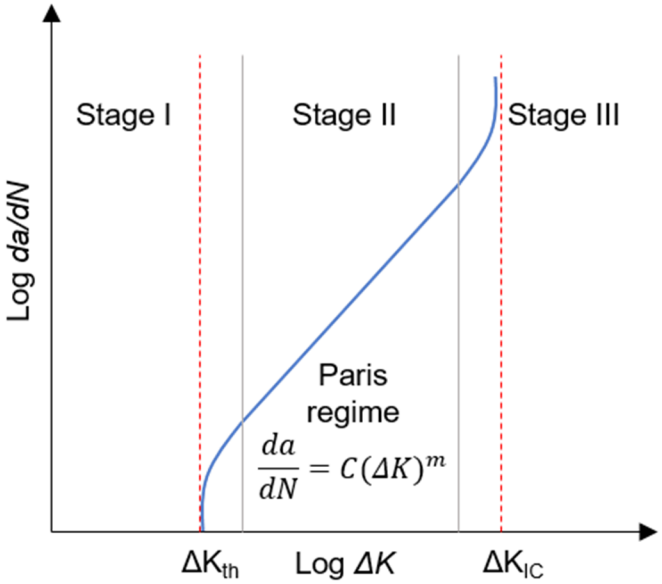

Figure 8.3 Complete fatigue curve demonstrating the three crack growth regimes and the material crack growth threshold ΔK_{th} and fracture toughness ΔK_{IC}

For each sample, a curve was created for crack length (a), illustrated in Figure 8.1 which is taken from the PD measurement, versus cycles (N). Corresponding with ASTM E647, data points were taken at regular 0.1 mm crack growth intervals and the Secant method was adopted as a data reduction technique and to establish *da/dN*, calculating the slope between two adjacent data points on the *a* - *N* graph [201]. Expressed as:

$$(da/dN)_a = (a_{i+1} - a_i)/(N_{i+1} - N_i) \qquad 8\text{-}2$$

Since the computed *da/dN* is an average rate over the (a_{i+1}-a_i) increment, the average crack size ā = ½(a_{i+1}+a_i) is used to calculate *ΔK*. Equation 8-3 was used to calculated *ΔK*, which was plotted against *da/dN* to construct the FCGR curve [201].

$$\Delta K = \frac{\Delta P}{B\sqrt{W}} \frac{(2+\alpha)}{(1-\alpha)^{\frac{3}{2}}} (0.886 + 4.64\alpha - 13.32\alpha^2 + 14.72\alpha^3 - 5.6\alpha^4) \qquad 8\text{-}3$$

Where $\alpha = a/W$, ΔP is the load applied, and B and W are the specimen geometry, which for the samples is shown in Figure 8.1. The Paris constant C and exponent m from the Paris equation (8-4) were determined using Excel's in-built curve fitting function for the central linear region of the da/dN - ΔK curves for each specimen.

$$\frac{da}{dN} = C(\Delta K)^m \qquad 8\text{-}4$$

Each specimen was analysed individually and average results and FCGR curves created for wrought, 0%, 50%, and 100% spatter material to allow comparison. The test data covered the three regions of the fatigue curve, starting with short crack growth in region I and a typical bend into the linear region II, which produced the crack growth threshold K_{th} and the Paris constants C and m. The test was run until final fracture of the specimen to establish the critical failure threshold of the specimen, K_{IC}. K_{th} is most commonly established via load shedding techniques to obtain the crack growth at low da/dN (between 10^{-9} and 10^{-10} m/cycle). Only constant load testing was conducted in this study and the crack growth rate was in the range of 10^{-8} m/cycle, therefore, according to ASTM E647 [201] and BS ISO 12108 [202] the K_{th} was extrapolated for the ΔK corresponding to da/dN = 10^{-10} m/cycle from the linear fit of the first five data points. The extrapolation gives an approximation for the K_{th}.

8.1.3 Sample assessment

The surface roughness of the CT specimens were measured using an Alicona InfiniteFocus focus variation instrument using a 20x objective lens. Three surfaces were measured and an S_a = 0.17 ± 0.05 µm was measured for the polished surfaces. This was within the roughness guidelines set by the standards for the test, which were 1.6 µm in ASTM E647 and 0.4 µm in BS ISO 12108.

For the microstructural assessment a Hitachi TM3030 SEM was used to image the specimens. To prepare the specimen for metallurgical analysis, specimens were cross sectioned and mounted in non-conductive Bakelite resin. The cross sections were wet ground using P240 and P400 SiC paper before being polished progressively through diamond polishing

suspensions of 9 µm (Struers MD-Largo wheel) and 3 µm (Struers MD-Dac wheel) and finally with a 0.04 µm colloidal silica suspension (Struers MD-Chem wheel). Before imaging, the specimen were cleaned in an ultrasonic bath using Isopropanol.

The relative density of the specimen was measured using image analysis and the image processing software ImageJ [189,190]. SEM micrographs were taken from the xy, xz, and yz surfaces from the uncracked section of the CT specimen. The surfaces were imaged at least 1 mm away from the WEDM surface to ensure the microstructure was not affected. The SEM images were thresholded using ImageJ's automated threshold function 'Minimum' so that the bulk material was white and the voids black. The 'Minimum' function assumes a bimodal distribution of pixel grey values and the histogram is iteratively smoothed using a running average of size three, until there are only two local maxima. The threshold t is such that yt−1 > yt <= yt+1. The proportion of white pixels in the processed images represents the relative density of the material. The images from all three planes are then used to produce an average relative density and standard deviation.

After testing, the fracture surface of the specimens were imaged using a Nikon SMZ745 (Nikon Corporation, Japan) stereo microscope and the crack length measured. The fracture surface was interrogated further using the Hitachi TM3030 SEM with BSE mode and EDS to show details of the fatigue cracking and identify oxides. As depicted in Figure 8.4, the fracture surface was cross sectioned and the profile mounted, undergoing the same metallurgical preparation, to analyse the fracture profile.

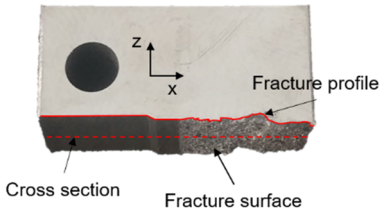

Figure 8.4 Illustration of fracture surface and profile of fatigued CT specimen analysed

The fracture profile of a 100% spatter sample was analysed using EBSD by the Nanoscale and Microscale Research Centre (NMRC) on a JEOL 7100F FEG-SEM. The scan was conducted on 30 frames in a 6 x 5 grid at x150 magnification with a step size of 6 µm which was then stitched

to produce the results. Two cycles of noise reduction were applied using four neighbours. The scan area of the EBSD was the fracture profile including the near region of 100% spatter material through to the transition to virgin material. The scan comprised a larger area of 100% spatter material but allows comparison between the microstructure, texture, and grains produced in the PBF-LB processing of each material. The scan was conducted by the NMRC and they provided the data for the different regions which was analysed and graphed by the author.

8.2 Results

8.2.1 Crack growth behaviour

The fatigue crack data for the CT specimens produced with different levels of spatter material and conventional wrought material are presented in Figure 8.5a, showing the average for each material. The *da/dN - ΔK* plots show a difference between the wrought material and the PBF-LB material, with the wrought material exhibiting a lower crack growth rate and higher *ΔK* range before failure. The PBF-LB specimen showed an increase in crack growth rate with increasing levels of spatter.

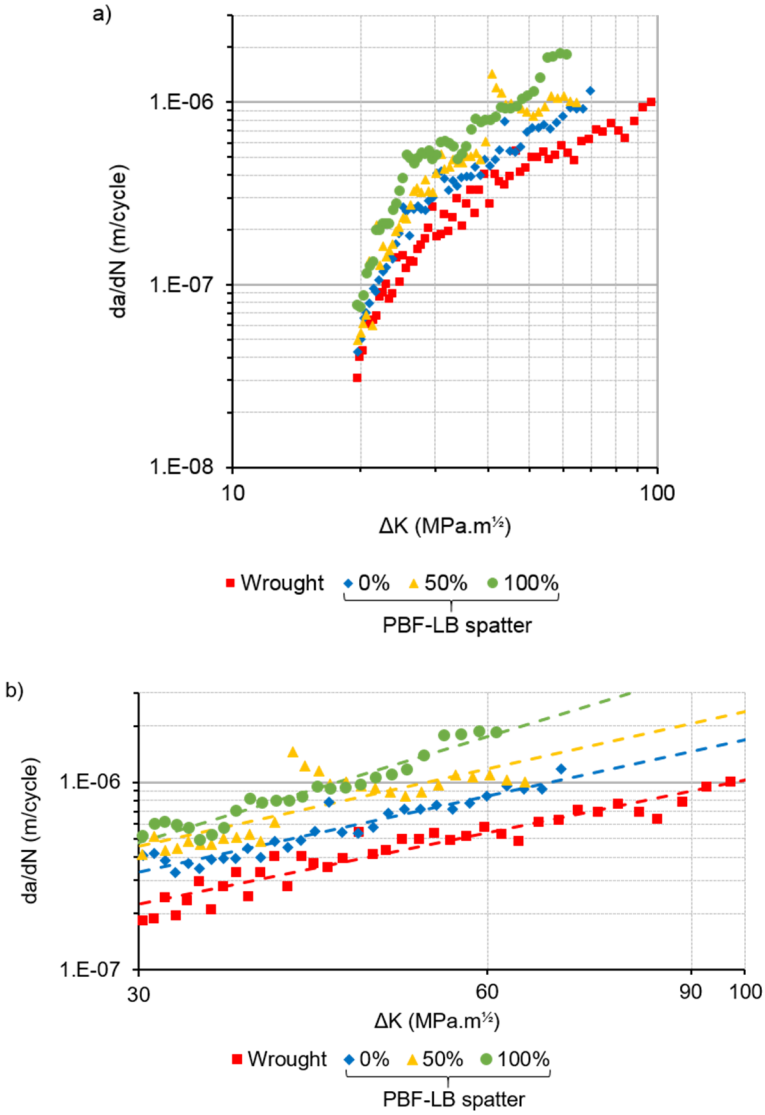

Figure 8.5 Average fatigue crack growth data for PBF-LB specimen with different levels of spatter and wrought material for a) the whole tested range and b) the Paris curve and regression fit for each material – the Paris constants C and m are listed in Table 8.1

Table 8.1 Average fatigue crack growth parameters for the material

	K_{th}	K_{IC}	C	m	R^2
Wrought	11.42 ±0.02	101.96 ±0.39	3.00×10^{-9} ±7.147×10^{-9}	1.27 ±0.07	0.91
0% spatter	10.42 ±0.01	69.96 ±0.59	3.29×10^{-9} ±5.098×10^{-9}	1.36 ±0.17	0.91
50% spatter	12.49 ±0.01	65.99 ±1.55	4.39×10^{-9} ±2.453×10^{-9}	1.37 ±0.20	0.64
100% spatter	9.08 ±0.01	65.52 ±1.78	8.01×10^{-9} ±1.202×10^{-10}	1.88 ±0.10	0.93

The crack initiated in stage I crack growth in all specimens and produced a typical 'knee' into the linear crack growth region II described by the Paris equation, shown in Figure 8.5b. The

constant *C* and exponent *m* in the Paris equation (Equation 8-4) are shown in Table 8.1 for each material. For comparison between the materials, *m* indicates the sensitivity of the crack growth to changes in load. The fatigue crack growth curves showed that the wrought material had the greatest resistance to fatigue crack growth and that within the PBF-LB specimens the increase in the proportion of spatter increased the crack growth rate. The materials displayed this trend with increasing spatter content for *m*, although the 50% spatter material exhibited a similar rate to the 0% material. The averaged results of the 50% material were influenced by a specimen, denoted as S50-3, with a particular spike in *da/dN* midway through the specimen, as can be seen in Figure 8.5. This specimen recorded the highest crack growth rate of any specimen with peak *da/dN* = 4.26 x 10^{-6} m/cycle and failed more quickly than all other 50% spatter samples. The specimen, and the significant spike in the data, skewed the Paris parameters for the 50% spatter average, as indicated by the low correlation factor (R^2) of 0.64. Without the specimen S50-3, *m* for the 50% material was 1.52 ± 0.1 (with an R^2 of 0.90), continuing the increasing trend in *m* with the rest of the materials.

The results found Paris exponents lower than those typically found in the literature for Inconel 718, for PBF-LB material [162] and for wrought material [205–207], and it could not be identified as to why. The Paris exponent is dependent on the stress range, the test environment, and testing procedure and therefore, may be due to the reduced specimen size for this testing [208,209]. However, the specimen size shouldn't cause significant change with the testing run according to the ASTM and BS ISO standards. Whilst the Paris exponents established may be different and limit comparison with other literature, it doesn't bear on the comparison between the samples in this study tested under the same conditions.

The other parameters obtained from the fatigue crack growth curve were the fracture toughness K_{IC} and the fatigue crack growth threshold K_{th}. K_{IC} critical stress intensity at which the specimens failed catastrophically showed a marked difference between the wrought material, with 101.96 MPa.m^{½}, to the 0% spatter PBF-LB material, with 69.96 MPa.m^{½}. The incorporation of spatter lead to a decrease in K_{IC} for the PBF-LB material, but the level of spatter did not appear to have much effect. The K_{th} is the value below which a crack will not propagate and is extrapolated from the data for the crack growth at 1 x 10^{-10} m/cycle as described in Section 8.1.2. The wrought material showed similarity to those found in literature for wrought Inconel 718 of 12 - 14 MPa.m^{½} [205,206], however, the K_{th} for the PBF-LB material

was higher than the previous study by Konečná *et al.* for PBF-LB Inconel 718 of 3 MPa.m^{½} [162]. Konečná *et al.* discussed that their reduced K_{th} could be due to their PBF-LB specimens' crack notches being an as-built geometry, introducing local microstructure variations and residual stresses. As for many of the other parameters, the 50% spatter samples K_{th} deviated from the trend shown by the other materials. This can again be partly attributed to the scatter in the data produced by the spatter material. As described in Section 8.1.2 the K_{th} was extrapolated from the first five data points and scatter in the 50% sample skewed the linear fit, increasing the K_{th} value. Although, without the S50-3 sample, the $K_{th}$was still 11.33 MPa.m^{½} and outside of the predicted decreasing trend of K_{th} with increased spatter content.

Scatter in the results is introduced by inconsistencies in the material. Despite the trends shown in Figure 8.5, the results from Table 8.1 showed that the results for the standard deviations for the Paris exponents and K_{IC} were large, and the changes, not statistically different. Figure 8.6 shows the full data from all PBF-LB specimens demonstrating the scatter and overlap between materials. This indicates that although trends can be seen, given the overlap of some data points, a greater sample size for testing would be required to produce statistically significant results. This could also be beneficial to assess the reproducibility of the results from build to build. However, to produce more samples for testing in this study, a significant quantity of spatter would need to be produced and collected. It is known that PBF-LB materials have variabilities due to defects, microstructure, and residual stress. Cain *et al*. [160] found high scatter in FCGR results introduced by these factors for PBF-LB Ti-6Al-4V. For the Inconel 718 specimens the greatest scatter was in the 50% spatter material. The spike which affected the trend in the Paris constants can be seen labelled (A) in Figure 8.6, which will be explored in greater detail in the following section, and labelled (B), the data points which skewed the K_{th} extrapolation can be seen. It was expected that the 100% material would exhibit the highest scatter due to the higher level of spatter material, however, this could likely be an example of the randomness that the spatter material can cause in the process, the variability which is found in the PBF-LB process, or the lower number of usable data sets for the 100% material. Despite the incorporation of more spatter, some specimen with 50 and 100% spatter material performed similarly or better than the lowest 0% material and some 50% material performed worse than the 100% material. Although overlap was found between some specimens, from the data collected it was possible to show the overall effect of increasing spatter content producing a reduction in fatigue performance in the specimens.

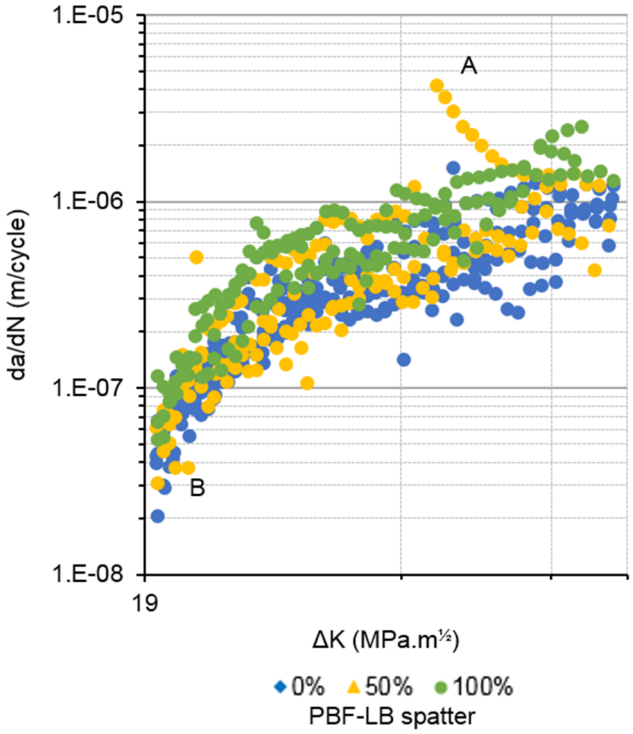

Figure 8.6 All fatigue crack growth data for the PBF-LB specimen demonstrating the large scatter in results and the overlap between the 0, 50, and 100 % spatter material

The effect of spatter and comparison between wrought and PBF-LB material can be most clearly seen in Figure 8.7, which shows the crack length as a function of cycles to failure for the various materials tested. The total crack growth cycles to failure for the wrought material was approximately 40% greater than that for the virgin PBF-LB material. The incorporation of 50 % spatter material decreased the cycles to failure of the PBF-LB specimen by 25 %, and with 100% material, the cycles to failure decreased by 54% compared to the virgin material. Figure 8.7 also shows the large variation in the 50% material with cycles to failure above and below the average levels of the 0% and 100% material indicating the high scatter. The PBF-LB materials all show greater scatter than the wrought material.

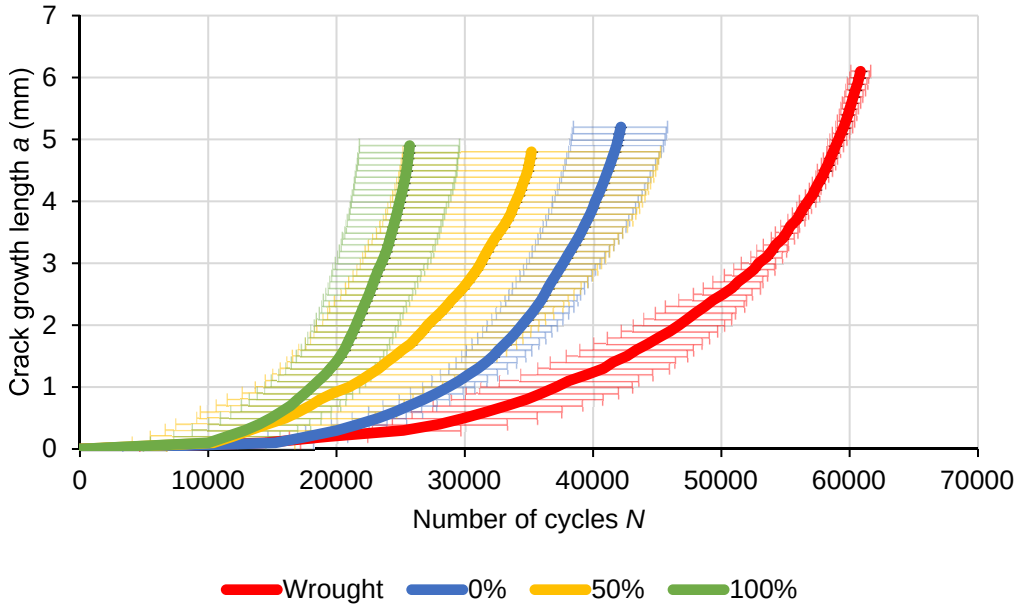

Figure 8.7 Crack length (a) against average number of cycles (N) to failure for each level of spatter material and the wrought specimen with scatter bands represented by the standard deviation of N for each a

8.2.2 Fracture analysis

8.2.2.1 Fatigue crack growth

The local crack growth rate is determined by the microstructure, residual stresses, and defects present in the part. The influence of these factors can be seen in the fracture surface. The micrographs of fracture surfaces in Figure 8.8a&b show considerable differences between the different materials tested. In the stereo microscopy images the wrought material appears to have propagated in a mostly constant and homogenous manner, whereas the PBF-LB material shows many variations and inconsistencies in the fracture surface and therefore the crack growth. These can be seen in greater detail in Figure 8.8c&d, the wrought specimens produced local deviation in the crack path related to growth through the microstructure. The PBF-LB specimens exhibited larger deviations in the crack path compared to the wrought material which may be due to defects distributed throughout these specimens, with the fatigue crack path deviated to pass through areas where fracture resistance is lower. At higher magnification the fracture surface is characterised by transgranular cracking with ductile fatigue striations and fine secondary cracks for both materials. In the PBF-LB specimens oxides

were present on the surface and in Figure 8.8f a 2 µm oxide particle can be seen in the fracture surface. The fast fracture in Figure 8.8g&h showed ductile fracture caused by microvoid coalescence which produced the dimpled appearance. The reduced size of the dimples/voids in the PBF-LB specimen is likely related to the increased proportion of inclusions and defects, the finer microstructure, and the residual stresses present in the PBF-LB specimens. These factors also likely caused the 31% decrease in the K_{IC} for the PBF-LB specimens compared to the wrought.

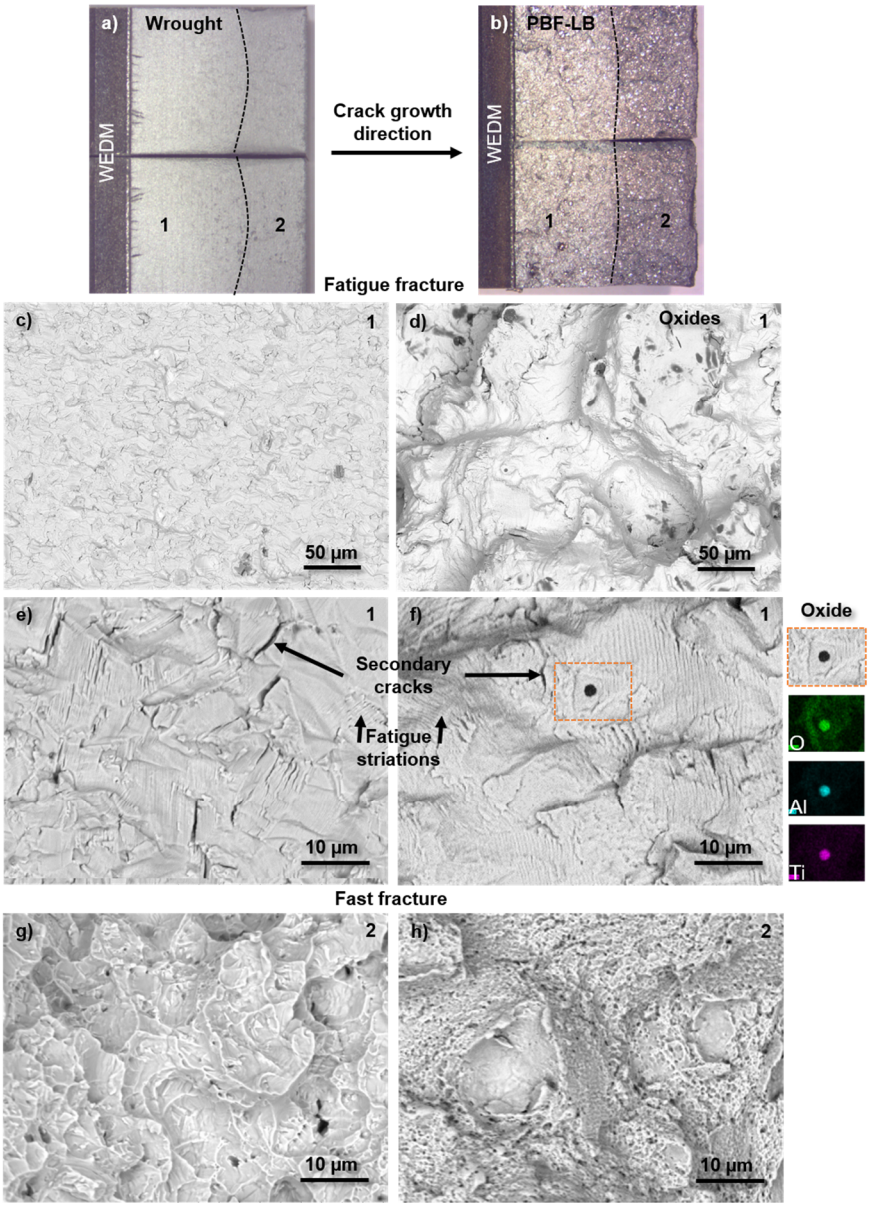

Figure 8.8 Fracture surfaces of wrought (a,c,e,g) and PBF-LB specimen with 0% spatter (b,d,f,h) stereo microscopy showing a general overview of the fracture surface (a&b), BSE-SEM of the fatigue fracture at two magnification levels (c-f), and BSE-SEM of the fast fracture surface (g&h). Crack growth is from left to right in each image.

8.2.2.2 Influence of defects on crack growth

The FCG rates in the PBF-LB specimen were influenced by the defects in the material. Figure 8.9 shows examples of the defects found on the fracture surface of the PBF-LB specimens which contributed to the crack growth rate. Evidence of each these defects were found in all of the PBF-LB materials.

A lack-of-fusion defect is shown in the fracture profile in Figure 8.9a right next to the WEDM notch where the crack initiated. It can be seen that the crack propagated straight for 84 µm before deviating and encountering the lack-of-fusion defect, the lack of material at this point meant that locally the crack skipped from 84 to 743 µm in length. The fracture surface in (c) shows the crack initiation denoted by the white line, with an oxide inclusion connected to it and another oxide and nitride inclusion just after initiation. These inclusions will likely have influenced the initiation and early propagation of the crack. The EDS maps in (e) show the aluminium oxides and titanium nitrides. The oxides and nitride inclusions in (c) were at different heights (related to build direction z) in the material and the fracture surface shows that the crack propagated along both heights to simultaneously travel through both these weaknesses in the material.

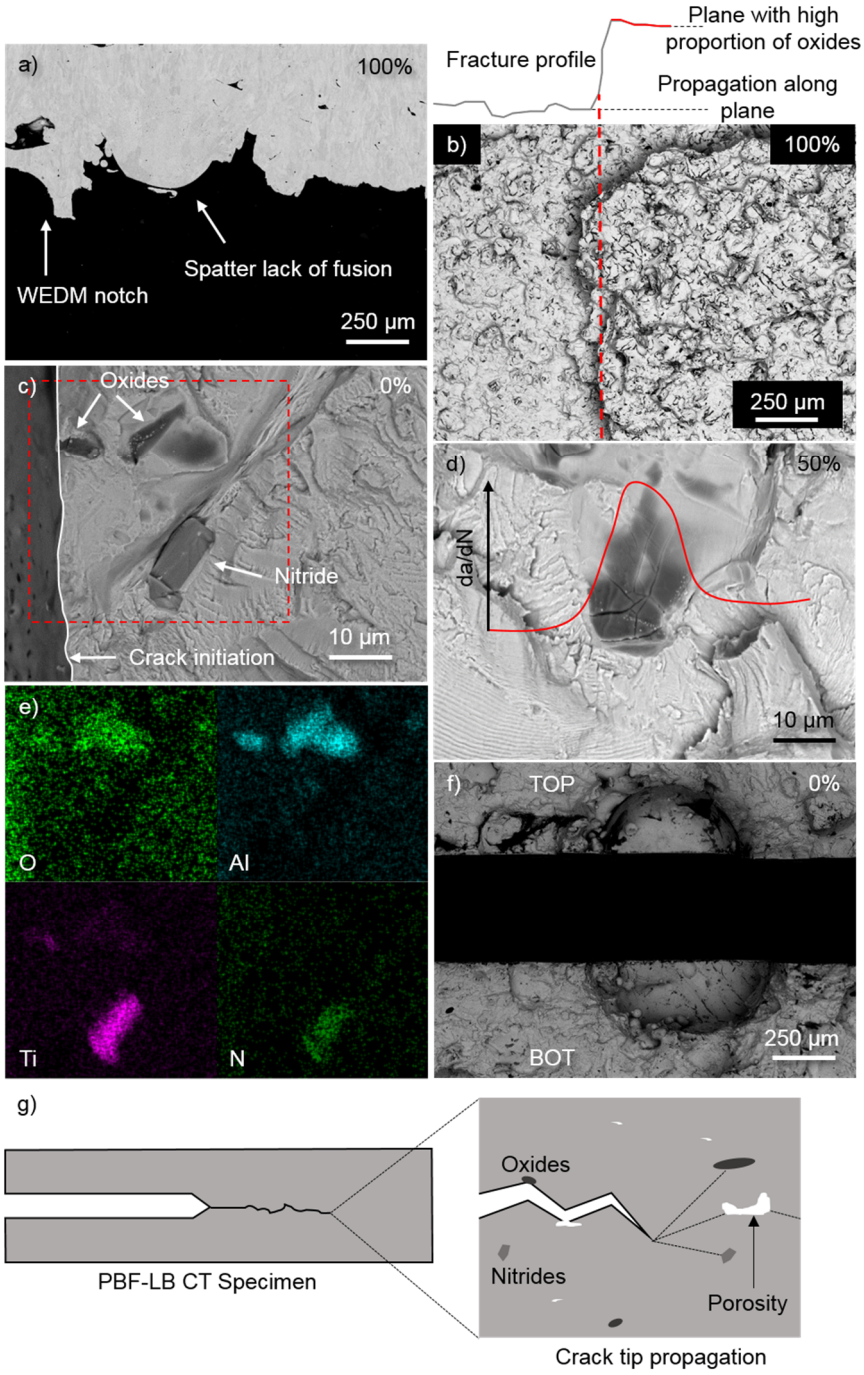

Figure 8.9 Range of defect types across the different PBF-LB material levels. The material the image is from is in the top right hand corner but evidence of all the defects were present in all the materials.

In certain sections of the PBF-LB materials the crack was found to have jumped to a different plane during propagation, an example of this is shown in Figure 8.9b. The crack was initially propagating along the plane on the left hand side of the image before it jumped to the relative higher plane on the right hand side which can be seen to have a higher proportion of dark

oxides. A schematic of what would be seen in the fracture profile relating to this is shown above the image. As discussed in previous chapters, the oxides do not wet with the material if they are not melted, therefore, where they are present in the material they are a void and the crack deviates and accelerates through the void. The schematic in Figure 8.9d demonstrates how the crack growth rate *da/dN* accelerates as it encounters these defects showing, as in Figure 8.8f earlier, how the striations propagated up to and then skip passed the defect. The micrograph in Figure 8.9f depicts the cup and cone type lack-of-fusion defect from a large (598 µm) spatter particle in the 0% spatter material. This is important in highlighting defects incorporated by spatter in the specimen processed by virgin material occurring from spatter landing back into the powder bed. Figure 8.9g shows a schematic of these effects. The crack propagates through the material, locating and propagating through weaker regions of inclusions and defects in the material present from the spatter particles and PBF-LB processing.

8.2.2.3 Specimen S50-3 case study

The scatter and decreased performance of the PBF-LB specimen and the decrease in performance was related to the level of defects in the material. The specimen which skewed the FCGR results of the 50% material most clearly, denoted as S50-3, demonstrated the influence of defects and defects playing a critical role in the performance of the material. Figure 8.10 depicts the defect which caused the spike in *da/dN* for S50-3. The spike was caused by two close defects present in the specimen which accelerated the crack growth and the crack jumped between. Figure 8.10a&b show an overview of the fracture surface and the spike, which occur at a crack length of 10 mm. (d) shows a magnified view of the two defects. The defect (II) was a large spatter particle, the underside of which is seen in (e) and the lack-of-fusion defect area where it landed can be seen in (g), with a diameter of 478 µm. The scan tracks of the surface below, and oxides along them are visible in (g). The EDS in (f) shows that the particles in (g) are Al and Ti oxides, as characterised previously in Chapter 5. This demonstrates that the laser did not melt the large spatter particle, causing the large lack-of-fusion defect. Defect (I) appeared to be due to balling. It produced a similar cup and cone type defect to the spatter defect (II) but the ball had connection to the bottom layer at the base of the ball, with lack-of-fusion occurring around it. The two halves of the fracture profile are shown in (c) showing the crack jumped from defect (I) up to the defect (II) and beyond this

started to onset shear and failure on this side of the specimen. The height difference between these defects indicates that they were produced about 16 layers apart during manufacture, calculated by identification of the features in (c). This specimen, S50-3, failed 30% earlier than the 50% spatter material average and at the same as the 100% spatter material average, leading to the skew in the data for the 50% material discussed previously. The premature failure of this specimen can be attributed to the effect of these two adjacent defects.

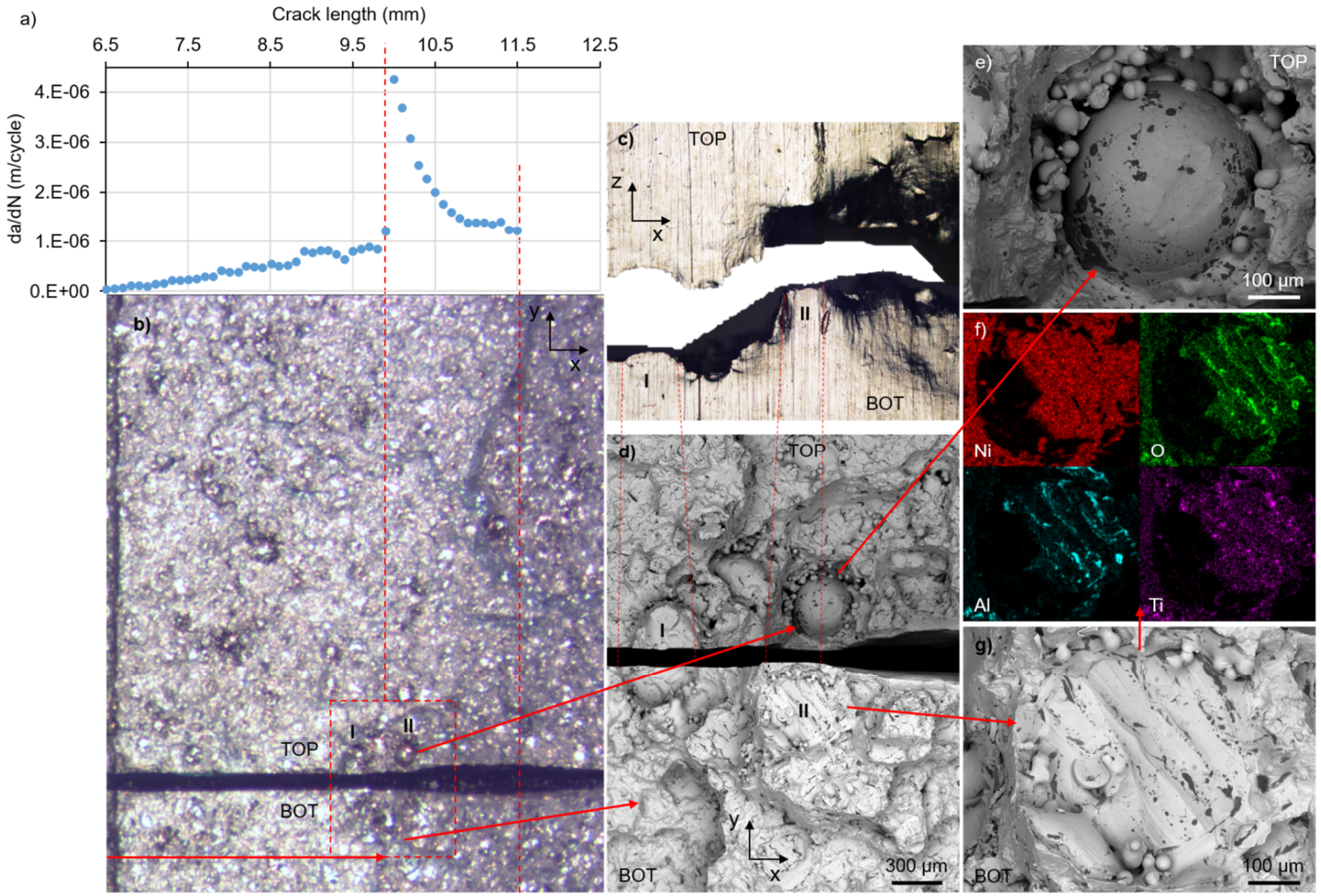

Figure 8.10 Analysis of the critical defect in specimen S50-3 of the 50% spatter material which produced the highest crack growth rate da/dN and contributed to large scatter and skew in the FCGR results: a) da/dN v crack length correlating the spike in da/dN to the defect on the fracture surface in (b), c) shows the fracture profile at the defect, d) shows the fracture surface at the defect, and e-g) shows either side of the defect due to a large spatter particle

8.2.3 As-built PBF-LB specimen

The as-built PBF-LB CT specimens were analysed to assess the effects of the incorporation of spatter material on the built specimens and features which may have influenced the fatigue crack growth rate.

8.2.3.1 Microstructure

The as-built CT specimens for each material demonstrated typical directional microstructures of PBF-LB Inconel 718, as has been reported in previous studies [124,125,127,210], and no visible difference was found between the 0, 50, and 100% spatter material. Figure 8.11 shows the grain alignment and structure of each material in all three planes. They exhibited an elongated columnar grain microstructure with epitaxial growth in the build direction (+z) through many build layers. This directional solidification occurred due to the vertical heat flux (-z) between the solidifying melt pool and cooler solidified material in the bulk/substrate. The columnar grains were of solid solution γ fcc matrix with γ'' bct-(Ni_3(Nb)) as shown in previous studies [128,211]. From the visual assessment the grain structure produced from each spatter powder level appeared to be similar.

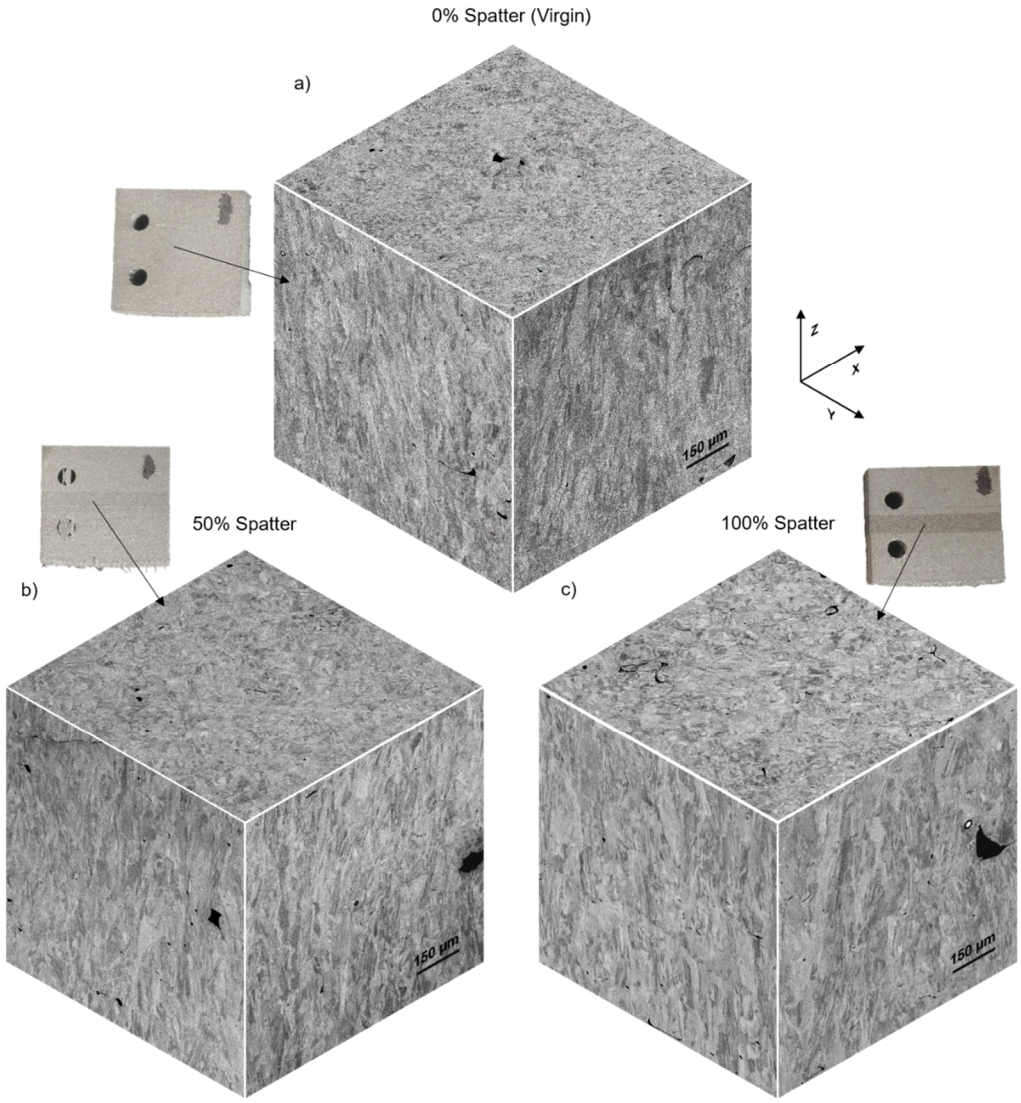

Figure 8.11 BSE-SEM micrographs showing the microstructure of the as-built material in the crack propagation area with a) 0% spatter or virgin material, b) 50% spatter, and c) 100% spatter specimen

Figure 8.11 shows the overall grain microstructures of the CT specimens for each spatter material investigated. Figure 8.12 shows the grain alignment and structure produced from 100% spatter material and the virgin material in a single specimen to assess the microstructure within a single specimen as well as between builds. This further indicates that there was minimal change in grain microstructure due to the changes in powder from virgin to spatter material.

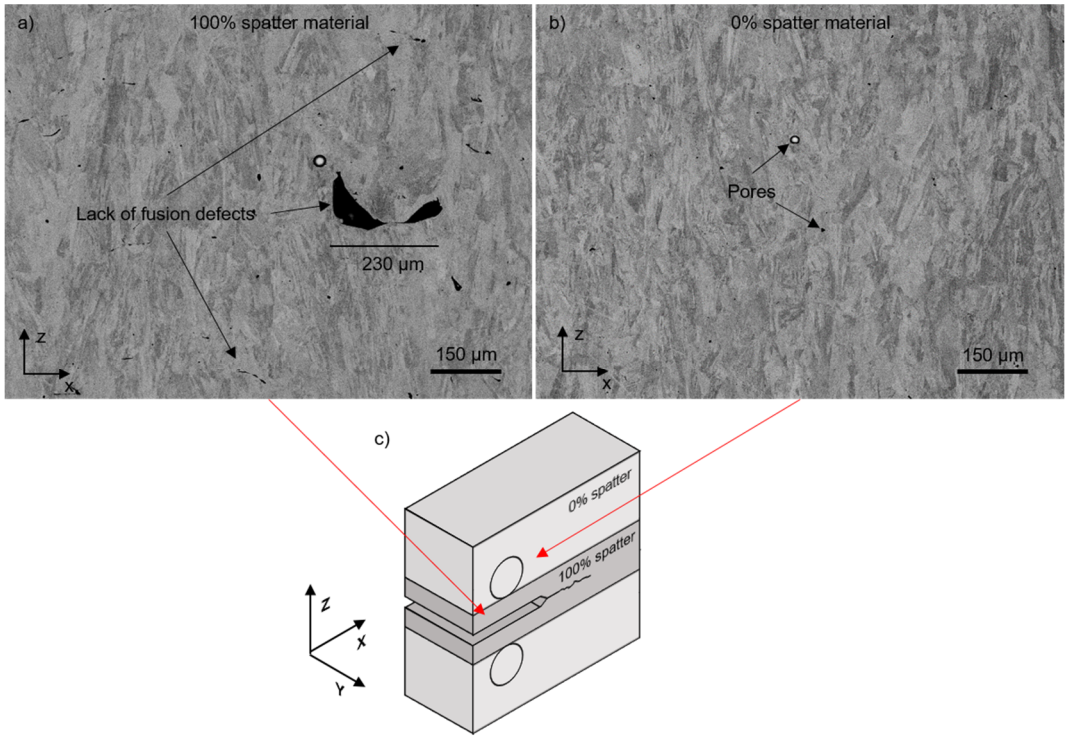

Figure 8.12 BSE-SEM micrographs of the x-z plane of 100% spatter specimen showing regions of a) 100% spatter material for crack propagation, b) 0% spatter fresh material section used to build the rest of the specimen, and c) illustration of the areas of the CT specimen imaged

8.2.3.2 Defects

Compared to the grain microstructure, greater difference was found in the defects present in the materials. The virgin material in Figure 8.12b showed predominantly small and regular porosity in the material indicating suitable processing. The 100% spatter material in Figure 8.12a showed a greater size and quantity of pores and defects in comparison. Many of those seen were lack-of-fusion defects, characterised by the high aspect ratio of the defects, which were generally orientated perpendicular to the build direction (z), in this case along the x-axis. This type of defect formation is demonstrated in Figure 8.12a by the large 230 µm diameter void in the material due to a large spatter particle which did not allow full penetration of the laser and full melting of the material. The other irregular pores may have be due to larger voids between the larger particles of the spatter material packed in the powder bed or due to oxides on the melt pool surface which did not melt and did not wet to the material above it. The spherical pores are likely due to gas porosity from vapour generation or gas entrapment in the powder or from the processing chamber.

Despite the difference in the 100% spatter and 0% spatter in the single specimen in Figure 8.12, comparison of the relative densities from the different specimens in Figure 8.11 did not show a marked difference between the samples built with different spatter proportions. The different relative densities for the samples were 99.52 ±0.21, 99.27 ±0.50, 99.43 ±0.10% for the 0, 50, and 100% spatter specimens respectively, measured across xz, yz, and xy planes. It is envisioned that this could be due to the difficulty of representing defects present throughout the bulk material with 2D reference planes. Using a 3D method such as XCT would be more appropriate for measuring the size, quantity, and distribution of defects throughout the specimens and would show a greater difference between the three proportions of spatter.

8.2.3.3 Texture

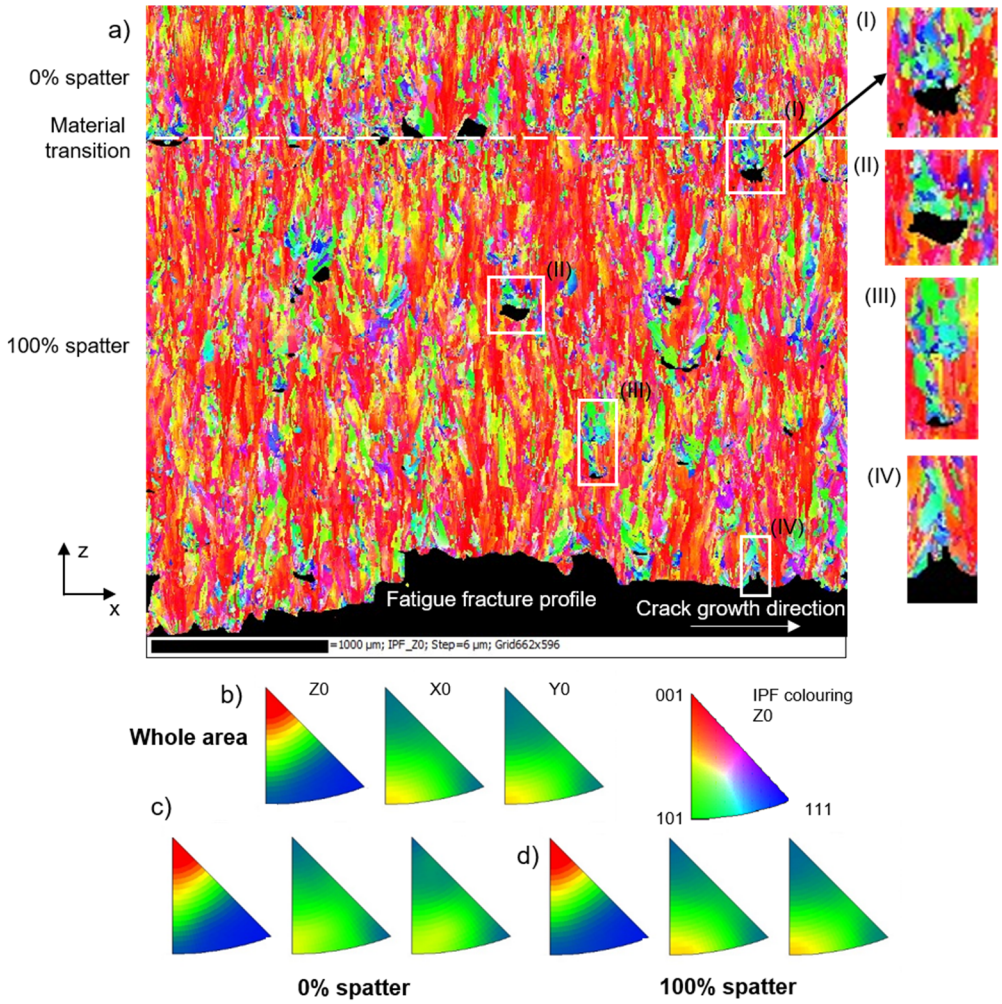

Figure 8.13 EBSD results from 100% spatter section including the fatigue crack and transition and 0% spatter region: a) showing the area scanned with columnar grain growth along the build direction and b-d) the inverse pole figures for each region and the whole scan showing strong <001> texture along the build direction Z0 and showing little difference between the 0% and 100% material regions

Similarities in the grain microstructure of the materials was further evident in the EBSD scan of the 100% spatter specimen and the transition into the virgin material. Figure 8.13 shows the grain texture and orientation from the fatigue fracture in the 100% material through to the transition to 0% spatter material. It can be seen that the grains are strongly textured along the <001> build direction and that there is minimal change between the two regions. It seems that there is a degree of misorientation of the grains above voids in the material as highlighted by the subsets (I-III), likely due to changed cooling conditions in these areas which are less directed and increase the misorientation. This could give an indication of areas of voids in the material which the crack propagated through, as seen in the fracture surfaces. Subset (IV) shows a possible example of misoreientated grains above a possible void in the crack profile. However, it is clear that there are areas of misorientated grains which do not appear to be related to a void, or at least not visible in the cross section.

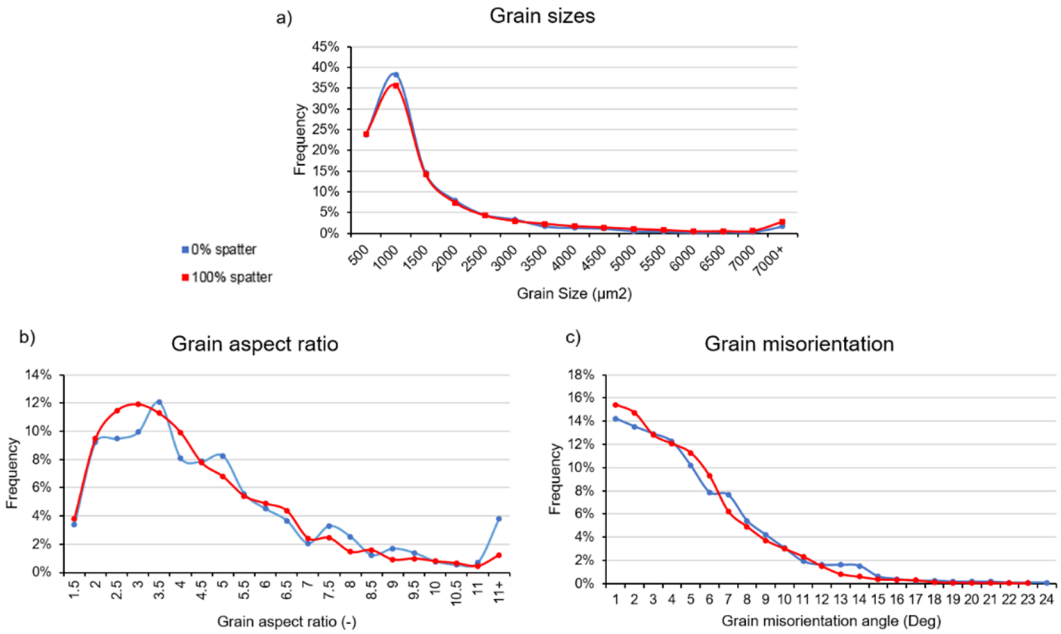

Figure 8.14 Comparison of the 100% spatter material and 0% spatter material for the a) grain size distribution, b) grain aspect ratio, and c) grain misorientation taken from the EBSD scan. The bins are for values under the bin size on the x-axis unless stated as over (+)

Further analysis of the grains in each region are presented in Figure 8.14. Little difference was found for the distribution of the grain size in (a) and misorientation (c). The aspect ratio (b) showed a degree of difference, with the largest change in the proportion of very high aspect ratio (11+) grains, but still with considerable overlap. The spatter material had a higher

proportion of lower aspect ratio grains, particularly between the ratios of 2 - 3.5, which could indicate that the oxides or larger defects in the specimen had the effect of inhibiting epitaxial growth. Overall, the analysis of the grains between the 100% spatter powder and virgin material regions from EBSD found little difference between the two grain microstructures, as indicated by the micrographs in Figure 8.11 and Figure 8.12.

8.2.3.4 Inclusions

A closer inspection of the transition from the 100% spatter to virgin material showed an enrichment of Oxygen and oxides along the region. This Oxygen rich layer can be seen below the white line in Figure 8.15 in the BSE-SEM micrograph (a&b) and in the EDS Oxygen mapping (c). EDS quantitative analysis either side of the transition gave an Oxygen content of 0.30 ± 0.12 wt% in the 0% spatter region and a 0.62 ± 0.14 wt% in the 100% spatter region. EDS is less sensitive for light elements so these values are not taken as absolute but indicative that there is an increase in Oxygen content between the 100% spatter processed material and the virgin material. This would correlate with the LECO analysis of the Oxygen content of each powder shown in Chapter 6. Figure 8.15d shows a section of the 100% spatter material and the presence of Al and Ti oxides that have formed in the material or been transferred to the material from the spatter particles. These oxides were also present in the material produced from virgin powder as was shown in previous chapters.

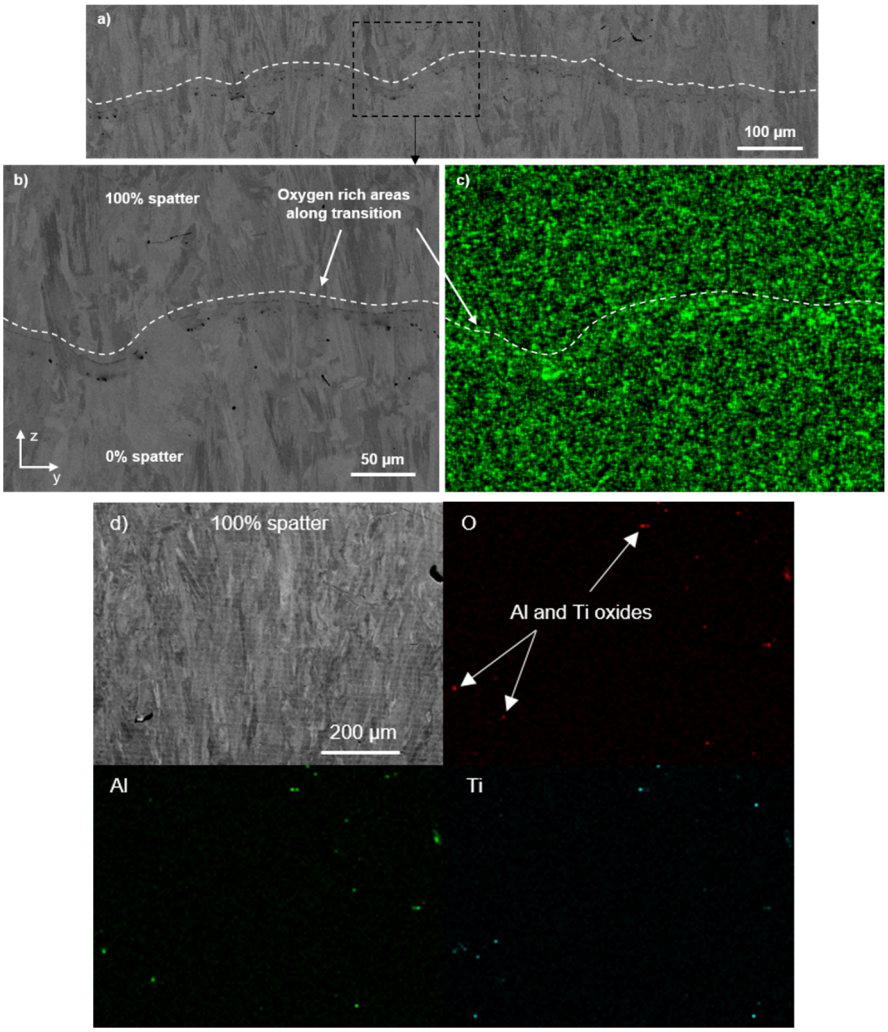

Figure 8.15 a) BSE-SEM micrographs of transition from 0% spatter to 100% spatter material showing an Oxygen rich layer along the transition line with b) showing a region with higher magnification, c) shows the corresponding Oxygen EDS map. The white line is included as a guide and is placed above the Oxygen rich layer. d)EDS maps showing oxides present within the 100% spatter material

As well as oxide inclusions due to incorporation from the oxides present in the spatter and oxides that were formed during the processing of the specimen, titanium nitrides were also present in the specimen, as seen on the fracture surfaces. Evidence of these particles are shown in Figure 8.16, remaining from inclusions within the feedstock powder, shown in Section 4.1, which are not melted or removed during processing.

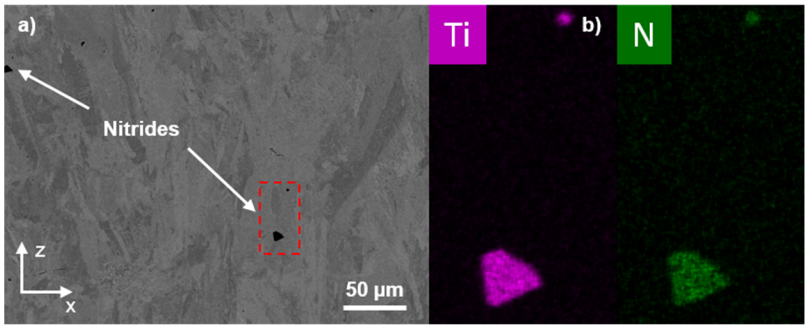

Figure 8.16 a) BSE-SEM micrograph of 0% spatter material showing the presence of titanium nitride inclusions and b) showing the corresponding Ti and N EDS maps

The results show that the primary differences between the virgin and spatter material are in defects related to inclusions and porosity in the specimens. The grain microstructures of specimens with different levels of spatter showed little variation and therefore any changes in fatigue performance can be attributed to changes in defects between the materials. These defects were found on the fracture surfaces contributing to the crack growth. The material produced with spatter particles showed evidence of larger lack-of-fusion defects and a larger proportion of these, although some were also present in the 0% spatter specimen. All of the materials had oxide and nitride inclusions, from the spatter and virgin powder used and the spatter generated during processing, with further oxides also being formed at the melt pool during processing. Visually the specimen produced with the spatter material included a greater proportion of these oxides due to the feedstock used. These defects influenced the FCG and variability in the materials.

8.3 Discussion

8.3.1.1 Fatigue crack growth results

The results of the FCGR testing showed that the PBF-LB specimens had a higher FCGR and lower K_{IC} and K_{th} than the wrought material, as shown in previous studies [159,163]. This was due to the proportion of defects present in the PBF-LB specimens. Previous studies have also indicated that the PBF-LB microstructure and residual stresses present in the specimens can increase the FCG and the variability [159,212]. The PBF-LB specimens demonstrated more brittle characteristics in the fast fracture surface, compared to the wrought material, a reduction in K_{IC} of 31% and a reduction in average crack growth cycles to failure of 29%.

Whereas for quasi-static mechanical properties, such as tensile and hardness, PBF-LB materials have demonstrated similar or improved properties to wrought material [119,124,127], there are still elements of the PBF-LB process which need to be optimised to improve FCG in the material. Post-processing has been shown to improve the FCG properties using heat treatments to relieve residual stresses and produce optimised microstructures and using HIP to close pores in the specimen, as shown by Leuders *et al.* [148] and Cain *et al.* [160] for PBF-LB Ti-6Al-4V. However, it would not be possible to remove the oxide and nitride inclusions seen in this work via these method.

The incorporation of spatter into the fatigue test specimen in this study effectively demonstrated the detrimental effect of spatter on PBF-LB parts. The primary defects observed were lack-of-fusion defects due to large spatter particles which did not allow penetration of the laser and melting into the layer below. Lack-of-fusion was also found with oxides which hadn't re-melted and did not wet with the layer melted above. These defects were found in all the PBF-LB materials, including the 0% spatter virgin material. This is important to note in terms of spatter produced during the build landing on the powder bed and being incorporated into parts and causing defects, as was shown with the oxides and lack-of-fusion defects in Figure 8.9c&f. It also showed that the reduction in fatigue resistance was seen with an increase in defects associated with increased levels of spatter in the material. The issue of oxides and lack of bonding in the material also raises questions as to whether greater oxygen control within the chamber could have a significant impact on the formation of these defects.

It is interesting that although a detrimental effect was seen in the cycles to failure and the Paris exponents of the PBF-LB material with the increase in spatter content, that there was not a considerable difference in the K_{th} and K_{IC} between the PBF-LB specimens with different spatter contents. It could perhaps be that these material properties were not so affected by the defects in the material. However, you would expect an increase in defects to contribute to a decrease in the threshold for crack propagation and failure of the specimen. More investigation would be required to understand why these parameters appeared less sensitive to the change in spatter content in the material.

8.3.1.2 Estimating spatter effects on fatigue properties

The increase in quantity of spatter material from 0 to 50% and 0 to 100% correlated to a 25 and 56% decrease in crack growth cycles to failure respectively, and a 12 and 39% increase in the FCGR related to the Paris exponent *m*, using the amended value for the 50% material excluding specimen S50-3. Figure 8.17 plots these results and the linear regression correlating the change in performance to the spatter content level, these show good agreement, with an $R^2 = 0.99$ for *m* and $R^2 = 0.96$ for *N* the number of crack growth cycles to failure. As stated, spatter is produced during processing which is incorporated into the powder bed and parts, therefore the 0% spatter specimens still include spatter particles in the built parts. Using the regression in Chapter 7 for the estimated actual spatter content in the powder bed, related to the surface area of the powder/build plate processed, the estimated spatter content in the 0% spatter specimens powder was 2.7% for the 14.4% build area usage. This was used to adapt the data from the FCGR results to calculate a trend of spatter content to fatigue performance. For the 50% specimen half of the 2.7% was used to adjust for the virgin material comprising half the feedstock powder which would have been processed and generated as spatter.

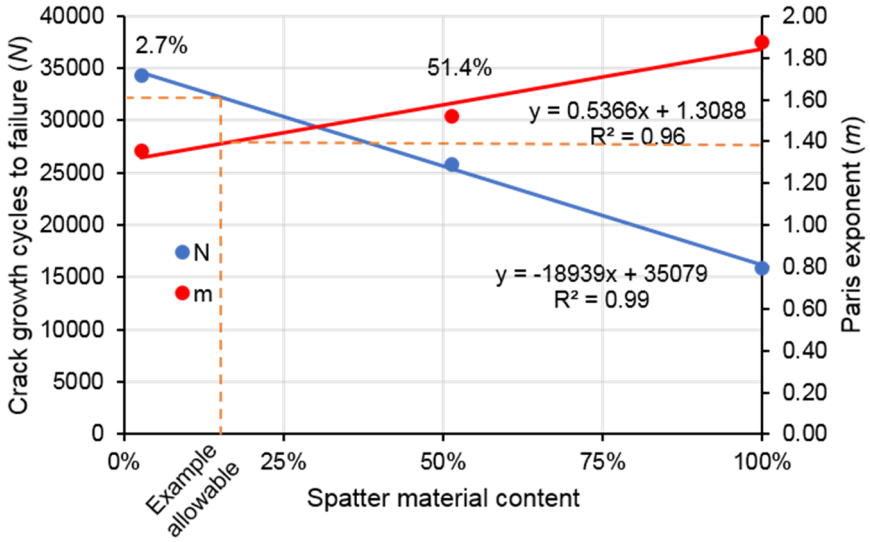

Figure 8.17 Plot showing the linear regression for change in crack growth cycles to failure (N) and the Paris exponent (m) for varying spatter content. The orange line shows an example of an allowable limit for spatter in the build for a defined N/m for an application

The levels of 50 and 100% spatter incorporation were extreme examples to establish and observe the effect of spatter particle incorporation and enable the effect on fatigue

performance up to the worst extreme to be defined. The levels of 1.6% spatter in the powder bed in Chapter 7 and the estimated content of 2.7% for the virgin processed material in this study were for 9.1% and 14.4% build area usage. As discussed in Chapter 7 and incorporated into the spatter estimation regression, the proportion of spatter in the powder bed content increases non-linearly with increased processing of the build area due to combined higher use of virgin powder and quantity of spatter powder generated. Therefore, these higher levels of spatter content may be achieved with very high usage of the build volume. However, for many builds, this level of spatter may not to have a significant impact on the fatigue performance due to the stochastic nature of the spatter distribution throughout the build chamber. The increase in build area usage will also increase the quantity of vaporised and plasma material produced, which will have ramifications for the gas and filter system, and the processing conditions due to attenuation of the laser.

Based upon the linear regression estimated for fatigue performance and inputting the results from the spatter estimation demonstrates the effect build usage could have on the part performance. Table 8.2 shows the results of the combined regressions indicating that high build utilisations of 70.0% could produce 38.0% spatter content in the powder bed leading to a 19.7% reduction in crack growth cycles to failure *N* and a 12.2% increase in FCG sensitivity related to *m*. These are important considerations for the throughput of the parts in PBF-LB as high build volume usage is desired for increased productivity of machines on the path towards industrialisation of the process.

Table 8.2 Estimated spatter content in the powder bed for different build usage levels using the regression from Chapter 7 and the correlate change in N and m from the regression in Figure 8.17

Build usage	Spatter content	*N* *Std Err: ±589*	% change	*M* *Std Err: ±0.08*	% change
9.1%	1.6%	34264	-0.2%	1.33	-1.7%
14.4%	2.7%	34063	-0.8%	1.34	-1.3%
25.0%	5.4%	33564	-2.2%	1.35	-0.9%
52.4%	17.9%	31266	-8.9%	1.42	4.5%
70.0%	38.0%	27572	-19.7%	1.52	12.2%
75.4%	50.0%	25352	-26.1%	1.58	16.9%

It is not proposed that these are absolute values. As discussed in Chapter 7, the spatter content estimations are based off one data point for spatter content related to build usage and the assumption that the quantity of spatter produced increases linearly with the area processed. It is important to emphasise The estimation is also related to the SLM125 PBF-LB system used and the spatter quantity generated using the process parameters and architecture in that system, which may not be completely applicable to the LMF1000 system used to manufacture the fatigue specimens. Particularly, the gas system and filter condition can have influence the spatter generation and distribution. Also the results of Paris exponents indicated that they would require more samples tested to produce statistically significantly different results. However, the results from these studies and the analysis raises important considerations for the PBF-LB process which are required to gain full understanding and control of the process. This methodology could be used with more data points to produce rules and guidelines for processing and what allowables there are in a build. In this instance, for a particular application with a desired fatigue performance, a maximum spatter content/build usage could be established to ensure the parts are of the desired quality, as shown by the orange line in Figure 8.17.

Chapter 6 demonstrated that there were varying levels of spatter across the powder bed, this could also be adapted to the part performance prediction. As shown with the change in spatter distribution across the bed, for a range of different parts to be produced in a build, some of which may be cyclically loaded in service, the build layout could be adapted to ensure the critical parts are acceptable. Table 8.3 demonstrates the potential combination of the spatter content estimation with the variation in spatter content across the bed and the effect on fatigue performance. The table shows spatter content for the sections of the build plate near the gas outlet, in the centre, and near the gas inlet gas inlet and the corresponding decrease in fatigue performance that would be expected for parts manufactured near the gas outlet.

Table 8.3 Demonstration of spatter content variation across the build plate for different build usage levels and the correlated change in fatigue properties. This is shown for the sections of the build plate near the gas outlet, centre of the build plate, and near the gas inlet which correspond to capsule positions AC, O, and BD respectively from Chapter 7

Build usage: 10%	Spatter content	*N* *Std Err: ±589*	Change	*M* *Std Err: ±0.08*	Change
Outlet	2.7%	34070	-0.7%	1.34	-1.3%
Centre	1.5%	34288	-0.1%	1.33	-1.8%
Inlet	1.2%	34335	0.0%	1.33	-1.9%
Build usage: 50%					
Outlet	24.1%	30117	-12.3%	1.45	6.9%
Centre	13.5%	32079	-6.5%	1.39	2.8%
Inlet	11.2%	32500	-5.3%	1.38	1.9%
Build usage: 70%					
Outlet	56.3%	24187	-29.5%	1.62	19.3%
Centre	31.5%	28765	-16.2%	1.49	9.8%
Inlet	26.1%	29747	-13.3%	1.46	7.7%

An example of a progression from this study would be to conduct the fatigue experiment using spatter powder that is sieved to the original or recycling specification. Then acceptable levels of spatter powder could then be set for the part properties or quality required. Combining the spatter analysis conducted previously in this thesis with this proposed study could establish the size distribution, quantity of spatter, and quantity of oxidised particles which will be recycled in the next cycle of powder, and the expected change in part performance.

8.3.1.3 Effect of large spatter particle in creep failure of PBF-LB Inconel 718 in previous work

The FCGR results were used to analyse the effect of spatter quantity on the part performance. It also highlighted the potential effect that just two large spatter induced defects can play on the part performance. In Figure 8.10 it was demonstrated the effect that two nearby defects had on the crack growth rate and the onset of failure of the specimen. Figure 8.9 showed inclusions and voids near the crack initiation and on the edge of the specimen, found in specimens manufactured with virgin material. These defects are weaknesses in the parts which could be critical to its failure. Xu *et al.* [213] conducted a staged creep test for PBF-LB

Inconel 718 using a two-bar creep specimen, with testing paused intermittently to allow XCT scanning and assessment of pore development. Their results successfully predicted fracture to occur at the region of the bar with the highest porosity from the XCT analysis. The defect which lead to this higher porosity can be seen in the as-built sample in the XCT scan and volume reconstruction in Figure 8.18a&b. The cause of defect was not detailed in the original study but from this study can be identified as a lack-of-fusion porosity, likely caused by a spatter particle of ~157 µm. The original data and images from the study have been reprocessed with permission for Figure 8.18 for the purpose of this analysis. The XCT data was reprocessed using ImageJ to volumetrically represent these critical defects more clearly in Figure 8.18c&d. The pore growth due to creep can be seen in the change from (c) to (d) which shows a volumetric view of the porosity in the as-built condition and mid-way through creep testing. It can also be seen that a collection of small pores near the lack-of-fusion defect in the specimen coalesce during creep to contribute to the failure in the specimen. These defects can then be seen on the fracture surface shown in (b) to contribute to the initiation and development of creep to the final failure of the part. The smaller defects found in this fatigue fracture study from oxide and nitride inclusions, or the collection of oxide spots on the spatter particles shown in Chapter 5, could play a similar role as the small pore coalescence shown in the creep testing. If these defects or those from larger spatter particles occur in critical area of components with high stresses and loads it could lead to premature failure of components and likely contributes to the variability in part properties found in the literature [119,155,214].

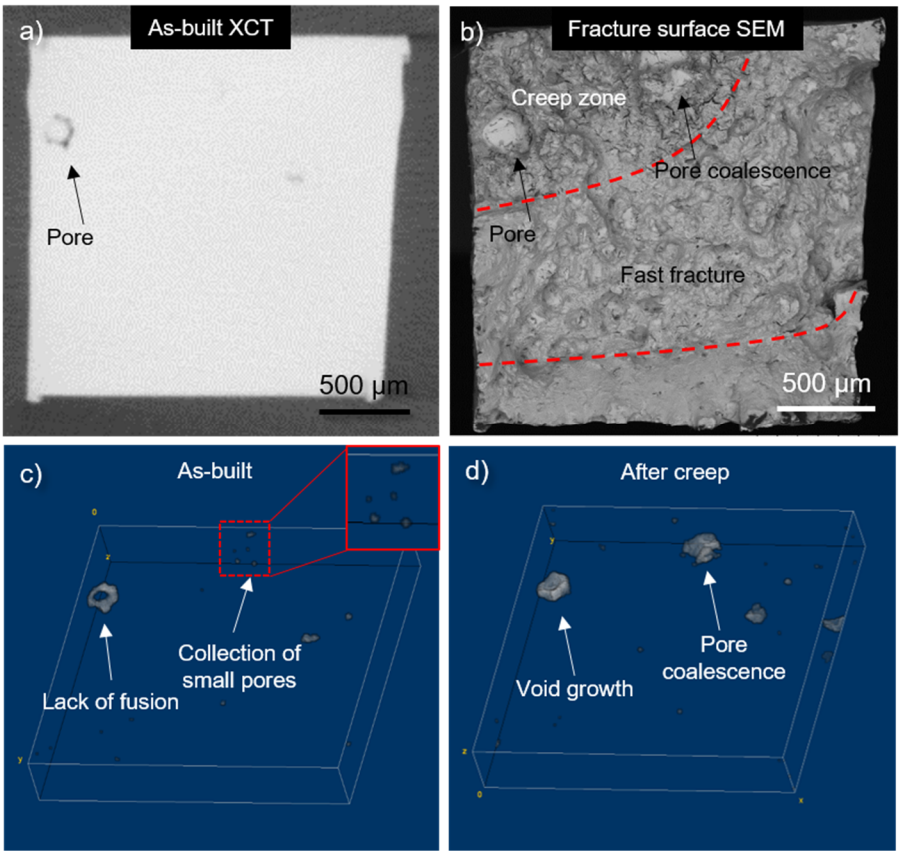

Figure 8.18 Staged creep testing showing the development of defects from the as-built specimen to failure of the part by Xu et al. [213]. *a) XCT slice of the lack-of-fusion defect in the as-built specimen, b) SEM micrograph of the failed specimen showing the relevant defects and the zones of creep and fast fracture contributing to failure of the part, and c&d) volumetric reconstruction of the pores from XCT scans showing the defect development from as-built to mid-way through creep testing. The images have been adapted and the original data reprocessed with permission.*

The evidence from the study of specimen S50-3 for fatigue testing, shown in Figure 8.10, and from Xu *et al.* [213] for creep testing show the critical effect large defects caused by spatter can have on PBF-LB manufactured parts. This is a critical issue for quality control in the process and highlights that it may not be the quantity of spatter which is critical but the large particles and where they are distributed. As the generation of spatter is currently inherent to laser melting in the process, research needs to be undertaken into the mitigation of the generation of these particles. The next step should be to understand the formation principles and the effect of processing parameters on the generation of spatter particles. Subsequently, how these parameters can be manipulated, whilst still ensuring optimum part quality, to reduce the generation of spatter or control it, such as strategically ejecting particles in the direction of the gas flow. In this regard, it could also be that a larger quantity of spatter generated but

redistributed away from the powder bed could have a lesser effect on part quality than a smaller quantity of powder distributed over the powder bed.

It also highlights that it is important to remove these large particles from the powder in the recycling process. Therefore, whilst Chapter 6 showed that larger sieve sizes could be used for recycling without greatly affecting the powder, there must be a cut off where particles are large enough to cause these defects. It is suggested that a cut off could be used as the laser diameter or the effective layer height, however, these would require further investigations to confirm.

8.3.1.4 Wider issue of oxides in previous Nickel-based superalloy work

Figure 8.19 shows the fracture surface of fatigue specimen in a study by Yamashita *et al.* [215] (a&b) and tensile specimen in studies by Wang *et al.* [216] for Hastelloy X in (c) and by Nguyen *et al.* [217] for Inconel 718 in (d). These studies reported un-melted particles present in the fracture surface of the test specimen which contributed to failure, these are highlighted by the arrows in Figure 8.19. In Figure 8.19a&b Yamashita *et al*. showed lack-of-fusion defects in their fatigue samples which initiated the crack, reduced the fatigue life, and increased the variation in fatigue life in their investigation. Oxides can be seen on the surface from BSE-SEM which are of the same nature as seen in this work which will likely have contributed to the lack-of-fusion, however, these were not identified or mentioned in the study. These are similar to the defects connected to the surface found in this work in Figure 8.10 and Figure 8.9. The particles seen in Figure 8.19c&d were identified in the studies as un-melted powder particles, however, they are smaller than the feedstock powder used in these studies so are unlikely to be un-melted powder particles. Based on the oxides found in this work and identified on the fracture surface for the fatigue samples in Figure 8.9, it is assumed that the particles in the studies by Wang *et al.* and Nguyen *et al.* are oxides and not un-melted particles which have contributed to the failure. Another indicator is that the particle in Figure 8.19d, which was previously labelled as an un-melted particle, has a crack running through it which is common in the oxide formations found in this work and this feature would not occur with a powder particle. The particles in Figure 8.19c&d were likely not picked up as oxides as the images are from secondary electron SEM imaging which does not show the composition difference and un-melted particle was their most likely explanation for the phenomena. It has

been shown in this work that such oxides do form in these materials, in the melt pool and in the spatter particles, so will be incorporated in the final material. These studies identify the lack of identification of these issues in PBF-LB of these Nickel-based superalloys. It is likely that there are other studies which similarly have not been able to identify these defects, which will have contributed to the failure of the specimen or results of their studies.

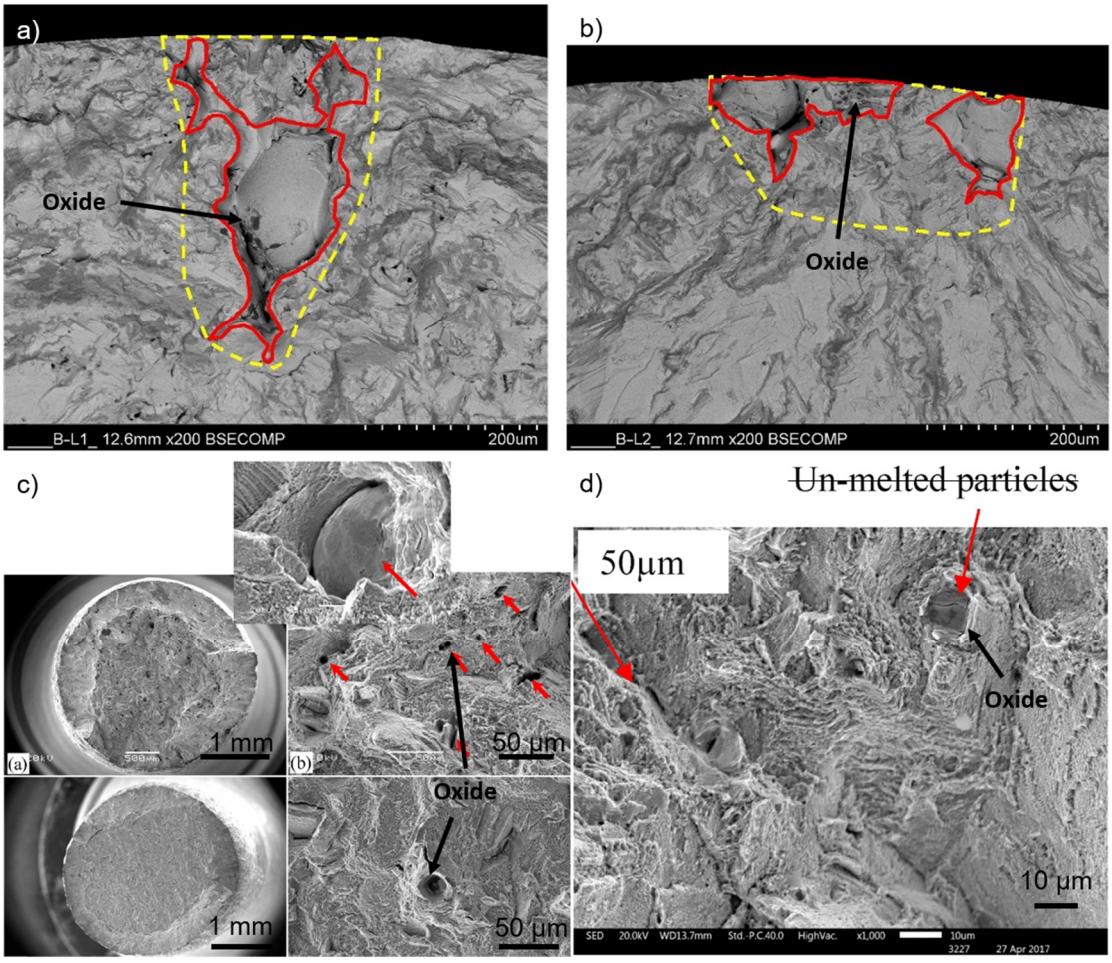

Figure 8.19 Fracture surface of tensile specimen in studies by a) Yamashita et al. [215] *for Inconel 718, b) Wang* et al. [216] *for Hastelloy X and c) by Nguyen* et al. [217] *for Inconel 718 in with particles identified as un-melted powder but are likely to be oxides*

The oxide inclusions from the studies discussed could have formed at the melt pool or could have been included from spatter particles generated or present in the powder used. With the effect that these particles can have on the performance of the parts, and therefore the results of the studies, this highlights a difficulty of comparing studies as the powder history or spatter content is not detailed, discussed, or considered.

8.3.1.5 Defect formation in parts due to spatter

The defects caused by the spatter particles can be summarised into three main types which have been discussed throughout this work. Their formations are depicted in Figure 8.20 with the particles initially in the powder bed of the laser path in (a), the particles when the next layer is spread in (b), and then in the final part in (c). Region (I) in Figure 8.20 depicts how oxides present in the spatter can be retained in the part due to their low absorption of the laser energy and high melting temperature, as seen in the fracture surface in Figure 8.9 and in Figure 5.11a&b. These oxides may be affected by the re-melting of subsequent layers in which they may move with the flow or be melted if they are at the surface. Region (II) in Figure 8.20 depicts the lack-of-fusion defects which are common with large spatter particles. The laser cannot penetrate through to the layer below or fully melt the large particle, creating connected porosity beneath the particle. Or as the laser mostly interacts with the melt pool, there may not be sufficient conduction from the melt pool to melt these particles. Region (III) in Figure 8.20 shows how oxidised spatter particles may be fully melted but create Oxygen enriched areas within the part as seen in Figure 8.15. As discussed, the difficulty is that the spatter particles may be redistributed anywhere in the powder bed and these particles lead to defects in the part at random.

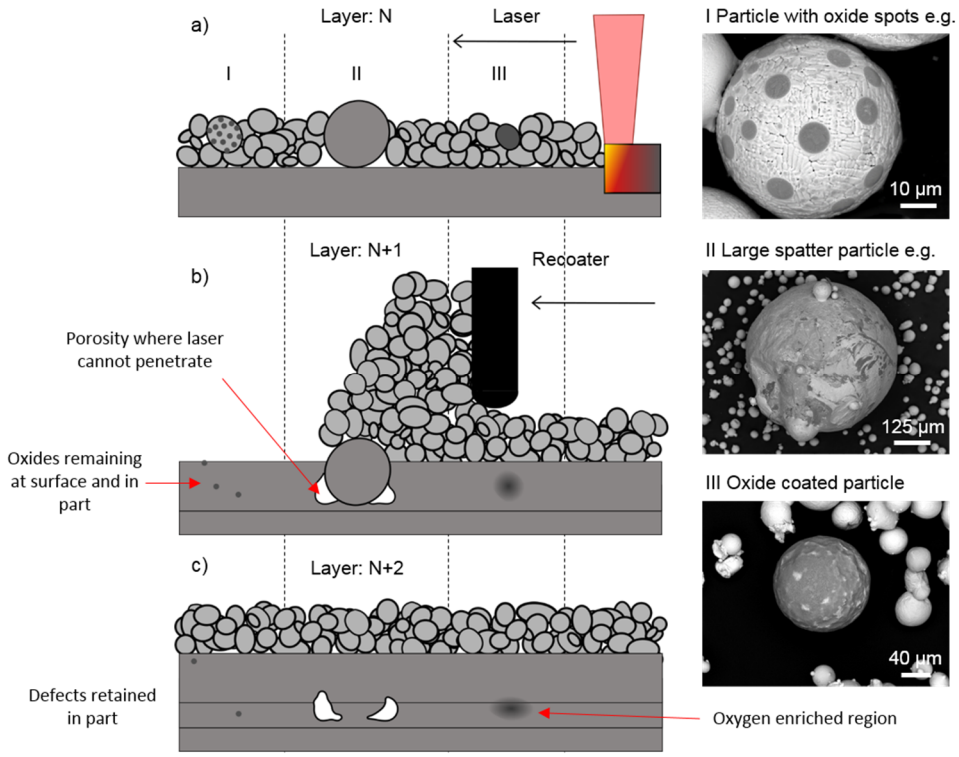

Figure 8.20 Schematic of the development of defects from spatter inclusion in the powder bed and part. I) Oxide inclusion from spatter (can also be form melt pool surface), II) large spatter causing lack-of-fusion defect, and III) oxidised spatter particle causing localised Oxygen increase

8.4 Summary

The aim of this chapter was to assess whether spatter particles created during processing which land and have been shown to remain in the powder bed have an effect on the performance of parts in PBF-LB. The results of the fatigue study concluded that the particles do contribute to a detriment in the fatigue performance of the specimen. The levels of spatter that were investigated were much higher than would likely occur in a typical build but demonstrated a trend which could be used to infer the effect of lower proportions of the particles. It was demonstrated that singular or low proportions of these particles could produce defects which influence the mechanical performance of the parts. The key conclusions from the results are:

- PBF-LB CT specimens were manufactured with different levels of spatter powder incorporated into the builds. The change in level of spatter powder in the material did

not appear to change the grain microstructure but lead to an increase in Oxygen content in the material

- Fatigue crack growth testing of the PBF-LB CT specimens showed decreased performance compared to wrought specimens tested. PBF-LB samples exhibited more brittle behaviour with a higher crack growth rate. They exhibited a 31% decrease in K_{IC} and a 29% decrease in average crack growth cycles to failure
- The increase in spatter content in the PBF-LB specimen correlated with an increase in the crack growth rate. Only slight changes in the K_{th} and K_{IC} values occurred with the different materials. Decreases of 25 and 54% for average crack growth cycles to failure occurred for the 50 and 100% spatter material compared to 0%
- The PBF-LB materials showed considerable scatter as had been reported previously in literature and was typified by a 50% spatter specimen which produced the highest crack growth rate and skewed the average results for this material
- The decrease in FCGR with spatter content was linked to the proportion and severity of defects in the specimens introduced by the spatter material. Defects from lack-of-fusion from large spatter particles and oxides as well as oxide and nitride inclusions were found. These defects were shown to have significant local effects on the crack growth and in cases lead to the onset of failure of the specimens
- Trends in the change in fatigue properties of the Paris exponent *m* and crack growth cycles to failure *N* related to the spatter level were shown with high correlation. It was shown how this could be used in combination the spatter content in the powder bed estimations developed in Chapter 7. This was proposed for averages in the build and the effect of spatter distribution across the bed. This demonstrated a method which could be used for qualifying the process and allowable levels of spatter in builds related to part performance
- As well as large quantities of spatter in the powder influencing part properties the findings also highlighted the effects single or small amounts of spatter defects can impact parts. Results from a previous study in PBF-LB Inconel 718 creep performance were reanalysed to show how a lack-of-fusion defect from a large spatter particle and a cluster of small defects can combine to cause premature failure in specimen
- It was shown that oxide particles were likely present and contributed to failure in other studies of Inconel 718 and Hastelloy X but were not identified as oxides. This

highlights that spatter and oxides have likely been contributing to issues with PBF-LB of these materials but it has not yet been established

This study demonstrated that investigation of the spatter particles and their proportion in the powder bed in the previous chapters is important for the process, as these particles can contribute to variability and decrease in part properties in PBF-LB.

Chapter 9 Summary & conclusions

9.1 Thesis objectives and key understandings

The aim of this work was to give an understanding of spatter and oxidation in PBF-LB, particularly for Nickel-based superalloys, and the implications it can have for quality in the process. To fill the knowledge gaps in the literature assessed in Chapter 2, the objectives addressed in this work were:

- Establish the difference between spatter and the virgin feedstock material and understand the link between spatter particles and their generation mechanisms (Chapter 5)
- Understand oxide formation in the processing of Nickel-based superalloys in parts and in spatter as inclusion of oxides can inhibit processing and decrease mechanical performance (Chapter 5 and 6)
- Investigate the difference in spatter generated by different PBF-LB systems and materials and quantify the characteristics of the particles using particle imaging and compositional analysis (Chapter 6)
- Investigate a methodology to assess and understand the distribution of spatter and other powder characteristics across the powder bed and how this contributes to part quality (Chapter 7)
- Establish the effect of spatter on the fatigue crack growth performance of PBF-LB parts using different levels of spatter powder as a feedstock. The fatigue results can then give an indication of the effect of the level of spatter processed in the powder bed on the properties of the parts produced (Chapter 8)

The results in Chapters 5-8 helped in answering these research objectives and the research has drawn understandings about the effect of spatter and oxidation throughout the PBF-LB process chain. The results were discussed in each chapter in context of other work in the field which it has built upon and the shortcomings and improvements relevant to the studies. Figure 9.1 shows the PBF-LB process chain presented in Figure 1.2 updated with the key understanding gained in aspects of the process.

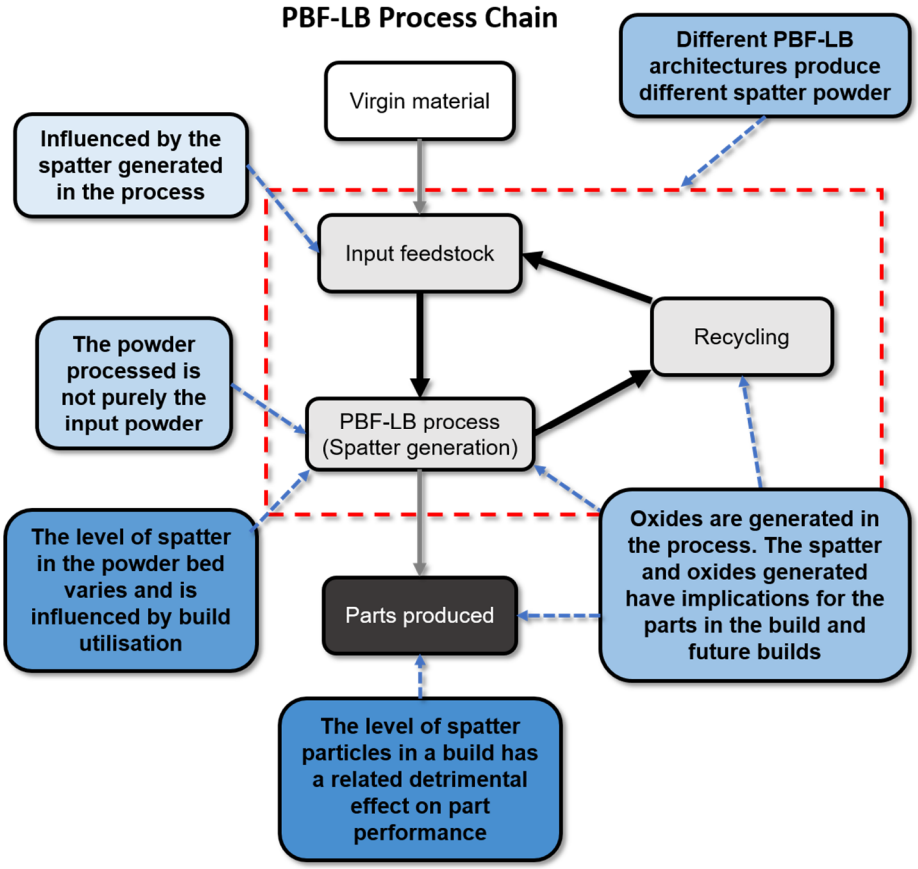

Figure 9.1 Key understandings gained from the work and relation to the PBF-LB process chain

9.2 Summary

In Chapter 5, building on work in understanding the generation of spatter in PBF-LB, the spatter particles were able to be linked and classified by their generation mechanisms: hot and cold entrainment, melt ejection, and vaporisation. This was achieved using their shape, size, morphology, and the presence of oxides in the particles, and improved on classification present in the literature. It was found that a proportion of the spatter particles show little difference to the virgin material, either as they have been redistributed from the bed with minimal changes or they have been generated as new, similar, gas atomised particles. The four types of process by-product characterised in this work are the current best understanding of the output of the spatter process, these can be used to feedback experimental data to the simulations which have been conducted for the spatter generation. As new and better techniques for simulating and analysing the melt pool are developed, this proposed model will likely be improved and updated.

It was found that the oxides form at the melt pool, which transfers to the spatter particles as they are ejected, and form as spots and slag within, and at the surface, of the parts produced. This was important as the oxides have been shown to inhibit processing and introduce defects due to their high melting point and lower laser energy absorptivity compared to the bulk material. In this work the oxide formations were found in the Inconel 718 material processed on four different PBF-LB machines, and for two Inconel 718 powders to establish that it is a general issue for the material in the PBF-LB process. It raised that the issue has not been given enough attention and has implications for materials processed by PBF-LB. Inconel 718 produced Al_2O_3 and TiO_2 oxides in the material. Processing of Hastelloy X from one supplier showed SiO_2, Cr_2O_3 and Al_2O_3 oxides with different formations at the melt pool, part surface, and in the spatter particles indicating different formation mechanisms in each section of the process. Processing of a second Hastelloy X with reduced Si content showed the oxide formation transition from Si and Cr dominant oxide formations to Ti and Al dominant formations. This indicated the need for tighter controls and new standards for PBF-LB alloys, and the need for bespoke alloys designed for the process.

As it was found that a proportion of the spatter was out-of-specification and likely to be detrimental to processing it was important to understand the quantity of these particles produced. Results of the particle characterisation in Chapter 6 showed that a significant proportion of spatter was morphologically different to the virgin material, with on average 50% of the spatter particles being non-spherical, compared to 16% in the virgin gas atomised material, and the spatter contained between 2.5 - 18% of oxidised particles in Inconel 718 and 30% in Hastelloy X. The proportion of oxidised particles was found to be correlated with the Oxygen pickup in the powders. It was considered that these characteristics were important with regards to their size. Large particles will affect the parts in the build the spatter is generated in but many will be sieved out during recycling. The analysis found that many of the undesirable spatter particles would be removed for sieving to common sieve mesh sizes 45, 53, and 63 µm used in industry. The spatter characteristics differed between the PBF-LB architectures which generated them and analysis of the characteristics allowed interpretation that the spatter produced from the AM125 would have the least detriment to the powder in subsequent recycling. This study combined with the wider research shows that spatter and oxidation is a wider issue for the PBF-LB process that is unique for each material and is different based upon the PBF-LB architecture. This is likely driven by the build environment,

thermodynamics, and fluid dynamics within a given system. However, the individual effects of the machine architecture and processing parameters have not been concluded and raise further questions for the process.

In Chapter 7, a new method was proposed and shown to be effective in order to investigate the powder which is processed in the bed and estimate the spatter distribution across the build plate. The method showed promising results in assessing the variation between the powder feedstock input and the powder in the bed that the laser interacts with. This has important implications for the characterisation of powder and understanding of the powder through the process, as well as demonstrating how local variations in the powder bed could contribute to variations and location dependence on part properties. The results found spatter and oxidised particles present in all sections of the powder bed, including >200 µm particles found closest to the gas inlet where the gas flow is highest. The results of the spatter distribution across the build area found agreement with other studies, finding increased spatter content in the powder bed near the gas outlet. However, the maximum content of spatter in the powder bed found in the study was 2.41% by the gas outlet and an average of 1.63%, for a build utilisation of 9.1%. The method showed small local variations in the PSD and PBD across the bed and larger variations between builds indicating powder handling produces greater variability in the powder bed content than the recoating mechanism, for the PBF-LB architecture used. It was established that these variations can cause increased porosity in components but further work is required in this area. Shortcomings of the method were considered and a range of further improvements were proposed which could be made to improve the accuracy and applicability of the method. It was discussed how a combination of the powder characteristics assessed for spatter in Chapter 6 and correlation of the build utilisation and quantity of spatter generated could provide a better metric for assessing the recycling of powders for PBF-LB.

Chapter 8 assessed the effect of spatter particles on the fatigue crack growth of PBF-LB material for 0% spatter (virgin material), 50% spatter, and 100% spatter feedstock powder. The results showed that the spatter particles had no major effect on the grain microstructure of the specimen produced but lead to higher Oxygen content in the material compared to the use of virgin material. The fatigue testing found the PBF-LB specimens performed worse than wrought Inconel 718 material. The effect of increased spatter particle content was an increase

in FCGR and decrease in cycles to failure. This developed upon work in the literature into the decrease in quasi-static mechanical properties due to incorporation of spatter. The effect of spatter on the FCGR was attributed to the proportion of defects in the material caused by the spatter. It was shown that large particles and oxides caused lack-of-fusion defects and the crack propagated between these and other defects, such as oxides and nitrides inclusions, which remained in the parts during processing. The quantity of spatter particles investigated for the builds assessed the full spectrum of data and the worst case scenario, which included contents higher than would be achieved in common processing. However, the estimation of spatter content from Chapter 7 using the build utilisation indicated that for more common levels of build utilisation of 25-50% would lead to a spatter content of 5-16% in the powder bed. The results indicated that these levels of spatter in the powder bed would have minor effect on the fatigue crack growth and may contribute less than other factors in the processing. However, it could have implications for high build utilisation in PBF-LB which would be used for mass manufacturing and is important to make the process economic. Spatter particles were also shown to be capable of producing critical defects which could cause crack initiation and onset of failure in components. It was shown that this had occurred in previous studies, but the effect of oxides and spatter had not been identified as causes. There is a difficulty that the effects of spatter in other studies may be hard to identify given the variability in mechanical properties produced in PBF-LB. Investigation of the spatter produced from the 100% spatter powder build also showed that the detrimental qualities of spatter compound with reuse of the material.

9.3 Significance for the field

The work and understandings in this thesis have significance for both academia and industry in the endeavour of industrialising PBF-LB. The work has identified the issues of spatter and oxidation in reducing and contributing to variation in mechanical properties of PBF-LB components. These were identified as general issues for the processing of Nickel-based superalloys and it was shown how the issues have been present in other studies. Therefore, this has a wider significance to the PBF-LB processing of these materials within academia and for industry, and needs to be addressed.

The effect of the spatter particles on part properties is from; spatter generated in the build and spatter particles retained in recycled powder. It is not possible for academia and industry to use only virgin material, and most powder used for builds will have been processed to some degree. Being able to quantify the condition of the powder and its change from its virgin state is important to be able to use the powders and to establish the influence on the build or part properties. This work has provided greater understanding about the change in the powder with regards to the new particles generated by spatter and proposed better techniques for how to qualify recycled powders. This can be of great significance to industry where powder can be assessed on its history and graded for different applications to ensure all powder can be used. Guidelines for the processing of Inconel 718 and Hastelloy X on the machines and in the conditions studied is that the used powder can be recycled at a higher sieve size (63 µm) and sieving to a smaller size does not remove much more of the undesirable particles. Therefore, higher yields from sieving could be achieved, however, it would need to be monitored to ensure that processing parameters remained optimum.

The identification of oxide formation at the melt pool, which remains at the surface and within parts, is important for all users of these Nickel-based superalloys. It identifies for machine manufacturers that oxidation occurs within the 'inert' environment of their build chambers and will be difficult to remove. Therefore, it would be recommended to process at low O_2 levels (<0.1% or 0.01%), however, the level at which the additional cost of reducing the O_2 compared to the change in oxidation needs to be established. The change in oxide formation between Hastelloy X alloys with different Si content identifies to powder manufacturers, and users of the alloy, the importance of composition control in the alloy. It is likely that micro-alloying element compositions will play a similar role in other alloys and raises the need for better alloy design for PBF-LB.

The method for analysing the powder bed in Chapter 7 has benefits for both academia and industry. The method, and capsule, are designed to be adaptable and applicable for many potential studies. For academia, the powder bed data can be used to assess different powders for use in the machines, such as different PSD, powder blends, or modified powders. The powder bed data could also be used for experimental validation of recoating simulations. For industry, the method could be used as part of a validation for a build of parts or for calibrating

the PBF-LB machine. The method could also be explored for what can be achieved with cheaper or lower grade powder, which will be a key area for cost saving in PBF-LB.

From the results in Chapter 7 and 8, it could be recommended that due to the increased level of spatter towards the gas outlet that more critical components in a build should be built by the gas inlet. Also for part positioning in a build that as much as possible, parts are not 'downwind' of other parts along the x-axis of the build plate. The level of build usage should also be considered as a compromise between risks from spatter based defects and the cost effectiveness of build volume packing. It is important to note from the findings that these measures and guidelines will be specific for material-PBF-LB system-application combinations with regards to the spatter generated, distribution, and acceptable properties for the components. This work has provided new methods and important aspects to consider within these guidelines.

These contributions from this work are important to achieve industrialisation of the process and manufacture of high-performance components. The work identified an area of the process which contributes to variation and inconsistencies in the properties of parts produced and proposes potential methods for addressing these. These play a role for all users of the technology and need to be considered to produce consistent quality. This is required to achieve the ideal of AM in manufacturing high-performance components and bespoke one-off parts with known properties.

9.4 Final remarks

Spatter has previously been given little consideration as part of the PBF-LB process, as most consideration has been given to successfully processing different alloys and assessing mechanical properties of parts. The technology has now advanced to a point where acceptable mechanical performance has been achieved for some alloy-application combinations, however, wider adoption is still hampered by inconsistencies and variabilities in the process. This work demonstrated that spatter contributes to decrease in part performance and that it makes up a proportion of the powder bed which is consolidated into the final material. Spatter is generated from the first scan track of the build and is redistributed throughout the build chamber, some of which lands in the powder bed.

Therefore, the powder bed is always some proportion of spatter and feedstock powder, even for the first layer using virgin powder. This finding agrees with the results from other studies of spatter distribution in the process but the implications of this have not be thoroughly considered. It must be appreciated though that the proportion of spatter particles in the powder bed is generally low and in many builds it is unlikely to have a significant effect on the part quality. Also, that there are many other factors in the process which may contribute more significantly to reduction mechanical properties. However, there is still possibility that a large spatter particle could land on an un-scanned area of the powder bed and cause a defect in a critical area of the component, and that it plays a role in the change and evolution of the powder. This raises particular quality concerns for safety critical applications in highly demanding environments such as components in aerospace and power turbine engines where failure cannot be tolerated, particularly for these Nickel-based superalloys investigated.

Chapter 10 Recommendations for future work

The PBF-LB process has many factors which influence the properties of parts produced in the process and that contribute to the variability which is currently present in the process. This variability and a need for consistent quality in the process is a barrier to its industrialisation for demanding applications. The present research has identified spatter and oxide formation as a source of quality concern and contributor to the variability. Further work is required to understand oxides, spatter, and powder in the system to qualify the process. Suggestions for developments on the work presented and in the field, for both short and long term, are discussed here.

10.1 Short term

10.1.1 Understanding spatter generation

To build on from this work it would be important to understand the effect of different processing parameters and conditions on the generation of spatter to correlate the processing with the particles generated. Key parameters such as the laser powder, scan speed, hatch spacing, beam shape, laser type will influence the melting and vaporisation of the powder which generates the spatter. The processing conditions with regards to the system architecture, the gas and filter system, and also the powder will also be important for understanding the spatter generation. These results will be useful in developing better processing conditions to improve part quality in the melting and also in the reduction of spatter generation. This could also allow better understanding of the processing between different PBF-LB systems. This would further the results in this work in understanding the spatter generated and the effect on the powder system. Simulations could be key to developing understanding of these parameters effects and then could help create developmental models regarding prediction of part and powder quality from builds.

10.1.2 Spatter effects on build quality

Further work is required to fully understand the role of spatter particles on the mechanical properties of PBF-LB parts. A development to the fatigue investigation in this work would be to measure the volumetric size and distribution of the defects in the specimen via XCT and evaluate these with a critical defect size for the material using linear elastic fracture mechanics. If this were conducted with more levels of spatter incorporation, closer to the proportion which would occur in a certain build of interest, then a statistical model could be produced to predict the likelihood of defect formation and the effect on the specimen for applications. This could possibly be developed combining XCT measurements, fracture analysis of the critical defects, and a machine learning algorithm to predict the key factors of spatter particles' effect on part properties.

As discussed in the results for the fatigue study, this further fatigue investigation could be combined with improvements in the powder bed content methodology to produce a predictive model of the spatter generated in the build and its subsequent effect on the part performance. The designed volume for XCT analysis in the improvements discussed could be used to assess if critical defect sizes would be produced, their quantity and likelihood, and their distribution. The part performance could also be mapped across the build plate and inform part positioning in the build. To achieve this, the improved methodology proposed in Chapter 7 should be repeated for different build utilisation levels to develop a model which can reliably predict the quantity of spatter produced for a certain build utilisation. This model could then be used to predict the level of spatter in the powder bed, and if combined with size and shape analysis as in Chapter 6, could assess the level of spatter recycled and the change in the recycled powder. Further development of this work would be to be able to assess the powder bed metrics in this study (PSD, PBD, and spatter quantity) at an individual layer level instead of averaged over a build. It is unclear at the moment how this would be achieved for the required resolution and accuracy over the powder bed but would be worthy investigation.

10.1.3 Recycling and powder developments

The fatigue study investigated spatter in its 'as generated' form, simulating the effect of spatter generated during the process and incorporated into the powder bed. The next step would be to analyse the effect of the level of sieved spatter on the materials performance. The results of this investigation could then be combined with the size and shape analysis performed in this research to understand the change in the recycled powder due to processing and the subsequent implications on part properties.

The recycling of powders in PBF-LB requires much greater understanding and the studies conducted on the topic require improvement. The recycling of powder is crucial to the economic viability of the PBF-LB process. As discussed in Chapter 7, the studies conducted in literature are often lacking in required detail and all use different metrics and methods to assess the recycling of powders. It was suggested that future recyclability investigations should analyse the powder more fundamentally via the components which contribute to it and that this could be assessed using a metric such as build utilisation. These studies should be combined with studies specific to the effect of change in powder properties. This would allow tolerances of change in powder to be produced for desired part quality metrics. Investigations should hopefully lead to a set of standards and guidelines for how to assess and measure the recycling of powders in PBF-LB.

10.1.4 Powder and localised powder bed related processing

Studies have been conducted to correlate the characteristics of the powder feedstock to the part quality in PBF-LB. As shown in this work, the powder input to the machine can vary across the powder bed due to the recoating and the incorporation of spatter. Further work should be conducted into the relationship between the input powder and the powder the laser actually interacts with across the bed. These should then be correlated to the properties of the parts or layers produced. For the differences in powder the laser parameters should be optimised for the powder which the laser melts. This could be achieved using a scanning system in the recoater blade which measures the powder bed after it is spread, as investigated in the literature. If the properties of the laser can be optimised for the powder used this could provide great benefit in processing recycled powder without loss in part properties. This form

of in situ monitoring could also be used to identify large spatter particles which have landed in the powder bed, and would likely cause a lack-of-fusion defect, and the parameters could be optimised to avoid this defect occurring. Eventually it is envisioned that the PBF-LB machines will be able to optimise the laser parameters 'on-the-fly' for the specific powder layer which is spread to produce consistent melting and quality of parts.

An important aspect of understanding the relationship between the powders processed, the parameters used, and the quality of parts produced is to establish what metrics for powders are really required to produce consistent and appropriate quality in the process. If a wider size span and less spherical powder can be used and achieve the required properties then this can change the demands on powder suppliers and more cost effective feedstock powders could be used. Gas atomised powders can be used over the much more expensive PREP powders, and depending on the application, EIGA and VIGA, may not be required, or water atomised powders could even be used. This could also lead to powders being able to be recycled more. It is also important that the powders are considered not just to achieve the best possible properties, but for properties suitable for the application. The cost of PBF-LB is a significant barrier to its wider adoption and the powder feedstock is major part of this so what can be done to reduce this would be highly beneficial.

10.1.5 Assessment for different alloys

The research suggests that spatter and oxide formation is unique to alloy systems and compositions. Considering the potential these have to affect part quality the oxidation and spatter should be investigated for each material. This can provide further understanding of the effects of constituent elements in the formation of oxides. This could be helpful in designing alloys specifically for the PBF-LB process.

10.1.6 Machine developments

The spatter generated in different PBF-LB systems produced different characteristics. The research work was conducted on PBF-LB systems designed to operate in 'inert' Argon atmospheres, however, it was found, even with a pre-vacuum process in the AM125, that oxidation occurred. To further understand these issues for the PBF-LB process and mitigation,

it would be of interest to assess the formation of spatter and oxides in a vacuum PBF-LB system, and with the PBF-EB process, which also occurs in a vacuum. Comparison with these systems could provide answers as to source of the oxidation and if it can be avoided.

So far spatter has had little consideration for its effects on the process, and thus only two studies found in the literature have investigated the reduction or removal of spatter generation. The spatter-less processing was achieved at very slow processing speeds which are impractical for all but the smallest of components. Therefore, further investigation into the parameters that influence the generation of spatter and demonstrate a reduction in spatter generation, whilst also producing optimal part quality would be of great interest for the process. Another alternative for mitigation of spatter on the powder bed is the use of optimised scan strategies which eject the spatter in the direction of the gas flow to facilitate removal of the spatter from the powder bed. At the moment it is not envisioned how the generation of spatter, led by vaporisation of the melt pool, can be completely avoided without significant control of the heating regime which isn't currently possible at high scanning speeds required and with current laser technology. Future improvements to lasers may change this. Another option could be for the temperature in the powder be to be raised to just below the melting point so that the laser just raises the temperature slightly to produce melting, as occurs in PBF-EB and selective laser sintering. However, the effect this would have on the surrounding power feedstock would need to be established.

10.2 Long term

10.2.1 Multiple laser considerations

The industry is moving towards more lasers and larger build volumes in PBF-LB systems. These progressions of the system architecture will compound the effect of spatter in the process. In the simultaneous processing of multiple lasers the spatter produced by each laser can affect the process zones of other lasers. It could be that with optimisation of the processing strategies it could be possible to reduce the effects of spatter using multiple lasers. The increase in build area will increase the difficulty of removing spatter from the powder bed. Studies have shown that the gas flow is more effective at redistributing spatter by the gas inlet

and less effective by the gas outlet, this will be exacerbated with larger build areas unless more advanced gas flow systems can be designed.

10.2.2 Statistical process control powder and part manufacturing system

For the industrialisation of PBF-LB, which will look to establish serial production and mass manufacture of components using the technology, it is likely that a standard build configuration will be established for components. Many of the techniques in this research and the further work proposed could be used to qualify the build configuration for a component, for a material, and for a PBF-LB machine. This could then produce metrics as to the expected part performance, with upper and lower limits, the recyclability of the powder and a reuse plan for the powder. In a wider manufacturing context, it could then be implemented as to how that recycled powder could be used in other builds for components in the same material but with less stringent quality or part property demands.

Integrated smart systems and factories

Further in the future, the direction of the industry is likely to be towards 'plug and play' machines which are completely self-contained and automated from powder input to part output and post processing. All linked together as an integrated factory. This can already be seen in the development of machines such as the FAB1 PBF-LB production line from Additive Industries and the M Line Factory production line from GE Additive, but it will likely be taken much further. At the moment there is not enough understanding of the effect of every input to the machine, from powder metrics, recoating, gas flow, filters, number and power of lasers, spatter generation, etc. As discussed in the literature review there are over 130 parameters which can influence the final part. Research in industry and academia will need to work together to understand the influence of these parameters. From this there will then be three important aspects, the ability to simulate the effect, and the ability to control each of these parameters in the machine, and the capability for feedback loops between the simulations and machines. There will be a need for simulations of the processing parameters (including requirements on the feedstock etc) based on the application, scheduling this on the machine with other components in a build and with integrated MRP systems, and then to be able to create a digital twin of the component/build including the expected properties based on the

processing. The incorporation of this with the capability in the machine to assess, select, and process powder according to the simulations, monitor aspects of the processing to detect any anomalies and feed data back into the simulations and digital twins. Then to be able to move the finished PBF-LB build on for post-processing whilst re-processing powder and preparing for the next build. Large networks of these machines would then be linked up to an Internet of Things and Industry 4.0 digital factory which can monitor and control each aspect of the manufacture and provide consistent and repeatable components each and every time.

References

[1] S.A. Khairallah, A.T. Anderson, A. Rubenchik, W.E. King, Laser powder-bed fusion additive manufacturing: Physics of complex melt flow and formation mechanisms of pores, spatter, and denudation zones, Acta Mater. 108 (2016) 36–45. doi:10.1016/j.actamat.2016.02.014.

[2] S. Ly, A.M. Rubenchik, S.A. Khairallah, G. Guss, M.J. Matthews, Metal vapor micro-jet controls material redistribution in laser powder bed fusion additive manufacturing, Sci. Rep. 7 (2017) 4085. doi:10.1038/s41598-017-04237-z.

[3] M. Tang, P.C. Pistorius, Oxides, porosity and fatigue performance of AlSi10Mg parts produced by selective laser melting, Int. J. Fatigue. 94 (2017) 192–201. doi:10.1016/j.ijfatigue.2016.06.002.

[4] E. Louvis, P. Fox, C.J. Sutcliffe, Selective laser melting of aluminium components, J. Mater. Process. Technol. 211 (2011) 275–284. doi:10.1016/j.jmatprotec.2010.09.019.

[5] M. Simonelli, C. Tuck, N.T. Aboulkhair, I. Maskery, I. Ashcroft, R.D. Wildman, R. Hague, A Study on the Laser Spatter and the Oxidation Reactions During Selective Laser Melting of 316L Stainless Steel, Al-Si10-Mg, and Ti-6Al-4V, Metall. Mater. Trans. A Phys. Metall. Mater. Sci. 46 (2015) 3842–3851. doi:10.1007/s11661-015-2882-8.

[6] M. Saunders, Renishaw plc, Oxygen algebra - minimising oxygen pick-up, Linked In. (2017). https://www.linkedin.com/pulse/oxygen-algebra-minimising-pick-up-marc-saunders/ (accessed January 18, 2019).

[7] Renishaw plc, Investigating the effects of multiple re-use of Ti6Al4V powder in additive manufacturing (White Paper), 2016.

[8] I. Gibson, D.W. Rosen, B. Stucker, Additive manufacturing technologies: Rapid prototyping to direct digital manufacturing, 2010. doi:10.1007/978-1-4419-1120-9.

[9] J.-P. Kruth, M.C. Leu, T. Nakagawa, Progress in Additive Manufacturing and Rapid Prototyping, CIRP Ann. - Manuf. Technol. 47 (1998) 525–540. doi:10.1016/S0007-8506(07)63240-5.

[10] W.E. King, A.T. Anderson, R.M. Ferencz, N.E. Hodge, C. Kamath, S.A. Khairallah, A.M. Rubenchik, Laser powder bed fusion additive manufacturing of metals; physics, computational, and materials challenges, Appl. Phys. Rev. 2 (2015) 041304. doi:10.1063/1.4937809.

[11] P.K. Gokuldoss, S. Kolla, J. Eckert, Additive Manufacturing Processes: Selective Laser Melting, Electron Beam Melting and Binder Jetting-Selection Guidelines., Mater. (Basel, Switzerland). 10 (2017). doi:10.3390/ma10060672.

[12] SLM Solutions Group AG, SLM 280 2.0, 2018. https://slm-solutions.com/fileadmin/user_upload/downloads/en/121en171015-01-002-slm280-20_web.pdf (accessed January 3, 2019).

[13] C. Körner, Additive manufacturing of metallic components by selective electron beam melting — a review, Int. Mater. Rev. 61 (2016) 361–377. doi:10.1080/09506608.2016.1176289.

[14] K. Osakada, M. Shiomi, Flexible manufacturing of metallic products by selective laser melting of powder, Int. J. Mach. Tools Manuf. 46 (2006) 1188–1193. doi:10.1016/j.ijmachtools.2006.01.024.

[15] L. Löber, C. Flache, R. Petters, U. Kühn, J. Eckert, Comparison of different post processing technologies for SLM generated 316l steel parts, Rapid Prototyp. J. 19 (2013) 173–179. doi:10.1108/13552541311312166.

[16] I. Yadroitsava, J. Els, G. Booysen, I. Yadroitsev, PECULIARITIES OF SINGLE TRACK

FORMATION FROM TI6AL4V ALLOY AT DIFFERENT LASER POWER DENSITIES BY SELECTIVE LASER MELTING, South African J. Ind. Eng. 26 (2015) 86–95.

[17] M. Rombouts, J.P. Kruth, L. Froyen, P. Mercelis, Fundamentals of Selective Laser Melting of alloyed steel powders, CIRP Ann. 55 (2006) 187–192. doi:10.1016/S0007-8506(07)60395-3.

[18] C.Y. Yap, C.K. Chua, Z.L. Dong, Z.H. Liu, D.Q. Zhang, L.E. Loh, S.L. Sing, Review of selective laser melting: Materials and applications, Appl. Phys. Rev. 2 (2015). doi:10.1063/1.4935926.

[19] R. Li, J. Liu, Y. Shi, L. Wang, W. Jiang, Balling behavior of stainless steel and nickel powder during selective laser melting process, Int. J. Adv. Manuf. Technol. 59 (2012) 1025–1035. doi:10.1007/s00170-011-3566-1.

[20] J.P. Kruth, G. Levy, F. Klocke, T.H.C. Childs, Consolidation phenomena in laser and powder-bed based layered manufacturing, CIRP Ann. - Manuf. Technol. 56 (2007) 730–759. doi:10.1016/j.cirp.2007.10.004.

[21] M. Tsukamoto, S. Masuno, Y. Sato, R. Higashino, K. Tojo, K. Asuka, Development of high intensity blue diode laser system for materials processing (Conference Presentation), in: M.S. Zediker (Ed.), High-Power Diode Laser Technol. XVI, SPIE, 2018: p. 5. doi:10.1117/12.2291239.

[22] H. Lee, C. Huat, J. Lim, M.J. Low, N. Tham, V. Matham Murukeshan, Y.-J. Kim, Lasers in Additive Manufacturing: A Review, Int. J. Precis. Eng. Manuf. Technol. 4 (2017) 307. doi:10.1007/s40684-017-0037-7.

[23] M. Brandt, Laser Additive Manufacturing : Materials, Design, Technologies, and Applications., Elsevier Science, 2016. https://books.google.co.uk/books?id=H32nCgAAQBAJ&dq=blue-diode+laser+copper+additive+melting&lr=&source=gbs_navlinks_s (accessed January 7, 2019).

[24] N.K. Tolochko, Y. V. Khlopkov, S.E. Mozzharov, M.B. Ignatiev, T. Laoui, V.I. Titov, Absorptance of powder materials suitable for laser sintering, Rapid Prototyp. J. 6 (2000) 155–161. doi:10.1108/13552540010337029.

[25] E.O. Olakanmi, R.F. Cochrane, K.W. Dalgarno, A review on selective laser sintering/melting (SLS/SLM) of aluminium alloy powders: Processing, microstructure, and properties, Prog. Mater. Sci. 74 (2015) 401–477. doi:10.1016/J.PMATSCI.2015.03.002.

[26] J.C. Ion, Laser Processing of Engineering Materials, Laser Process. Eng. Mater. (2005) 41–103. doi:10.1016/B978-075066079-2/50006-4.

[27] J. Trapp, A.M. Rubenchik, G. Guss, M.J. Matthews, In situ absorptivity measurements of metallic powders during laser powder-bed fusion additive manufacturing, Appl. Mater. Today. 9 (2017) 341–349. doi:10.1016/j.apmt.2017.08.006.

[28] A.A. Martin, N.P. Calta, S.A. Khairallah, J. Wang, P.J. Depond, A.Y. Fong, V. Thampy, G.M. Guss, A.M. Kiss, K.H. Stone, C.J. Tassone, J. Nelson Weker, M.F. Toney, T. van Buuren, M.J. Matthews, Dynamics of pore formation during laser powder bed fusion additive manufacturing, Nat. Commun. 10 (2019) 1–10. doi:10.1038/s41467-019-10009-2.

[29] T. Furumoto, K. Egashira, K. Munekage, S. Abe, Experimental investigation of melt pool behaviour during selective laser melting by high speed imaging, CIRP Ann. 67 (2018) 253–256. doi:10.1016/j.cirp.2018.04.097.

[30] C.D. Boley, S.A. Khairallah, A.M. Rubenchik, Calculation of laser absorption by metal powders in additive manufacturing., Appl. Opt. 54 (2015) 2477–82. doi:10.1364/AO.54.002477.

[31] W.E. King, H.D. Barth, V.M. Castillo, G.F. Gallegos, J.W. Gibbs, D.E. Hahn, C. Kamath, A.M. Rubenchik, Observation of keyhole-mode laser melting in laser powder-bed fusion additive manufacturing, J. Mater. Process. Technol. 214 (2014) 2915–2925. doi:10.1016/J.JMATPROTEC.2014.06.005.

[32] A.F.H. Kaplan, J. Powell, Spatter in laser welding, 23 (2011). doi:10.2351/1.3597830.

[33] D.K.Y. Low, L. Li, A.G. Corfe, Characteristics of spatter formation under the effects of different laser parameters during laser drilling, J. Mater. Process. Technol. 118 (2001) 179–186. doi:10.1016/S0924-0136(01)00910-4.

[34] M.J. Zhang, G.Y. Chen, Y. Zhou, S.C. Li, H. Deng, Observation of spatter formation mechanisms in high-power fiber laser welding of thick plate, Appl. Surf. Sci. 280 (2013) 868–875. doi:10.1016/j.apsusc.2013.05.081.

[35] G.G. (Gennadiĭ G. Gladush, I. Smurov, Physics of laser materials processing : theory and experiment, Springer, 2011. https://books.google.co.uk/books?hl=en&lr=&id=-ny_BUmCk1sC&oi=fnd&pg=PR3&dq=Gladush,+G.+G.+%26+Smurov,+I.+Physics+of+Laser+Materials+Processing&ots=ggi2NmyvNb&sig=lvrZiI9VBMIJj3_E74rqarZq3aA#v=onepage&q=spatter&f=false (accessed January 11, 2019).

[36] H. Nakamura, Y. Kawahito, K. Nishimoto, S. Katayama, Elucidation of melt flows and spatter formation mechanisms during high power laser welding of pure titanium, J. Laser Appl. 27 (2015) 032012. doi:10.2351/1.4922383.

[37] F. Hugger, K. Hofmann, S. Kohl, M. Dobler, M. Schmidt, Spatter formation in laser beam welding using laser beam oscillation, Weld. World. 59 (2015) 165–172. doi:10.1007/s40194-014-0189-9.

[38] M. Schweier, J.F. Heins, M.W. Haubold, M.F. Zaeh, Spatter Formation in Laser Welding with Beam Oscillation, Phys. Procedia. 41 (2013) 20–30. doi:10.1016/j.phpro.2013.03.047.

[39] M.J. Matthews, G. Guss, S.A. Khairallah, A.M. Rubenchik, P.J. Depond, W.E. King, Denudation of metal powder layers in laser powder bed fusion processes, Acta Mater. 114 (2016) 33–42. doi:10.1016/j.actamat.2016.05.017.

[40] P. Bidare, I. Bitharas, R.M. Ward, M.M. Attallah, A.J. Moore, Fluid and particle dynamics in laser powder bed fusion, Acta Mater. 142 (2017) 107–120. doi:10.1016/j.actamat.2017.09.051.

[41] C.L.A. Leung, S. Marussi, R.C. Atwood, M. Towrie, P.J. Withers, P.D. Lee, In situ X-ray imaging of defect and molten pool dynamics in laser additive manufacturing, Nat. Commun. 9 (2018) 1–9. doi:10.1038/s41467-018-03734-7.

[42] V. Gunenthiram, P. Peyre, M. Schneider, M. Dal, F. Coste, R. Fabbro, Analysis of laser–melt pool–powder bed interaction during the selective laser melting of a stainless steel, J. Laser Appl. 29 (2017) 022303. doi:10.2351/1.4983259.

[43] R. Fabbro, S. Slimani, I. Doudet, F. Coste, F. Briand, Experimental study of the dynamical coupling between the induced vapour plume and the melt pool for Nd-Yag CW laser welding, J. Phys. D. Appl. Phys. 39 (2006) 394–400. doi:10.1088/0022-3727/39/2/023.

[44] Y. Liu, Y. Yang, S. Mai, D. Wang, C. Song, Investigation into spatter behavior during selective laser melting of AISI 316L stainless steel powder, Mater. Des. 87 (2015) 797–806. doi:10.1016/j.matdes.2015.08.086.

[45] D. Wang, S. Wu, F. Fu, S. Mai, Y. Yang, Y. Liu, C. Song, Mechanisms and characteristics of spatter generation in SLM processing and its effect on the properties, Mater. Des. 117 (2017) 121–130. doi:10.1016/j.matdes.2016.12.060.

[46] M. Lutter-Günther, M. Bröker, T. Mayer, S. Lizak, C. Seidel, G. Reinhart, Spatter formation during laser beam melting of AlSi10Mg and effects on powder quality, Procedia CIRP. 74 (2018) 33–38. doi:10.1016/j.procir.2018.08.008.

[47] A. Ladewig, G. Schlick, M. Fisser, V. Schulze, U. Glatzel, Influence of the shielding gas flow on the removal of process by-products in the selective laser melting process, Addit. Manuf. 10 (2016) 1–9. doi:10.1016/j.addma.2016.01.004.

[48] A. Bin Anwar, Title Effect Of Inert Gas Flow Velocity And Unidirectional Scanning On The Formation And Accumulation Of Spattered Powder During Selective Laser Melting EFFECT OF INERT GAS FLOW VELOCITY AND UNIDIRECTIONAL SCANNING ON THE FORMATION AND ACCUMULATION OF SPA, (2016) 531–536. http://hdl.handle.net/10220/41780 (accessed July 23, 2017).

[49] A. Bin Anwar, Q.C. Pham, Selective laser melting of AlSi10Mg: Effects of scan direction, part placement and inert gas flow velocity on tensile strength, J. Mater. Process. Technol. 240 (2017) 388–396. doi:10.1016/j.jmatprotec.2016.10.015.

[50] A. Bin Anwar, Q.C. Pham, Study of the spatter distribution on the powder bed during selective laser melting, Addit. Manuf. 22 (2018) 86–97. doi:10.1016/j.addma.2018.04.036.

[51] H. Gong, K. Rafi, T. Starr, B. Stucker, The Effects of Processing Parameters on Defect Regularity in Ti-6Al-4V Parts Fabricated By Selective Laser Melting and Electron Beam Melting, n.d. https://sffsymposium.engr.utexas.edu/Manuscripts/2013/2013-33-Gong.pdf (accessed January 11, 2019).

[52] D.S. Nguyen, H.S. Park, C.M. Lee, Effect of cleaning gas stream on products in selective laser melting, Mater. Manuf. Process. 00 (2018) 1–7. doi:10.1080/10426914.2018.1512132.

[53] H.W. Mindt, M. Megahed, N.P. Lavery, M.A. Holmes, S.G.R. Brown, Powder Bed Layer Characteristics: The Overseen First-Order Process Input, Metall. Mater. Trans. A Phys. Metall. Mater. Sci. 47 (2016) 3811–3822. doi:10.1007/s11661-016-3470-2.

[54] F. j. Gürtler, M. Karg, M. Dobler, S. Kohl, I. Tzivilsky3, M. Schmidt, Influence of powder distribution on process stability in laser beam melting: Analysis of melt pool dynamics by numerical simulations, Solid Free. Symp. Texas. (2014) 1099–1117.

[55] B.K. Foster, E.W. Reutzel, A.R. Nassar, B.T. Hall, S.W. Brown, C.J. Dickman, Optical, layerwise monitoring of powder bed fusion, n.d. https://sffsymposium.engr.utexas.edu/sites/default/files/2015/2015-24-Foster.pdf (accessed January 11, 2019).

[56] B. Liu, R. Wildman, C. Tuck, I. Ashcroft, R. Hague, Investigation the effect of particle size distribution on processing parameters optimization in selective laser melting process, in: SFF, Austin, Texas, 2009: pp. 227–238.

[57] M. Taheri Andani, R. Dehghani, M.R. Karamooz-Ravari, R. Mirzaeifar, J. Ni, Spatter formation in selective laser melting process using multi-laser technology, Mater. Des. 131 (2017) 460–469. doi:https://doi.org/10.1016/j.matdes.2017.06.040.

[58] K.A. Mumtaz, N. Hopkinson, Selective Laser Melting of thin wall parts using pulse shaping, J. Mater. Process. Technol. 210 (2010) 279–287. doi:10.1016/j.jmatprotec.2009.09.011.

[59] Y. Sato, M. Tsukamoto, T. Shobu, Y. Yamashita, S. Yamagata, T. Nishi, R. Higashino, T. Ohkubo, H. Nakano, N. Abe, Preheat effect on titanium plate fabricated by sputter-free selective laser melting in vacuum, Appl. Phys. A. 124 (2018) 288. doi:10.1007/s00339-018-1712-4.

[60] Y. Sato, M. Tsukamoto, Y. Yamashita, K. Yamashita, S. Yamagata, R. Higashino, N. Abe, Effect on beam profile of Ti alloy plate fabrication from powder by sputter-less selective laser melting, (2017) 100950Z. doi:10.1117/12.2251393.

[61] Y. Sato, M. Tsukamoto, Y. Yamashita, S. Masuno, N. Abe, Experimental study on Ti alloy plate fabrication by vacuum selective laser melting, (2016) 97381C.

doi:10.1117/12.2212654.

[62] W.J. Sames, F.A. List, S. Pannala, R.R. Dehoff, S.S. Babu, The metallurgy and processing science of metal additive manufacturing, Int. Mater. Rev. 6608 (2016) 1–46. doi:10.1080/09506608.2015.1116649.

[63] A. Basak, S. Das, Epitaxy and Microstructure Evolution in Metal Additive Manufacturing, Annu. Rev. Mater. Res. 46 (2015) 125–149. doi:10.1146/annurev-matsci-070115-031728.

[64] J.J. Lewandowski, M. Seifi, Metal Additive Manufacturing: A Review of Mechanical Properties, Annu. Rev. Mater. Res. 4614 (2016). doi:10.1146/annurev-matsci-070115-032024.

[65] A.B. Spierings, M. Voegtlin, T. Bauer, K. Wegener, Powder flowability characterisation methodology for powder-bed-based metal additive manufacturing, Prog. Addit. Manuf. 1 (2016) 9–20. doi:10.1007/s40964-015-0001-4.

[66] A.B. Spierings, G. Levy, Comparison of density of stainless steel 316L parts produced with selective laser melting using different powder grades, Proc. Solid Free. Fabr. Symp. (2009) 342–353.

[67] A.B. Spierings, N. Herres, G. Levy, Influence of the particle size distribution on surface quality and mechanical properties in AM steel parts, Rapid Prototyp. J. 17 (2011) 195–202. doi:10.1108/13552541111124770.

[68] J. Dawes, R. Bowerman, R. Trepleton, Introduction to the Additive Manufacturing Powder Metallurgy Supply Chain, Johnson Matthey Technol. Rev. 59 (2015) 243–256. doi:10.1595/205651315X688686.

[69] L.-H. Chiu, C.-H. Wu, P.-Y. Lee, Comparison between oxide-reduced and water-atomized copper powders used in making sintered wicks of heat pipe, China Particuology. 5 (2007) 220–224. doi:10.1016/J.CPART.2007.04.001.

[70] H.P. Tang, G.Y. Yang, W.P. Jia, W.W. He, S.L. Lu, M. Qian, Additive manufacturing of a high niobium-containing titanium aluminide alloy by selective electron beam melting, Mater. Sci. Eng. A. 636 (2015) 103–107. doi:10.1016/J.MSEA.2015.03.079.

[71] Malvern Instruments Ltd., White paper - Optimizing metal powders for additive manufacturing, Malvern, 2017. www.malvern.com/contact (accessed February 12, 2019).

[72] S. Lagutkin, L. Achelis, S. Sheikhaliev, V. Uhlenwinkel, V. Srivastava, Atomization process for metal powder, Mater. Sci. Eng. A. 383 (2004) 1–6. doi:10.1016/J.MSEA.2004.02.059.

[73] A.J. Yule, J.J. Dunkley, Atomization of melts for powder production and spray deposition, Clarendon Press, 1994.

[74] L.V.M. Antony, R.G. Reddy, Processes for production of high-purity metal powders, JOM. 55 (2003) 14–18. doi:10.1007/s11837-003-0153-4.

[75] M. Wei, S. Chen, J. Liang, C. Liu, Effect of atomization pressure on the breakup of TA15 titanium alloy powder prepared by EIGA method for laser 3D printing, Vacuum. 143 (2017) 185–194. doi:10.1016/J.VACUUM.2017.06.014.

[76] S. Dietrich, M. Wunderer, A. Huissel, M.F. Zaeh, A New Approach for a Flexible Powder Production for Additive Manufacturing, Procedia Manuf. 6 (2016) 88–95. doi:10.1016/j.promfg.2016.11.012.

[77] B. Engel, D.L. Bourell, Rapid Prototyping Journal Titanium alloy powder preparation for selective laser sintering Article information, (n.d.). doi:10.1108/13552540010323574.

[78] M. Entezarian, F. Allaire, P. Tsantrizos, R.A.L. Drew, Plasma atomization: A new process for the production of fine, spherical powders, JOM. 48 (1996) 53–55. doi:10.1007/BF03222969.

[79] Z.Z. Fang, J.D. Paramore, P. Sun, K.S.R. Chandran, Y. Zhang, Y. Xia, F. Cao, M. Koopman, M. Free, Powder metallurgy of titanium – past, present, and future, Int. Mater. Rev. 63 (2018) 407–459. doi:10.1080/09506608.2017.1366003.

[80] M. Baumers, P. Dickens, C. Tuck, R. Hague, The cost of additive manufacturing: machine productivity, economies of scale and technology-push, Technol. Forecast. Soc. Change. 102 (2016) 193–201. doi:10.1016/j.techfore.2015.02.015.

[81] J.H. Tan, W.L.E. Wong, K.W. Dalgarno, An overview of powder granulometry on feedstock and part performance in the selective laser melting process, Addit. Manuf. 18 (2017) 228–255. doi:10.1016/j.addma.2017.10.011.

[82] J. Yang, A. Sliva, A. Banerjee, R.N. Dave, R. Pfeffer, Dry particle coating for improving the flowability of cohesive powders, Powder Technol. 158 (2005) 21–33. doi:10.1016/j.powtec.2005.04.032.

[83] P. Karapatis, A sub-process approach of selective laser sintering, EPFL, 2002. doi:10.5075/EPFL-THESIS-2506.

[84] J. Zheng, W.B. Carlson, J.S. Reed, The packing density of binary powder mixtures, J. Eur. Ceram. Soc. 15 (1995) 479–483. doi:10.1016/0955-2219(95)00001-B.

[85] E.O. Olakanmi, Direct selective laser sintering of aluminium alloy powders, (2008). http://etheses.whiterose.ac.uk/1476/ (accessed January 14, 2019).

[86] N.P. Karapatis, G. Egger, P.-E. Gygax, R. Glardon, OPTIMIZATION OF POWDER LAYER DENSITY IN SELECTIVE LASER SINTERING, n.d. https://sffsymposium.engr.utexas.edu/Manuscripts/1999/1999-029-Karapatis.pdf (accessed January 14, 2019).

[87] H.H. Zhu, J.Y.H. Fuh, L. Lu, The influence of powder apparent density on the density in direct laser-sintered metallic parts, Int. J. Mach. Tools Manuf. 47 (2007) 294–298. doi:10.1016/J.IJMACHTOOLS.2006.03.019.

[88] J. Bennett, J. Smith, Fundamentals of Refractory Technology, 2012. https://books.google.com/books?hl=en&lr=&id=Hn6XJifYzAcC&oi=fnd&pg=PR5&ots=dxri12IsFN&sig=DLgTDNbAdhALwm8pLOA0SnXlm7g (accessed January 14, 2019).

[89] ASTM B214, Standard Test Method for Sieve Analysis of Metal Powders, ASTM Stand. (2016). doi:10.1520/C0429-01R06.2.

[90] ASTM B822, Standard Test Method for Particle Size Distribution of Refractory Metal Powders and Related Compounds by Light Scattering, ASTM Int. West Conshohocken, PA. (2010). doi:10.1520/B0822-10.

[91] G.B.J. de Boer, C. de Weerd, D. Thoenes, H.W.J. Goossens, Laser Diffraction Spectrometry: Fraunhofer Diffraction Versus Mie Scattering, Part. Part. Syst. Charact. 4 (1987) 14–19. doi:10.1002/ppsc.19870040104.

[92] R.N. Kelly, F.M. Etzler, WHAT IS WRONG WITH LASER DIFFRACTION? A Critical Review of Current Laser Diffraction Methods for Particle Size Analysis, (2006). http://www.donner-tech.com/whats_wrong_with_ld.pdf (accessed October 9, 2018).

[93] Malvern Instruments Ltd, Morphologi G3 User Manual, (2008) 1–262.

[94] J.A. Slotwinski, E.J. Garboczi, P.E. Stutzman, C.F. Ferraris, S.S. Watson, M.A. Peltz, Characterization of Metal Powders Used for Additive Manufacturing, J. Res. Natl. Inst. Stand. Technol. 119 (2014) 460. doi:10.6028/jres.119.018.

[95] C.I. Niu HJ, Selective laser sintering of gas and water atomized high speed steel powders, Scr. Mater. 41(1) (1999) 25–30. https://www.infona.pl/resource/bwmeta1.element.elsevier-cb267eeb-983f-3a10-a9f7-2a85dcc53ce6 (accessed January 14, 2019).

[96] A.J. Pinkerton, L. Li, Direct additive laser manufacturing using gas- and water-atomised H13 tool steel powders, Int. J. Adv. Manuf. Technol. 25 (2005) 471–479.

doi:10.1007/s00170-003-1844-2.
[97] A.J. Pinkerton, L. Li, Rapid prototyping using direct laser deposition—the effect of powder atomization type and flowrate, Proc. Inst. Mech. Eng. Part B J. Eng. Manuf. 217 (2003) 741–752. doi:10.1243/09544050360673134.
[98] H. Qi, M. Azer, A. Ritter, Studies of Standard Heat Treatment Effects on Microstructure and Mechanical Properties of Laser Net Shape Manufactured INCONEL 718, Metall. Mater. Trans. A. 40 (2009) 2410–2422. doi:10.1007/s11661-009-9949-3.
[99] X. Zhao, J. Chen, X. Lin, W. Huang, Study on microstructure and mechanical properties of laser rapid forming Inconel 718, Mater. Sci. Eng. A. 478 (2008) 119–124. doi:10.1016/J.MSEA.2007.05.079.
[100] E.O. Olakanmi, Effect of mixing time on the bed density, and microstructure of selective laser sintered (sls) aluminium powders, Mater. Res. 15 (2012) 167–176. doi:10.1590/S1516-14392012005000031.
[101] J.W. Carson, B.H. Pittenger, Bulk Properties of Powders, (1998). doi:10.1361/asmhba0001530.
[102] E. Attar, Simulation of Selective Electron Beam Melting Processes, Universit¨at Erlangen-N¨urnberg, 2011. https://d-nb.info/1013101472/34 (accessed January 15, 2019).
[103] Z. Snow, Understanding Powder Spreadability in Powder Bed Fusion, Penn State University, 2018. https://etda.libraries.psu.edu/catalog/15740zus31.
[104] J. Zielinski, S. Vervoort, H.-W. Mindt, M. Megahed, Influence of Powder Bed Characteristics on Material Quality in Additive Manufacturing, BHM Berg- Und Hüttenmännische Monatshefte. 162 (2017) 192–198. doi:10.1007/s00501-017-0592-9.
[105] J. Zielinski, H.-W. Mindt, J. Du¨chting, D. Du¨chting, J.H. Schleifenbaum, M. Megahed, Numerical and Experimental Study of Ti6Al4V Components Manufactured Using Powder Bed Fusion Additive Manufacturing, J. Mater. 69 (2017) 2711–2718. doi:10.1007/s11837-017-2596-z.
[106] F. Calignano, M. Lorusso, J. Pakkanen, F. Trevisan, E.P. Ambrosio, D. Manfredi, P. Fino, Investigation of accuracy and dimensional limits of part produced in aluminum alloy by selective laser melting, Int. J. Adv. Manuf. Technol. 88 (2017) 451–458. doi:10.1007/s00170-016-8788-9.
[107] B. Vandenbroucke, J.-P. Kruth, Selective laser melting of biocompatible metals for rapid manufacturing of medical parts, Rapid Prototyp. J. 13 (2007) 196–203. doi:10.1108/13552540710776142.
[108] L. Thijs, F. Verhaeghe, T. Craeghs, J. Van Humbeeck, J.P. Kruth, A study of the microstructural evolution during selective laser melting of Ti-6Al-4V, Acta Mater. 58 (2010) 3303–3312. doi:10.1016/j.actamat.2010.02.004.
[109] C.C. Ng, M.M. Savalani, H.C. Man, I. Gibson, Layer manufacturing of magnesium and its alloy structures for future applications, Virtual Phys. Prototyp. 5 (2010) 13–19. doi:10.1080/17452751003718629.
[110] D. Gu, Y. Shen, Balling phenomena in direct laser sintering of stainless steel powder: Metallurgical mechanisms and control methods, Mater. Des. 30 (2009) 2903–2910. doi:10.1016/j.matdes.2009.01.013.
[111] V. Seyda, N. Kaufmann, C. Emmelmann, Investigation of Aging Processes of Ti-6Al-4 V Powder Material in Laser Melting, Phys. Procedia. 39 (2012) 425–431. doi:10.1016/j.phpro.2012.10.057.
[112] R. O'Leary, R. Setchi, P.W. Prickett, An investigation into the recycling of Ti-6Al-4V powder used within SLM to improve sustainability, (2015). http://orca.cf.ac.uk/81260/

(accessed January 15, 2019).
[113] A. Strondl, O. Lyckfeldt, H. Brodin, U. Ackelid, Characterization and Control of Powder Properties for Additive Manufacturing, Jom. 67 (2015) 549–554. doi:10.1007/s11837-015-1304-0.
[114] L.C. Ardila, F. Garciandia, J.B. Gonzalez-Diaz, P. Alvarez, A. Echeverria, M.M. Petite, R. Deffley, J. Ochoa, Effect of IN718 recycled powder reuse on properties of parts manufactured by means of Selective Laser Melting, Phys. Procedia. 56 (2014) 99–107. doi:10.1016/j.phpro.2014.08.152.
[115] Q.B. Nguyen, M.L.S. Nai, Z. Zhu, C.-N. Sun, J. Wei, W. Zhou, Characteristics of Inconel Powders for Powder-Bed Additive Manufacturing, Engineering. 3 (2017) 695–700. doi:10.1016/J.ENG.2017.05.012.
[116] ASTM International, Standard Practices for Sampling Metal Powders, West Conshohocken, PA, 2015. doi:10.1520/B0215-15.
[117] A.T. Clare, P.R. Chalker, S. Davies, C.J. Sutcliffe, S. Tsopanos, Selective laser melting of high aspect ratio 3D nickel-titanium structures two way trained for MEMS applications, Int. J. Mech. Mater. Des. 4 (2008) 181–187. doi:10.1007/s10999-007-9032-4.
[118] F. Campbell, Manufacturing Technology for Aerospace Structural Materials, 2006. doi:10.1016/B978-1-85617-495-4.X5000-8.
[119] X. Wang, X. Gong, K. Chou, Review on powder-bed laser additive manufacturing of Inconel 718 parts, Proc. Inst. Mech. Eng. Part B J. Eng. Manuf. 231 (2017) 1890–1903. doi:10.1177/0954405415619883.
[120] S.F. Diltemiz, S. Zhang, Superalloys for super jobs, in: S. Zhang, D. Zhao (Eds.), Aerosp. Mater. Handb., CRC Press, London, 2013: pp. 1–76.
[121] C.T. (Chester T. Sims, W.C. Hagel, The superalloys., 1972. https://infoscience.epfl.ch/record/60261 (accessed August 8, 2016).
[122] M.K. Thompson, G. Moroni, T. Vaneker, G. Fadel, R.I. Campbell, I. Gibson, A. Bernard, J. Schulz, P. Graf, B. Ahuja, F. Martina, Design for Additive Manufacturing: Trends, opportunities, considerations, and constraints, CIRP Ann. - Manuf. Technol. 65 (2016) 737–760. doi:10.1016/j.cirp.2016.05.004.
[123] ASTM International, ASTM B637 - 18 Standard Specification for Precipitation-Hardening and Cold Worked Nickel Alloy Bars, Forgings, and Forging Stock for Moderate or High Temperature Service, West Conshohocken, PA, 2018. doi:10.1520/B0637-18.
[124] E. Chlebus, K. Gruber, B. Kuźnicka, J. Kurzac, T. Kurzynowski, Effect of heat treatment on microstructure and mechanical properties of Inconel 718 processed by selective laser melting, Mater. Sci. Eng. A. 639 (2015) 647–655. doi:10.1016/j.msea.2015.05.035.
[125] Q. Jia, D. Gu, Selective laser melting additive manufacturing of Inconel 718 superalloy parts: Densification, microstructure and properties, J. Alloys Compd. 585 (2014) 713–721. doi:10.1016/j.jallcom.2013.09.171.
[126] Y. Lu, S. Wu, Y. Gan, T. Huang, C. Yang, L. Junjie, J. Lin, Study on the microstructure, mechanical property and residual stress of SLM Inconel-718 alloy manufactured by differing island scanning strategy, Opt. Laser Technol. 75 (2015) 197–206. doi:10.1016/j.optlastec.2015.07.009.
[127] T. Trosch, J. Strößner, R. Völkl, U. Glatzel, Microstructure and mechanical properties of selective laser melted Inconel 718 compared to forging and casting, Mater. Lett. 164 (2016) 428–431. doi:10.1016/j.matlet.2015.10.136.
[128] A. Mostafa, I. Picazo Rubio, V. Brailovski, M. Jahazi, M. Medraj, Structure, Texture and Phases in 3D Printed IN718 Alloy Subjected to Homogenization and HIP Treatments,

Metals (Basel). 7 (2017) 196. doi:10.3390/met7060196.
[129] A.A. Popovich, V.S. Sufiiarov, I.A. Polozov, E. V. Borisov, Microstructure and Mechanical Properties of Inconel 718 Produced by SLM and Subsequent Heat Treatment, Key Eng. Mater. 651–653 (2015) 665–670. doi:10.4028/www.scientific.net/KEM.651-653.665.
[130] D. Zhang, W. Niu, X. Cao, Z. Liu, Effect of standard heat treatment on the microstructure and mechanical properties of selective laser melting manufactured Inconel 718 superalloy, Mater. Sci. Eng. A. 644 (2015) 32–40. doi:10.1016/j.msea.2015.06.021.
[131] M.J. Donachie, S.J. Donachie, Superalloys : a technical guide, ASM International, 2002. https://books.google.co.uk/books?hl=en&lr=&id=vjCJ5pI1QpkC&oi=fnd&pg=PR1&dq=donachie+matthew&ots=LJgXIgpYV8&sig=jt78R-Keb4fymG5pD5-AStVmVjA#v=onepage&q=donachie matthew&f=false (accessed January 16, 2019).
[132] ASTM International, ASTM B435-06(2016) Standard Specification for UNS N06002, UNS N06230, UNS N12160, and UNS R30556 Plate, Sheet, and Strip, West Conshohocken, PA, 2016. doi:10.1520/B0435-06R16.
[133] H. Brodin, O. Andersson, S. Johansson, Mechanical testing of a selective laser melted superalloy, Vol. 5A Ind. Cogener. Manuf. Mater. Metall. Mar. Microturbines, Turbochargers, Small Turbomachines. 5 A (2013) V05AT21A009. doi:10.1115/GT2013-95878.
[134] H. Brodin, J. Saarimäki, Mechanical properties of lattice truss structures made of a selective laser melted superalloy, 13th Int. Conf. Fract. (2013) 1–10. doi:10.1115/GT2013-95878.
[135] J. Saarimäki, The mechanical properties of lattice truss structures with load- bearing shells made of selectively laser melted Hastelloy X^{TM}, (2011) 145. doi:476.
[136] D. Tomus, T. Jarvis, X. Wu, J. Mei, P. Rometsch, E. Herny, J.F. Rideau, S. Vaillant, Controlling the microstructure of Hastelloy-X components manufactured by Selective Laser Melting, Phys. Procedia. 41 (2013) 823–827. doi:10.1016/j.phpro.2013.03.154.
[137] D. Tomus, P.A. Rometsch, M. Heilmaier, X. Wu, Effect of minor alloying elements on crack-formation characteristics of Hastelloy-X manufactured by selective laser melting, Addit. Manuf. 16 (2017) 65–72. doi:10.1016/j.addma.2017.05.006.
[138] N.J. Harrison, I. Todd, K. Mumtaz, Reduction of micro-cracking in nickel superalloys processed by Selective Laser Melting: A fundamental alloy design approach, Acta Mater. 94 (2015) 59–68. doi:10.1016/j.actamat.2015.04.035.
[139] R. Mertens, S. Dadbakhsh, J. Van Humbeeck, J.-P. Kruth, Application of base plate preheating during selective laser melting, Procedia CIRP. 74 (2018) 5–11. doi:10.1016/j.procir.2018.08.002.
[140] T. Etter, K. Kunze, F. Geiger, H. Meidani, Reduction in mechanical anisotropy through high temperature heat treatment of Hastelloy X processed by Selective Laser Melting (SLM), IOP Conf. Ser. Mater. Sci. Eng. 82 (2015) 12097. doi:10.1088/1757-899X/82/1/012097.
[141] D. Herzog, V. Seyda, E. Wycisk, C. Emmelmann, Additive manufacturing of metals, Acta Mater. 117 (2016) 371–392. doi:10.1016/j.actamat.2016.07.019.
[142] E. Wycisk, A. Solbach, S. Siddique, D. Herzog, F. Walther, C. Emmelmann, Effects of defects in laser additive manufactured Ti-6Al-4V on fatigue properties, Phys. Procedia. 56 (2014) 371–378. doi:10.1016/j.phpro.2014.08.120.
[143] E. Wycisk, C. Emmelmann, … S.S.-A. materials, undefined 2013, High cycle fatigue (HCF) performance of Ti-6Al-4V alloy processed by selective laser melting, Trans Tech Publ. (n.d.). https://www.scientific.net/AMR.816-817.134 (accessed January 17, 2019).

[144] Q. Liu, J. Elambasseril, S. Sun, … M.L.-A.M., undefined 2014, The effect of manufacturing defects on the fatigue behaviour of Ti-6Al-4V specimens fabricated using selective laser melting, Trans Tech Publ. (n.d.). https://www.scientific.net/AMR.891-892.1519 (accessed January 17, 2019).

[145] W. Xu, S. Sun, J. Elambasseril, Q. Liu, M. Brandt, M. Qian, Ti-6Al-4V Additively Manufactured by Selective Laser Melting with Superior Mechanical Properties, JOM. 67 (2015) 668–673. doi:10.1007/s11837-015-1297-8.

[146] K. Rekedal, D. Liu, Fatigue Life of Selective Laser Melted and Hot Isostatically Pressed Ti-6Al-4v Absent of Surface Machining, in: 56th AIAA/ASCE/AHS/ASC Struct. Struct. Dyn. Mater. Conf., American Institute of Aeronautics and Astronautics, Reston, Virginia, 2015. doi:10.2514/6.2015-0894.

[147] H.K. Rafi, T.L. Starr, B.E. Stucker, A comparison of the tensile, fatigue, and fracture behavior of Ti–6Al–4V and 15-5 PH stainless steel parts made by selective laser melting, Int. J. Adv. Manuf. Technol. 69 (2013) 1299–1309. doi:10.1007/s00170-013-5106-7.

[148] S. Leuders, T. Lieneke, S. Lammers, … T.T.-J. of M., undefined 2014, On the fatigue properties of metals manufactured by selective laser melting–The role of ductility, Cambridge.Org. (n.d.). https://www.cambridge.org/core/journals/journal-of-materials-research/article/on-the-fatigue-properties-of-metals-manufactured-by-selective-laser-melting-the-role-of-ductility/41F715871681AB7319F3CA6403976AD0 (accessed January 17, 2019).

[149] H. Gong, K. Rafi, … T.S.-S. freeform, U. 2012, EFFECT OF DEFECTS ON FATIGUE TESTS OF, (n.d.). http://sffsymposium.engr.utexas.edu/Manuscripts/2012/2012-39-Gong.pdf (accessed January 17, 2019).

[150] P. Edwards, M. Ramulu, Fatigue performance evaluation of selective laser melted Ti–6Al–4V, 598 (2014) 327–337. doi:10.1016/J.MSEA.2014.01.041.

[151] D.M. Lambert, Evaluation of the Effect of Surface Finish on High-Cycle Fatigue of SLM-IN718, JANNAF Propuls. Meet. 63rd; (2016).

[152] L. Huynh, J. Rotella, M.D. Sangid, Fatigue behavior of IN718 microtrusses produced via additive manufacturing, Mater. Des. 105 (2016) 278–289. doi:10.1016/j.matdes.2016.05.032.

[153] A.B. Spierings, T.L. Starr, K. Wegener, Fatigue performance of additive manufactured metallic parts, Rapid Prototyp. J. 19 (2013) 88–94. doi:10.1108/13552541311302932.

[154] E. Herderick, Additive manufacturing of metals: A review, Mater. Sci. Technol. Conf. Exhib. 2011, MS T'11. 2 (2011) 1413–1425. http://www.scopus.com/inward/record.url?eid=2-s2.0-84856301323&partnerID=40&md5=e02018d10b2ca37a7e2ae1773e4fcaec.

[155] W.E. Frazier, Metal additive manufacturing: A review, J. Mater. Eng. Perform. 23 (2014) 1917–1928. doi:10.1007/s11665-014-0958-z.

[156] H. Gong, K. Rafi, T. Starr, B. Stucker, T. Starr, EFFECT OF DEFECTS ON FATIGUE TESTS OF AS-BUILT TI-6AL-4V PARTS FABRICATED BY SELECTIVE LASER MELTING, (2012). http://sffsymposium.engr.utexas.edu/Manuscripts/2012/2012-39-Gong.pdf (accessed January 17, 2019).

[157] E. Charkaluk, V. Chastand, Fatigue of Additive Manufacturing Specimens: A Comparison with Casting Processes, Proceedings. 2 (2018) 474. doi:10.3390/ICEM18-05352.

[158] Y.-L. Lee, Fatigue testing and analysis : theory and practice, Elsevier Butterworth-Heinemann, 2005. https://books.google.co.uk/books?hl=en&lr=&id=mrPFTVr2hH4C&oi=fnd&pg=PP2&dq=review+fatigue+testing+methods&ots=nNYahaMbqb&sig=8kZ6OVmVumD60meXQ

H5bsYJ9u4Y#v=onepage&q=review fatigue testing methods&f=false (accessed January 17, 2019).

[159] B. Van Hooreweder, D. Moens, R. Boonen, J.-P. Kruth, P. Sas, Analysis of Fracture Toughness and Crack Propagation of Ti6Al4V Produced by Selective Laser Melting, Adv. Eng. Mater. 14 (2012) 92–97. doi:10.1002/adem.201100233.

[160] V. Cain, L. Thijs, J. Van Humbeeck, B. Van Hooreweder, R. Knutsen, Crack propagation and fracture toughness of Ti6Al4V alloy produced by selective laser melting, Addit. Manuf. 5 (2015) 68–76. doi:10.1016/j.addma.2014.12.006.

[161] B. Vrancken, Study of Residual Stresses in Selective Laser Melting, PhD Thesis; KU Leuven Arenb. Dr. Sch. Fac. Eng. Sci. (2016) 1–253. https://lirias.kuleuven.be/bitstream/123456789/542751/1/thesis+Bey+Vrancken+v01-06-2016+FINAL_compressed.pdf.

[162] R. Konečná, L. Kunz, G. Nicoletto, A. Bača, Long fatigue crack growth in Inconel 718 produced by selective laser melting, Int. J. Fatigue. 92 (2016) 499–506. doi:10.1016/j.ijfatigue.2016.03.012.

[163] R. Konečná, G. Nicoletto, L. Kunz, A. Bača, Microstructure and directional fatigue behavior of Inconel 718 produced by selective laser melting, Procedia Struct. Integr. 2 (2016) 2381–2388. doi:10.1016/j.prostr.2016.06.298.

[164] ASTM International, ASTM B212 - 17 Standard Test Method for Apparent Density of Free-Flowing Metal Powders Using the Hall Flowmeter Funnel, West Conshohocken, PA, 2017. doi:10.1520/B0212-17.

[165] LPW Techonology Ltd., Using LPW's lab to rapidly complete a Root Cause Analysis of Powder Contamination, Runcorn, UK, 2017.

[166] T.M. Smith, M.F. Kloesel, C.K. Sudbrack, Relationship of Powder Feedstock Variability to Microstructure and Defects in Selective Laser Melted Alloy 718, in: 28th Annu. Int. Solid Free. Fabr. Symp., Austin, TX, 2017. https://ntrs.nasa.gov/search.jsp?R=20170008114 (accessed November 1, 2018).

[167] SAE International, AMS 5390 - Nickel Alloy, Corrosion and Heat-Resistant, Investment Castings 47.5Ni - 22Cr - 1.5Co - 9Mo - 0.60W - 18.5Fe (N-12MV) As-Cast, (2014). doi:https://doi.org/10.4271/AMS5390G.

[168] Y. Zhang, J.R.G. Evans, S. Yang, Corrected values for boiling points and enthalpies of vaporization of elements in handbooks, J. Chem. Eng. Data. 56 (2011) 328–337. doi:10.1021/je1011086.

[169] L. Thijs, J. Van Humbeeck, K. Kempen, E. Yasa, J. Kruth, M. Rombouts, Investigation on the inclusions in maraging steel produced by Selective Laser Melting, Innov. Dev. Virtual Phys. Prototyp. (2011) 297–304. doi:10.1201/b11341-48.

[170] H.J.T. Ellingham, Transactions and Communications, J. Soc. Chem. Ind. 63 (1944) 125–160. doi:10.1002/jctb.5000630501.

[171] G.A. Rao, M. Srinivas, D.S. Sarma, Effect of oxygen content of powder on microstructure and mechanical properties of hot isostatically pressed superalloy Inconel 718, Mater. Sci. Eng. A. 435–436 (2006) 84–99. doi:10.1016/j.msea.2006.07.053.

[172] Y.N. Zhang, X. Cao, P. Wanjara, M. Medraj, Oxide films in laser additive manufactured Inconel 718, Acta Mater. 61 (2013) 6562–6576. doi:10.1016/j.actamat.2013.07.039.

[173] R.C. Reed, The Superalloys Fundamentals and Applications, 2006. doi:https://doi.org/10.1017/CBO9780511541285.

[174] P. Nandwana, W.H. Peter, R.R. Dehoff, L.E. Lowe, M.M. Kirka, F. Medina, S.S. Babu, Recyclability Study on Inconel 718 and Ti-6Al-4V Powders for Use in Electron Beam Melting, Metall. Mater. Trans. B. 47 (2016) 754–762. doi:10.1007/s11663-015-0477-9.

[175] Y.J. Liu, S.J. Li, H.L. Wang, W.T. Hou, Y.L. Hao, R. Yang, T.B. Sercombe, L.C. Zhang, Microstructure, defects and mechanical behavior of beta-type titanium porous structures manufactured by electron beam melting and selective laser melting, Acta Mater. 113 (2016) 56–67. doi:10.1016/j.actamat.2016.04.029.

[176] S. Das, Physical Aspects of Process Control in Selective Laser Sintering of Metals, Adv. Eng. Mater. 5 (2003) 701–711. doi:10.1002/adem.200310099.

[177] T. Boegelein, E. Louvis, K. Dawson, G.J. Tatlock, A.R. Jones, Characterisation of a complex thin walled structure fabricated by selective laser melting using a ferritic oxide dispersion strengthened steel, Mater. Charact. 112 (2016) 30–40. doi:10.1016/j.matchar.2015.11.021.

[178] A.N.D. Gasper, B. Szost, X. Wang, D. Johns, S. Sharma, A.T. Clare, I.A. Ashcroft, Spatter and oxide formation in laser powder bed fusion of Inconel 718, Addit. Manuf. (2018). doi:10.1016/J.ADDMA.2018.09.032.

[179] A.N.D. Gasper, S. Catchpole-Smith, A.T. Clare, In-situ synthesis of titanium aluminides by direct metal deposition, J. Mater. Process. Technol. 239 (2017). doi:10.1016/j.jmatprotec.2016.08.031.

[180] P.C. Collins, D.A. Brice, P. Samimi, I. Ghamarian, H.L. Fraser, Microstructural Control of Additively Manufactured Materials, Annu. Rev. Mater. Res. (2015). doi:10.1146/annurev-matsci-070115-031816.

[181] C. Qiu, M. Al Kindi, A.S. Aladawi, I. Al Hatmi, A comprehensive study on microstructure and tensile behaviour of a selectively laser melted stainless steel, Sci. Rep. 8 (2018) 7785. doi:10.1038/s41598-018-26136-7.

[182] R.J. Smith, G.J. Lewi, D.H. Yates, Development and application of nickel alloys in aerospace engineering, Aircr. Eng. Aerosp. Technol. 73 (2001) 138–147. doi:10.1108/00022660110694995.

[183] J. Clayton, R. Deffley, Optimising metal powders for additive manufacturing, Met. Powder Rep. 69 (2014) 14–17. doi:10.1016/S0026-0657(14)70223-1.

[184] Measure properties of image regions - MATLAB regionprops - MathWorks United Kingdom, (n.d.). https://uk.mathworks.com/help/images/ref/regionprops.html (accessed January 7, 2019).

[185] B. Ferrar, L. Mullen, E. Jones, R. Stamp, C.J. Sutcliffe, Gas flow effects on selective laser melting (SLM) manufacturing performance, J. Mater. Process. Technol. 212 (2012) 355–364. doi:10.1016/j.jmatprotec.2011.09.020.

[186] D.L. Bourell, Perspectives on Additive Manufacturing, Annu. Rev. Mater. Res. 46 (2016) annurev-matsci-070115-031606. doi:10.1146/annurev-matsci-070115-031606.

[187] J.A. Slotwinski, E.J. Garboczi, Metrology Needs for Metal Additive Manufacturing Powders, Jom. 67 (2015) 538–543. doi:10.1007/s11837-014-1290-7.

[188] N.N. (Norman N. Greenwood, A. (Alan) Earnshaw, Chemistry of the elements, Butterworth-Heinemann, 1997.

[189] C.T. Rueden, J. Schindelin, M.C. Hiner, B.E. DeZonia, A.E. Walter, E.T. Arena, K.W. Eliceiri, ImageJ2: ImageJ for the next generation of scientific image data, BMC Bioinformatics. 18 (2017) 529. doi:10.1186/s12859-017-1934-z.

[190] T. Pietzsch, S. Preibisch, P. Tomancák, S. Saalfeld, ImgLib2--generic image processing in Java., Bioinformatics. 28 (2012) 3009–11. doi:10.1093/bioinformatics/bts543.

[191] T.W. Ridler, S. Calvard, Picture Thresholding Using an Iterative Selection Method, IEEE Trans. Syst. Man. Cybern. 8 (1978) 630–632. doi:10.1109/TSMC.1978.4310039.

[192] J.A. Slotwinski, E.J. Garboczi, K.M. Hebenstreit, Porosity Measurements and Analysis for Metal Additive Manufacturing Process Control, J. Res. Natl. Inst. Stand. Technol. 119 (2014) 494. doi:10.6028/jres.119.019.

[193] B. Liu, Further Process Understanding and Prediction on Selective Laser Melting of Stainless Steel 316L, Dr. Thesis. (2013).
[194] A.M. Philo, C.J. Sutcliffe, S. Sillars, J. Sienz, S.G.R. Brown, N.P. Lavery, A STUDY INTO THE EFFECTS OF GAS FLOW INLET DESIGN OF THE RENISHAW AM250 LASER POWDER BED FUSION MACHINE USING COMPUTATIONAL MODELLING, (2017) 1203–1219.
[195] M. Baumers, Economic aspects of additive manufacturing: benefits, costs and energy consumption, (2014) 81–87. doi:10.1007/s13398-014-0173-7.2.
[196] V. Seyda, D. Herzog, C. Emmelmann, Relationship between powder characteristics and part properties in laser beam melting of Ti–6Al–4V, and implications on quality, J. Laser Appl. 29 (2017) 022311. doi:10.2351/1.4983240.
[197] L.T. Phuc, M. Seita, A high-resolution and large field-of-view scanner for in-line characterization of powder bed defects during additive manufacturing, Mater. Des. 164 (2018) 107562. doi:https://doi.org/10.1016/j.matdes.2018.107562.
[198] A. Thompson, I. Maskery, R.K. Leach, X-ray computed tomography for additive manufacturing: a review, Meas. Sci. Technol. 27 (2016) 072001. doi:10.1088/0957-0233/27/7/072001.
[199] M. Seifi, M. Gorelik, J. Waller, N. Hrabe, N. Shamsaei, S. Daniewicz, J.J. Lewandowski, Progress Towards Metal Additive Manufacturing Standardization to Support Qualification and Certification, JOM. 69 (2017) 439–455. doi:10.1007/s11837-017-2265-2.
[200] A. Townsend, N. Senin, L. Blunt, R.K. Leach, J.S. Taylor, Surface texture metrology for metal additive manufacturing: a review, Precis. Eng. 46 (2016) 34–47. doi:10.1016/J.PRECISIONENG.2016.06.001.
[201] ASTM International, ASTM E647 - Standard Test Method for Measurement of Fatigue Crack Growth Rates, 03 (2016) 1–49. doi:10.1520/E0647-15E01.2.
[202] BSI, BS ISO 12108:2012 Metallic materials — Fatigue testing — Fatigue crack growth method, BSI Stand. Publ. (2012) 1–54.
[203] ASTM E399, Standard Test Method for Linear-Elastic Plane-Strain Fracture Toughness K1C of Metallic Material, E 399. (2013) 1–33. doi:10.1520/E0399-12E03.2.
[204] P. Paris, F. Erdogan, A Critical Analysis of Crack Propagation Laws, J. Basic Eng. 85 (1963) 528. doi:10.1115/1.3656900.
[205] M. Clavel, A. Pineau, Frequency and Wave-Form Effects on the Fatigue Crack Growth Behavior of Alloy 718 At 298 K and 823 K., Met. Trans A. 9 A (1978) 471–480. doi:10.1007/BF02646402.
[206] C. Mercer, A.B.O. Soboyejo, W.O. Soboyejo, Micromechanisms of fatigue crack growth in a forged Inconel 718 nickel-based superalloy, Mater. Sci. Eng. A. 270 (1999) 308–322. doi:10.1016/S0921-5093(99)00214-2.
[207] R. Molins, G. Hochstetter, J.C. Chassaigne, E. Andrieu, Oxidation effects on the fatigue crack growth behaviour of alloy 718 at high temperature, Acta Mater. 45 (1997) 663–674. doi:10.1016/S1359-6454(96)00192-9.
[208] K. Tanaka, S. Matsuoka, A tentative explanation for two parameters, C and m, in Paris equation of fatigue crack growth, Int. J. Fract. 13 (1977) 563–583. doi:10.1007/BF00017293.
[209] S. Li, The Paris law in metals and ceramics, 1995. https://link.springer.com/content/pdf/10.1007%2FBF00633140.pdf (accessed February 7, 2019).
[210] K.N. Amato, S.M. Gaytan, L.E. Murr, E. Martinez, P.W. Shindo, J. Hernandez, S. Collins, F. Medina, Microstructures and mechanical behavior of Inconel 718 fabricated by selective laser melting, Acta Mater. 60 (2012) 2229–2239.

doi:10.1016/j.actamat.2011.12.032.

[211] L.E. Murr, E. Martinez, S.M. Gaytan, D.A. Ramirez, B.I. MacHado, P.W. Shindo, J.L. Martinez, F. Medina, J. Wooten, D. Ciscel, U. Ackelid, R.B. Wicker, Microstructural architecture, microstructures, and mechanical properties for a nickel-base superalloy fabricated by electron beam melting, Metall. Mater. Trans. A Phys. Metall. Mater. Sci. 42 (2011) 3491–3508. doi:10.1007/s11661-011-0748-2.

[212] B. Vrancken, V. Cain, R. Knutsen, J. Van Humbeeck, Residual stress via the contour method in compact tension specimens produced via selective laser melting, Scr. Mater. 87 (2014) 29–32. doi:10.1016/j.scriptamat.2014.05.016.

[213] Z. Xu, C.J. Hyde, A. Thompson, R.K. Leach, I. Maskery, C. Tuck, A.T. Clare, Staged thermomechanical testing of nickel superalloys produced by selective laser melting, Mater. Des. 133 (2017) 520–527. doi:10.1016/j.matdes.2017.08.009.

[214] D.D. Gu, W. Meiners, K. Wissenbach, R. Poprawe, Laser additive manufacturing of metallic components: materials, processes and mechanisms, Int. Mater. Rev. 57 (2012) 133–164. doi:10.1179/1743280411Y.0000000014.

[215] Y. Yamashita, T. Murakami, R. Mihara, M. Okada, Y. Murakami, Defect analysis and fatigue design basis for Ni-based superalloy 718 manufactured by selective laser melting, Int. J. Fatigue. 117 (2018) 485–495. doi:10.1016/j.ijfatigue.2018.08.002.

[216] F. Wang, X.H. Wu, D. Clark, On direct laser deposited Hastelloy X: dimension, surface finish, microstructure and mechanical properties, Mater. Sci. Technol. 27 (2011) 344–356. doi:10.1179/026708309X12578491814591.

[217] Q.B. Nguyen, D.N. Luu, S.M.L. Nai, Z. Zhu, Z. Chen, J. Wei, The role of powder layer thickness on the quality of SLM printed parts, Arch. Civ. Mech. Eng. 18 (2018) 948–955. doi:10.1016/J.ACME.2018.01.015.

Appendices

Appendix A.1

A1.1

The following script was used for the image analysis of oxidised particles in the spatter powder. The script was written by Duncan Hickman specifically for the investigation in Chapter 6. The program is summarised by the flowchart in Figure 6.2.

```
function Particle_Analysis_GUI
%% Image analysis for powder Particles
% HELP PAGE
% duncan.hickman@nottingham.ac.uk


%% Create figure window
fig.h1                                                              =
figure('CloseRequestFcn',@my_closereq,'Name','1','Units','norm
alized','Position',[0.02 0.35 0.45 0.55]);
% Ensure it's on screen in the correct place
movegui(fig.h1,'onscreen')
% Create tabs for images and axes for imshow to use later
tgroup = uitabgroup('Parent', fig.h1);
tab1 = uitab('Parent', tgroup, 'Title', 'Original Image');
tab2 = uitab('Parent', tgroup, 'Title', 'Binary Image');
tab3 = uitab('Parent', tgroup, 'Title', 'Identified Particles');
axes(tab1,'OuterPosition',[0 0.1 1 0.9]);
axes(tab2,'OuterPosition',[0 0.1 1 0.9]);
axes(tab3,'OuterPosition',[0 0.1 1 0.9]);


%% Create push buttons
btnSetThresh = uicontrol('Parent',fig.h1,'Style', 'pushbutton',
'String', 'Set Threshold',...
    'Position', [20 70 100 20],...
    'Callback', @SetThresh);

% Create push buttons
btnSetSpotty = uicontrol('Parent',fig.h1,'Style', 'pushbutton',
'String', 'Spotty Params',...
    'Position', [20 45 100 20],...
    'Callback', @SetSpottyParams);

% Create push button
```

```
btnFindParticles      =      uicontrol('Parent',fig.h1,'Style',
'pushbutton', 'String', 'Find Particles',...
    'Position', [140 70 100 20],...
    'Callback', @FindParticles);

% Create push button
btnFindSpottyParticles   =   uicontrol('Parent',fig.h1,'Style',
'pushbutton', 'String', 'Find Spotty',...
    'Position', [260 70 100 20],...
    'Callback', @FindSpottyParticles);
% Create push button
btnAddSpottyParticles    =    uicontrol('Parent',fig.h1,'Style',
'pushbutton', 'String', 'ADD Spotty',...
    'Position', [266 45 88 20],...
    'Callback', @ADDSpottyParticles);
% Create push button
btnRemoveSpottyParticles  =  uicontrol('Parent',fig.h1,'Style',
'pushbutton', 'String', 'REMOVE Spotty',...
    'Position', [266 20 88 20],...
    'Callback', @REMOVESpottyParticles);

% Create push button
btnPickClust = uicontrol('Parent',fig.h1,'Style', 'pushbutton',
'String', 'Remove Clusters',...
    'Position', [380 70 100 20],...
    'Callback', @PickClust);

% Create push button
btnPushAllParticles     =     uicontrol('Parent',fig.h1,'Style',
'pushbutton', 'String', 'Push Particles',...
    'Position', [500 70 100 20],...
    'Callback', @PushAllParticles);

% Create push button
btnSavetoExcel       =       uicontrol('Parent',fig.h1,'Style',
'pushbutton', 'String', 'Save to Excel',...
    'Position', [500 45 100 20],...
    'Callback', @SaveToExcel);

% Create push button
btnLoadImage = uicontrol('Parent',fig.h1,'Style', 'pushbutton',
'String', 'Next Image',...
    'Position', [500 15 100 20],...
    'Callback', @LoadImage);


%% Set default variables/containers for use later
I = [];
filename = '';
globalThresh = 85;
allParticles = struct([]);
spotThresh = 12;
```

```
spotGrayThresh = 110;

% run load image function to start app
LoadImage

%% GUI Functions

% Load in the next image/initilaize app
    function LoadImage(hObject,eventdata)

        % Read in image and GUI set up
        filename   =   uigetfile({'*.jpg;*.tif;*.png;*.gif','All
Image Files';...
            '*.*','All Files' },'Select Image')
        I = imread(filename);

        movegui(fig.h1,'onscreen')

        % Show image that has been opened (Other images will
appear once buttons have been pushed)p
        imshow(I,'Parent', tab1.Children)
        title(tab1.Children,'Original Image')

    end


% find particles function
    function FindParticles(hObject,eventdata)

        fig.h2                                                  =
figure('Name','2','Units','normalized','Position',[0.5     0.35
0.45 0.55]);
        fig.h2.CurrentAxes = axes();
        movegui(fig.h2,'onscreen')

        BW = I > globalThresh;
%         subplot(1,3,2)
        imshow(BW,'Parent', tab2.Children)
        title(tab2.Children,'Binary Image')

        BW2 = imfill(~BW,'holes');
        % figure
        % imshow(BW2)
        BW3 = BW&BW2;
        % figure
        % imshow(BW3)



        % Find particles in image using 'regionprops' function
```

```
        allParticles        =        regionprops(BW3,        I,
{'Centroid','PixelValues','BoundingBox','Area','MajorAxisLengt
h','MinorAxisLength','Perimeter'});

        % Add to the structure 'allParticles' and show which
particles we've found
        % so far...
        % RegionID - An unique ID for each particle
        % RegionPixels - An image of each particle
        % BW -BW version of this image using a new threshold
value 'spotGrayThresh'
        % RegProps - The data from 'regionprops' used on image
of each particle


%         subplot(1,3,3)
        imshow(I,'Parent', tab3.Children)
        title(tab3.Children,'Identified Particles')


        numObj = numel(allParticles);
        for i = 1:numObj
            allParticles(i).RegionID = i;

            allParticles(i).RegionPixels                      =
I(round(allParticles(i).BoundingBox(2)):floor(allParticles(i).
BoundingBox(2))+floor(allParticles(i).BoundingBox(4)),round(al
lParticles(i).BoundingBox(1)):floor(allParticles(i).BoundingBo
x(1))+floor(allParticles(i).BoundingBox(3)));

            allParticles(i).BW                                =
allParticles(i).RegionPixels<spotGrayThresh;

            %                           allParticles(i).BWArea  =
sum(sum(~[allParticles(i).RegionPixels<globalThresh]));

            allParticles(i).RegProps                          =
regionprops(allParticles(i).BW,
{'Centroid','BoundingBox','Eccentricity'});

            allParticles(i).Aspect                            =
allParticles(i).MinorAxisLength./allParticles(i).MajorAxisLeng
th;

            %                           allParticles(i).Circ  =
(4*pi*[allParticles(i).BWArea])./([allParticles(i).Perimeter].
^2);
```

```
%                                                   measurements    =
regionprops([allParticles(i).RegionPixels<globalThresh],
'Perimeter', 'Area');
            allParticles(i).Circ                                    =
2.*(pi.*[allParticles(i).Area])^0.5./[allParticles(i).Perimete
r];

            allParticles(i).Spotty = 0;

            allParticles(i).Cluster = 0;



rectangle(tab3.Children,'Position',allParticles(i).BoundingBox
,'EdgeColor','w')

        end


        % Show 'Identified Particles' image full size with
global particle ID's
%                                                       fig.h2      =
figure('Name','2','Units','normalized','Position',[0.5     0.35
0.45 0.55]);
        imshow(I,'Parent',fig.h2.CurrentAxes)
        movegui(fig.h2,'onscreen')
        title(fig.h2.CurrentAxes,'Identified Particles')
        axes(fig.h2.CurrentAxes)
        % Add boxes and text
        for i = 1:numObj

text(allParticles(i).Centroid(1,1),allParticles(i).Centroid(1,
2),num2str(allParticles(i).RegionID),'Color','y',...
                'FontSize',14,'FontWeight','bold');

rectangle('Position',allParticles(i).BoundingBox,'EdgeColor','
w')

        end
        assignin('base','allParticles',allParticles);

    end

% find Spotty Particles
    function FindSpottyParticles(hObject,eventdata)
        % Create a table called 'spottyParticles' that contains
just the
        % information about the 'spotty' particles and highlight
these particles
        % with red boxes
```

```
        % spotThresh is the minimum number of spots per particle
to be classed as a
        % spotty particle

        % spotThresh = 12;
        numObj = numel(allParticles);

        for i = 1:numObj
            if length(allParticles(i).RegProps)>spotThresh

rectangle(fig.h2.CurrentAxes,'Position',allParticles(i).Boundi
ngBox,'EdgeColor','r')
                allParticles(i).Spotty = 1;
            end
        end

    end

% Manually add spotty Particles
    function ADDSpottyParticles(hObject,eventdata)
        [xi,yi] = getpts(fig.h2); %A shift-, right-, or double-
click adds a final point and ends the selection. Pressing Return
or Enter ends the selection without adding a final point.
Pressing Backspace or Delete removes the previously selected
point.

        endi = numel(allParticles);

        for i = 1:endi
            for k = 1:numel(xi)
                try
                    BoxPts = allParticles(i).BoundingBox;
                    xv(1) = BoxPts(1);
                    xv(2) = BoxPts(1) + BoxPts(3);
                    xv(3) = BoxPts(1) + BoxPts(3);
                    xv(4) = BoxPts(1);

                    yv(1) = BoxPts(2);
                    yv(2) = BoxPts(2);
                    yv(3) = BoxPts(2) + BoxPts(4);
                    yv(4) = BoxPts(2) + BoxPts(4);

                    in = inpolygon(xi(k),yi(k),xv,yv);

                    if in
                        disp([allParticles(i).RegionID])
                        [lia,              locb]             =
ismember([allParticles(i).RegionID],[allParticles.RegionID]);

                        hold on
```

```
rectangle('Position',allParticles(locb).BoundingBox,'EdgeColor
','g')
                        pause(0.5)

rectangle('Position',allParticles(locb).BoundingBox,'EdgeColor
','r')
                        allParticles(locb).Spotty = 1;

                    end
                catch
                    disp('ping-ADDspotty')%
disp({'Loop out of bounds',[i]})
                end
            end
%             endi = numel(allParticles);
        end

    end

% Manually REMOVE spotty Particles
    function REMOVESpottyParticles(hObject,eventdata)
        [xi,yi] = getpts(fig.h2); %A shift-, right-, or double-
click adds a final point and ends the selection. Pressing Return
or Enter ends the selection without adding a final point.
Pressing Backspace or Delete removes the previously selected
point.

        endi = numel(allParticles);

        for i = 1:endi
            for k = 1:numel(xi)
                try
                    BoxPts = allParticles(i).BoundingBox;
                    xv(1) = BoxPts(1);
                    xv(2) = BoxPts(1) + BoxPts(3);
                    xv(3) = BoxPts(1) + BoxPts(3);
                    xv(4) = BoxPts(1);

                    yv(1) = BoxPts(2);
                    yv(2) = BoxPts(2);
                    yv(3) = BoxPts(2) + BoxPts(4);
                    yv(4) = BoxPts(2) + BoxPts(4);

                    in = inpolygon(xi(k),yi(k),xv,yv);

                    if in
                        disp([allParticles(i).RegionID])
                        [lia,              locb]              =
ismember([allParticles(i).RegionID],[allParticles.RegionID]);

                        hold on
```

```
rectangle('Position',allParticles(locb).BoundingBox,'EdgeColor
','g')
                        pause(0.5)

rectangle('Position',allParticles(locb).BoundingBox,'EdgeColor
','w')
                        allParticles(locb).Spotty = 0;

                    end
                catch
                    disp('ping-REMOVEspotty')%
disp({'Loop out of bounds',[i]})
                end
            end
%             endi = numel(allParticles);
        end

    end


% Remove clusters function
    function PickClust(hObject,eventdata)
        [xi,yi] = getpts(fig.h2); %A shift-, right-, or double-
click adds a final point and ends the selection. Pressing Return
or Enter ends the selection without adding a final point.
Pressing Backspace or Delete removes the previously selected
point.

        endi = numel(allParticles);

        for i = 1:endi
            for k = 1:numel(xi)
                try
                    BoxPts = allParticles(i).BoundingBox;
                    xv(1) = BoxPts(1);
                    xv(2) = BoxPts(1) + BoxPts(3);
                    xv(3) = BoxPts(1) + BoxPts(3);
                    xv(4) = BoxPts(1);

                    yv(1) = BoxPts(2);
                    yv(2) = BoxPts(2);
                    yv(3) = BoxPts(2) + BoxPts(4);
                    yv(4) = BoxPts(2) + BoxPts(4);

                    in = inpolygon(xi(k),yi(k),xv,yv);

                    if in
                        disp([allParticles(i).RegionID])
                        [lia,              locb]             =
ismember([allParticles(i).RegionID],[allParticles.RegionID]);
```

```
                        hold on

rectangle('Position',allParticles(locb).BoundingBox,'EdgeColor
','g')
                        pause(0.5)

rectangle('Position',allParticles(locb).BoundingBox,'EdgeColor
','k')
                        allParticles(locb).Cluster = 1;

                    end
                catch
                    disp('ping-pickClust')%
disp({'Loop out of bounds',[i]})
                end
            end
%             endi = numel(allParticles);
        end
    end

    function SetSpottyParams(hObject,eventdata)
        prompt = {'Enter Number of Spots Value:','Grayscale
Threshold Value used to find spots:'};
        dlg_title = 'Input Threshold';
        num_lines = 1;
        defaultans                                          =
{num2str(spotThresh),num2str(spotGrayThresh)};
        answer                                              =
inputdlg(prompt,dlg_title,num_lines,defaultans);
        spotThresh = str2num(answer{1});
        spotGrayThresh = str2num(answer{2});

    end




% Set thresholding function
    function SetThresh(hObject,eventdata)
        prompt = {'Enter Threshold Value:'};
        dlg_title = 'Input Threshold';
        num_lines = 1;
        defaultans = {'40'};
        answer                                              =
inputdlg(prompt,dlg_title,num_lines,defaultans);
        globalThresh = str2num(answer{1});
        BW = I > globalThresh;
%         subplot(1,3,2),
        imshow(BW,'Parent', tab2.Children)
        title(tab2.Children,'Binary Image')
```

```
    end

% Update particle list in workspace function
    function PushAllParticles(hObject,eventdata)
        %         saveToExcel(filename,allParticles,h2)
        assignin('base','allParticles',allParticles);

        spottyParticles1                                        =
allParticles([allParticles.Spotty]==1);
        spottyParticles                                         =
spottyParticles1([spottyParticles1.Cluster]==0);
        assignin('base','spottyParticles',spottyParticles);
    end

% Save allParticles list to excel and save images
    function SaveToExcel(hObject,eventdata)

        newfolder = filename(1:end-4);

        mkdir(newfolder)

        oldFolder = cd(newfolder);

        filename(end-3:end) = '.xls';


xlswrite(filename,[allParticles.RegionID;allParticles.MinorAxi
sLength;allParticles.MajorAxisLength;allParticles.Perimeter;al
lParticles.Area;allParticles.Circ;allParticles.Aspect;allParti
cles.Spotty;allParticles.Cluster]','allParticles')

        filename(end-3:end) = '.png';

        saveas(fig.h2,filename)

        filename(end-3:end) = '.fig';

        saveas(fig.h2,filename)

        cd(oldFolder)

    end


% Close Request function to close down all windows open
    function my_closereq(src,callbackdata)
        % Close request function
        % to display a question dialog box
        selection = questdlg('Are you sure you want to close the
App?',...
            'Are you sure?',...
```

```
            'Yes','No','Yes');
        switch selection
            case 'Yes'
                delete(findall(0));
            case 'No'
                return
        end
    end

end
```

A1.2

To assess the effect of the threshold on the results from the image analysis, an image from the SLM50 was used with three different thresholds applied. The threshold of 40, which was used for the image set from the SLM50, and for a change of 10 higher and lower in the grey value level for the threshold. From the manual selection of the thresholding level the grey value was not altered larger than 10 points from the default threshold. The binarised images from the threshold are presented in Figure A.0.1.

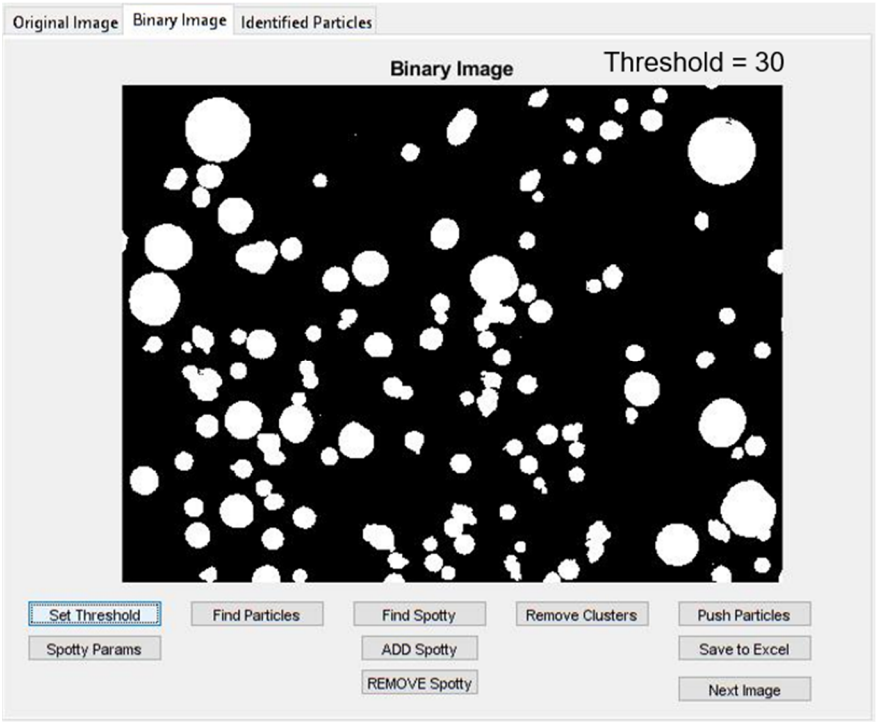

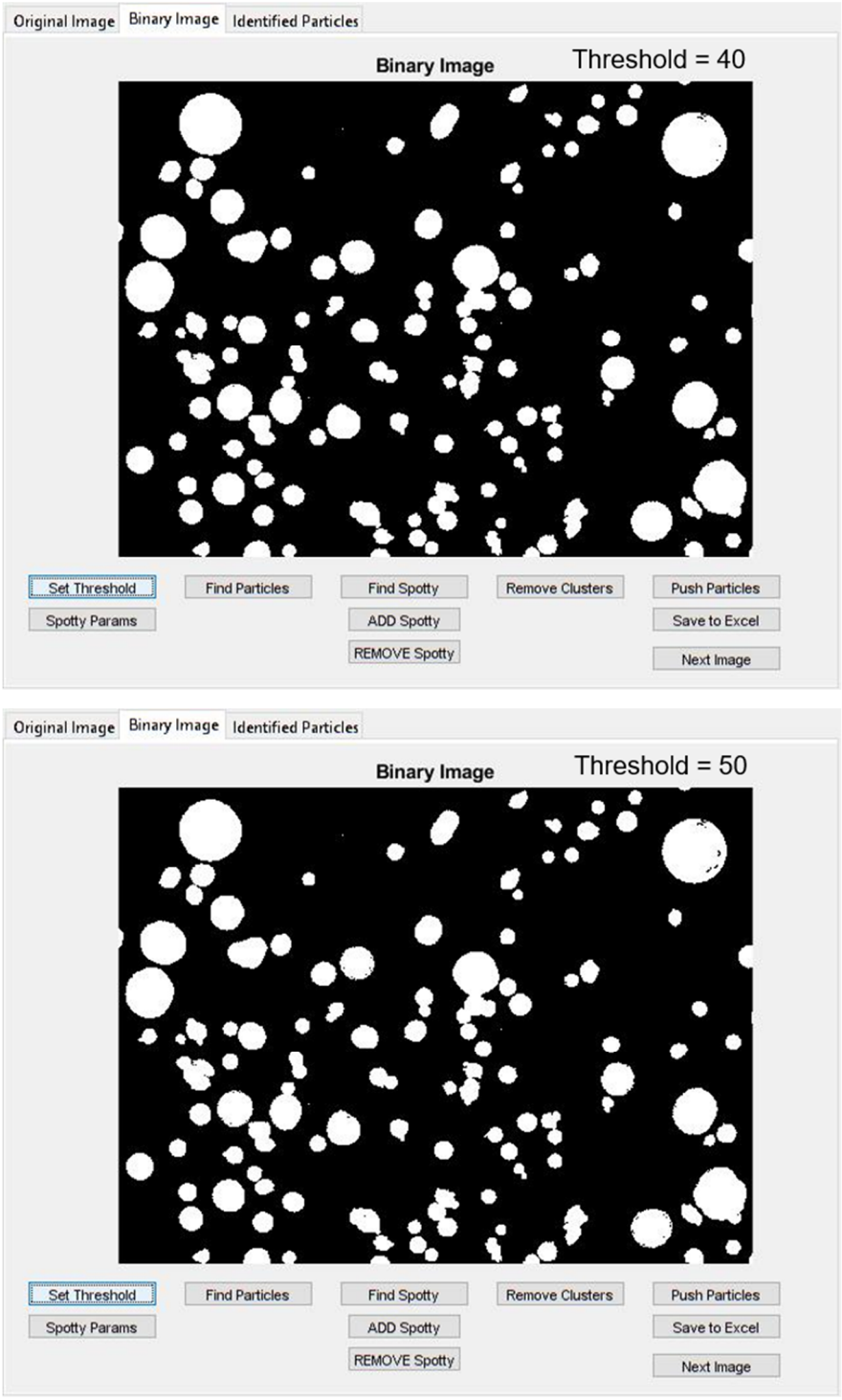

Figure A.0.1 Thresholding of particle image from SLM50 using a threshold of 30, 40, and 50

It can be seen that visibly there is not much difference with the change in thresholding. In the top right particle it can be seen that the threshold is starting to identify the darker oxides inside the particle region. The subsequent identification of the particles and oxidised particles in Figure A.0.2.

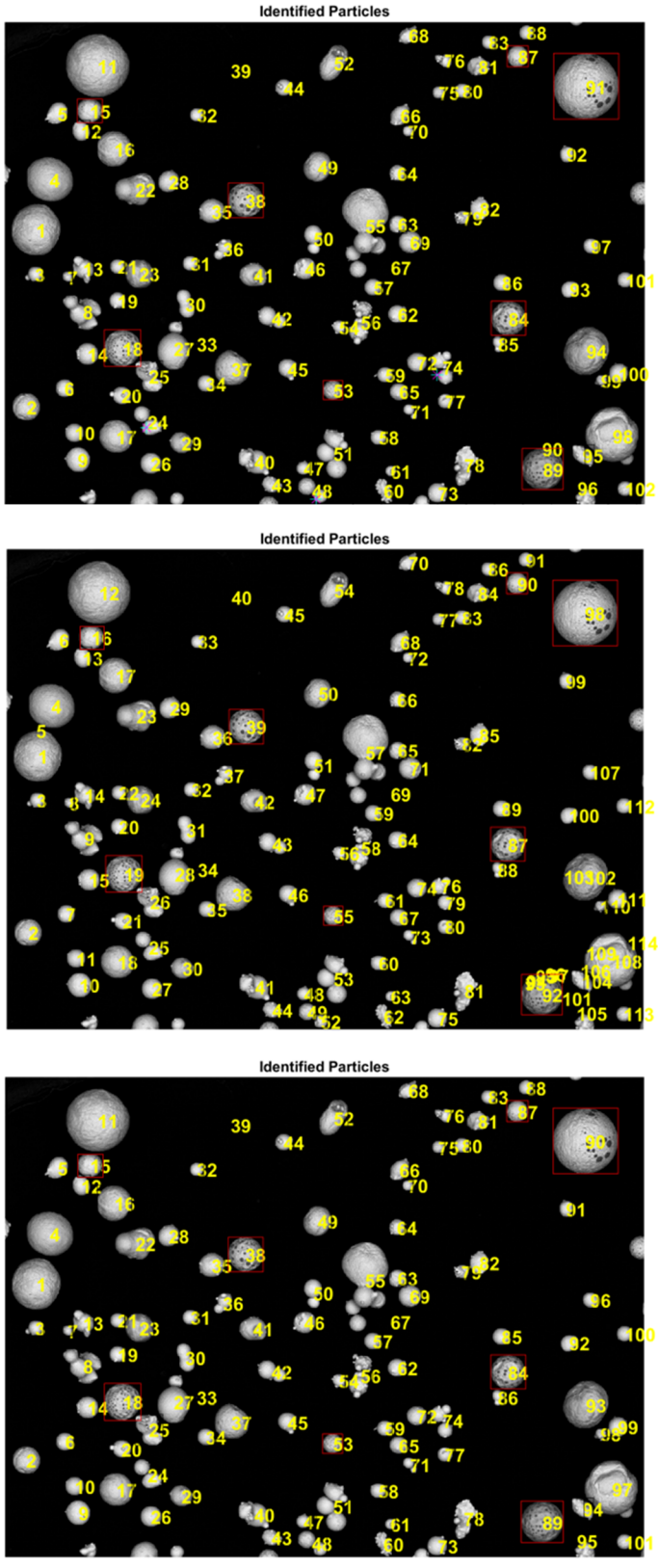

Figure A.0.2 Identification of particles and oxidised particles for each threshold

Table A.1 shows a summary of the results from the different thresholds of the same particle (ID 1), and for all the particles.

Table A.1 Comparison of image analysis results for particle 1 and all particles for the three thresholds

Threshold	ID	Min axis	Maj Axis	Perime	Area	CE	Min axis UM	Maj axis UM
30	1	97.60	103.22	317.10	7907.00	100.34	85.91	90.86
40	1	97.25	103.01	315.39	7863.00	100.06	85.61	90.68
50	1	96.64	102.50	323.53	7773.00	99.48	85.07	90.23

Threshold	ID	Perim UM	Area UM	CE UM	Circ	AR	Spotty	Cluster
30	1	279.1347	6960.387	94.13947	0.994074	0.945518	0	0
40	1	277.6347	6921.655	93.87718	0.99666	0.944125	0	0
50	1	284.7984	6842.43	93.33837	0.966014	0.942792	0	0

All particles

Threshold	N	N <5	N oxides	N removed	Avg Min width filtered	Avg min width all
30	101	4	8	2	43.54755	41.73753
40	102	5	8	1	42.63597	41.08045
50	114	15	8	1	42.5325	37.06138

From the results in Table A.1, it can be seen that a change in grey value of 10 for the threshold had a total impact of varying the minimum width (used for the analysis in Chapter 6) of particle 1 by 0.54 µm and a maximum change in average minimum width for all the particles of 0.90 µm. It can be seen that the average minimum width for all particles has a larger variation, this is due to the higher thresholding creating smaller pixels due to noise which are identified as particles, and for the lower threshold the joining of multiple particles identified as a single particle. As discussed in Section 6.1.2 and shown in Figure 6.3, the filter of particles <5 µm removes this noise and the manual correction of mis-identified particles removes the issue of conjoined particles. This comparison is only over ~100 particles in this image, for the samples there was an average of 1809 particles analysed which will further reduce the error that might be caused by manual user input threshold levels. It is accepted that there will be errors but all thresholding techniques have disadvantages and it has been shown that the thresholding in this investigation does not affect the main purpose of the investigation. In terms of identifying particle size, the change in size by the thresholding is less than the change in size produced by using a circular equivalent instead of the minimum width.

A1.3

Morphologi results

Table A.2 Morphologi G3 results for circularity over size bins for virgin 718 and the spatter produced from the different PBF-LB systems

Circularity	Volume	Size						
Highly-spherical	>=0.95	<15	15-30	30-35	45-53	53-63	>63	Total
Virgin powder	50.20%	0.19 %	10.92 %	28.35 %	8.93%	1.82%	0.00%	50.20 %
SLM50 spatter	30.64%	0.01 %	1.38%	14.27 %	7.26%	3.25%	4.47%	30.64 %
AM125 spatter	29.15%	0.03 %	1.98%	9.32%	6.52%	3.22%	8.09%	29.15 %
SLM125 spatter	22.38%	0.05 %	1.88%	5.74%	4.87%	3.88%	5.96%	22.38 %
Slightly-spherical	0.95>x>=0.85	<15	15-30	30-35	45-53	53-63	>63	Total
Virgin powder	33.41%	0.03 %	3.53%	18.68 %	8.37%	2.54%	0.28%	33.41 %
SLM50 spatter	20.98%	0.00 %	0.19%	6.47%	6.24%	3.71%	4.36%	20.98 %
AM125 spatter	22.35%	0.01 %	0.55%	6.29%	6.70%	4.03%	4.76%	22.35 %
SLM125 spatter	21.19%	0.01 %	0.78%	5.24%	4.54%	4.34%	6.29%	21.19 %
Non-spherical	<0.85	<15	15-30	30-35	45-53	53-63	>63	Total
Virgin powder	16.38%	0.01 %	0.51%	4.03%	4.69%	4.65%	2.49%	16.38 %
SLM50 spatter	48.38%	0.00 %	0.00%	0.80%	2.73%	4.61%	40.24 %	48.38 %
AM125 spatter	48.50%	0.00 %	0.03%	1.17%	2.03%	3.44%	41.83 %	48.50 %
SLM125 spatter	56.43%	0.00 %	0.07%	1.75%	2.07%	6.09%	46.45 %	56.43 %

A1.4

Morphologi G3 SOP parameters used for the study in Chapter 6.

Morphologi G3 SOP

Measurement control

Fixed no. slides/plates	
TRUE	1

Sample carrier

SDU Glass Plate

180 x 110 mm

Sample Dispersion Unit

injectionPressure	injectionTime	SettlingTime	UsesEntrainment	UsingSDU
1	20	60	TRUE	TRUE

Illumination settings

LightCalInt	LightIntTol
80	20

Optics selection

Lens	Size range	Overlap	Threshold
10x	3.5-210	40%	121

Analysis settings

Trash size	Segmentation	Fill holes
10 pixels	NONE	TRUE

Filters

	Mean intensity value
Dust	<100
	CE Diameter
Sub 5um	<5

Classification

	Circ
Highly spherical	>=0.95
Slightly spherical	0.85=<x<0.95
Non spherical	<0.85

Appendix A.2

Figure A. shows the rig used to extract the powder from the capsules as described in Section 3.2.2.2. The capsule is rigged up to free flow into the glass container which is secured to the table. The arm holding the capsule has a pneumatic ball vibrator attached to it. The vibrator operates a wide range of frequencies which were used to ensure that all powder had been emptied into the glass container.

Figure A.3 Rig used to fully empty the capsule contents for measurement. The pneumatic ball vibrator has a variable frequency to vibrate the capsule and ensure all the contents are emptied into the glass container

The full data and results for Chapter 7 are presented in the tables below. The experiment was conducted at room temperature using the density of de-ionised water (ρ_{water}) at 20 °C of 0.9982 g.cm^{-3}. The density of the Inconel 718 material was 8.22 g.cm^{-3}. The calculations are as shown and discussed in Section 7.1.2:

$$m = FV - EV \; and \; V = \frac{FC - EC}{\rho_{water}}$$

$$\rho_{pow} = \frac{m}{V}$$

$$PBD = \frac{\rho_{pow}}{\rho_{718}}$$

The total errors from the weight measurements (±0.00005 g) in the PBD calculation are ~0.0005%, calculated using:

$$\frac{\Delta\rho}{\rho} = \sqrt{\left(\frac{\Delta EV}{EV}\right)^2 + \left(\frac{\Delta FV}{FV}\right)^2 + \left(\frac{\Delta EC}{EC}\right)^2 + \left(\frac{\Delta FC}{FC}\right)^2}$$

Table A.3 Data and results for build 1 in Chapter 7

	Empty Vial (g) (*EV*) ±0.00005	Full Vial (g) (*FV*) ±0.00005	Powder Weight (g) (*m*)	Empty Capsule (EC) ±0.00005	Water Full Capsule (g) (*FC*) ±0.00005	Water Weight (g) (*mw*)	Volume (g/mm3) (*V*)	Density (g/mm^3) (ρ_{pow})	% density (*PBD*)	Total % Error	Volume variation from V_d=12.5 cm^3 (g/cm^3)	% deviation from V_d
A1	14.8132	77.2237	62.4105	25.7136	38.0994	12.3858	12.40813	5.029805	61.190%	0.00042%	-0.09187	-0.735%
A2	14.8629	76.9822	62.1193	25.8241	38.2108	12.3867	12.40904	5.005973	60.900%	0.00041%	-0.09096	-0.728%
A3	14.9982	76.9785	61.9803	25.546	37.9226	12.3766	12.39892	4.998847	60.813%	0.00041%	-0.10108	-0.809%
A4	14.8565	76.9815	62.125	25.7026	37.9816	12.279	12.30114	5.050344	61.440%	0.00042%	-0.19886	-1.591%
AB	14.8007	77.3808	62.5801	25.7726	38.1371	12.3645	12.3868	5.052162	61.462%	0.00042%	-0.1132	-0.906%
B1	14.8286	77.3597	62.5311	25.9474	38.3221	12.3747	12.39701	5.044045	61.363%	0.00041%	-0.10299	-0.824%
B2	14.7716	77.1442	62.3726	25.9843	38.3601	12.3758	12.39812	5.030812	61.202%	0.00042%	-0.10188	-0.815%
B3	14.9655	76.9393	61.9738	26.6365	39.0139	12.3774	12.39972	4.998	60.803%	0.00041%	-0.10028	-0.802%
B4	14.7558	76.9844	62.2286	26.6893	39.0729	12.3836	12.40593	5.016036	61.022%	0.00041%	-0.09407	-0.753%
BD	14.9178	77.3483	62.4305	26.0129	38.3971	12.3842	12.40653	5.032067	61.217%	0.00041%	-0.09347	-0.748%
C1	14.9222	77.3288	62.4066	25.6495	38.0302	12.3807	12.40303	5.031563	61.211%	0.00041%	-0.09697	-0.776%
C2	14.8797	77.0394	62.1597	25.6972	38.0871	12.3899	12.41224	5.007935	60.924%	0.00041%	-0.08776	-0.702%
C3	14.8372	76.8404	62.0032	25.6565	38.0406	12.3841	12.40643	4.997666	60.799%	0.00042%	-0.09357	-0.749%
C4	14.8808	76.8814	62.0006	25.5951	37.9724	12.3773	12.39962	5.000202	60.830%	0.00042%	-0.10038	-0.803%
AC	14.8612	77.0044	62.1432	26.3566	38.7137	12.3571	12.37938	5.019895	61.069%	0.00041%	-0.12062	-0.965%
D1	14.8735	77.3049	62.4314	25.8437	38.2111	12.3674	12.3897	5.038975	61.301%	0.00041%	-0.1103	-0.882%
D2	14.77	77.1937	62.4237	25.9686	38.3513	12.3827	12.40503	5.032128	61.218%	0.00042%	-0.09497	-0.760%

D3	14.792	76.7555	61.9635	25.7006	38.0735	12.3729	12.39521	4.998987	60.815%	0.00042%	-0.10479	-0.838%
D4	14.7903	76.9555	62.1652	25.7428	38.1065	12.3637	12.38599	5.018991	61.058%	0.00042%	-0.11401	-0.912%
CD	14.7964	77.4562	62.6598	25.7217	38.0793	12.3576	12.37988	5.061421	61.574%	0.00042%	-0.12012	-0.961%
O	14.7965	76.8384	62.0419	25.5487	37.9175	12.3688	12.3911	5.006971	60.912%	0.00042%	-0.1089	-0.871%
Avg	14.84622	77.09149	62.24527	25.87192	38.2429	12.37098	12.39328	5.022516	61.101%	0.00041%	-0.10672	-0.854%
Std dev	0.064002	0.203718	0.215347	0.315032	0.318388	0.022531	0.022572	0.019406	0.236%	1.8E-08	0.022572	0.181%

Table A.4 Data and results for build 2 in Chapter 7. Capsule O had powder spilled during removal so was discarded from the analysis

	Empty Vial (g) (*EV*) ±0.00005	Full Vial (g) (*FV*) ±0.00005	Powder Weight (g) (*m*)	Empty Capsule (EC) ±0.00005	Water Full Capsule (g) (*FC*) ±0.00005	Water Weight (g) (*mw*)	Volume (g/mm3) (*V*)	Density (g/mm^3) (ρ_{pow})	% density (*PBD*)	Total % Error	Volume variation from V_d=12.5 cm^3 (g/cm^3)	% deviation from V_d
A1	10.8767	72.6868	61.8101	27.8689	40.2515	12.3826	12.40493	4.982705	60.617%	0.00051%	-0.09507	-0.761%
A2	10.8464	72.3056	61.4592	28.1686	40.5429	12.3743	12.39661	4.957741	60.313%	0.00051%	-0.10339	-0.827%
A3	10.8384	72.3042	61.4658	27.7048	40.0839	12.3791	12.40142	4.956351	60.296%	0.00052%	-0.09858	-0.789%
A4	10.8841	72.5084	61.6243	27.5921	39.9966	12.4045	12.42687	4.958957	60.328%	0.00051%	-0.07313	-0.585%
AB	10.9679	72.9253	61.9574	28.1871	40.55	12.3629	12.38519	5.002538	60.858%	0.00051%	-0.11481	-0.918%
B1	10.8387	72.713	61.8743	28.6519	41.0166	12.3647	12.387	4.995101	60.768%	0.00051%	-0.113	-0.904%
B2	10.7878	72.4898	61.702	28.5358	40.8916	12.3558	12.37808	4.984779	60.642%	0.00052%	-0.12192	-0.975%
B3	10.8705	72.3565	61.486	27.9179	40.2885	12.3706	12.39291	4.961386	60.357%	0.00051%	-0.10709	-0.857%

B4	10.8841	72.5298	61.6457	28.0887	40.3613	12.2726	12.29473	5.013994	60.997%	0.00051%	-0.20527	-1.642%
BD	10.9184	72.612	61.6936	28.5755	40.9621	12.3866	12.40894	4.971707	60.483%	0.00051%	-0.09106	-0.729%
C1	10.8212	72.6054	61.7842	27.666	40.0437	12.3777	12.40002	4.982589	60.615%	0.00052%	-0.09998	-0.800%
C2	10.8808	72.4192	61.5384	27.7488	40.1374	12.3886	12.41094	4.9584	60.321%	0.00051%	-0.08906	-0.712%
C3	10.7884	72.3248	61.5364	27.6129	39.9981	12.3852	12.40753	4.9596	60.336%	0.00052%	-0.09247	-0.740%
C4	10.7895	72.3121	61.5226	27.4641	39.8497	12.3856	12.40793	4.958327	60.320%	0.00052%	-0.09207	-0.737%
AC	10.8486	72.2346	61.386	28.9605	41.3286	12.3681	12.3904	4.954318	60.272%	0.00051%	-0.1096	-0.877%
D1	10.837	72.6468	61.8098	28.4267	40.7832	12.3565	12.37878	4.993205	60.745%	0.00051%	-0.12122	-0.970%
D2	10.8448	72.5323	61.6875	28.4549	40.8225	12.3676	12.3899	4.978853	60.570%	0.00051%	-0.1101	-0.881%
D3	10.8414	72.3165	61.4751	27.7848	40.1525	12.3677	12.39	4.96167	60.361%	0.00052%	-0.11	-0.880%
D4	10.8387	72.3996	61.5609	27.9367	40.2939	12.3572	12.37948	4.972817	60.497%	0.00051%	-0.12052	-0.964%
CD	11.0911	73.1944	62.1033	27.9052	40.2759	12.3707	12.39301	5.011157	60.963%	0.00051%	-0.10699	-0.856%
O	10.9018	72.0149	61.1131	28.1786	40.4875	12.3089	12.3311	4.956015	60.292%	0.00051%	-0.1689	-1.351%
Avg	10.86649	72.52086	61.65613	28.0626	40.43153	12.36893	12.39123	4.97581	60.533%	0.00051%	-0.10877	-0.870%
Std dev	0.065798	0.230801	0.183364	0.405969	0.399708	0.02521	0.025256	0.018756	0.228%	2.84E-08	0.025256	0.00202

Table A.5 Data and results for build 3 in Chapter 7

	Empty Vial (g) (*EV*) ±0.00005	Full Vial (g) (*FV*) ±0.00005	Powder Weight (g) (*m*)	Empty Capsule (EC) ±0.00005	Water Full Capsule (g) (*FC*) ±0.00005	Water Weight (g) (*mw*)	Volume (g/mm3) (*V*)	Density (g/mm^3) (ρ_{pow})	% density (*PBD*)	Total % Error	Volume variation from V_d=12.5 cm^3 (g/cm^3)	% deviation from V_d
A1	10.8257	71.2261	60.4004	26.644	39.0195	12.3755	12.39782	4.871858	59.268%	0.00052%	-0.10218	-0.817%
A2	10.8194	70.73	59.9106	26.8709	39.2393	12.3684	12.3907	4.835125	58.821%	0.00052%	-0.1093	-0.874%
A3	10.8354	70.8252	59.9898	26.3973	38.7725	12.3752	12.39752	4.838857	58.867%	0.00052%	-0.10248	-0.820%
A4	10.8118	70.9675	60.1557	26.2013	38.5777	12.3764	12.39872	4.851768	59.024%	0.00052%	-0.10128	-0.810%
AB	10.8794	71.5504	60.671	27.0339	39.4011	12.3672	12.3895	4.896969	59.574%	0.00052%	-0.1105	-0.884%
B1	10.8133	71.3644	60.5511	26.9527	39.2922	12.3395	12.36175	4.898262	59.590%	0.00052%	-0.13825	-1.106%
B2	10.8734	71.2031	60.3297	27.0506	39.4022	12.3516	12.37387	4.875571	59.314%	0.00052%	-0.12613	-1.009%
B3	10.8494	70.9672	60.1178	26.6413	39.0047	12.3634	12.38569	4.853809	59.049%	0.00052%	-0.11431	-0.914%
B4	10.8013	71.0834	60.2821	26.6962	39.0626	12.3664	12.3887	4.865894	59.196%	0.00052%	-0.1113	-0.890%
BD	10.8885	71.3416	60.4531	27.2303	39.5983	12.368	12.3903	4.879066	59.356%	0.00052%	-0.1097	-0.878%
C1	10.8754	71.2129	60.3375	26.4827	38.8552	12.3725	12.39481	4.867965	59.221%	0.00052%	-0.10519	-0.842%
C2	10.8624	70.8978	60.0354	26.3198	38.583	12.2632	12.28531	4.886762	59.450%	0.00052%	-0.21469	-1.717%
C3	10.8648	70.9407	60.0759	26.3218	38.7054	12.3836	12.40593	4.842515	58.911%	0.00052%	-0.09407	-0.753%
C4	10.7561	70.8004	60.0443	26.2816	38.6609	12.3793	12.40162	4.841649	58.901%	0.00052%	-0.09838	-0.787%
AC	10.8124	70.7899	59.9775	27.4484	39.8038	12.3554	12.37768	4.845617	58.949%	0.00052%	-0.12232	-0.979%

D1	10.825	71.3514	60.5264	26.8097	39.1707	12.361	12.38329	4.887748	59.462%	0.00052%	-0.11671	-0.934%
D2	10.7924	71.1553	60.3629	26.8619	39.23	12.3681	12.3904	4.871746	59.267%	0.00052%	-0.1096	-0.877%
D3	10.9252	71.0885	60.1633	26.5995	38.969	12.3695	12.39181	4.855088	59.064%	0.00052%	-0.10819	-0.866%
D4	10.8646	71.0834	60.2188	26.571	38.9367	12.3657	12.388	4.86106	59.137%	0.00052%	-0.112	-0.896%
CD	10.8749	71.6888	60.8139	26.4853	38.8551	12.3698	12.39211	4.907471	59.702%	0.00052%	-0.10789	-0.863%
O	10.8695	71.035	60.1655	26.9032	39.2863	12.3831	12.40543	4.849933	59.002%	0.00052%	-0.09457	-0.757%
Avg	10.84382	71.10967	60.26584	26.70492	39.06791	12.36299	12.38528	4.86594	59.196%	0.00052%	-0.11572	-0.93%
Std dev	0.038465	0.247473	0.235685	0.322006	0.323192	0.024474	0.024518	0.020656	0.251%	1.89E-08	0.024696	0.20%